High Dose Rate Brachytherapy Treatment Verification using a Flat Panel Detector

Ryan Lee Smith

BSc, MAppSci (Monash University)

A thesis submitted in fulfilment of the requirements for the degree of Doctor of Philosophy

School of Science

College of Science, Engineering and Health

RMIT University

June 2017

Declaration

I certify that except where due acknowledgement has been made, the work is that of the author alone; the work has not been submitted previously, in whole or in part, to qualify for any other academic award; the content of the thesis is the result of work which has been carried out since the official commencement date of the approved research program; any editorial work, paid or unpaid, carried out by a third party is acknowledged; and, ethics procedures and guidelines have been followed.

I acknowledge the support I have received for my research through the provision of an Australian Government Research Training Program Scholarship.

Ryan Lee Smith

June 2017

Acknowledgements

This thesis is the result of an idea that I had after many years of treating HDR prostate brachytherapy patients at Alfred Health Radiation Oncology. I appreciate the enthusiasm of Professor Peter Johnston and Professor Rick Franich when I suggested this as a potential research project.

I would like to thank the Medical Physics Team at The Alfred, many times they have felt the additional burden of a staff member attempting a part-time degree. Specifically, I would like to thank Dr Trevor Ackerly, A/Prof Jeff Crosbie, Craig Lancaster, Dr Vanessa Panettieri, Frank Gagliardi, Dr Matthew Haynes, Clem Conheady for their support and valued discussions. Also, special thanks to Dr Duncan Butler at ARPANSA for the time spent at that facility characterising the detector for this project. Kirsten Bell and Peter Douglas, formally of Nucletron Australia Pty Ltd, have been great supporters of this project and I sincerely thank you both.

I would sincerely like to thank the fantastic Brachytherapy team at Alfred Health Radiation Oncology for their support and encouragement during this project. The system has grown into what it is today because of this great team: Professor Jeremy Millar, Dr Bronwyn Matheson, Dr Ben Hindson, Catherine Beaufort, Steph Miller, Hayley Mack, Natasha Mason, Deborah Stokes, and Karen Scott.

I would also like to thank the current and past students at RMIT; Max Hanlon, Michael Taylor, Leon Dunn, Adam Yeo, Steph Keehan, Jeremy Supple and Kyle Ewert for their companionship and helpful discussions during this time.

I would also like to acknowledge the kind words and support at conferences and meetings from many colleagues in the brachytherapy field.

I would like to thank my co-supervisors Professor Annette Haworth, Professor Jeremy Millar, Dr Michael Taylor and Dr Leah McDermott for their input, comments and

suggestions into this project and feedback. Special thanks to my senior supervisor Rick Franich for his friendship and enthusiasm for this project, many times going above and beyond to get this thesis across the line.

Thanks to the awesome crew at Montrose CFA for their continuous encouragement and support during this period. Also thanks to Tex Perkins and Murray Paterson for the soundtrack to this work.

My family have been inspirational during this long project. My parents, Des and Denise, for initially providing me with the opportunity to explore science as a young man and the emphasis on the value of education. Thank you to my sister Sarah for your continuous support and encouragement.
My extended family have been very supportive and encouraging, particularly Brian and Judy, and I thank you all for this.

To my three beautiful children Charlotte, Veronique and Jean, I thank you for being so understanding and patient these past years. I have often been distracted by this study and I certainly look forward to more free time to spend with all of you.

It is hard to put into words how much I appreciate the incredible love and support my wife Melissa has given me during this work. She has always been there for me and has given me the confidence and drive to complete this degree. You have inspired me to make a difference, and I dedicate this work to you. I love you Melissa.

Table of Contents

List of Abbreviations

^{192}Ir	Iridium 192
2D	Two Dimensional
3D	Three Dimensional
A-P	Anterior-Posterior
a-Si	Amorphous Silicon
AHRO	Alfred Health Radiation Oncology
AKR	Air Kerma Rate
ARPANSA	Australian Radiation Protection and Nuclear Safety Agency
BB	Ball Bearing
COM	Centre of Mass
CT	Computed Tomography
EBRT	External Beam Radiation Therapy
EPID	Electronic Portal Imaging Device
FID	Focus to Imager Distance
FPD	Flat Panel Detector
FOV	Field of View
FWHM	Full Width Half Maximum
FW80M	Full Width 80% Maximum
HDR	High Dose Rate
HVL	Half Value Layer
IAS2	Image Acquisition System version 2
ICRP	International Commission on Radiological Protection
IGRT	Image Guided Radiation Therapy
IGBV	Image Guided Brachytherapy Verification
INF	Inferior
IVD	In vivo Dosimetry
LINAC	Linear Accelerator
LT	Left
MOSFET	Metal Oxide Semiconductor Field Effect Transistor
MRI	Magnetic Resonance Imaging
OAR	Organ at Risk
PTV	Planning Target Volume
R-L	Right-Left
RMSE3D	3D Root Mean Square Error
ROI	Region Of Interest
RT	Right

S-I	Superior-Inferior
SDD	Source to Detector Distance
SUP	Superior
TG-43	Task Group 43
TLD	Thermoluminscent Dosimeter
TPS	Treatment Planning System
TRUS	Trans Rectal Ultrasound
US	Ultrasound

Publications

Peer Reviewed Journals

Smith RL, Hanlon M, Panettieri V, Millar JL, Matheson B, Haworth A, and Franich RD. *An Integrated System for Clinical Treatment Verification of HDR Prostate Brachytherapy combining Source Tracking with Pre-Treatment Imaging,* Brachytherapy, 2017 Sep 22. S1538-4721(17) 30426-9.

Smith RL, Haworth A, Panettieri V, Millar JL, and Franich RD *3D catheter reconstruction in HDR prostate brachytherapy for pre-treatment verification using a flat panel detector,* Physica Medica, Phys Med. 2017 Jul;39:121-131.

Smith RL, Haworth A, Panettieri V, Millar JL, and Franich RD. *A method for verification of treatment delivery in HDR prostate brachytherapy using a flat panel detector for both imaging and source tracking*. Med Phys. 2016;43(5):2435.

Smith RL, Taylor ML, McDermott LN, Haworth A, Millar JL, and Franich RD. *Source position verification and dosimetry in HDR brachytherapy using an EPID.* Med Phys. 2013;40(11):111706.

Book Chapters

Beaulieu L, **Smith RL**, Franich RD. *Real-Time In-Vivo Dosimetry*. In: Song WY, Tanderup K and Pieters B, editors. *Emerging Technologies in Brachytherapy,* CRC Press, Series in Medical Physics and Biomedical Engineering, May 2017, p.416, ISBN 9781498736527.

Venselaar JLM , Beaulieu L, Chen Z, **Smith RL**. *Advances in Brachytherapy Physics*. In: Godfrey DJ, Van Dyk J, Das SK, Curran BH, Wolbarst AB, editors. Advances in Medical Physics, Volume 6. Madison, WI: Medical Physics Publishing; July 2016. p.203. ISBN 9781930524903.

Published Conference Abstracts

Smith RL, Haworth A, Panettieri V, Millar JL, and Franich RD *Identification of Catheter Displacements in HDR Prostate Brachytherapy Using a 'Shift Image' Reconstruction Technique*, Brachytherapy, 16(3)Supp., S106, May 2017, DOI: 10.1016/j.brachy.2017.04.204

Smith RL, Haworth A, Hanlon M, Matheson B, Millar JL, Panettieri V, and Franich RD *Clinical Application of Pre-Treatment Image Verification of Catheter Positions for HDR Prostate Brachytherapy*, Brachytherapy, 16(3)Supp., S114, May 2017, DOI: 10.1016/j.brachy.2017.04.223

Smith RL, Haworth A, Panettieri V, Millar JL, and Franich RD *Treatment Delivery Error Trapping in HDR Brachytherapy*, Brachytherapy, 15:S39, May 2016, DOI: 10.1016/j.brachy.2016.04.040

Smith, R. L., J. Millar, B. Matheson, B. Hindson, M. Taylor, and R. Franich. (2015). *"Clinical implementation of in vivo source position verification in high dose rate prostate brachytherapy."* Radiol Oncol 115:S87.

Ryan L. Smith, Jeremy L Millar, Annette Haworth, Michael L Taylor, Rick D Franich. *In vivo treatment delivery error trapping in HDR prostate brachytherapy* J Contemp Brachy. vol.7,p103, 2015.

Natasha Mason, **Ryan L. Smith**, Vanessa Panettieri, Bronwyn Matheson, Jeremy L. Millar. *Evaluation of HDR prostate brachytherapy catheter displacement between planning and treatment using a flat panel detector.* J Contemp Brachy. vol.7,p104, 2015.

Smith RL, *Verifying Brachytherapy Treatment of Prostate Cancer*. Monash Comprehensive Cancer Consortium (MCCC), Annual Research Report 2013-14

Smith RL, *High Dose Rate (HDR) Brachytherapy Treatment Verification Using An Electronic Portal Imaging Device (EPID)*, Post Forum Report, International Congress on Radiotherapy & Oncology, 2nd ESTRO Forum, Geneva, Switzerland, p34-35, April 2013.

Smith RL, *High Dose Rate (HDR) Brachytherapy Treatment Verification Using An Electronic Portal Imaging Device (EPID)*, Post Forum Report, International Congress on Radiotherapy & Oncology, 2nd ESTRO Forum, Geneva, Switzerland, p34-35, April 2013.

Patents

Smith RL and Franich RD, Patent: "*Brachytherapy dose verification apparatus, system and method"*, WO 2012034157 A1, RMIT University, Filing date Sep. 13th, 2010.

Smith RL, Australian Innovation Patent, AU 2008100728 *"A real time treatment dose verification system for afterloader brachytherapy systems"*, 2008.

Abstract

High dose rate (HDR) brachytherapy treatments are usually delivered in large dose fractions and have the clinical advantage of highly conformal dose distributions due to the steep dose gradient produced by the ^{192}Ir source. The routine use of 3D imaging for treatment planning enables clinical teams to finely optimise the dose distribution around the defined target while limiting dose to the surrounding organs at risk. A significant challenge in brachytherapy is to ensure the dose is delivered to the patient as planned, which can be challenging due to factors that impact the accuracy of dose delivery. Due to the high degree of manual processes in brachytherapy, the relative risk of treatment delivery error is high when compared to other radiotherapy modalities. Additionally, interstitial and intracavitary brachytherapy suffer from anatomical motion and swelling due to catheter (or applicator) implant trauma.

There are two fundamental ways to verify a HDR brachytherapy treatment delivery: (i) verify the source dwell positions and times are as per the treatment plan, or (ii) perform a measurement in vivo with a dosimeter. Although reported in many small patient studies, in vivo dosimetry (IVD) has many limitations (*e.g. detector position uncertainty and limited sampling*) making the interpretation of results for treatment verification difficult. These challenges may be the reason for the limited routine application of IVD as a treatment verification technique. Since the treatment plan is a planned set of dwell positions and times, the former approach has the potential to verify the dose over the entire treatment volume.

This thesis addresses the need to improve the methodology for treatment verification in HDR brachytherapy. This work aims to establish a verification technique that can be used routinely in the clinical environment, not impact the patient and provide data that can be confidently interpreted to verify the entire treatment delivery. To achieve this, a novel approach to treatment verification was investigated, avoiding the challenges of directly measuring dose. Measurements of the source position, during the treatment

delivery (source tracking) were made, enabling direct comparison with the treatment plan for verification. Additionally, a method to establish a structured approach for performing this treatment verification process was accomplished, with the objective to enable routine use and widespread uptake of this process. The overall goal of this novel verification approach was to improve the quality of treatment delivery and patient safety in HDR brachytherapy.

To investigate this new approach, a flat panel detector (FPD) was employed as the measurement device. The detector, originally designed for use as an electronic portal imaging device, was characterised for use with an ^{192}Ir brachytherapy source. The FPD response and the image acquisition timing were investigated to demonstrate its capability for this work. The images of the response to the ^{192}Ir source, acquired with the FPD, were interpreted by a range of algorithms, extracting metrics that could be correlated with the position of the source. A concept for integration into a clinical environment was developed, by placing the FPD in the treatment couch, immediately below the target volume. The potential for the brachytherapy implant to displace due to anatomical and other influences was addressed by performing pre-treatment image verification. An imaging geometry was established, allowing registration with the treatment plan, enabling identification and quantification of implant displacement (in the treatment bunker) immediately prior to treatment delivery. The relationship established between the measurement frame of reference and the treatment plan permitted direct comparison of the measured dwell positions with the planned dwell positions for verification of treatment delivery. Treatment delivery metrics were developed to detect the occurrence of a treatment error, and based on the unique signature of the error, identification of the error source was possible. This concept of treatment verification was transferred into the clinical environment and a patient measurement was performed to understand the challenges of clinical implementation.

The FPD responded to the ^{192}Ir source, for a range of clinically relevant distances (20 to 200 mm) away from the FPD despite the low dose rates and the changing photon spectrum. The image acquisition time was one image capture every 1.8 seconds, and although not designed for this application, the FPD was adequate to perform this proof of principle work. Using a range of algorithms, the images acquired by the FPD were processed to determine the source position. It was determined that a centre of mass approach was the most accurate method (x and y s.d. 0.3 and 0.1 mm, up to 200 mm

from the FPD imaging plane) to determine source position in the 2D plane of the FPD. The influence of inhomogeneities and finite phantom geometry were quantified relative to their influence on the accuracy of determining the source position when applied in a clinical scenario. A structured approach to pre-treatment imaging was developed, with a robust method to perform a 3D reconstruction of the implant in the treatment bunker using a 'shift image' technique. A registration between the treatment planning system (TPS) and the measurement space (FPD) was established allowing quantitative evaluation of the implant changes since treatment planning imaging. Pre-treatment imaging was capable of identifying catheter displacements in the order of 2.0 mm with a confidence of 95%. Identification of a treatment delivery error was possible with the use of metrics that when combined define an error 'signature' that suggest the source of the error. The absolute relationship between the measurement space and the TPS allow error trapping to identify errors that would otherwise go undetected, for example an incorrect channel length definition error. This verification approach was applied successfully in a clinical setting. Pre-treatment imaging allowed confirmation that the implanted catheters had not significantly displaced prior to treatment and source tracking results confirmed the treatment was delivered as planned. The clinical implementation had minimal impact on the workflow, increasing the patient setup (and imaging) time by only 15 minutes while not adding any additional time to the radiation dose delivery portion of the treatment.

This initial work using a FPD for treatment verification in HDR brachytherapy has highlighted the benefits of this approach. This novel approach provides multiple layers of verification, including pre-treatment imaging (in 2D and 3D) to identify potential sources of error prior to treatment delivery. Source tracking, in conjunction with pre-treatment imaging, provides quantitative verification of the entire treatment delivery, currently not possible with other methods. This approach establishes a new standard of verification which has the potential to improve the quality of treatment delivery and improves patient safety in HDR brachytherapy.

Chapter 1
Introduction

1. Overview and Aim

High dose rate (HDR) brachytherapy treatments are usually delivered in large dose fractions. Poor execution in the delivery of a planned treatment would have significant clinical impact, because high doses are delivered in seconds and mistakes in an individual fraction cannot be easily rectified. Two recent brachytherapy review articles [1, 2] highlight the need for an independent and comprehensive treatment verification system in HDR brachytherapy to ensure patient safety.

In this thesis, a novel, non-invasive treatment verification system is described along with its initial clinical implementation. A treatment verification system based on a flat panel detector (FPD) is characterised, and used to perform pre-treatment image verification and HDR brachytherapy source tracking for direct comparison with the treatment planning system (TPS) to validate correct treatment delivery. The verification system described in this work is sensitive to most of the treatment delivery error types identified in Table I of the review article by Tanderup *et al* [1].

1.1 High Dose Rate Brachytherapy

HDR brachytherapy is a radiation therapy modality used for treating cancer across almost all sites of the human body. HDR brachytherapy is practiced by placing a single radioactive source within or at short distances from the treatment (tumour) volume. Treatment can be achieved by delivering the radioactive source within body cavities (intracavitary), within the lumen of organs (intraluminal) or into soft tissue (interstitial). A common application of interstitial HDR brachytherapy is the treatment of prostate

cancer, where the source is delivered through the perineum, via a number of hollow catheters, into the prostate organ, and represents the clinical examples provided in this work.

HDR brachytherapy offers highly conformal dose distributions, allowing large doses to be delivered to the treatment volume while sparing surrounding healthy tissue [3, 4]. It achieves excellent local control rates and relatively low side effects when compared to other treatment options [4, 5].

Treatment is performed by implanting the patient with applicators, designed to sit against or within the target volume. These implanted applicators define the path the radioactive source will travel and so correct placement relative to the patient's anatomy is crucial. The position of these applicators can be accurately placed by the Surgeon or Radiation Oncologist without the risk of radiation exposure. The radioactive source is then later introduced into each applicator channel and the treatment delivered as programmed by a remote robotic afterloading machine and depicted in figure 1.1.

Figure 1.1. The microSelectron HDR brachytherapy robotic afterloader used in this work from Elekta (Elekta, Stockholm, Sweden).

Understanding the process of treatment planning, patient preparation, and treatment delivery helps one understand the potential for mistakes to occur. Mistreatment could be due to software or hardware malfunctions, operator errors, or anatomical changes in the patient. The consequences could include under-dosing of the target (potentially failing to cure the patient) or over-dosing normal tissues with a corresponding increased risk of side effects or radiation injury.

1.2 Treatment Planning

HDR brachytherapy planning techniques typically involve three dimensional (3D) reconstruction or modelling of the implanted applicator(s) in a dedicated brachytherapy TPS. The TPS is a custom computer workstation which can provide the user with the functions and visualisations to create a radiation dose treatment plan for the patient.

Images of the implanted applicator(s), commonly referred to as the 'implant', are captured using computed tomography (CT) imaging[6], ultrasound (US) imaging [7], or magnetic resonance imaging (MRI) if the implant materials are compatible [8, 9]. Clear and accurate imaging of the implant and surrounding anatomy is necessary as this forms the basis for treatment planning.

The treatment planning procedure can be divided into three main steps, anatomical contouring, implant reconstruction and radiation dose planning, each of which have their own uncertainties [10-12] and risk of errors occurring. The contouring procedure involves a Radiation Oncologist defining in the TPS the anatomical planning target volume (PTV) and the surrounding organs at risk (OAR). The implant reconstruction process requires the brachytherapy source travel paths to be clearly defined, orientation of the applicator to be correctly identified and the channel numbering system to be clear to avoid possible confusion at treatment. An example of a reconstructed prostate implant is shown in figure 1.2. The contoured PTV is shown in red and the rectum OAR is shown in blue. The reconstructed applicator, in this case 18 prostate catheters, is shown as green paths passing through the PTV region.

The aim of radiation dose planning is to achieve a dose distribution that covers the PTV with the prescription dose while minimising (below specified threshold values) the dose to surrounding tissues and OAR. A treatment plan is constructed from an array of brachytherapy source stop positions, known as 'dwell positions', defined along each

implant channel path. The planner creates active dwell positions by specifying where the source stops and how long the source dwells at each position (dwell time). Figure 1.2(a) illustrates active dwell positions (red spheres) and inactive dwell positions (green spheres).The 3D array of active dwell positions create a cumulative dose 'cloud', shown as yellow in figure 1.2(b), as the source moves from one dwell position to the next. It is critically important, to achieve the treatment plan objectives, that the source is accurately delivered to each active dwell position relative to the surrounding anatomy.

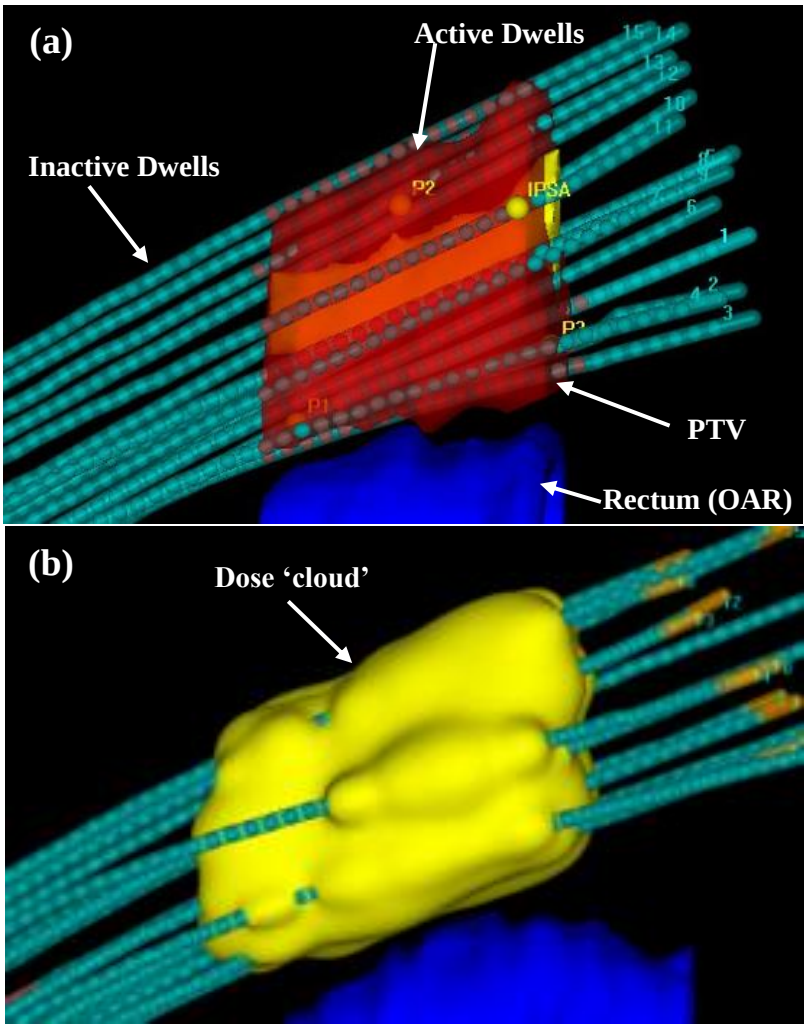

Figure 1.2. (a) An example of a prostate HDR treatment plan, showing the implant catheter paths (green), the PTV (red), rectum OAR (blue) and active and inactive dwell positions in each catheter, red and green spheres respectively. (b) The cumulative dose 'cloud' shown in yellow covering the PTV with the prescription dose produced by all contributing active dwell positions.

Activation of source dwell positions can be performed manually by the treatment planner but is not practical for complex brachytherapy implants consisting of many treatment channels or 'catheters' (e.g. prostate). These implants require advanced dosimetric optimisation algorithms that can auto-activate dwell positions and modulate the dwell time in order to achieve the prescribed PTV dose coverage while minimising the dose to OAR. A number of dosimetric optimisation algorithms exist and further details can be found in the following references [13, 14] .

1.3 Treatment Delivery

HDR brachytherapy treatment is administered using a robotic remote afterloading machine, as shown in figure 1.1. The implanted applicator channels are connected to the afterloader by transfer tubes, using a channel numbering system defined on the afterloader interface plate as shown in figure 1.3(a). The afterloader drives the radioactive source via each programmed channel, through the transfer tube and into the catheter in the patient, to deliver the programmed treatment. The distance the source travels into each channel, to reach the treatment volume (PTV), is specified at the time of treatment planning and is defined as the indexer length. The indexer length to be specified by the user depends on the lengths of the transfer tubes and catheters used. Treatment delivery occurs with the patient in a shielded bunker while the staff monitors the treatment progression from the safety of the control room.

Isotopes used in HDR brachytherapy exhibit characteristics such as high specific activities enabling small sources to be produced with clinically adequate dose rates. One of the most commonly used isotopes is Iridium 192 (^{192}Ir), which is exclusively used in Australia and is the subject of this work. Different manufacturers of HDR brachytherapy afterloaders produce sources that vary slightly in their geometry, but the general design consists of the isotope material confined within a titanium capsule which is then welded to a stainless steel cable. In this work, the source is contained in a titanium capsule 4.5 mm long, 0.9 mm in diameter, and is welded onto the end of a stainless steel cable as depicted in figure 1.3(b) and (c). The robotic remote afterloader machine drives the source to the specified active dwell position and dwells the source for the programmed length of time. The source is then stepped to the next active dwell position and again dwells for the programmed time. The process is repeated for all implanted catheters (applicator channels) until the entire treatment has been delivered.

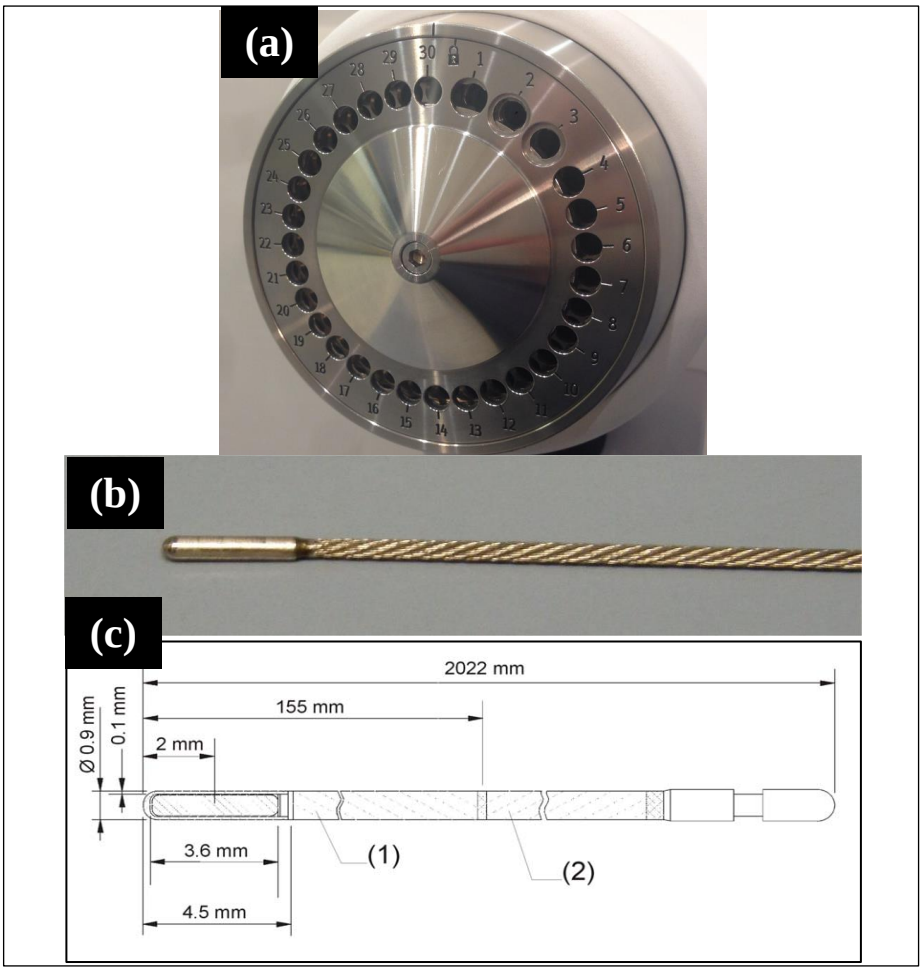

Figure 1.3. (a) A HDR brachytherapy remote afterloader interface plate showing the channel numbering system. (b) A photo of the ^{192}Ir source used in this afterloader and (c) the details of the source geometry (from *microSelectron V3 reference manual*, Elekta Stockholm, Sweden).

1.4 Treatment Verification

Treating any patient with radiation carries the risk of misadministration. A treatment error may result in an under dose or over dose to the patient or even a complete geographical miss of the target volume. In many documented cases, the main contributor to radiation delivery treatment errors is human mistakes[15]. In order to reduce (and ideally eliminate) the frequency and severity of these errors, systematic processes are introduced into the treatment delivery process integrated with advanced technology to identify and trap errors before they impact the patient. Modern HDR brachytherapy afterloader systems contain a number of safety features to minimise the risk of error, but many opportunities for incorrect delivery of treatment remain.

There currently exists a disparity between external beam radiation therapy (EBRT) and HDR brachytherapy in validating correct treatment delivery. Treatment verification for EBRT includes various integrated systems to provide multiple levels of authentication. These include systems to ensure the correct patient treatment plan is loaded, pre-treatment imaging (ionising and non-ionising) to ensure the patient's treatment position is correct[16-19], position verification imaging during the radiation delivery[20, 21], patient dose measurement for the treatment field[22-24], and more recently dynamic verification allowing target tracking as the tumour moves during treatment delivery[25-27]. Many of these systems are considered essential in EBRT to ensure patient safety and have enabled safe dose escalation improving tumour control and/or minimising harm to surrounding organs at risk[28-30].

1.5 Treatment Verification in HDR Brachytherapy

HDR brachytherapy treatment quality assurance processes can be considered as two stages; (i) pre-treatment imaging to verify the implanted catheter (or applicator) is in the correct (as planned) position relative to the surrounding anatomy and (ii) verification of treatment delivery (monitored during or validated after treatment) to ensure the correct plan and dose is administered to the patient. The time pressure in the clinic and the lack of commercial verification tools available both influence the extent of routine verification that is performed in HDR brachytherapy.

Deviation of treatment delivery from the plan can occur for two main reasons: (a) a treatment error due to human mistake[15] or system malfunction and (b) anatomical movement[31-34], where the implant moves inside the patient relative to the anatomy after treatment planning. Manual cross checking procedures, performed by many brachytherapy institutions, identify some treatment delivery errors, but their value is limited as they can be bypassed, forgotten, or incorrectly performed, and do not identify all possible errors. An independent system to verify treatment parameters, identify potential errors and ensure patient safety, both before and during treatment delivery, is sorely needed.

1.5.1 Pre-treatment Verification Imaging

Pre-treatment verification imaging is an important step but is often not performed routinely, possibly due to the lack of available treatment room imaging equipment and

software tools to swiftly perform verification. Changes to the brachytherapy implant geometry, between treatment planning and treatment delivery will potentially result in a geographical-miss delivery error.

In HDR prostate brachytherapy, uncorrected catheter displacement can have a significant impact on dosimetry, with approximately every centimetre of catheter displacement resulting in the prostate V100 (prostate volume receiving 100% of the prescription dose) being decreased by 20% [35]. The catheter displacement is largely in the cranial-caudal direction with oedema, swelling and other external influences typically driving this catheter movement[31]. Identification of catheter displacement has been reported between treatment fractions [31, 32, 34, 36] and also between treatment planning and delivery, where the time frame is on the order of a few hours[33, 37]. External visual inspection of the catheters and template is important but does not truly capture the internal catheter to anatomy relationship. An imaging approach at the time of treatment, ideally with the patient in the treatment position, is necessary to correctly identify any catheter displacement relative to the target volume and ensure the accuracy of the dose delivered.

An unidentified treatment misadministration (geographical miss) could potentially occur if pre-treatment imaging is not performed, although from the user/operator perspective, the treatment appears to be delivered correctly by the brachytherapy afterloader system.

A systematic and reliable approach to capture the implant position relative to the surrounding anatomy, with software tools to compare against the expected (TPS) position is needed. A technique to express any observed deviations as a simple result is desirable, as informed clinical decisions need to be made promptly, at the treatment console.

1.5.2 In vivo Dosimetry

Treatment delivery verification in HDR brachytherapy has mainly employed *in vivo* dosimetry (IVD) as the detection mechanism [38-44]. At present IVD in HDR brachytherapy has failed to achieve widespread implementation as routine clinical practice and typically is applied in a research context. IVD is an attractive approach to verifying the treatment delivery as this provides a direct measurement of the patient

dose. IVD is well established in EBRT [22], but when applied to HDR brachytherapy additional challenges are introduced. Previous clinical studies of IVD have used point dose detectors, such as thermoluminescent dosimeters (TLDs) [45], metal oxide semiconductor field effect transistors (MOSFETs) [46] , diodes [39, 47, 48], and scintillation detectors [42, 49, 50].

Treatment verification using IVD approaches provide valuable information, particularly in terms of individual organ protection. For example rectal wall dosimetry [38, 39, 48, 51, 52] and urethral dosimetry [40, 45, 50, 53] can be used to confirm that the dose limit to an organ is not exceeded. Most of these approaches are inherently invasive, requiring the dosimeter or a probe containing it, to be inserted into the patient's rectum or urethra or require the insertion of an additional interstitial catheter. However, point measurements such as these do not necessarily provide sufficient information to verify the correct delivery of a treatment plan. Some interstitial measurement approaches [54] using detectors inserted into adjacent treatment catheters for example, sample the dose (or dose rate) within or near the treatment volume.

Challenges associated with the uncertainty of the detector position relative to the source, coupled with the presence of high dose gradients, make the interpretation of these measurements for the purpose of treatment delivery error detection extremely difficult[1]. Discrepancies of -31 % to +90 % between measured and expected doses have been reported [47] but not attributed to having detected a treatment delivery error. The discrepancies have been regarded as an inherent uncertainty of measuring dose *in vivo* due to source-to-detector distance uncertainties. Improving the confidence in identifying an error, if it is present, requires sophisticated analysis of measurements such as the statistical error detection algorithm implemented by Kertzscher *et al* [55]. This typically reflects the difficulty in knowing where the detector is relative to the source during treatment delivery [47, 51]. A notable improvement is the combination of a point dosimeter coupled to a position sensor as demonstrated by Reniers *et al* [56], although it has not been implemented clinically.

IVD will continue to be a challenge to implement in the clinic due to the added workload, potential sterilization issues, interference in existing workflow practices and the invasive nature of the approach. Even if the detector position is well known, a

single (or a few) point measurements has limited power to verify the entire treatment delivery due to under-sampling.

1.5.3 Source Position Verification

An alternative approach for treatment verification is to determine the position of the source throughout the treatment delivery, identify where these source positions are relative to the implanted catheters/applicator, and where they occur in relation to the surrounding anatomy. From this positional information, combined with the time the source dwells at each position, it is possible to verify that the treatment was delivered as planned and reconstruct the dose that was delivered to the tumour and/or organs at risk.

Some previous studies have investigated source position measurements aimed at system quality assurance [57, 58] and the potential for the source position approach to treatment verification [59-61], but none have progressed to clinical implementation as *in vivo* devices.

1.6 An Ideal Verification System

A comprehensive HDR brachytherapy treatment verification system should be able to provide the user with information about the implant prior to treatment as well as monitor the treatment as it is delivered. The following is a list of attributes that an ideal treatment verification system in HDR brachytherapy should exhibit:

- Non-invasive to the patient (to minimise risk of harm e.g. via infection) and not create additional discomfort
- Not significantly increase the treatment time
- Be simple for the treating staff to operate, enabling routine use
- Be sensitive to all potential treatment errors
- Integrate seamlessly with the TPS and treatment console system
- Be independent of the treatment console/delivery mechanism
- Provide real-time feedback to the operator
- Allow treatment interrupt when substantial deviations from planned treatment are observed
- Document the delivered treatment as a dose logging mechanism

- Upload the delivered dose to the TPS for fraction summation and potential adaptive planning

1.7 Thesis Aim

The aim of this thesis was to develop a treatment verification system for HDR brachytherapy, that can be used to validate correct treatment, detect deviations and ultimately ensure patient safety.

The approach taken in this thesis employs source tracking, whereby a FPD device is used to measure the source radiation exiting the patient surface during treatment delivery. The acquired radiation distribution at the FPD imaging plane is then processed to determine the position of the source inside the patient.

By including an external x-ray unit, and using the same FPD as the image acquisition device, both 2D and 3D pre-treatment image verification can be performed. Combining the pre-treatment imaging with the source tracking, the aim is to perform absolute source position verification, relative to the implant and patient anatomy. Additionally, by processing the information provided by this system, and comparing against the treatment plan, error trapping could be performed as the treatment is delivered.

The final objective is to integrate this concept into a clinical environment and perform pre-treatment and treatment delivery verification for HDR prostate brachytherapy.

1.8 Measurement Device

The detector device used in this work is an amorphous silicon electronic portal imaging device (EPID) (aS500, Varian Medical Systems, Palo Alto, CA, USA) removed from the linear accelerator and operated in a standalone mode. This FPD was not strategically selected for the purpose of HDR brachytherapy treatment verification, but rather was acquired by means of opportunity. The FPD was utilised to perform a proof-of-principle concept for verification.

1.9 Thesis Scope and Structure

The primary aim of this work was to improve the quality of treatment delivery and patient safety in HDR brachytherapy. The goal is to establish a verification system that is robust, non–invasive and simple to use enabling routine use and widespread uptake

of such a process. The scope of this thesis covers the proof-of-principle measurements in treatment verification to establish a practical process that can potentially be used in a clinical environment. The thesis concludes with these concepts being applied in a true clinical environment.

A review of the literature in the field of HDR brachytherapy with a focus on techniques to validate treatment delivery is provided in Chapter 2. The literature recently published on HDR brachytherapy verification highlights the need for a system that can provide independent verification of the delivered parameters. Many of the publications use IVD as the mechanism for treatment verification, while a few systems have applied source position measurement to perform quality assurance testing and not treatment verification.

The FPD used in this work is optimised for megavoltage photon beams and so the response of the detector to a HDR brachytherapy source was characterised. In Chapter 3, the experimental steps taken to characterise the FPD for use with the ^{192}Ir source is described. This includes the response to photon energy, dose rate, depth dependent spectral change, response reproducibility and source-detector angular response. A method for calibrating the FPD to measure dose was established. A simple phantom case of measuring a dose plane and comparing to the TPS was also achieved. In later work, the detector was operated as a radiograph imaging receptor, and so the plane below the detector front surface where the image is formed was also determined.

The images obtained by the FPD, when exposed to the brachytherapy source in a phantom, can be interpreted to obtain the position of the source. Chapter 4 contains a description of the algorithms used to determine the position of the source inside the phantom/patient.

For the verification system to validate the measured source position against the patient's anatomy, a method of localising the patient and FPD relative to each other was required. Chapter 5 describes the pre-treatment imaging approach used, how the radiograph data can be used to validate the geometry of the implant, and describes the methods applied to reduce position uncertainties.

Identification of treatment errors and termination of the treatment before they have a significant impact on the patient is an ideal characteristic of a treatment verification

system. Chapter 6 describes the comparisons undertaken to determine if the treatment delivered is correct or represents a treatment error. Methods to identify the cause of the error are also investigated.

Chapter 7 describes the initial clinical implementation of the FPD, methods to determine source position, and the pre-treatment imaging.

1.10 Research Outputs: Awards, Patents, Publications, Conference Presentations and Invited Seminars Arising From This Work

Awards

Ian Snook Physics Prize awarded to a Physics PhD candidate on the basis of outstanding research potential. RMIT University 2016.

ESTRO-Elekta Brachytherapy Award presented to the most innovative abstract submitted for presentation at the 3rd ESTRO Forum 2015, Barcelona, Spain. Title: *'Clinical implementation of in vivo source position verification in high dose rate prostate brachytherapy'*

Patents

Smith RL, Australian Innovation Patent, AU 2008100728 *A real time treatment dose verification system for afterloader brachytherapy systems*, 2008.

Smith RL and Franich RD, Patent: "*Brachytherapy dose verification apparatus, system and method"*, WO 2012034157 A1, RMIT University, Filing date Sep. 13th, 2010.

Publications

Smith RL, Hanlon M, Panettieri V, Millar JL, Matheson B, Haworth A, and Franich RD. *An Integrated System for Clinical Treatment Verification of HDR Prostate Brachytherapy combining Source Tracking with Pre-Treatment Imaging* Brachytherapy. 2017 Sep 22. S1538-4721(17) 30426-9.

Smith RL, Haworth A, Panettieri V, Millar JL, and Franich RD *3D catheter reconstruction in HDR prostate brachytherapy for pre-treatment verification using a flat panel detector* Phys Med. 2017 Jul;39:121-131.

Smith RL, Haworth A, Panettieri V, Millar JL, and Franich RD *Identification of Catheter Displacements in HDR Prostate Brachytherapy Using a 'Shift Image' Reconstruction Technique*, Brachytherapy, 16(3)Supp., S106, May 2017, DOI: 10.1016/j.brachy.2017.04.204

Smith RL, Haworth A, Hanlon M, Matheson B, Millar JL, Panettieri V, and Franich RD *Clinical Application of Pre-Treatment Image Verification of Catheter Positions for HDR Prostate Brachytherapy*, Brachytherapy, 16(3)Supp., S114, May 2017, DOI: 10.1016/j.brachy.2017.04.223

Beaulieu L, **Smith RL,** Franich RD. Real-Time In-Vivo Dosimetry. In: Song WY, Tanderup K and Pieters B, editors. Emerging Technologies in Brachytherapy, CRC Press, Series in Medical Physics and Biomedical Engineering, March 2017, p.408, ISBN 9781498736527; *In Press*.

Venselaar JLM, Beaulieu L, Chen Z, **Smith RL**. Advances in Brachytherapy Physics. In: Godfrey DJ, Van Dyk J, Das SK, Curran BH, Wolbarst AB, editors. Advances in Medical Physics, Volume 6. Madison, WI: Medical Physics Publishing; July 2016. p.203. ISBN 9781930524903

Smith RL, Haworth A, Panettieri V, Millar JL, and Franich RD *Treatment Delivery Error Trapping in HDR Brachytherapy*, Brachytherapy, 15:S39, May 2016, DOI: 10.1016/j.brachy.2016.04.040

Smith RL, Haworth A, Panettieri V, Millar JL, and Franich RD. *A method for verification of treatment delivery in HDR prostate brachytherapy using a flat panel detector for both imaging and source tracking*. Med Phys. 2016;43(5):2435.

Smith, R.L., J. Millar, B. Matheson, B. Hindson, M. Taylor, and R. Franich. *"Clinical implementation of in vivo source position verification in high dose rate prostate brachytherapy."* Radiol Oncol 115:S87, 2015.

Ryan L. Smith, Jeremy L Millar, Annette Haworth, Michael L Taylor, Rick D Franich. *In vivo treatment delivery error trapping in HDR prostate brachytherapy* J Contemp Brachy. vol.7,p103, 2015.

Natasha Mason, **Ryan L. Smith**, Vanessa Panettieri, Bronwyn Matheson, Jeremy L. Millar. *Evaluation of HDR prostate brachytherapy catheter displacement between planning and treatment using a flat panel detector.* J Contemp Brachy. vol.7,p104, 2015.

Smith RL, *Verifying Brachytherapy Treatment of Prostate Cancer*. Monash Comprehensive Cancer Consortium (MCCC), Annual Research Report 2013-14

Smith RL, *High Dose Rate (HDR) Brachytherapy Treatment Verification Using An Electronic Portal Imaging Device (EPID)*, Post Forum Report, International Congress on Radiotherapy & Oncology, 2nd ESTRO Forum, Geneva, Switzerland, p34-35, April 2013.

Smith RL, Taylor ML, McDermott LN, Haworth A, Millar JL, and Franich RD. *Source position verification and dosimetry in HDR brachytherapy using an EPID*. Med Phys. 2013;40(11):111706.

Franich RD, **Smith RL**. *Curing cancer with radiation - Safely*. Stories of Australian Science 2011, Science in Public publication.

Conference Presentations

R.L. Smith, A Haworth, V. Panettieri, J.L. Millar, and R.D. Franich *"A 'Shift Image' 3D Reconstruction Technique for Identification of Catheter Displacement in HDR Prostate Brachytherapy"* EPSM (Australian Medical Physics) Scientific Meeting, Nov 2016, Sydney, NSW, Australia

R.L. Smith, A Haworth, V. Panettieri, J.L. Millar, and R.D. Franich *"Treatment Delivery Error Trapping in HDR Brachytherapy"* World Congress of Brachytherapy, June 2016 San Francisco, U.S.A.

R.L. Smith, A Haworth, V. Panettieri, B. Matheson, S Miller, H Mack, J.L. Millar and R.D. Franich *"An update of clinical treatment delivery verification of HDR*

prostate brachytherapy at Alfred Health" Australasian Brachytherapy Group, Annual Scientific Meeting, Mar 2016, Fremantle, WA, Australia

R.L. Smith, J.L. Millar, A Haworth, M.L. Taylor and R.D. Franich *"In vivo Image Guided Brachytherapy Verification (IGBV) in high dose rate prostate brachytherapy - Initial Clinical Experience"* World Congress of Medical Physics, June 2015 Toronto, Canada

R.L. Smith, J.L. Millar, A Haworth, M.L. Taylor and R.D. Franich *"Clinical implementation of in vivo source position verification in high dose rate prostate brachytherapy"* 3rd ESTRO Forum, April 2015, Barcelona, Spain

R.L. Smith, J.L. Millar, A Haworth, M.L. Taylor and R.D. Franich *"In vivo treatment delivery error trapping in HDR prostate brachytherapy"* Australasian Brachytherapy Group, Annual Scientific Meeting, Mar 2015, Sydney, NSW, Australia

R.L. Smith, J.L. Millar, A Haworth, M.L. Taylor and R.D. Franich *"Clinical implementation of in vivo source position verification for high dose rate (HDR) prostate brachytherapy using a flat panel imager"* Combined Scientific Meeting (CSM), Sept 2014, Melbourne, VIC, Australia

R.L. Smith, J.L. Millar, A Haworth, M.L. Taylor and R.D. Franich *"Initial Clinical Experience with HDR Treatment Verification Using a Flat Panel Detector"* Australasian Brachytherapy Group, Annual Scientific Meeting, Mar 2014, Adelaide, SA, Australia

R.L. Smith, M.L. Taylor, A Haworth, L.N. McDermott, J.L. Millar and R.D. Franich *"High dose rate (HDR) brachytherapy treatment verification using an electronic portal imaging device (EPID)"* Highlights: Best of Brachytherapy 2013 Session, 2nd ESTRO Forum, April 2013, Geneva, Switzerland

R.D. Franich, **R.L. Smith**, M.L. Taylor, A Haworth, L.N. McDermott and J.L. Millar *"Independent validation of high dose rate (HDR) brachytherapy source localization using an EPID",* 2nd ESTRO Forum, April 2013, Geneva, Switzerland

R.D. Franich, **R.L. Smith**, M.L. Taylor, A Haworth, L.N. McDermott and J.L. Millar *"Independent validation of high dose rate (HDR) brachytherapy source localization using an EPID",* AAPM Meeting

R.L. Smith, J.L. Millar, A Haworth, M.L. Taylor and R.D. Franich *"HDR Brachytherapy Source Position Verification and Dosimetry using an Electronic Portal Imaging Device [EPID]"* Australasian Brachytherapy Group, Annual Scientific Meeting, Mar 2013, Brisbane, QLD, Australia

R.L. Smith, J.L. Millar, A Haworth, M.L. Taylor and R.D. Franich *"Real-time in vivo Dosimetry in High Dose Rate Brachytherapy Using an Electronic Portal Imaging Device"* EPSM (Australian Medical Physics) Scientific Meeting, Nov 2011, Darwin, NT, Australia

R.L. Smith, J.L. Millar, A Haworth, M.L. Taylor and R.D. Franich *"High Dose Rate (HDR) brachytherapy in vivo treatment verification using an EPID"* 11th International Workshop on Electronic Portal Imaging (EPI2kX), Apr 2010, Leuven, Belgium

Invited Seminars

R.L. Smith, *"HDR Prostate Brachytherapy Treatment Verification - from benchtop to bedside"* Alfred Health Radiation Oncology, Department Seminar Series, Mar 2017, Melbourne, Australia

R.L. Smith, *"HDR brachytherapy treatment verification using a flat panel detector"* GEC-ESTRO *In Vivo* Dosimetry Seminar, 5th Dec., 2014 Brussels, Belgium

R.L. Smith, *"HDR Brachytherapy Treatment Verification"*, Australian Radiation Protection and Nuclear Safety Agency (ARPANSA), Department Seminar Series, Oct 2014, Yalambie, VIC, Australia

R.L. Smith, *"Verifying Brachytherapy Treatment of Prostate Cancer"* Southern Melbourne Cancer Symposium, 18th Sept 2014, Monash Comprehensive Cancer Consortium (MCCC), Clayton, VIC, Australia

R.L. Smith, *"HDR brachytherapy treatment verification – Necessary but difficult"* Department Seminar, February, 2014, Calvary Mater Newcastle, Newcastle, NSW, Australia

R.L. Smith, *"HDR Brachytherapy Treatment Verification using a Flat Panel Detector- System Concept and Dosimetry Application"* Nucletron Corporate Headquarters, April 2013, Vaanendaal, The Netherlands

R.L. Smith, *"HDR Brachytherapy Source Position Verification and Dosimetry using an Electronic Portal Imaging Device [EPID]"* William Buckland Radiotherapy Centre, Department Seminar Series, Mar 2013, Melbourne, Australia

R.L. Smith, *"Toward routine treatment verification in HDR brachytherapy"* EPSM (Australian Medical Physics) Scientific Meeting, Dec 2012, Gold Coast, QLD, Australia

R.L. Smith, *"High Dose Rate (HDR) Brachytherapy in vivo Treatment Verification using an EPID"* Netherland Cancer Institute (NKI), Department Seminar, April 2010, Amsterdam, The Netherlands

Chapter 2
Literature Review

2 Overview

Treatment delivery verification in HDR brachytherapy is warranted as potential treatment errors can occur without clinical staff noticing, primarily because of human mistakes and/or changes to the implant geometry post treatment planning imaging. Some of the potential error types that can occur are incorrect treatment plan selection, incorrect specification of the channel length for the selected applicator or catheter, the source step size incorrectly specified, and swapped channels connecting the afterloader to the patient. Implant geometry changes, due to swelling of the tissue, has the potential to displace the catheters relative to the surrounding anatomy and/or relative to each other. Therefore, a treatment verification system should be sensitive to these error types to ensure the patient receives a high quality of treatment.

Approaches to treatment delivery verification in HDR brachytherapy have mainly employed IVD techniques. The dose measured by a dosimeter at one (or several) points within or near the treatment volume, is then compared with the expected planned dose at those points. IVD in HDR brachytherapy has been performed with a variety of detector types and used in various anatomical locations and these approaches to verification are reviewed in more detail below.

One significant challenge with this approach is accurately knowing the relative positions of both the brachytherapy source and dosimeter at the time of treatment in order to confidently interpret the measurements for error detection. In clinical practice, an observed discrepancy of the measured dose from the expected dose may be due to the detector position changes and high dose gradients typical in HDR brachytherapy

and not necessarily a treatment delivery error. Furthermore, IVD only provides dosimetric information at the point(s) of measurement and therefore must make assumptions about what is occurring throughout the rest of the treatment volume in order to accomplish treatment verification.

An alternative approach to achieve treatment delivery verification is to perform source tracking during the treatment. If the position of the (stepping) source is measured during the treatment and in combination with the time the source dwells at each position the overall treatment delivery can be verified. The concept of source tracking potentially avoids the uncertainties associated with IVD detector positioning and permits dose reconstruction throughout the entire treatment volume. Pre-treatment imaging performed immediately prior to source tracking, could be used to account for geometric changes in the brachytherapy implant, therefore producing a treatment verification process that can adapt to this new geometry.

The recent vision 20/20 publication of Tanderup *el al* [1] promotes development and implementation of routine IVD for the purposes of treatment verification. Treatment verification in HDR brachytherapy is far from routine in most clinical brachytherapy practices with many challenges still to be overcome. This chapter reviews approaches to performing HDR brachytherapy treatment delivery verification in a clinical scenario and highlights the existing challenges that still need to be overcome.

2.1 In vivo Dosimetry

The approach to IVD performed in HDR brachytherapy has been established using the concepts of IVD developed for EBRT. In simple terms, a dosimeter is placed on or in a patient and the treatment delivery is confirmed by measuring a dose and comparing it against an expected value predicted by the TPS. In contrast to brachytherapy, the position of the radiation source in EBRT is fixed relative to the dosimeter and generally the position of the dosimeter is well known relative to the treatment field, via visual or by pre-treatment imaging techniques. Dosimeter placement in low dose gradient regions is also desirable to reduce position derived dose uncertainties. IVD in HDR brachytherapy is an extremely challenging arena to achieve treatment verification. The geometric relationship between the source and the dosimeter is changing throughout the

treatment, the dosimeter is often inserted inside the patient making localisation more difficult, detector temperature response effects need to be accounted for, infection control (sterilisation) needs to be considered and dosimeters are often positioned in high dose gradients. In spite of these potential problems with achieving treatment verification, IVD is the most commonly used approach and many authors have made significant contributions in order to overcome some these challenges.

IVD techniques have changed considerably over the past 10 years, with previous approaches employing passive detectors that require post-processing of the dosimeter before a measurement can be determined. More recently the drive has been toward real time verification and so active detectors that can deliver measurement data in real-time have been the devices used in recent publications.

In one of the largest patient studies using a passive IVD technique, Nose *et al*[62] used radiophotoluminescence glass dosimeters to evaluate dose to organs at risk in 66 patients undergoing HDR brachytherapy for pelvic malignancies. Post treatment analysis revealed that discrepancies of over 20% were observed between measured and expected dose, with most discrepancies attributed to detector position uncertainty. Similar IVD studies involving TLDs have been also been performed. Toye *et al* [53] performed simultaneous measurements of dose profile along the urethra and rectum during HDR prostate brachytherapy using TLDs for comparison with the TPS and to evaluate apparent implant shifts. The peak differences between the measured and planned doses ranged from -34% to 66% for the urethra and -36% to 101% for the rectum. The accuracy of the rectal dosimetry measurements were hampered by the instability of the rectal catheter containing the TLDs. Anagnostopoulos *et al* [54] investigated the potential of TLD for IVD in transperineal prostate HDR brachytherapy. The study reported results for 18 treatment fractions (5 patients). For 2 of the 5 patients an additional catheter was implanted into the prostate to accommodate the train of TLDs. For the remaining 3 patients, the TLDs were inserted into treatment catheters. In this case, the treatment was delivered for all planned catheters, the TLDs were removed, and the remaining catheter was used. The agreement of measured values with the TPS values after correction of volume averaging effects and transit dose contributions showed a range from -2.7% to 8.6% over all measured fractions. No trend of increasing or decreasing deviations with fraction number was observed indicating that inter-fraction catheter displacement was not occurring. The study provided

relatively good agreement between measured and planned dose. However, the authors concluded that TLD IVD would be difficult to implement on a daily basis in clinical practice due to: (i) the invasive nature of TLD IVD, (ii) the subsequent time consuming reading and dose calculation procedure, (iii) the application of relevant correction factors and (iv) the fact that TLDs are not real time dosimeters not allowing monitoring of operational mistakes and enabling immediate correction. Brezovich *et al* [40] reported IVD measurements with TLDs along the urethra during HDR prostate brachytherapy. A linear array of 20 TLDs were loaded into a catheter. At treatment this catheter was inserted into the Foley urethral catheter and pushed up to the distal end. No imaging was performed at imaging to align the TLD array with the treatment region. For the 7 patient fractions reported the peak dose difference range was -11.7% to 8.0%. The uncertainty in the position of the TLDs along the urethra was identified as a weakness of the method. To address this limitation the authors suggested including radiopaque markers in the TLD array and perform imaging for localisation.

These passive IVD approaches to treatment verification may be acceptable in EBRT[63], where dosimetric corrections can be made over many fractions, but this technique has limited value in modern HDR brachytherapy where large doses are generally delivered one or over only a few fractions.

Recent dosimeter developments and clinical implementation have focused on active IVD techniques that can provide a dosimetric result during or immediately after treatment delivery. Waldhausl *et al* [47] used semiconductor diodes to verify the dose delivered to the rectum and bladder for 55 brachytherapy applications for cervix cancer patients. The measured doses were compared to the planned dose and for the rectum 36 of 55 measurements differed by more than 10%, while 12 of 29 measurements of the bladder differed by more than 10%. The rectal dose differences showed large variations, ranging between -31% to 90% with most measurements reporting a lower dose than planned (44 of 55). The authors suggest the observed dose differences are due to detector movement (2.5 to 3.5 mm) causing dose differences of more than 10%. A geometrical shift of the probe after treatment planning imaging, movements of the patient, movement of the organs and applicator are all suggested as contributors to the discrepancies in measured dose.

Zaman *et al* [52] also used 5 semiconductor diodes to measure the rectal dose during HDR brachytherapy of 11 cervical cancer patients. The measurements differed from the predicted TPS values ranging from -8.5% to 41.2%. The authors acknowledged that the magnitude of the percentage differences were large and comparable with deviations reported by Waldhausl *et al* [47]. The authors suggest that two of the diodes were more prone to geometrical shift in between treatment planning and treatment delivery leading to the large observed dose differences. To address the observed dose differences due to geometrical displacement, the authors recommend the patient be imaged with a C-arm device to confirm the position of the diodes in the rectum just before treatment is delivered.

Seymour *et al* [48] reported a study for rectal IVD using an array of 5 semiconductor diodes during intraoperative TRUS guided HDR prostate brachytherapy using the SWIFT^{TM} TPS (SWIFT, Elekta, Stockholm, Sweden) In an attempt to address the previously reported IVD measurement uncertainties due to movement of the dosimeter in the rectum, the authors developed a device that would retain the position of the dosimeter between imaging and treatment delivery. A replica of the TRUS probe was constructed to host the diodes to perform the IVD. After the plan was completed the TRUS probe was replaced with the replica probe and aligned to fiducial markers using imaging. The coordinates for dose point comparisons was determined based on the updated positions of the diodes in the probe. The dose differences for the 28 patients included in this study ranged from -42% to 35% with 71% of the measurements experiencing a difference of less than 10%. The authors concluded that the performing dosimetry verification long term on a regular basis may not be economical due to the extra work involved.

In another approach to address the detector position uncertainty issue, Carrara *et al*[64] have reported on the use of a novel prototype device integrating MOSkin dosimeters[65] with a trans-rectal ultrasound (TRUS) probe. The advantage of this approach is that imaging and the IVD dosimeter is in the same frame of reference, reducing the measurement uncertainty due to source to detector position uncertainty. Although the source to detector position uncertainty is reduced, the reported difference between measured and predicted values ranged from -18% to 19%. It was determined that this difference was due to changes in the prostate post imaging (for planning) due to swelling therefore introducing discrepancies. Re-imaging the prostate immediately

after treatment to re-calculate the source to detector distance (and hence an updated expected dose) reduced this measurement discrepancy range down to ~ +/-6%. In this case a reduction in dose difference was achieved but required post processing, similar to the passive IVD detectors, and therefore may limit the capacity to identify treatment delivery errors in real-time.

In a recent study by Mason *et al*[46], a single MOSFET detector was used to perform IVD treatment verification of HDR prostate brachytherapy. The study reported the largest component contributing to the measurement uncertainty budget (from ~6 to 55%) was the brachytherapy catheter position uncertainty (i.e. the source to detector relationship). In that study, a MOSFET was introduced into the mid region of a prostate using an additional catheter. Point dose comparisons were made once for each catheter and for the total treatment contribution at that point. The largest discrepancies occurred for measurements of catheters that were closest to the MOSFET, where the dose gradient is greatest, and therefore the positional uncertainties dominated. In a worst case example, the total predicted dose at the dosimeter position was due to a single catheter and therefore the total treatment uncertainty was large. These large associated measurement uncertainties and the use of using one detector (no spatial information), in this case limited IVD from achieving overall treatment verification with a high degree of confidence.

The clinical use of a novel scintillation detector system for measuring urethral dose during HDR prostate brachytherapy was reported by Suchowerska et al [50]. The fibre optic dosimeter (FOD) was inserted into the urinary catheter, for 14 patients, before treatment and located with reference to the position of the catheter balloon in the bladder. To improve the detector localisation, the FOD was refined to include a radio-opaque marker. A pre-treatment radiograph was used to adjust the dosimeter position prior to treatment delivery for a further 10 patients. For the initial 14 patients measured, the reported dose differences ranged from -67% to 9%, with the largest discrepancy being attributed to incorrect dosimeter placement. The improvement of detector localisation using imaging dramatically improved the agreement with the expected dose, with all 10 patients exhibiting a deviation of less than 10% from predicted. These reported deviations were suspected to arise from unaccounted for changes in patient anatomy.

Metal-oxide-semiconductor field-effect transistors (MOSFETs)[64], radioluminescence (RL) and plastic scintillation detectors (PSD)[66] all provide some level of real-time dose (or dose rate) readout to the operator during the treatment delivery. A summary of IVD detector characteristics can be found in Table III of Tanderup *et al* [1](2013), (reproduced in table 2.1) highlighting the strengths and weaknesses of each detector type that has been used clinically for IVD in brachytherapy.

Table 2.1. Characteristics of detectors and dosimetry systems of importance for precise routine IVD in brachytherapy. The items are rated according to: advantageous (++), good (+), and inconvenient (-). (reproduced from Table III of Tanderup *et al* [1](2013))

	TLD	**Diode**	**MOSFET**	**Alanine**	**RL**	**PSD**
Size	+	+/-	+/++	-	++	++
Sensitivity	+	++	+	-	++	+/++
Energy dependence	+	-	-	+	-	++
Angular dependence	++	-	+	+	++	++
Dynamic range	++	++	+	-	++	++
Calibration procedures, QA, stability, robustness, size of system, ease of operation	+	++	++	-	-/+	+/++
Commercial availability	++	++	++	++	-	+
Online dosimetry	-	++	+	-	++	++
Main advantages	No cables, well studied system	Commercial systems at reasonable price, well studied system	Small size, commercial system at reasonable price	Limited energy dependence, no cables	Small size, high sensitivity	Small size, no angular and energy dependence, sensitivity
Main disadvantages	Tedious procedures for calibration and readout, not online dosimetry	Angular and dependence	Limited life of detectors, energy dependence	Not sensitive to low doses, tedious procedures for calibration and readout, not online dosimetry, expensive readout equipment not available in clinics	Needs frequent recalibration, stem effect, not commercially available	Stem effect

The capability of IVD approaches to identify treatment delivery errors is limited by the uncertainty budget associated with performing the measurement in vivo. Kertzscher *et al* [55] identified that many IVD approaches for identifying a treatment delivery error judge these treatments based on static reconstructions of the detector position. The large reported deviations between measured and planned doses from previous IVD studies suggest that only gross treatment errors could be confidently identified. In the reported study, the authors did not base the error detection algorithm on *a priori* dosimeter position but instead used a data driven approach. The study showed that IVD sensitivity to treatment errors could be improved by adopting this approach, but for a single dosimeter implementation, a swapped channel error was less likely to be identified.

One common limiting theme for many reported IVD studies is the source to detector position uncertainties contributing to a large uncertainty in the ability to detect treatment errors. IVD approaches lack the spatial information required to identify certain error types. IVD can provide valuable information about the dose received by the organ containing the dosimeter. In this application, IVD can act as a monitoring system verifying the dose received by the organ does not exceed some specified threshold.

2.2 Treatment Delivery Verification

In principle, the HDR brachytherapy treatment can be verified without measuring dose, but by measuring the position of the source within the patient and the time the source dwells at each position. If these parameters are correct, and their absolute position relative to the patient anatomy is correct, then it can be concluded that the treatment was delivered as intended. This is only strictly true if the specified TPS air kerma rate (AKR) of the source matches the actual source in the afterloader. Unlike EBRT, where the beam output parameters may be incorrect, the HDR brachytherapy source AKR is a well defined function of the initial measured AKR and time. The source AKR is an afterloader machine parameter that should be correctly defined during the quality assurance program in conjunction with other afterloader functionality tests. The inclusion of a dose rate, or activity, sensitive detector measurement is a useful addition to source position and dwell time verification.

2.2.1 Source Tracking

The notion of tracking the HDR brachytherapy source as it moves through the programmed treatment has been previously reported for the purposes of afterloader quality assurance. Evans *et al* [67] described the use of radiochromic film to perform source position verification. This approach provided an accurate method to verify programmed dwell positions against measured dwell positions, and is particularly useful during applicator commissioning. Rickey *et al* [68] designed a useful tool that also incorporated radiochromic film to validate programmed source dwell positions. The custom device was intended as a pre-treatment quality assurance tool to perform source position and dwell time checks. Nakano *et al* [69]reported on a feasibility study to determine the position of the source using three diamond detectors to perform a triangulation calculation based on the response from each detector. The authors reported challenges associated with detector correction factors and the uncertainties associated with source to detector distances. Duan *et al* [59] investigated the possibility of using a pinhole camera imaging system for real time monitoring of the source position. A commercial dual-pinhole collimator was used for measurements and was able to reconstruct the source positions in 3D. The approach was unable to resolve source step sizes of 2.5 mm and data was processed retrospectively. The use of an imaging detector to locate the brachytherapy source was reported by Song *et al* [70]. In this phantom based study, the detector was coupled to an array of ball bearings and the projected shadows were used to determine the source position. A sequence of 10 mm spaced dwell positions were measured and the system determined the distance between dwells to a mean difference of 0.7 mm. The authors noted the significantly larger uncertainty (approximately 10 times) in measured SDD compared with the position in the plane of the detector. Another challenge of this system was ensuring the projected ball bearing shadows remained on the sensitive region of the detector. The novel 'magic phantom' device, consisting of a 2D (11 ×11) array of diodes, was reported by Espinoza *et al* [60, 71]. The magic phantom was used to verify synthetic patient plans delivered to the solid water phantom and identify errors that had been introduced to the plan. The authors reported the system can identify source position errors greater than 1.3 mm and dwell time errors greater than 0.3 seconds. A plastic scintillator block and a charge-coupled device camera system was used by Kojima *et al* [72] to measure source position applying a method previously used for particle beam quantification. For the

purpose of quality assurance, the authors were able to measure a source step size of 5 mm to a very high precision.

The approaches described above all attempt to verify the position and movement of the source in a phantom geometry for system quality assurance or plan pre-treatment verification. As far as the author is aware, there has been no published data on quantitative approaches to source tracking in the clinical setting. This may represent the significant challenges that need to be overcome to achieve such a system. The use of continuous imaging during the patient's treatment has been reported for treatment verification. A recent publication by Nose *et al* [73] used a modified C-arm fluoroscopic unit to perform real-time source tracking for the purposes of treatment verification. The approach uses continuous imaging to observe that the source is in the vicinity of the planned positions and correct relative to the patient's anatomy. The system has the advantage of real-time monitoring enabling treatment interruption if required. Quantitative determination of source positions was not performed in that study, but rather the treatment staff observe the source travel during treatment and refer to a plan printout for verification. The approach is likely only to identify gross source position errors, and as reported by the authors, an error detection limit of 5 mm was possible but may be greater due to the subjective approach to compare the plan printout to the fluoroscope image in real time.

2.3 Pre-Treatment Verification Imaging

Pre-treatment verification of the catheter positions for HDR prostate brachytherapy has been reported by many authors. Early attempts to verify the catheter positions were performed using film. Damore *et al* [32] performed a retrospective study on 96 patients to determine if significant displacement of the catheters had occurred between treatment fractions. The first and second fraction AP radiograph films were analysed and the catheter displacements determined based on implanted fiducial markers. A mean displacement of 7.6 mm was reported and as a result the authors recommended large margins (up to 10 mm) to be added to the treatment volume to account for the shifts observed in this study.

Martinez *et al* [74] also assessed inter-fraction catheter motion by performing fluoroscopic imaging on 10 patients between treatment fractions. The study compared catheter positions with bony anatomy, and reported a mean inferior displacement of 20

mm. Hoskin *et al* [31] used CT data to evaluate inter-fraction catheter displacement for 20 patients. A CT scan was acquired on day 2 prior to treatment delivery to assess displacement relative to the prostate. The CT data sets were evaluated by comparing the position of catheter tips with bony landmarks and the prostate gland from day1 to day 2 CT. A mean displacement of 11.5 mm relative to the prostate was reported. The authors acknowledged that catheter movement is an important issue and recommended that routine CT imaging be performed before each treatment fraction, and that flexibility is built into the implant to allow adjustments to be made.

Many studies have followed evaluating catheter displacements, with the majority using CT as the preferred imaging modality and fiducial markers in the prostate as the reference element to assess displacement. A summary of these recent studies is shown in table 2.2

Table 2.2. A summary of the studies performed to assess inter and intra-fraction catheter displacement in HDR prostate brachytherapy. P-F2 indicates the assessment was performed between the period of treatment planning imaging and second treatment fraction. P-F1 indicates the assessment was performed between treatment planning imaging and pre-treatment imaging.

Study (Year)	No. Patients	Imaging modality	Assessment	Period	Mean displ. (mm)
Damore (2000) [32]	96	Film	Fiducial markers	P-F2	7.6
Martinez (2001) [74]	10	Fluoroscopic	Bony anatomy	P-F2	20.0
Hoskin (2003) [31]	20	CT	Bone & Prostate anatomy	P-F2	11.5
Mullokandov (2004) [36]	50	CT	Bony anatomy	P-F2	2.0
Kim (2007) [34]	10	CT	Fiducial markers	P-F2	5.5
Simnor (2009) [75]	20	CT	Prostate	P-F2	7.9
Tiong (2010) [76]	91	Radiograph	Fiducial markers	P-F2	5.4
Yoshida (2010) [77]	64	CT	Fiducial markers	P-F2	7.0*
Whitaker (2011) [33]	25	Radiograph	Fiducial markers	P-F1	7.5*
Holly (2011) [35]	20	CBCT	Fiducial markers	P-F1	11.1
Takenaka (2012) [78]	30	CT	Fiducial markers	P-F2	4.3
Kovalchuk (2012) [79]	26	CT	Fiducial markers	P-F2	2.3+
Huang (2013) [80]	13	CT	Fiducial markers	P-F1	6.2
Kawakami (2014) [37]	30	CT	Fiducial markers	P-F1	6.0
Peddada (2015) [81]	33	CT	Fiducial markers	P-F2	1.0

* Yoshida &Whitaker report the median displacement.

+ Kovalchuk report mean displacement after readjustment.

Some of the studies in table 2.2 report measured catheter displacements calculated between the imaging data used for treatment planning (commonly CT) to imaging performed prior to treatment of fraction 2 (denoted as P-F2). Of these studies, 64% reported a mean catheter displacement of at least 5 mm and a maximum mean displacement of 20 mm. Often the period between treatment planning imaging and the delivery of the first fraction is on the order of many hours, and so some studies have evaluated the catheter displacement occurring during this period. Of these studies shown in table 2.2, all report a mean displacement of at least 6.0 mm. All of these authors recognised the potential impact this displacement could have on the patient's dosimetry and suggested catheter position adjustment to correct the observed shifts. One notable outlier of these studies is the reported 1.0 mm mean displacement from Peddada *et al* [81]. The authors suggest the method for performing the procedure (preparation, implantation and postprocedural care) most likely account for the negligible catheter displacements observed.

Many of the studies in table 2.2 use CT based treatment planning and so the patient is moved multiple times between the operating theatre (the implant procedure), imaging and treatment (bunker). An alternative approach is to perform all of these steps in the one setting. Known as 'intra-operative' or 'real time' HDR prostate brachytherapy[82], the approach is performed in a shielded operating theatre, with the patient anaesthetised in the lithotomy position. The Radiation Oncologist implants the prostate with TRUS guided imaging, which is also used to acquire the volumetric data of the prostate for treatment planning. The treatment plan is created and the treatment is delivered to the patient while still in the lithotomy position. The trade-off for this approach is a dedicated bunker (or operating theatre) is required, and additional specialised medical staff available. Typically, the time between implanting the catheters and the delivery of the first fraction on the order of a few hours, the influence of catheter displacement is reduced but not eliminated and still warrants confirmation. The study by Carrara *et al* [64] showed that re-imaging the prostate after treatment improved the IVD result. The study also noted that times greater than 1.5 hours between US image acquisition for planning and treatment delivery significantly increased the verification measurement uncertainty due to source to detector position changes resulting from intra-fraction changes of the prostate. Similar intra-fraction displacements have been identified by

Whitaker *et al* [33] showing up to 23.9 mm catheter displacement possible in the relatively short period between planning and treatment.

The pre-treatment imaging studies have identified displacements, but in most cases these imaging assessments are not performed in the treatment bunker, and so patient transfer and setup for treatment may induce additional catheter displacements. The ideal approach would be to evaluate catheter displacements in the treatment bunker immediately prior to treatment delivery.

Electromagnetic tracking (EMT) technology is an emerging development that has been applied to HDR prostate brachytherapy in preliminary proof of principle studies[83-85]. The system uses an electromagnetic field generator and a sensing unit to map the position of a sensor as it is passed through each brachytherapy catheter. to define the implanted catheter paths within the patient. The system reported by Beaulieu *et al* [86] can reconstruct a catheter path in the order of 10 seconds and define the catheter tip to better than 1mm accuracy. The system has the capability to define catheter paths for planning and repeat the process for verification as subsequent treatment fractions.

2.4 Summary

The efforts to perform treatment verification in HDR brachytherapy highlight three major shortcomings; (i) the source to detector uncertainty in IVD is a considerable challenge to overcome and has been acknowledged by many authors, (ii) the prohibitive nature of the additional work and time required to perform verification and (iii) the localisation of measured source dwell positions relative to the patient's anatomy is a key element in order to validate treatment to the correct (spatial) target/anatomy. A true solution to treatment verification will overcome all of these limitations.

To perform treatment verification effectively in the clinical setting, that is pre-treatment image verification and source tracking, a structured approach is required to achieve a reliable reference to compare against. Current methods to detect catheter displacements in prostate HDR brachytherapy use successive imaging and typically apply point based measurements (from the catheter tip) to evaluate any implant changes. The catheter tip is not (usually) the clinically relevant region of the implant, but the catheter positions need to be correct where the dose will be delivered. Therefore, verification should be performed against the treatment plan, assessing the path of the catheter, to provide a

detailed assessment of the implant geometry. In the clinical treatment verification scenario, there are 4 frames of reference that need to be combined in order to implement a quantitative verification approach. These are the patients' anatomy, the brachytherapy implant (catheters/applicator), the source tracking/pre-treatment imaging device and the treatment plan. The current status of the field of HDR brachytherapy lacks any mechanism to combine these frames of reference to provide a reference set for verification. EBRT has been verifying treatment delivery against the treatment plan in a quantitative approach for some time, using the technologies of treatment room imaging[87, 88] and portal dosimetry[89, 90]. HDR brachytherapy needs to achieve the same standard of quality treatment delivery.

The aim of this work was to develop a system to perform source tracking during treatment delivery. The proposed solution was to use a FPD for both source tracking and pre-treatment imaging. This would enable verification of the implanted catheters with the positions defined by the treatment plan, and allow verification of source dwell positions relative to the patient's anatomy.

This thesis aims to characterise the response of the FPD to the ^{192}Ir source (spectrum), develop methods to determine the position of the source in 2D (detector plane) and 3D (inside the patient), establish methods to perform pre-treatment imaging (2D and 3D) in the treatment bunker, register the measurement space with the TPS and identify catheter possible displacements to a clinically relevant uncertainty. An additional aim is to integrate the approach into a clinical environment to better understand the practical needs of clinical staff.

Chapter 3
Flat Panel Detector Characterisation for ^{192}Ir Measurement

3 Introduction

The detector device used during this study was a FPD, which previously was used as an EPID on a Varian linear accelerator (LINAC) (2100C Clinac, Varian Medical Systems, Palo Alto, CA, USA). The FPD was physically removed from the LINAC during decommissioning and operated as a stand-alone detector.

EPIDs were originally designed for geometric verification of the patient setup during EBRT, but have also been used to obtain dosimetric information – either pre-treatment verification or for *in vivo* dosimetry[91-94]. In principle, the dosimetric and geometric verification techniques developed in EBRT, can, with adaptation, be applied to HDR brachytherapy. Dose response characteristics of EPIDs have previously been determined for the megavoltage x-ray range[95, 96], but have not been demonstrated for an ^{192}Ir HDR brachytherapy source.

This chapter covers the measurements performed to characterise the response of this FPD for use with the ^{192}Ir HDR brachytherapy source. Each characterisation experiment has its own section describing the method and results obtained, with the overall outcomes discussed at the end of the chapter. The content of this chapter is based on the publication Smith *et al*[97]. Part of that publication describes algorithms used to determine the brachytherapy source position, and that work is described in chapter 4.

3.1 Detector Characteristics

The flat panel detector is an amorphous silicon (a-Si) electronic portal imaging device model *aS-500*. The device has a 400 × 300 mm^2 detection area with a pixel pitch of 0.784 mm (512 × 384 pixels), a 1 mm copper build-up layer, a scintillating screen of Gadolinium Oxide (Gd_2O_2S:Tb) and hydrogenated amorphous silicon (a-Si:H) photodiode array[98]. The flat panel detector is controlled using the image acquisition system (IAS2) hardware controller and operated using the 'AM-Maintenance' software version 7.1.2005.628 on a computer workstation, as shown in figure 3.1.

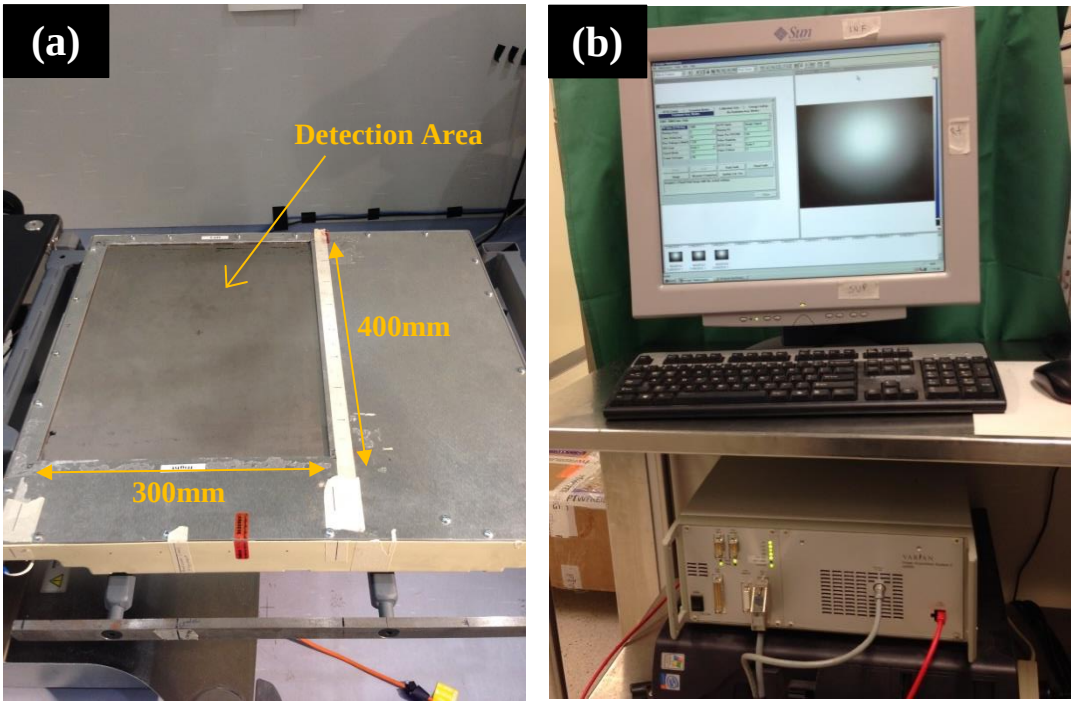

Figure 3.1. (a) The flat panel detector used in this work, model as-500 EPID from Varian Medical Systems. (b) The image acquisition system (IAS2) and the '*AM-Maintenance'* software used to control the detector.

The detector system is used to acquire images, where an image is defined as the average of all frames captured between start and stop signals and is corrected for dark current and response non-uniformity of the detector pixel array. A single frame is the read-out of the entire detector pixel array and an image is the average of frames acquired during the capture period. The FPD response (image or pixel array value) represents the *average dose rate* at the detection plane.

It should be noted that the term *image* when used in context for capturing the 2D distribution from the ^{192}Ir source refers to an array of pixels, and does not contain a one-to-one correspondence of points in the image to points in the object, as in the 'optics' sense.

3.2 Initial Evaluation

Exposures acquired from the brachytherapy source contain information that can be interpreted to potentially obtain source position and dosimetric data. Figure 3.2 illustrates the change of FPD response as the source is moved away from the detection plane. The intensity of the response and shape of the profile clearly changes with source to detector distance (SDD), reflecting the change in dose rate. The distribution can also be used to localise the source position in the 2D plane of the detector and potentially the perpendicular distance from the detector plane.

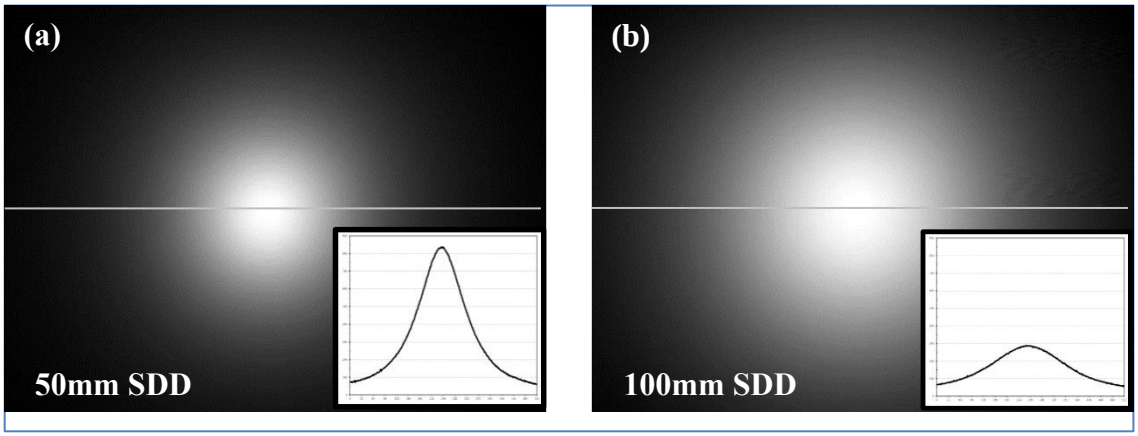

Figure 3.2. Images acquired with the FPD system for the brachytherapy source at two different source to detector distances (SDD). (a) A SDD of 50mm and a line profile showing the intensity and shape of the detector response and (b) at a SDD of 100mm.

Using the principles of EBRT verification, it is possible to interpret the FPD image as a transit (exit) dose distribution for a source within the patient. In order to initially evaluate this detector response, the acquired FPD image was compared to the dose exported from the TPS, for a source in a solid water phantom as shown in figure 3.3.

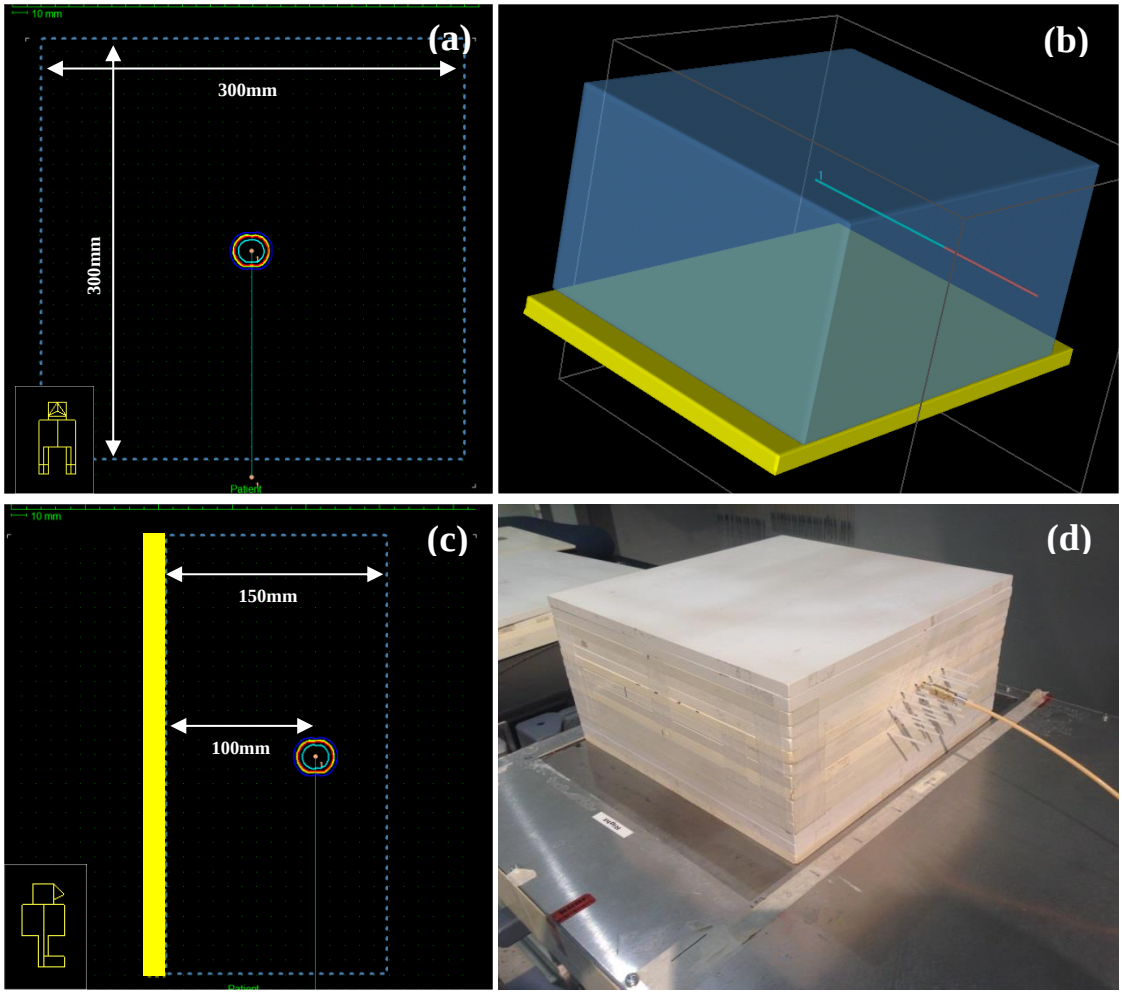

Figure 3.3. (a) The TPS sagittal view of the solid water phantom used for experimentation showing a single catheter path, a dwell position and the surrounding isodoses. (b) A 3D visualisation of the catheter path within the reconstructed phantom above the flat panel detector depicted in yellow. (c) The TPS coronal view of the source in the phantom showing the distance of the source to the flat panel detector. (d) A photo of the solid water phantom with a transfer tube attached, placed above the flat panel detector.

We can compare the response with that generated by a TPS, which uses the TG-43 dose calculation formalism[99], in order to establish the raw agreement, normalised at the maximum response. It is observed in figure 3.4 that there are differences in the raw response, but also similarities that suggest the detector is a useful tool for treatment verification.

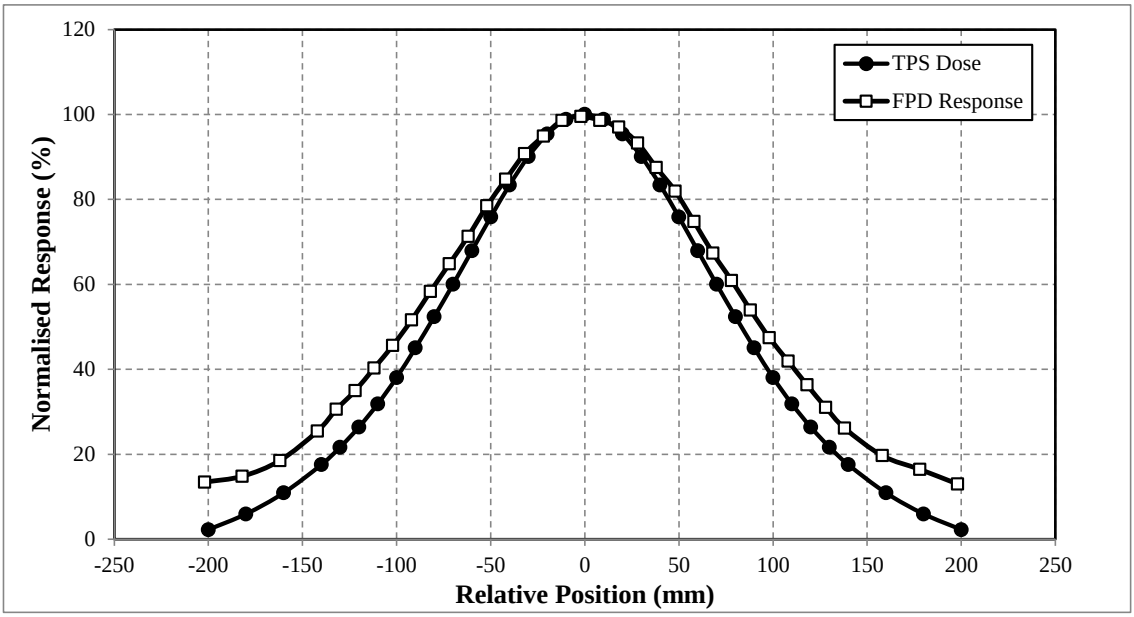

Figure 3.4. The comparison of FPD response with the response predicted by the TPS using a TG-43 calculation algorithm. For comparison, the data is normalised at the maximum response and profiles aligned to this normalisation position.

There are a number of factors expected to contribute to the observed discrepancy in detector response. These include the detector not being tissue equivalent, possible dose rate non-linearity, detector directional dependence, and finite phantom geometry size causing a reduced or asymmetric photon scatter field which may also influence the response. Energy dependent response of the FPD, as other authors have shown[95], may also impact the response, as a large fraction of photons reaching the detector at extended distances are lower energy scatter. The TG-43 dose calculation is also a poor estimate of dose at large distances from the source or when inhomogeneities are present. Therefore, we can expect large discrepancies between the predicted TPS curve and the raw (uncorrected) FPD measurement.

The aim of this application is to use the FPD as a treatment verification device, it is not necessary for the FPD device to measure 'true' dose to water. The goal of treatment verification is to provide evidence the planned treatment is delivered without error, and so the response of the FPD should represent the expected result as predicted by the

TPS, and not deviate simply due to the limitations of the TG-43 algorithm. The evaluations made in the following sections reflect the comparisons of the FPD response with the TG-43 algorithm.

The response of the FPD was characterised across a range of exposure conditions. The following sections detail the experimental method performed, the results observed, and factors contributing to observed deviations are assessed and methods for correction are established.

3.3 Response to Photon Energy

To determine the response of the FPD as a function of x-ray energy, for the same dose at the FPD surface, the FPD was exposed to a range of photon sources using facilities at the ionising radiation standards laboratory of the Australian Radiation Protection and Nuclear Safety Agency (ARPANSA). The 'SIEFERT' orthovoltage x-ray system (Isovolt 450/9, Rich. Seifert & Co) produces ISO 4037 standard 'narrow-spectrum' series x-ray beams[100] using a constant potential tungsten target x-ray tube and specified filtration. The FPD was set at 1 m from the x-ray source and exposed to seven ISO 4037 beams, with effective energies ranging from 48 to 251 keV. The effective energy of the x-ray beam is defined as the energy of a mono-energetic beam having the same half value layer (HVL) in Cu as the ISO narrow x-ray beam.

To mimic the energy of the major peak in the ^{192}Ir spectrum[101] at 317.5 keV, the ISO 4037 formalism was extended to establish an additional higher energy x-ray beam on the 'SIEFERT' system. The x-ray tube potential (kVp) for this beam was 400 kV with a beam filtration of 6.6 mm Pb + 2 mm Sn + 4 mm Al, to produce an effective x-ray energy of 317.5 keV. The FPD was also exposed to ^{60}Co (1.2 MeV), ^{137}Cs (662 keV) and ^{192}Ir isotope sources and a 6 MV Varian EX linear accelerator beam.

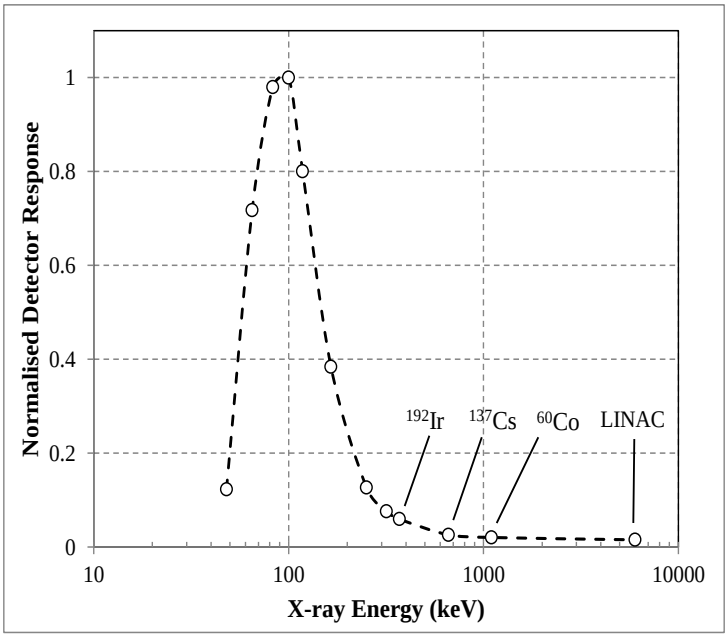

Figure 3.5. The normalised flat panel detector response for a range of incident kilovoltage photon beams, isotopes and a 6MV linear accelerator (LINAC) beam.

The FPD exhibits an over-response to incident photons at relatively low energies in the radiotherapy arena, with a peak response at approximately 100 keV, as seen in figure 3.5. This has implications for use as a dosimetry validation tool for HDR brachytherapy and energy dependence must be incorporated into the dose calibration procedure. When exposed to an ^{192}Ir source, at large distances, a substantial component of the dose to the FPD will consist of low energy scattered radiation[102] and this should be considered when applied in the clinical scenario where SDDs of 80 to 160 mm are expected.

The hypersensitivity of the FPD to low energy photons, also reported by Kirkby[95] in the EBRT case, is an important characteristic to consider when planning to use such a device for dosimetry purposes.

3.4 Response to Dose Rate

A dose rate response measurement was performed at a fixed SDD geometry of 100 mm, over the clinical life of the source, in order to achieve a decline in dose rate without a change in the energy spectrum. A 300 x 300 mm solid water phantom containing a brachytherapy catheter was placed against the face of the FPD and the source driven to a central position. Exposures were acquired with the source at the central position and

the response was recorded for a 5x5 pixel region of interest (ROI) centered at the peak of the response. Over the period of approximately 3 months, the source decayed from 3.866 to 1.680 cGy·m^2/h. The dose rate at the surface of the FPD for each measurement was calculated using the treatment planning system.

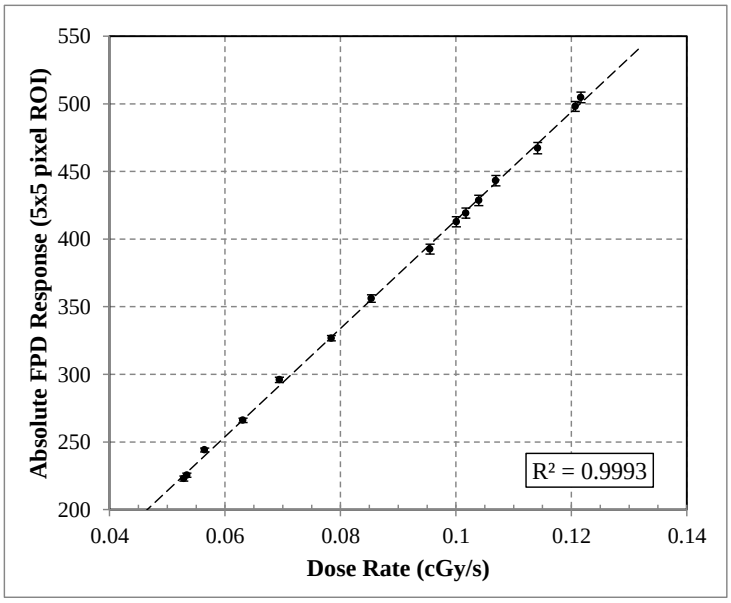

Figure 3.6. The dose rate response of the FPD measured in a solid water phantom, at a source to detector distance of 100 mm, over a period of approximately 3 months.

While maintaining a constant energy spectrum reaching the FPD by using a fixed geometry, the FPD shows a highly linear (R^2=0.9993) response to dose rate at 100 mm SDD (Figure 3.6). The SDD of 100 mm represents a typical patient source dwell position (mid-implant) to posterior treatment couch surface, as determined by evaluating approximately 50 patient CT scans. The error bars in figure 3.6 are approximately the size of the data point markers and represent one standard deviation of response of image pixels within the ROI (5x5 pixels) measured. These results show linearity over a clinical dose rate range at this SDD (approximately 0.05 to 0.12 cGy/s).

3.5 Response to Depth Dependent Spectral Change

The response of the FPD was shown to vary non-linearly with photon energy and so was therefore expected to vary as a function of source to detector distance. This change in response to depth dependent spectral change was evaluated using a 300 x 300 mm solid water phantom containing a brachytherapy catheter, as previously depicted in figure 3.3. The source was driven to the central position of the phantom and images acquired for a range of SDDs (50, 80, 100, 120, 150, 180, 200 and 250 mm) for the same source activity.

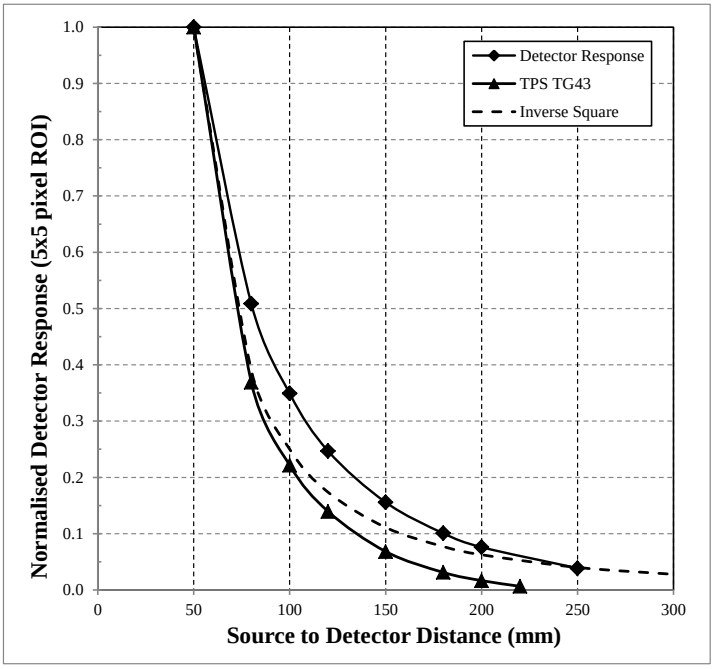

Figure 3.7. The normalised FPD response measured in the solid water phantom of figure 3.3, at an SDD of 50, 80, 100, 120, 150, 180, 200 and 250 mm. The TPS TG-43 dose and the inverse square curve is also shown for comparative purposes.

The over response of the FPD to scattered (low energy) radiation implies that the relationship between dose rate and FPD response output will change with SDD due to the changing primary to scatter ratio. Figure 3.7 compares the measured response fall-off and an inverse square curve normalised to a SDD of 50 mm. The measured response lies above the inverse square curve, rather than below as would be expected considering photon attenuation (See TG-43 curve in figure 3.7). This highlights the influence of FPD over response to low energy scattered radiation at intermediate source to detector

distances. In section 3.10, we describe a solution to manage the spectral dependence, by employing a semi-emperical depth dependent calibration procedure.

3.6 Response Reproducibility

The response reproducibility of the FPD was investigated for a range of SDDs (50 to 180 mm) using images acquired with 250, 100, 10 and 2 frames per image, to quantify the effect of image acquisition time.

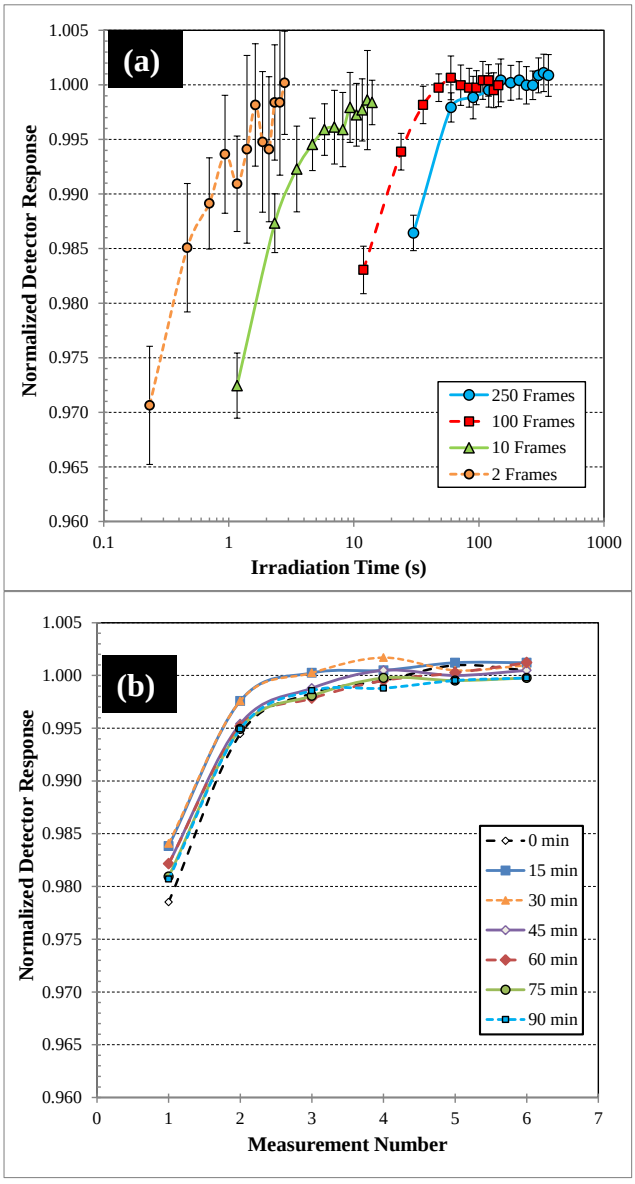

Figure 3.8. The normalised detector response measured in the solid water phantom detailed in Figure 1, with an SDD of 100 mm. (a) Measurements acquired with 2, 10, 100 and 250 frames. (b) Consecutive measurements acquired at 15 minute intervals with 250 frames.

To evaluate charge build-up effects (slight under response observed in short irradiations) as identified in EBRT studies[103], a series of consecutive acquisitions was made for each acquisition duration (2, 10, 100 and 250 frames; frame rate = 8.6 frames/s).

To further investigate the response reproducibility over time, the process was repeated at 15 minute intervals, acquiring six consecutive images each with 250 frames.

The response of the FPD over successive images acquired with the source at a single dwell position shows an initial response lag over successive measurements until a stable value is achieved. This lag effect has also been reported by other investigators[103-105]. Decreasing the number of frames per image increases the number of measurements required, but decreases the irradiation time, before stability is reached (Figure 3.8(a)). Repeated measurements confirm that this behaviour is highly reproducible (see Figure 3.8(b)).

The response of the FPD over a series of images at 15 minute intervals shows that the lag effect is the same over a 90 minute time period (Figure 3.8(b)). All data sets fall within a range of 0.3 % of the first (0 minute) data set. All data points were normalised to the average response value of the last 5 data points of the first acquisition set collected at time of 0 minutes. Since the lag effect is so reproducible, we can be confident the implementation of an empirical correction factor can be applied to measurements taken within the first 3 image acquisitions of a sequence.

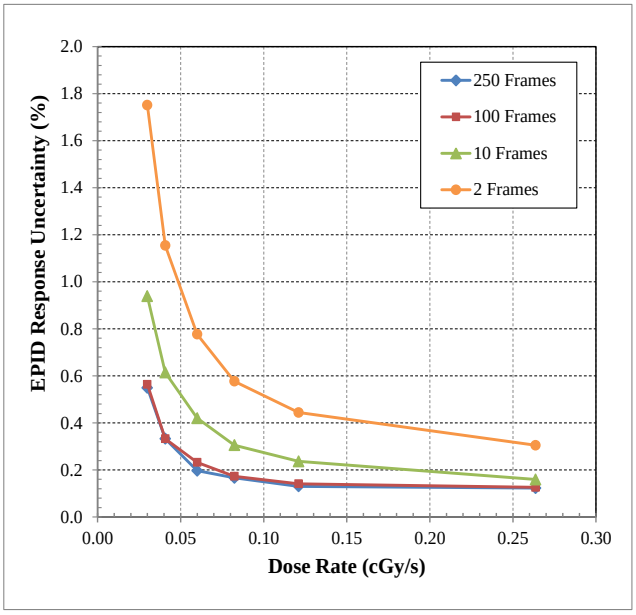

Figure 3.9. The FPD response uncertainty as a function of dose rate at the FPD for image acquisitions with 250, 100, 10 and 2 frames.

The uncertainty of the FPD response was determined by calculating one standard deviation of the pixel range in the 5x5 ROI used for calculation of the response. The standard deviation was assessed as a function of the number of frames used in the image acquisition. Figure 3.9 shows the increasing uncertainty of response as the number of frames are reduced. Typically measurements at larger SDDs will result in lower dose rates and an increased uncertainty.

3.7 Off Axis Response

Prompted by discrepancies in the SDD dependent response measurements the incident angle dependence was investigated. The under response of the FPD at off axis positions relative to points aligned with the HDR brachytherapy source central axis at an equal SDD (Figure 3.10) were plotted against incident angle, θ, at the FPD surface. This was used to derive a fitted angular correction factor.

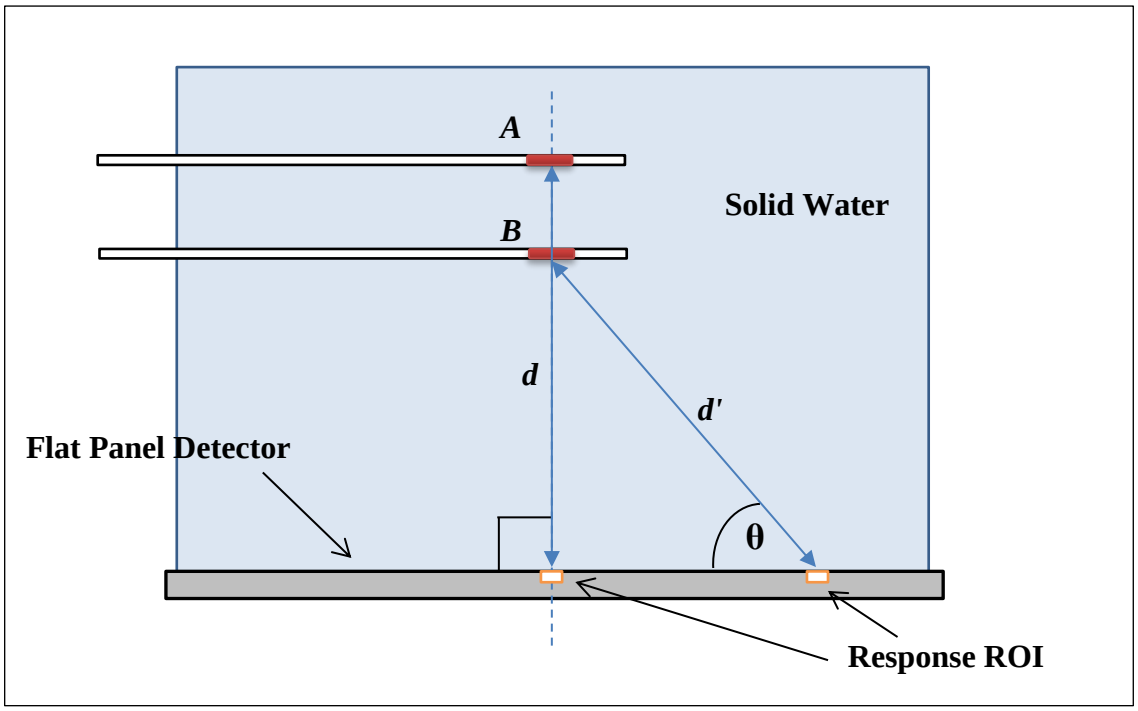

Figure 3.10. The linear distance *d* from the source at position A to the detector ROI is the same as the distance d' from the source at position B to the detector ROI with an incident angle of theta. The ratio of response between the two ROI for the same linear distance defines the incident angle response of the FPD.

The measured off axis response of the FPD was shown to under respond relative to the central axis case, where the linear distance from the source to the FPD surface was the same. This means that the calibration factor at the perpendicular position does not apply at the equivalent distance off axis from the source position (i.e. for a smaller SDD). The relative response as a function of incident angle between the FPD plane and the ray line from the source to the measurement point/pixel can be used as an empirical correction function to the dose rate calibration (Figure 3.11).

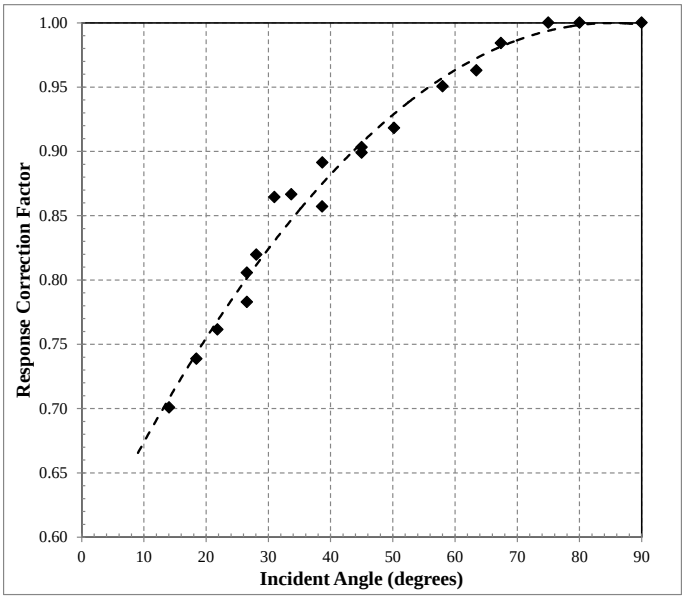

Figure 3.11. Incident angle correction factor for each pixel in the FPD image accounting for the observed off-axis response change. Note the truncated vertical axis.

Figure 3.11 represents the under-response of the FPD for pixels that are off axis relative to the central axis case, where the linear distance from the source to the FPD surface is the same. The response correction factor can be fitted with a polynomial given by equation 3.1.

$$Responce\ Corr. = -6 \times 10^{-5}\theta^2 + 0.0098\theta + 0.5815 \qquad \text{Eqn. (3.1)}$$

The reason for this under response at decreasing incident angles is not clear, but it is likely that the process of interaction of the photons with the scintillation layer at a narrow angle is different when compared to the perpendicular case. The deposition of charge to the photo diodes is less efficient or spatially less well defined for the narrow angle case. Additional reasons for under-response may be due to the greater effective thickness of the copper plate at narrow incident angles, especially for low energy photons, as well as the reduction of scatter off axis due to the finite size of the solid water phantom.

The observed behaviour of the response suggested as incident angle response, but further analysis indicated that it was a combination of incident response and scatter conditions. Isolation experiments were performed to establish the contribution from each component. These are described in the next 2 sections.

3.8 Response to Source Orientation

The orientation of the source relative to the plane of the FPD may influence the response observed. All previous investigations in this chapter have been performed with the long axis of the source parallel to the plane of the detector. In order to evaluate the influence of source orientation on detector response, a solid water slab was customised by cutting grooves to hold the plastic brachytherapy catheter at different angles relative to the FPD plane. The central piece was designed to rotate to allow each catheter to deliver the source to a rotational centre.

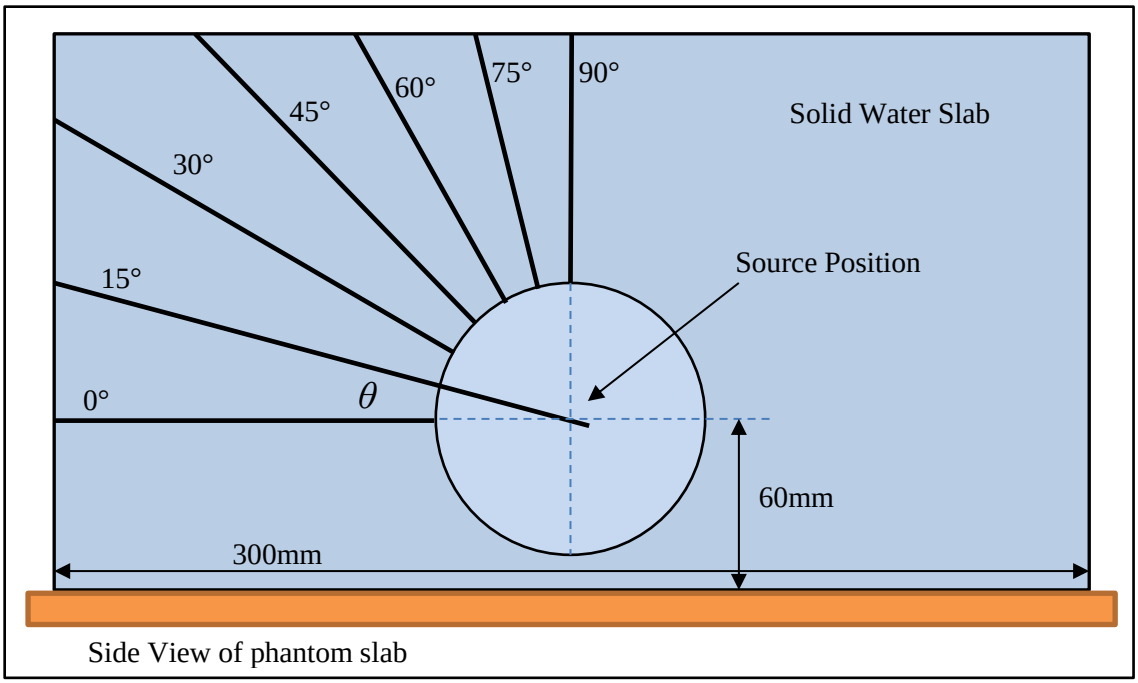

Figure 3.12. The solid water slab used to evaluate the influence of source orientation on the FPD imaging plane. The internal circular phantom can rotate to accommodate a brachytherapy catheter at each angular position θ.

The custom solid water slab depicted in figure 3.12 was set up in a solid water phantom (300×300×300 mm) with the slabs of the phantom oriented vertically to accommodate the custom rotational slab.

The brachytherapy catheter was initially setup parallel to the plane of the FPD (θ = 0°) and the source was driven to the central position of the phantom at the point of rotation and an image acquired. The catheter was then repositioned at each rotational position and images acquired at each increment.

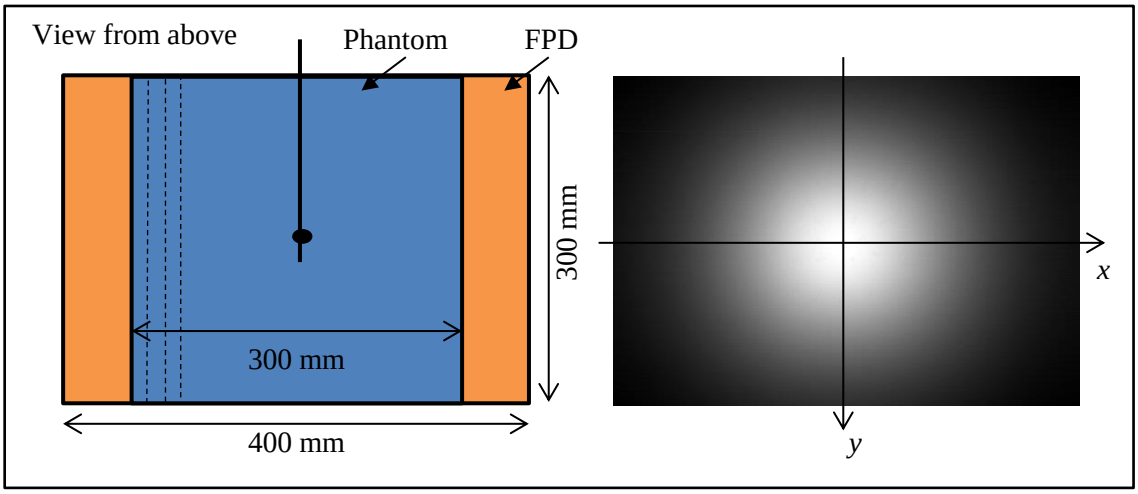

Figure 3.13. The experimental setup of the phantom to capture exposures with the brachytherapy source. The rotation of the source in the plane perpendicular to the FPD surface (out of the page). Profiles in the *x* and *y* axis were acquired as the source was rotated to each position. The orientation of the solid water phantom slabs are shown by the dashed lines.

To evaluate the response change as a function of source rotation, profiles were extracted from the acquired images in the *x* and *y* planes as illustrated by figure 3.13.

The acquired profiles were normalised to the central axis position of the FPD for the θ=0° acquisition, directly below the source. The results are shown in figure 3.14(a) for the *x* axis profiles and 3.14(b) for the *y* axis profiles.

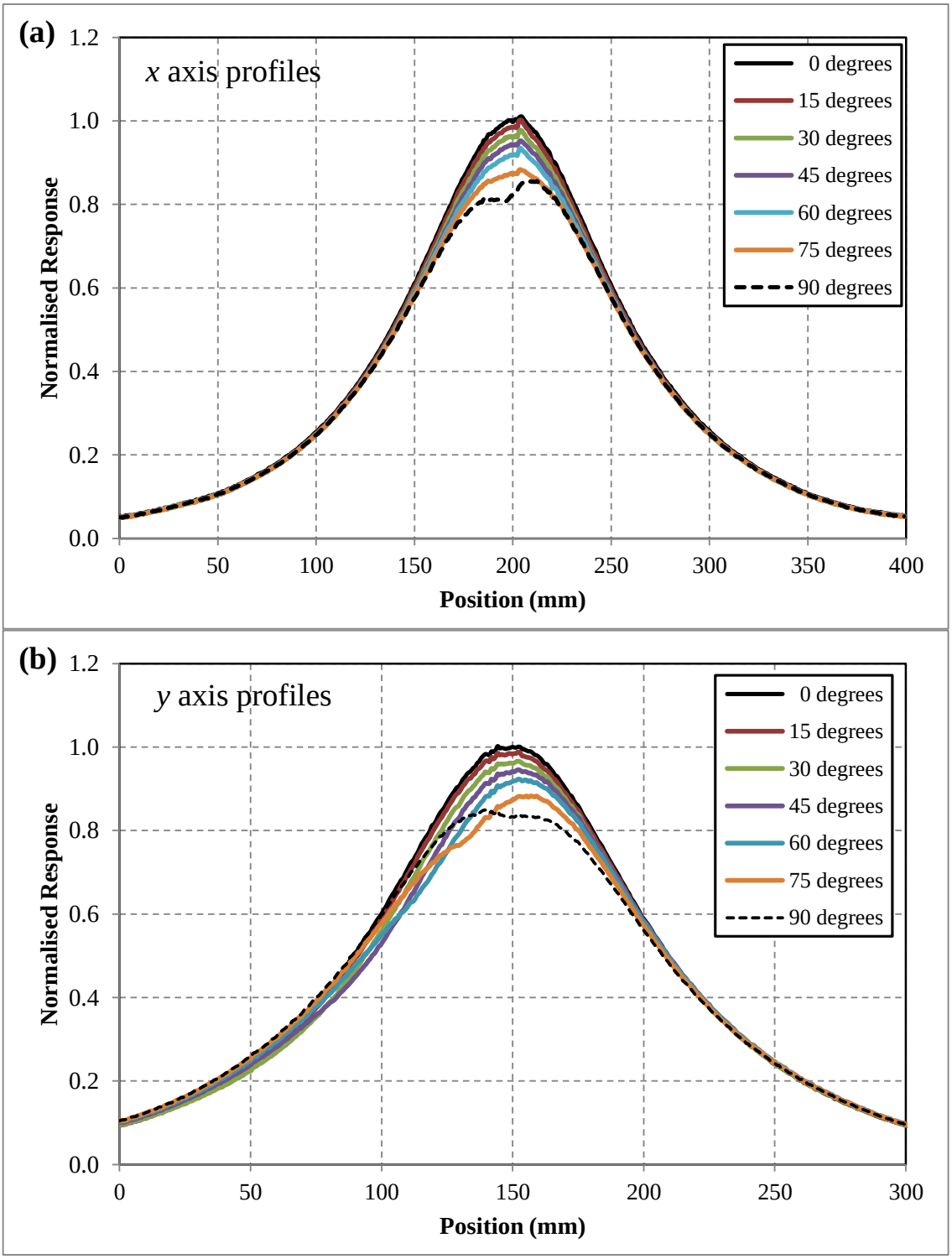

Figure 3.14. (a) The *x* axis profiles and (b) the *y* axis profiles of the acquired exposures of the source as the source is rotated from 0° to 90° relative to the imaging plane of the FPD.

The profiles acquired along the *x* axis show small discontinuities in the response near the profile peak. This arises from the vertical orientation of the solid water slabs, possibly due to a small gap, allowing transmission to occur between the slabs.

The observed decrease in response of the FPD as the source is rotated is illustrated in figure 3.15 and is primarily due to the self-attenuation of the source. The source cable does not contribute to attenuation as it is not between the source and FPD.

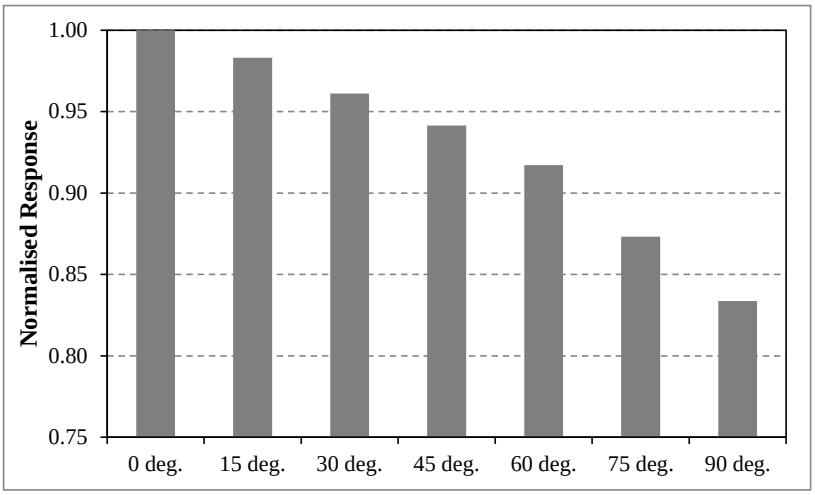

Figure 3.15. The central axis response of the FPD for a 5 x 5 pixel ROI as the source is rotated. Note the y axis scale.

As expected the shape of the profiles in the *x* axis do not change as the source is rotated. An asymmetry of the profiles in the *y* axis is observed as the source is rotated in this plane.

The potential application of this verification system will initially focus on prostate brachytherapy, where catheters are likely to be parallel or at an angle of up to 30 degrees to the FPD. The extension to gynaecological brachytherapy applications will potentially include brachytherapy applicators that will orientate the source at large angles relative to the FPD.

3.9 Finite Phantom Geometry

Finite phantom geometries are expected to be a contributing factor to discrepancies observed between the measured response of the FPD and what is predicted by the TPS, if the closest air boundary is near enough the measurement point. The TG-43 formalism assumes an infinite uniform phantom surrounding the source, but a finite phantom geometry will create photon scatter disequilibrium, and considering the observed over response of the detector to low photon energies, the measured FPD response is expected to be affected.

To investigate this influence of finite phantom geometry, a solid water phantom was created so slabs adjacent to the source could be removed, as illustrated in figure 3.16, to produce an asymmetric scattering geometry around the source position.

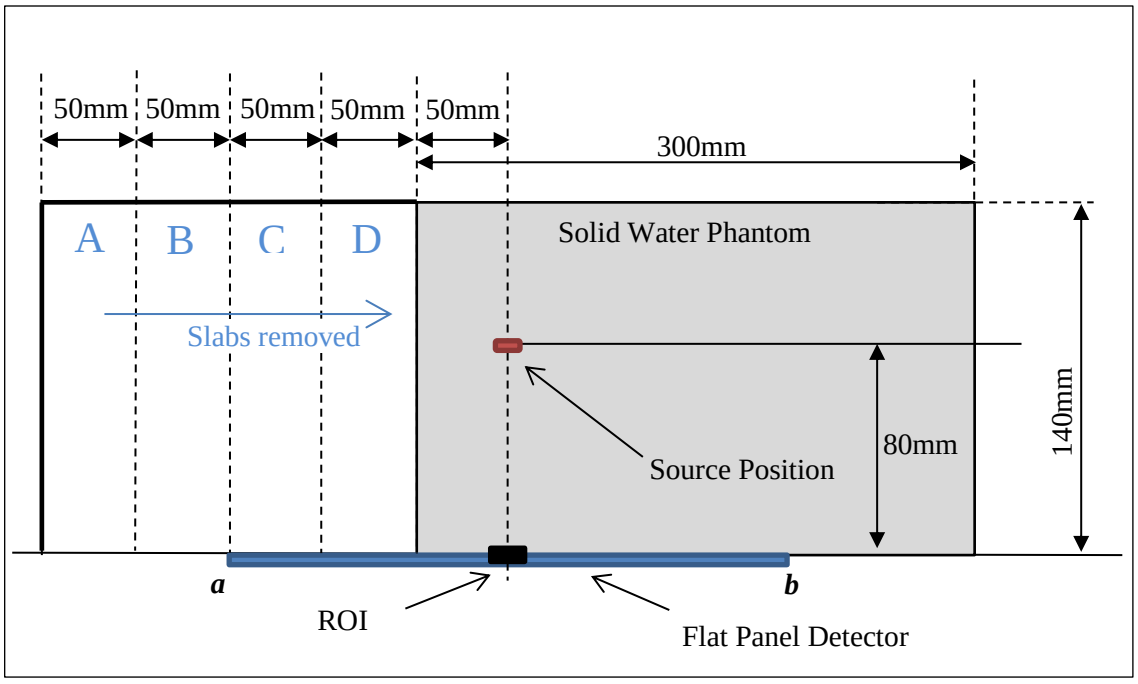

Figure 3.16. The experimental setup for investigating the influence of surrounding phantom geometry on FPD response. Slabs of solid water phantom are removed at each measurement increment to produce an asymmetric phantom geometry around the source position.

The phantom consisted of 300 × 300 mm solid water slabs, with an additional 4×50 mm slabs of solid water to create a symmetric phantom around the source dwell position. To mimic the geometry of a source inside a patient, a SDD of 80 mm was used with an additional 60 mm of solid water was placed above the source. The position of the

phantom and source was aligned to be at the centre of the FPD in order to evaluate the expected asymmetric response.

The source was driven to the dwell position and a FPD image was acquired. Solid water slabs of 50 mm thick increments (A, B, C and D) were removed and images acquired at each increment.

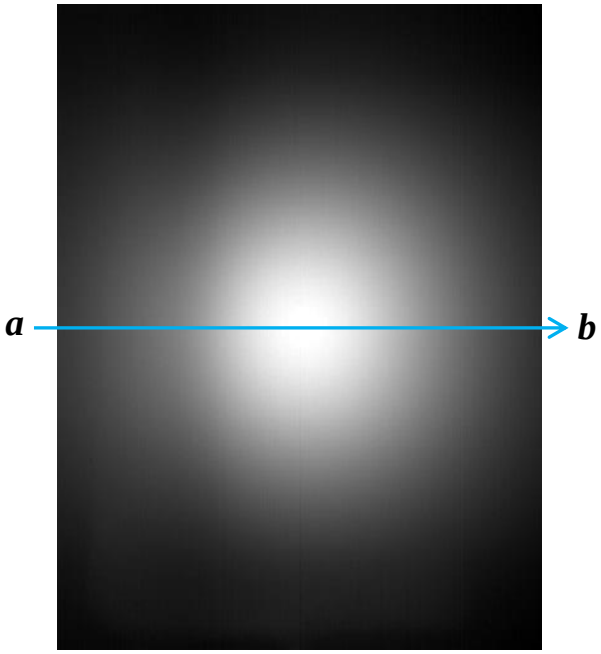

Figure 3.17. The FPD image for the asymmetric phantom geometry, with 50 mm of solid water adjacent to the source position. Image response profiles were extracted across the FPD from *a* to *b*, as illustrated.

The mean FPD response for a 5×5 pixel region of interest (ROI) located at the centre of the FPD was calculated for each image and normalised to the response for the symmetric phantom case. FPD response profiles were also extracted from the images, as shown in figure 3.17, at each phantom geometry.

The resulting FPD response as a function of adjacent phantom size is shown in figure 3.18. It can be seen that a minimum of 150 mm of surrounding phantom material is required to maintain equilibrium in the photon scatter field and not impact the detector response. With less than 150 mm of phantom material, the response of the detector at the ROI reduces, emphasizing that photons scattered from slab 'C' (figure 3.17) influence the response of the ROI below the source position.

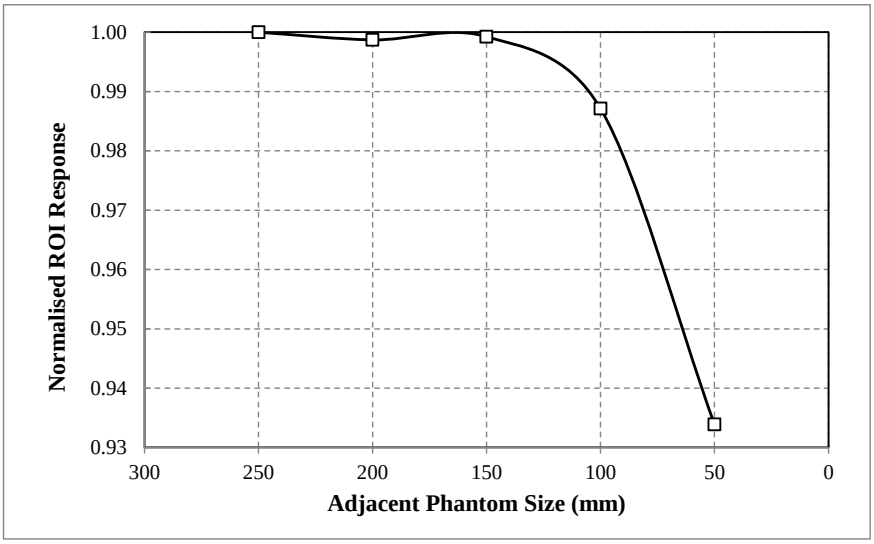

Figure 3.18. The FPD response at the ROI position depicted in figure 3.17 as a function of adjacent phantom size. Note the truncated vertical axis.

The influence of scattered photons on the response of the detector can also be evaluated by extracting response profiles (figure 3.19). It is clear for a full symmetric phantom geometry (250 mm of phantom material surrounding the source), the response profile is symmetric and the peak position appears at the source dwell position, centered on the FPD (at 150 mm). As the slabs are removed the profiles remain consistent for 200 and 150 mm, but exhibits a deviation for 100 mm of scatter material. The effect is then emphasized when only 50 mm of scattering material is present, causing the peak of the profile to shift slightly away from the edge of the phantom (see 50 mm Scatter profile in figure 3.19), and so not coinciding above the actual physical source position. A change in the tailing of the 50 mm Scatter profile can be seen at a position of approximately 80 mm, due to part of the FPD being uncovered (phantom material removed), and the attenuation path from the source being radiologically shorter.

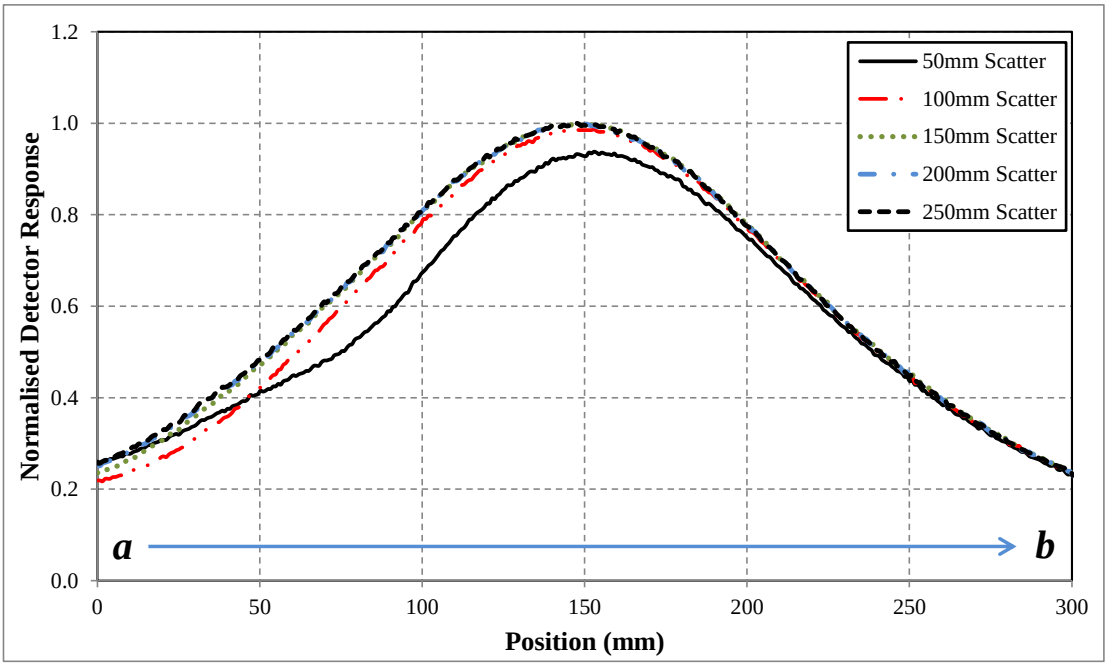

Figure 3.19. The FPD response profiles for changes in the adjacent phantom size for the source position as illustrated in figure 3.16.

The decrease of response in figure 3.18 indicates that a minimum of 150 mm adjacent scatter material is required to maintain an unchanging photon phantom scatter field, and not cause an asymmetric response of the FPD. This result is also supported by the earlier profile of figure 3.4 where the source was at the centre of a 300 × 300 mm phantom, producing a symmetric FPD response.

The influence of finite phantom geometry is an important characteristic when considering the use of this device in the patient case. Treatment sites close to the skin (e.g. Interstitial Breast) or for prostate, where the perineum space is less than 150 mm from the prostate, a reduced detector response is likely and will need to be considered.

3.10 Dose Rate Calibration

The potential use of the FPD as a dosimetric verification device required calibration of the detector response with dose. When performing a verification dose measurement, the purpose of this system will be to validate delivery of the planned treatment, therefore the system is calibrated against the TPS (TG-43). The FPD response to dose rate is photon energy spectrum dependent and therefore depth dependent, as well as incident

angle dependent. A semi-empirical calibration procedure was developed to include these dependencies.

A relationship between TPS derived dose rate and FPD response for a 5×5 pixel ROI was measured over a range of SDDs (50, 80, 100, 120, 150, 180 and 200 mm) and is shown in figure 3.20. A depth dependent calibration function was determined by fitting a curve to the dose rate response calibration points and is given by equation 3.2.

$$\frac{TPS dose\ rate}{FPD\ response} = -7 \times 10^{-6}(SDD)^2 - 0.0017(SDD) + 0.7729 \qquad \text{Eqn. (3.2)}$$

The distance (and therefore spectral) dependent dose rate calibration function is shown in Figure 3.20.

Across the set of all measurements, pixels with identical SDDs but different angles of incidence from the source were identified and used to derive an angular correction function, as shown previously in figure 3.11. The conversion of image pixel value to dose rate is achieved by combining the calibration function of figure 3.20 with the response lag correction of figure 3.8 and an angular correction factor from figure 3.11.

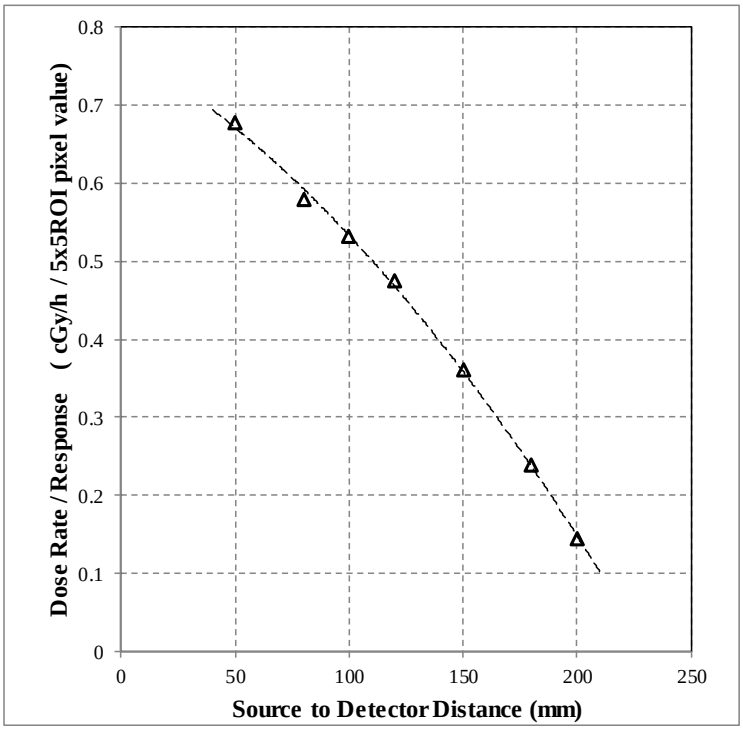

Figure 3.20. The TPS dose rate per FPD response as function of source to detector distance. The ratio of dose rate to FPD response decreases as the distance is increased due to the increase in scatter to primary photon ratio reaching the FPD .

3.11 Image Plane Determination

The FPD forms an image in the semi-conductor layer of the detector at a distance below the surface of the detector imaging face. In order to compare measured dose with the TPS or to determine the divergence correction factor that will be applied to a radiograph image, the imaging plane depth, where the image is formed, needs to be determined.

The imaging plane depth within the FPD was determined using an 'edge projection shift' technique. The FPD was aligned with its surface at the isocentre of a treatment simulator (Acuity^{TM}, Varian Medical Systems, Palo Alto, CA, U.S.A.). A thin copper sheet was placed flat against the FPD surface with an edge aligned at the isocentre. An image of the copper sheet was acquired with normal incidence (Gantry = 90 degrees), figure 3.21(a), and again with the gantry rotated to 45 degrees as shown in figure 3.21(b). Images were also acquired for a range of gantry angles (Gantry = 30, 45, 60, 70, 80 degrees), and the imaging plane depth was calculated using the geometric relationship depicted in figure 3.22.

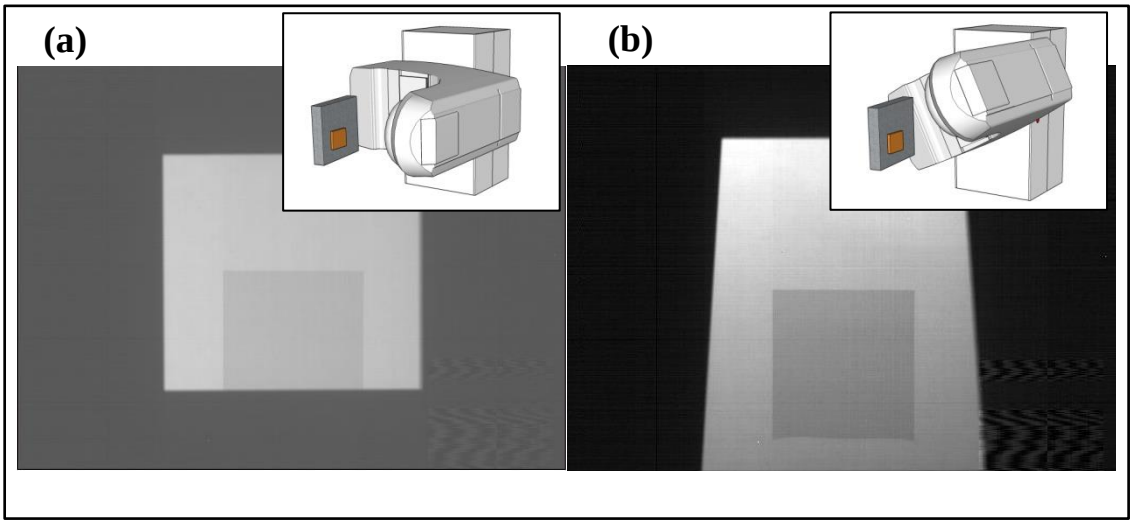

Figure 3.21. (a) The image of the copper sheet edge with the simulator gantry at 90 degrees, and at 45 degrees (b). The shift of the copper sheet edge was used to calculate the imaging plane depth below the FPD surface.

All acquired images were analysed using the ImageJ software (ImageJ ver. 1.44, Wayne Rasband, NIH, USA). The vertical pixel location (at the central axis) of the edge of the copper sheet was determined for each image. The difference between the

normal incidence projection and each rotated gantry angle projection, labelled *a*, was calculated.

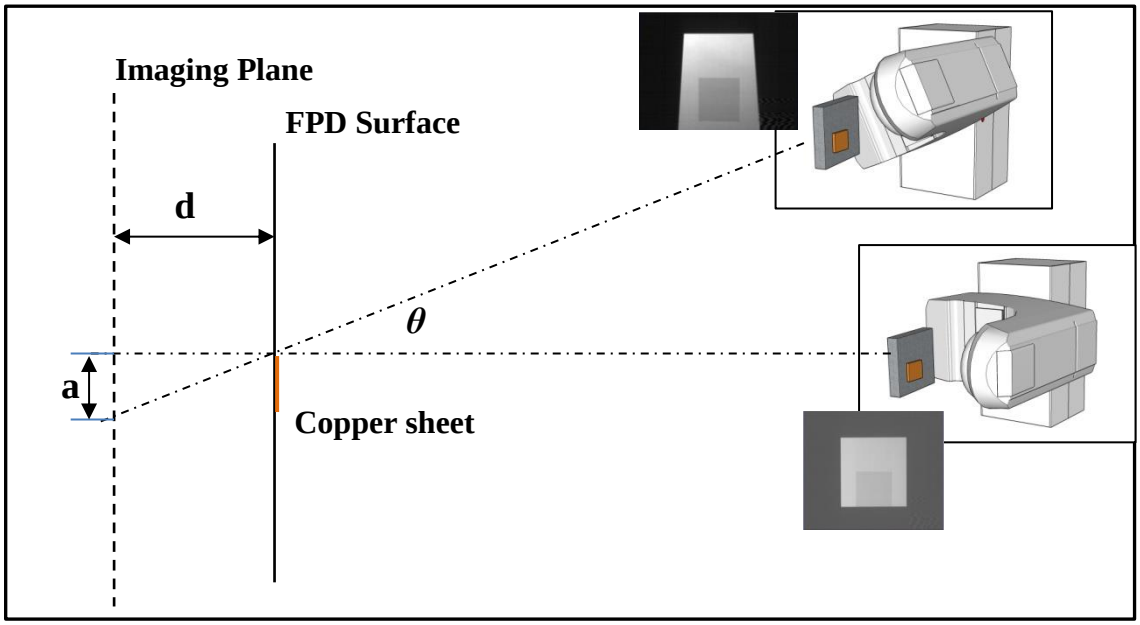

Figure 3.22. The geometric relationship between the two gantry positions, where *a* represents the observed shift of the copper sheet edge. This is then used to calculate the position of the measurement plane below the surface of the flat panel detector, *d*.

The FPD imaging plane depth is calculated by:

$$d = \frac{a}{tan\theta} \qquad \text{Eqn. (3.3)}$$

The measured data used to calculate the image depth is summarised in table 3.1.

Table 3.1. The measured data used to determine the depth below the surface of the FPD where the image is formed.

Gantry Position (deg.)	***θ* (deg.)**	***a* (mm)**	***d* (mm)**
30	60	22.7	13.1
45	45	13.3	13.3
60	30	7.5	12.9
70	20	4.7	12.9
80	10	2.4	13.3
Mean			**13.1**

The mean calculated depth below the FPD surface, *d*, where the image is formed is 13.1 mm (s.d. 0.2 mm). This imaging plane depth is included in the calculation of a

magnification correction factor when imaging geometries are described for pre-treatment imaging purposes as described later in chapter 5.

3.12 2D Dosimetric Verification

To illustrate the use of a FPD as a dosimetric verification device, two simple treatment plans were delivered to the phantom of figure 3.3. The dose calibration and correction factors were applied to the 2D FPD image response and the distribution was compared to that predicted by the TPS.

A single dwell position plan was delivered and a FPD image of 250 frames was captured while the source was stationary. The source position was calculated using an asymmetric Lorentz fitted function (details of methods to calculate the source position appear in chapter 4), and the FPD response converted to dose rate (using equation 3.2) and multiplied by the dwell time to obtain measured dose for direct comparison with TPS. A profile of measured dose was compared to the corresponding TPS dose profile. The TPS isodose distribution was compared to the measured isodoses using the FilmQA analysis software (3cognition LLC, New York, USA) and a dose difference map was generated.

A second plan was delivered containing two dwell positions. FPD measurements were acquired for each dwell position, delivered at a separation of 80 mm. Individual and combined dose profiles and isodoses were calculated to demonstrate the convolution of individual dwell contributions to the net dose distribution. The resulting profiles, isodose maps and difference images for the two delivered plans are shown in figure 3.23.

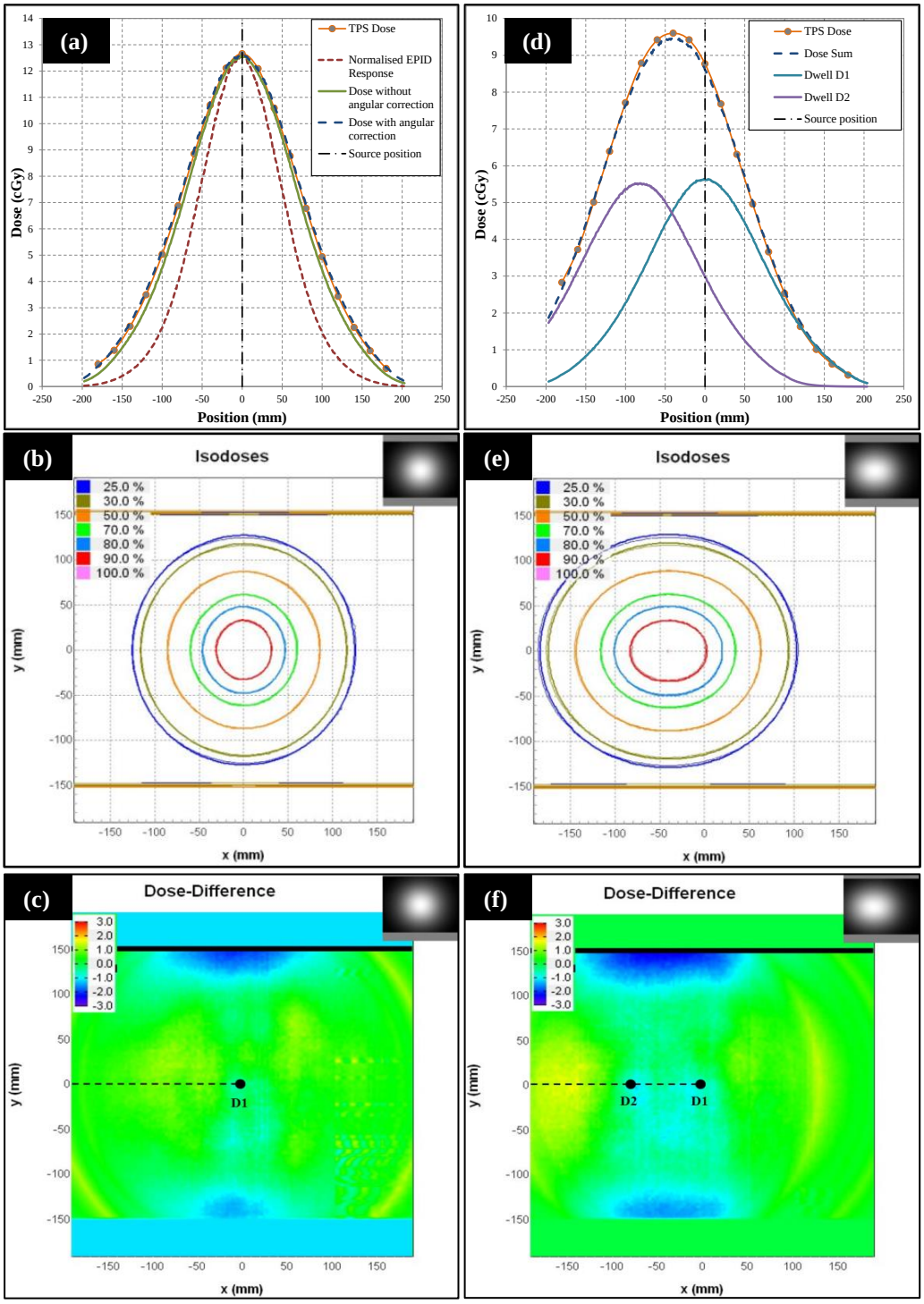

Figure 3.23: (a) A profile through the centre of the distribution showing the FPD response, dose uncorrected for angular response and corrected measured dose compared with the TPS predicted dose. (b) A comparison of isodoses measured (fine line) and TPS (heavy line) at 100 mm SDD. (c) The two dimensional dose difference, where the distribution is TPS minus measured dose, at 100 mm SDD. (d) A profile through the centre of a two dwell distribution showing the contribution each dwell to the total measured dose compared with the TPS. (e) A

comparison of isodoses measured (fineline) and TPS (heavy line) at 100 mm SDD. (f) The two dimensional dose difference, the distribution is TPS minus measured dose, at 100 mm SDD.

3.13 FPD image frame rate

The FPD can be operated in 'continuous acquisition' mode, allowing a sequence of images to be captured. The measurement of the position of the source, as it moves through a treatment catheter in time, can be performed by continually acquiring images with this mode. The frame rate of the image acquisition will define the minimum dwell time that can be captured.

To determine the frame rate, the source was driven to a single dwell position and programmed to dwell for 30, 60, 90 and 120 seconds. The capture of images with the FPD was started before the source reached the dwell position and was stopped after it returned to the afterloader. The image sequence was analysed and the image time stamp for the first and last image containing a static source distribution (not a source in transit) was used to calculate the imaging period. The continuous acquisition mode image frame rate was then calculated for each dwell time data set, by dividing the number of static source images by the imaging period. A summary of these results are shown below in table 3.1.

Table 3.1. The calculated FPD image frame rate when operating in continuous acquisition mode. The Image Time (s) represents the time for the system to acquire one image.

***Dwell Time* (s)**	**Imaging Period (s)**	**No. Images**	**Frame Rate (Images/s)**	**Image Time (s)**
30	30	17	0.57	1.8
60	59	34	0.58	1.7
90	93	53	0.57	1.8
120	122	70	0.57	1.7
Mean				**1.8**

3.14 Discussion

The FPD can capture exposures with the brachytherapy source at clinically relevant distances for treatment verification. The distribution observed on the acquired exposures of the source contain relevant information that can be interpreted as dose or used to determine the location of the source in space. The uncertainty of this determined position may increase with increasing source to detector distance, asymmetric or finite phantom geometry and inhomogeneties within the phantom. Approaches to determine the source position from the measured exposures and the geometric influences of the phantom geometry are described in chapter 4.

The detector response is x-ray energy dependent due to the composition of relatively high atomic number materials used in the construction, and so any dosimetric interpretation would have to include a correction, as described in section 3.10. Absolute dosimetry with non-water equivalent detectors is a very challenging field, but can be approximated using an empirical calibration function. And, as the objective in this work is treatment plan delivery verification, this is the preferred approach (calibrate to TG-43) given that it is known that TG-43 is inaccurate this far from the source, and we do not want error triggers just because the plan dose calculation differs from the true measured dose at exit surface.

For treatment verification with pelvic anatomical sites a logical approach would be to include the FPD in the treatment couch in such a way to minimise the distance between the detector and the source dwells within the patient. Such a design would enable *in-vivo* source position verification, termed ‘source tracking’. This proposed source tracking approach for treatment verification has some advantages over IVD. Source tracking is non-invasive, enables the possibility of pre-treatment imaging in the treatment bunker and measures the entire treatment volume during treatment delivery.

3.15 Chapter Conclusion

The *aS-500* FPD has been characterised for its use as a verification tool in HDR brachytherapy. The large detection area, pixel dimension and timing resolution make it acceptable to acquire exposures with the brachytherapy source.

This chapter briefly explored the possibility of measuring dose for the purposes of treatment verification. The rest of this work will now focus on the determination of

source position in order to achieve treatment verification. Measured source positions can be compared to the treatment plan for verification. With the inclusion of pre-treatment imaging, absolute source position verification relative to the anatomy can be achieved. Furthermore, with knowledge of source position and dwell time, the dosimetric distribution can also be reconstructed for comparison if desired.

With the determined characterisation of the FPD with the brachytherapy source, the following chapters will cover methods for source position determination, 2D and 3D pre-treatment implant verification and methods to perform *in-vivo* error trapping during treatment delivery.

Chapter 4
Source Tracking

4 Introduction

The previous chapter described the use of the FPD to capture exposures of the brachytherapy source distribution. These exposures acquired by the FPD contain information which can be processed to derive the position of the brachytherapy source relative to the FPD. This chapter describes the image analysis performed to extract parameters that can be used to determine the position of the source in 3 dimensions. These derived source positions are compared with the known (reference) position of the source determined using an independent method, to evaluate their accuracy and reproducibility.

The term ‘image’ in the context of source tracking refers to the exposure image acquired by the FPD of the ^{192}Ir source and not an x-ray projection image as used in chapter 5 (Pre-Treatment Verification Imaging).

The aim of this chapter is to investigate different image processing approaches that can be used to determine the 2D coordinate of the source from the acquired FPD image. A dual exposure approach, using an additional x-ray source, is initially performed to determine the true source position in the phantom. This result is used as a reference to benchmark several possible analysis techniques explored to derive the source coordinates from the FPD image alone, as would be done in the patient case. Additional parameters that correlate with SDD are also extracted from the images, potentially enabling the position of the source to be determined in 3D (inside the patient). The robustness of these source position approaches were evaluated for detector edge effects.

4.1 Source Tracking

The approach described by this proposed verification system is to verify measured dwell positions against the dwell positions specified by the treatment plan. This approach, termed 'source tracking', requires the FPD to capture images continuously during the treatment delivery. The captured image sequence is then processed to calculate the source dwell position over time, for verification with the treatment plan.

Potentially a single dwell position may appear across multiple captured images, and so a process to determine the measured dwell position from a sequence of image captures must be developed.

To avoid confusion the following terms are defined:

'*measured source coordinate*' is the calculated position of the source from a single image.

'*measured dwell position*' is the calculated position of the source determined from a collection of measured source coordinates.

A proposed process to determine a measured dwell position from the sequence of acquired images occurs in two steps:

(i) Image processing is performed on each image in the sequence and a measured source coordinate is calculated.
(ii) The array of measured source coordinates are processed to extract the measured source dwell position for verification against the plan.

This proposed process is described later in section 4.5.2.

4.2 Source Coordinate in 2D

The following sections describe approaches to determine the source coordinate in the plane of the FPD, (i.e. in 2D). These algorithms use a single image as the basis for processing, and calculate the source coordinate relative to the FPD image frame of reference.

The FPD coordinate system is defined as follows: the top left pixel in the image represents the origin and is assigned the pixel coordinate (0, 0), and the detector orientation relative to patient coordinates is illustrated in figure 4.1.

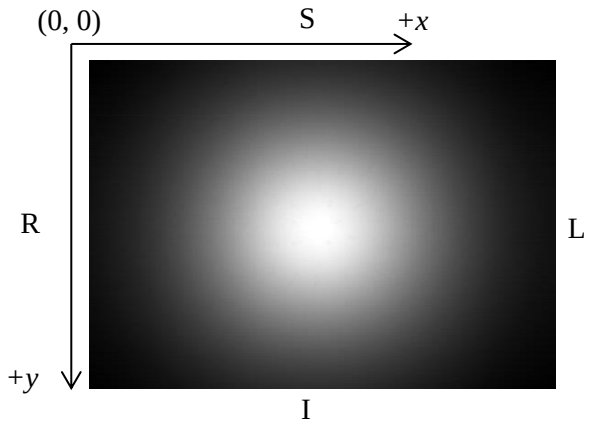

Figure 4.1. An acquired image for a source to detector distance (SDD) of 100 mm, illustrating the pixel coordinate system and the detector orientation relative to a patient coordinate system, viewed from above. I = inferior, S = superior, R = right, L = left.

4.2.1 Source Position in 2D Methods

To evaluate different approaches of determining the source position in 2D (position in the plane of the FPD), images of the source were acquired for a range of source to FPD distances. The parameter is known as the SDD and is the perpendicular distance from the FPD imaging plane to the brachytherapy source above.

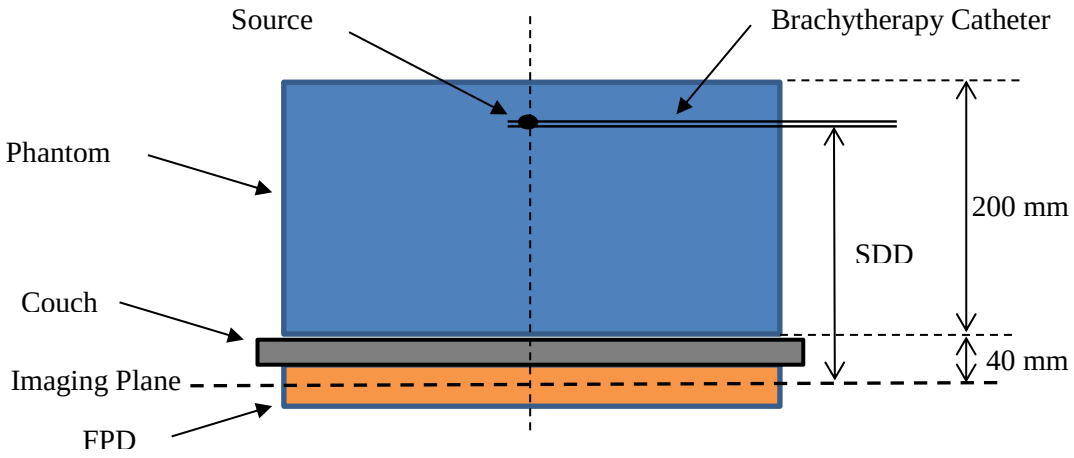

Figure 4.2. The geometric arrangement for acquiring images of the source distribution for different source to detector distances (SDD). The solid water phantom is placed on the couch and contains a plastic brachytherapy catheter.

The geometry used to acquire the images is shown in figure 4.2, where the detector imaging plane is 13.1 mm below the surface of the FPD, as determined in section 3.11 of chapter 3. In this application, the FPD is mounted below a carbon fibre couch, where the top of the couch is 40 mm above the detector imaging plane. (The distance from the surface of the FPD to the surface of the carbon fibre couch is 27 mm, resulting in couch top at a nominal distance of 40 mm above the imaging plane.) Mounting the FPD in the treatment couch is done to pre-empt its use with patients, and is described later in chapter 7. A 300×300×200 mm phantom of solid water slabs, containing a single plastic brachytherapy catheter, is placed on the couch top and centered over the FPD.

The phantom was positioned on the couch as shown in figures 4.1 and 4.2 with various SDDs of 60, 70, 80, 90, 100, 110, 120, 130, 140, 160, 180 and 200 mm. The source was driven to a single dwell position at the centre of the phantom, and for each SDD, an image was captured with the FPD. This set of images were then used to evaluate the different approaches for determining the source position in the 2D plane of the detector.

The next section describes the approach used to independently determine the reference source position, used to compare all other approaches. The following sections describe the different approaches used to determine the source position from the images obtained at different SDDs.

4.2.1.1 Reference Coordinate Technique: Dual Exposure Approach

An independent measure of the source position was performed, by using a dual exposure approach. This was achieved by capturing an image at the source dwell position, as shown in figure 4.3(a). During the source dwell, a ‘dual exposure’ image was captured containing a pulse from the x-ray tube positioned above the phantom and the ^{192}Ir source exposure (figure 4.3(b)).

The subtraction of the source dwell image from the dual exposure image then showed the position of the physical source capsule (figure 4.3(c)), which was used as the independent reference measure of the source coordinate. The dual exposure method was repeated at each SDD (60, 70, 80, 90, 100, 110, 120, 130, 140, 160, 180 and 200 mm) to determine the reference position for each case.

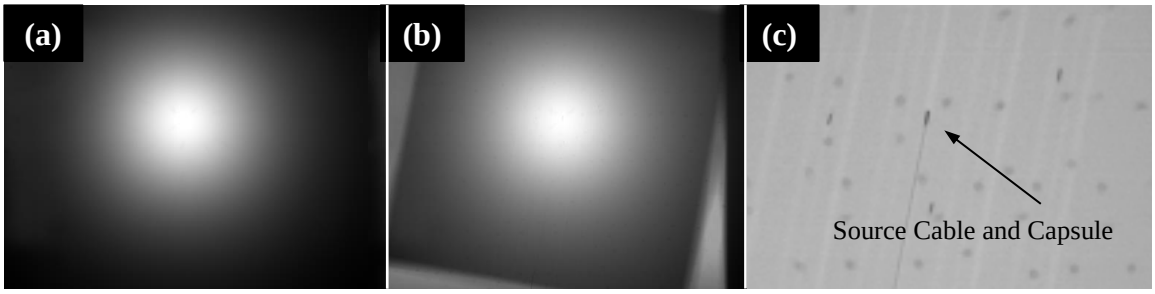

Figure 4.3. An example of the dual exposure approach. (a) The captured exposure of the ^{192}Ir source using the FPD. (b) The simultaneous FPD exposure of the ^{192}Ir source and the projection image of the phantom. (c) The result of subtraction of (a) from (b), showing a magnified view to illustrate the physical source capsule used as the reference source position. The source cable, carbon fibre couch structure and voids from the other unused empty catheter paths are visible.

The dual exposure approach described here is strictly used as an independent method to provide a reference measured source coordinate, and is not proposed for clinical implementation.

Several possible ways of deriving the measured source coordinate from the FPD image were explored, and these approaches are described in the following sections.

4.2.1.2 Technique 1: Near-Maximum Pixel Intensity

The pixel intensity distribution was used to determine the source coordinate based on the assumption that the highest intensity pixels in the image will represent the most likely position of the source. A histogram of the image pixel intensities was generated and the position of the maximum pixel value was determined. To filter possible pixel noise from the result, any potential maximum pixel value occurring only once in the histogram was excluded as illustrated in figure 4.4, where in this case, pixel values 546 and 547 are excluded. The source coordinate was determined by calculating the mean of the pixel coordinates with the determined near-maximum pixel intensity. The source coordinate using the near-maximum pixel intensity approach was calculated for all images acquired at different SDDs and compared to the reference source coordinates.

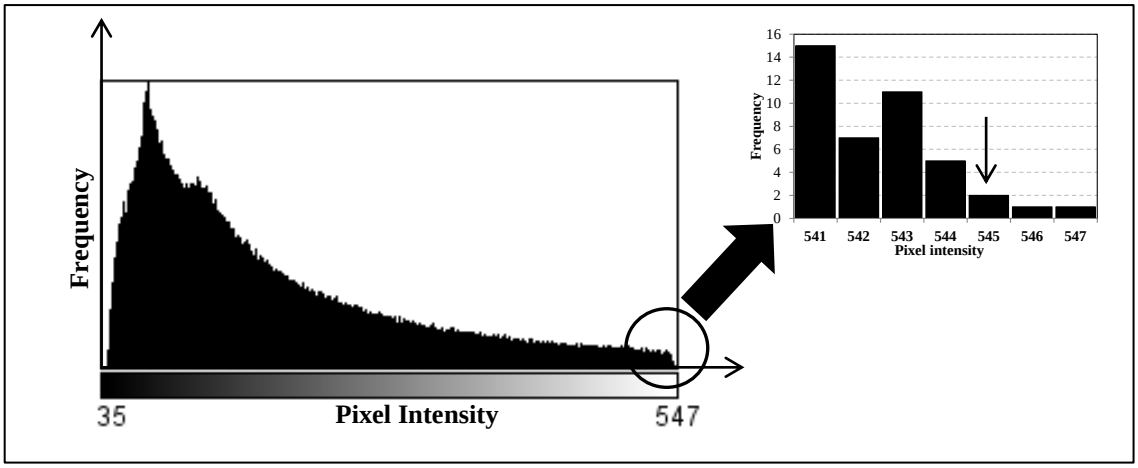

Figure 4.4. A histogram of a source dwell image showing the distribution of pixel intensity. The near-maximum pixel intensity selected is the greatest pixel value that has a minimum histogram bin count of at least 2 pixels. In this example, the maximum pixel intensity result is 545.

4.2.1.3 Technique 2: Centre of Mass

The near-maximum pixel method is a simple approach based on pixel intensity, and due to the small number of pixels contributing to the determined source coordinate, the method will likely be sensitive to different measurement situations. A potentially more robust approach is the centre of mass (COM) method, that use a larger number of pixels in the defined region to determine the source coordinate. The COM is defined as the mean pixel coordinate, for all pixels contributing to the defined region, where the region is defined by a pixel threshold range. The calculated COM pixel coordinate (x_c, y_c) is used as the source coordinate and the calculation can be expressed mathematically as:

$$x_c = \frac{1}{N}\sum_{i=1}^{N} x_i \qquad \text{Eqn. (4.1)}$$

and

$$y_c = \frac{1}{N}\sum_{i=1}^{N} y_i \qquad \text{Eqn. (4.2)}$$

where x_i and y_i are coordinates of each pixel in the defined object region and N is the total number of pixels in the object region. An object region was extracted from the

image, by thresholding (including) pixels that have an intensity value that falls within a specified range. Threshold ranges of 60% to 70%, 70% to 80% and 80% to 90% of the maximum pixel intensity in the image, were considered.

The COM process is illustrated in figure 4.5 where figure 4.5(a) shows an image acquired at a SDD of 100 mm, threshold ranges of 80 to 90%, 70% to 80% and 60% to 70% are shown in figure 4.5(b), (c) and (d) respectively. The annulus object defined (in red) is then used to calculate the COM source coordinate. The COM was calculated for each region across all images acquired at different SDDs and compared to the reference source coordinate.

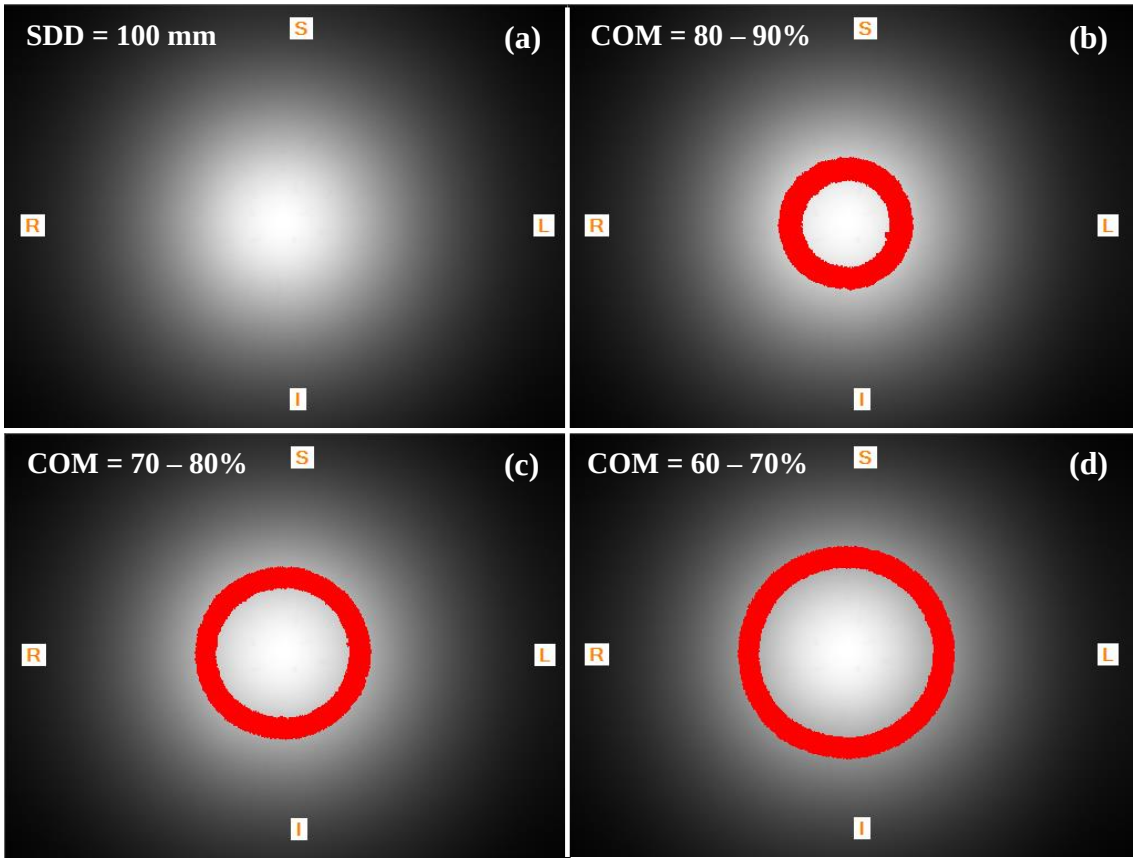

Figure 4.5. (a) An image acquired at a SDD of 100 mm. The centre of mass approach is illustrated by applying a threshold value of 80 to 90 (b), 70 to 80 (c) and 60 to 70 (d) percent of the maximum pixel intensity. The pixels included in the threshold range are shown in red.

4.2.1.4 Technique 3: Single Profile

The shape of a profile acquired through the distribution on the FPD image possibly provides metrics that can be correlated with the source coordinate. To evaluate this

method, single orthogonal profiles were considered as a method to calculate the source coordinate. A single profile along the *x* and *y* axes were extracted from the image and processed to determine the source coordinate. A starting point in the image was defined as the position of the maximum pixel intensity, and the orthogonal profiles were then extracted from this position. The single profile approach is illustrated in figure 4.6(a) showing the starting point and figure 4.6(b) showing location of the orthogonal single profiles in each axis.

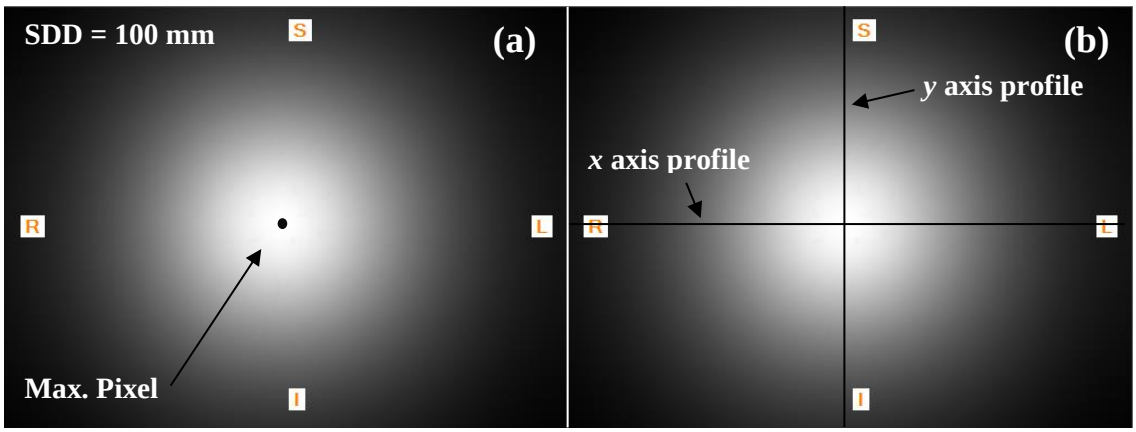

Figure 4.6. An example of an image acquired at 100 mm SDD showing (a) the position of the maximum pixel intensity used as the starting point and (b) the orthogonal profiles extracted from the image to determine the source coordinate.

The extracted *x* and *y* profiles were processed, and the mid-point of the line segment at 80% of the maximum profile intensity was calculated, as shown in figure 4.7. This position was determined for the *x* and *y* profile separately and was used as the calculated source coordinate. The process was repeated for all SDDs and the calculated vales were compared with the reference source coordinate.

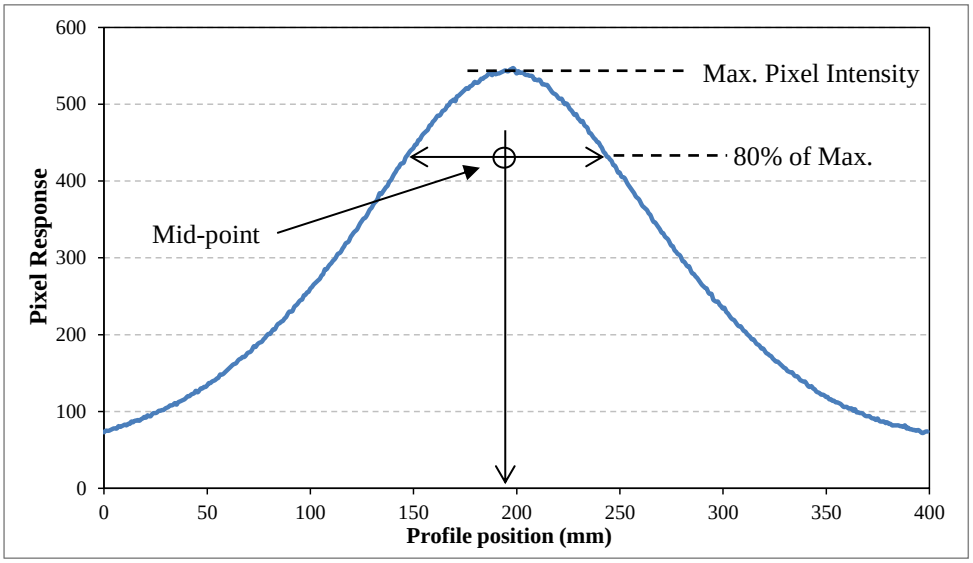

Figure 4.7. The extracted orthogonal profile processed to determine the source coordinate. The mid-point at the 80% of the maximum profile intensity is used as the source coordinate.

4.2.1.5 Technique 4: Multiple Profile

The single profile approach was modified to include multiple orthogonal profiles. The purpose was to improve the reliability of the approach by attempting to reduce the influence of image noise from a single profile. Figure 4.8(a) shows that the same starting point used for the single profile was used (the position of the maximum pixel intensity) and (figure 4.8(b)) a set of 21 orthogonal profiles at 1 pixel intervals were extracted.

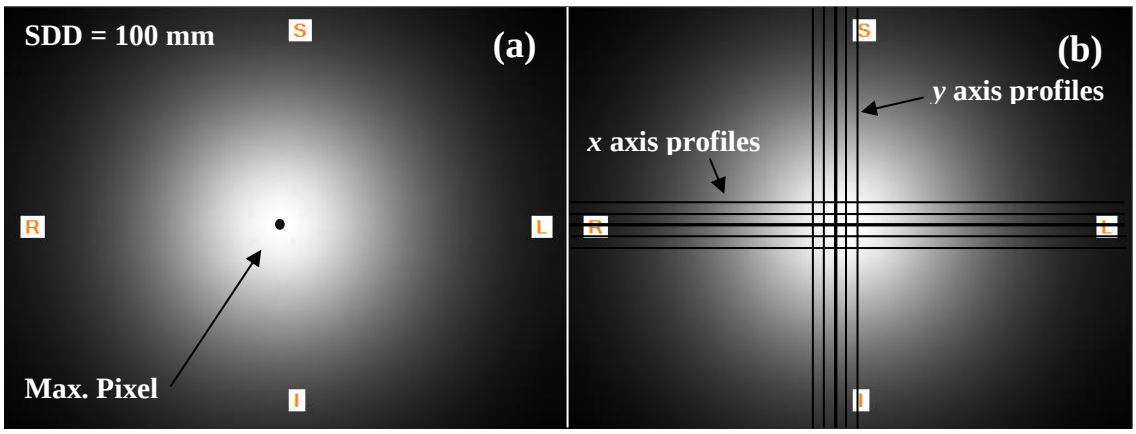

Figure 4.8. An example of an image acquired at 100 mm SDD showing (a) the profile position starting point and (b) an illustration of the 21 orthogonal profiles extracted in the image *x* and *y* axis. 10 profiles are extracted either side of the initial profile through the image start point.

The 21 extracted profiles in the *x* axis and the 21 profiles in the *y* axis were processed to calculate the mid-point of the segment at the 80% of the maximum profile intensity, as shown in figure 4.7. The source coordinate was determined by calculating the mean value for all profiles, and the calculated coordinates were compared to the reference source coordinate.

4.2.1.6 Technique 5: Symmetric Lorentz Single Profile

To improve on the Single Profile approach and to better represent the distribution of the acquired profile, a function was fitted to the data. The source coordinate was determined by fitting a symmetric Lorentz function to a profile extracted from the image. A single profile was extracted from the image using the process described in section 4.2.1.4. A symmetric Lorentz function in the form of equation 4.3 was then used to fit the extracted profiles in the *x* and *y* axis.

$$y = a + \frac{b}{\left[1 + \left(\frac{x - c}{d}\right)^2\right]} \qquad \text{Eqn. (4.3)}$$

The coefficients are the fit parameters where *a* is the baseline, b is the peak amplitude, *c* is the peak centre and *d* is the full width at half maximum, as illustrated in figure 4.9. The centre position of the fitted peak is used as the source coordinate value.

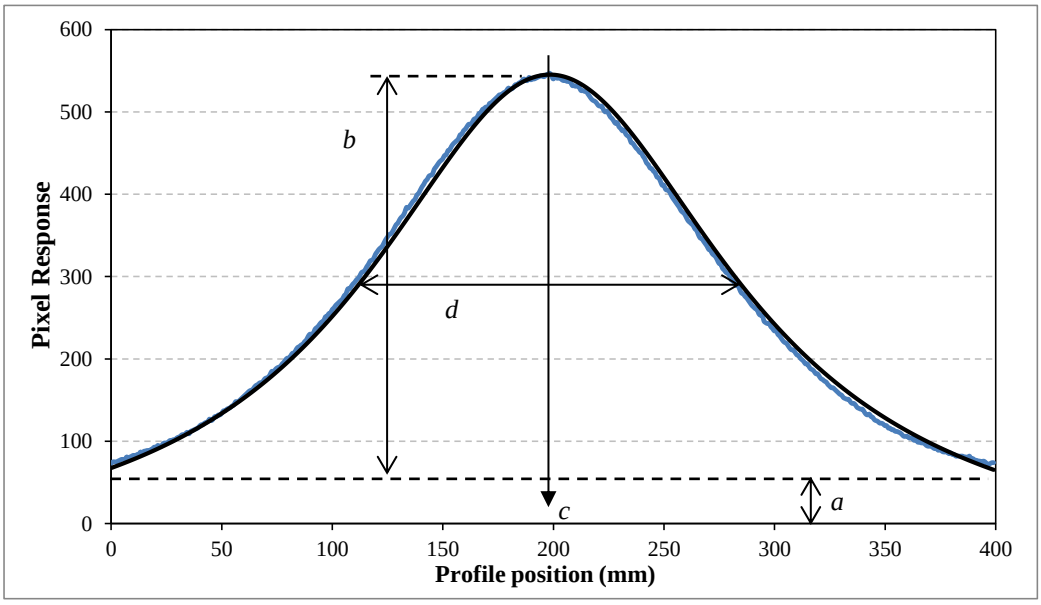

Figure 4.9. The symmetric Lorentz fit of the extracted profile, showing the coefficients *a* = baseline, *b* = peak amplitude, *c* = peak centre and *d* = full width at half maximum. The coefficient *c* is used as the source coordinate.

4.2.1.7 Technique 6: Asymmetric Lorentz Single Profile

To accommodate the likely possibility of an asymmetric distribution, and to better fit the profile data, the fitting function was modified to include an asymmetric weighting component. The Lorentz function was modified to the asymmetric Lorentz function in the form of equation 4.4 was then used to fit the profiles in the *x* and *y* axes.

$$y = a + \frac{b}{\left[1 + \left(\frac{x-c}{d}\right)^2\right]} + e(x-c) \qquad \text{Eqn. (4.4)}$$

The coefficients are the fit parameters where *a* is the baseline, b is the peak amplitude, *c* is the peak centre and *d* is the full width at half maximum, *e* is the asymmetry weighting component, as illustrated in figure 4.10. The centre position of the fitted peak is used as the source coordinate value.

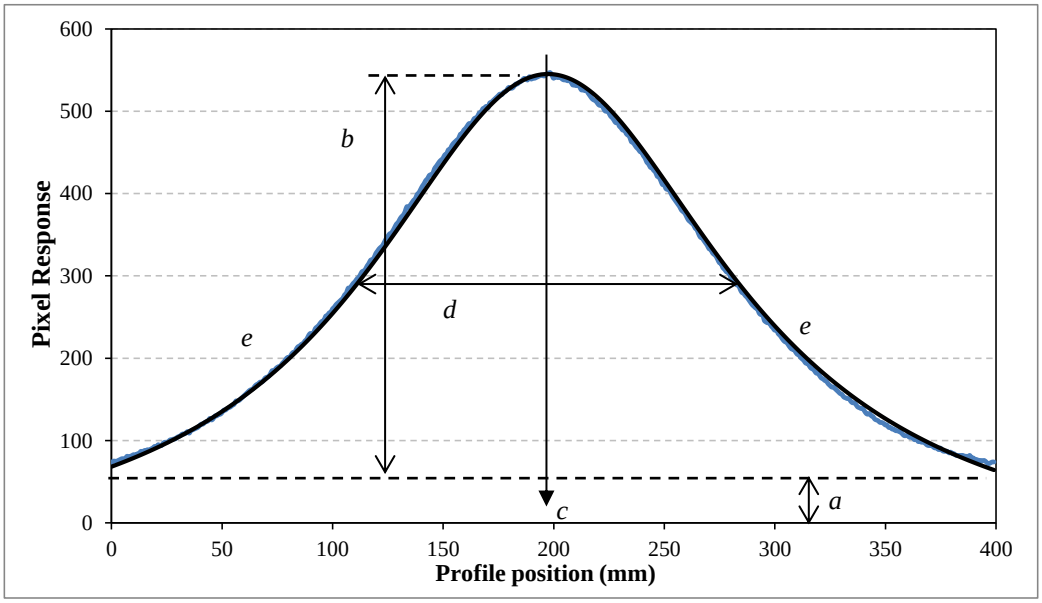

Figure 4.10. The asymmetric Lorentz fit of the extracted profile, showing the coefficients *a* = baseline, *b* = peak amplitude, *c* = peak centre, *d* = full width at half maximum and *e* the asymmetry weighting component driving the asymmetry of the fit. The coefficient *c* is used as the source coordinate.

4.2.2 Results: Source Coordinate in 2D

4.2.2.1 Reference Coordinate Technique: Dual Exposure Approach

The reference source position coordinate, determined using this subtraction method, is the centre pixel of the projected source capsule (captured with the x-ray pulse), with which all other approaches are compared. The projection of the source capsule is corrected for x-ray beam divergence, to determine the corrected source reference position (x_{ref}, y_{ref}). Further details of the divergence correction applied are provided later in chapter 5.

4.2.2.2 Technique 1: Near-Maximum Pixel Intensity

The difference of the measured source coordinate from the reference coordinate in the *x* and *y* FPD axis is shown in figure 4.11 for each SDD. The near-maximum pixel intensity approach demonstrated 92% of calculated source positions were within ±2 mm of the reference source position for SDDs ranging from 60 to 200 mm.

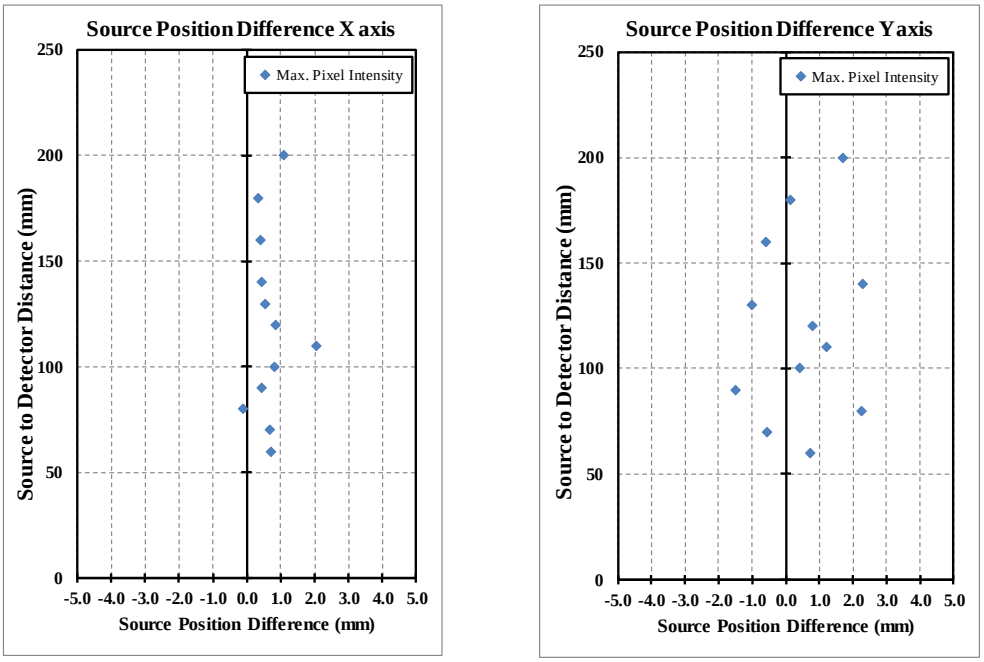

Figure 4.11. The determined source coordinate difference in the FPD *x* and *y* axes, using the near-maximum pixel intensity approach, as a function of the SDD.

4.2.2.3 Technique 2: Centre of Mass

The threshold ranges of 60% to 70% and 70% to 80% produce regions as illustrated in figure 4.5(c) and (d). The relatively large diameter of the defined region used for COM calculation, especially in the 60 to 70% example, has a diameter that is approximately 150 mm, making this threshold range impractical for source coordinate determination. A source that appears towards the edge of the detector, would not have the entire distribution of the annular region captured by the FPD and so report an incorrect COM source coordinate.

This effect is considerably worse for sources at larger SDDs, as illustrated in figure 4.12, In this example a source at 200 mm SDD, analysed for a threshold range of 80 to 90%(figure 4.12(a)) and 60 to 70%(figure 4.12(b)) produce annular diameters of 150 and 230 mm respectively. The large threshold region diameters are impractical for source coordinate determination due to compromised calculation of COM.

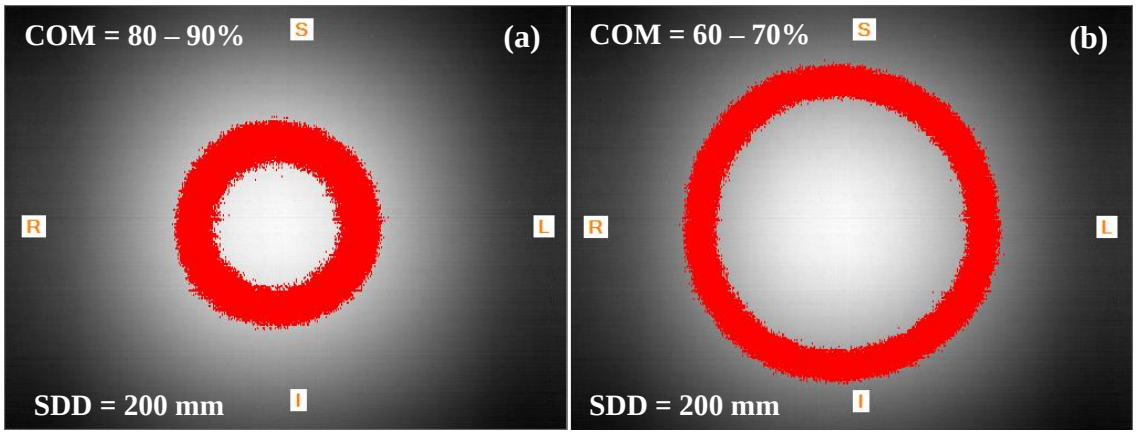

Figure 4.12. An illustration of the COM threshold applied to an image of the source at 200 mm SDD. The 80 to 90% range has a diameter of approximately 150 mm(a), while 60 to 70% range has a diameter of approximately 230 mm (b), which is impractical for source position localisation.

The source coordinates were calculated using the COM approach, only for a threshold range of 80% to 90. Source coordinates for all images acquired at different SDDs were calculated and compared to the reference source coordinates and the differences are shown in figure 4.13.

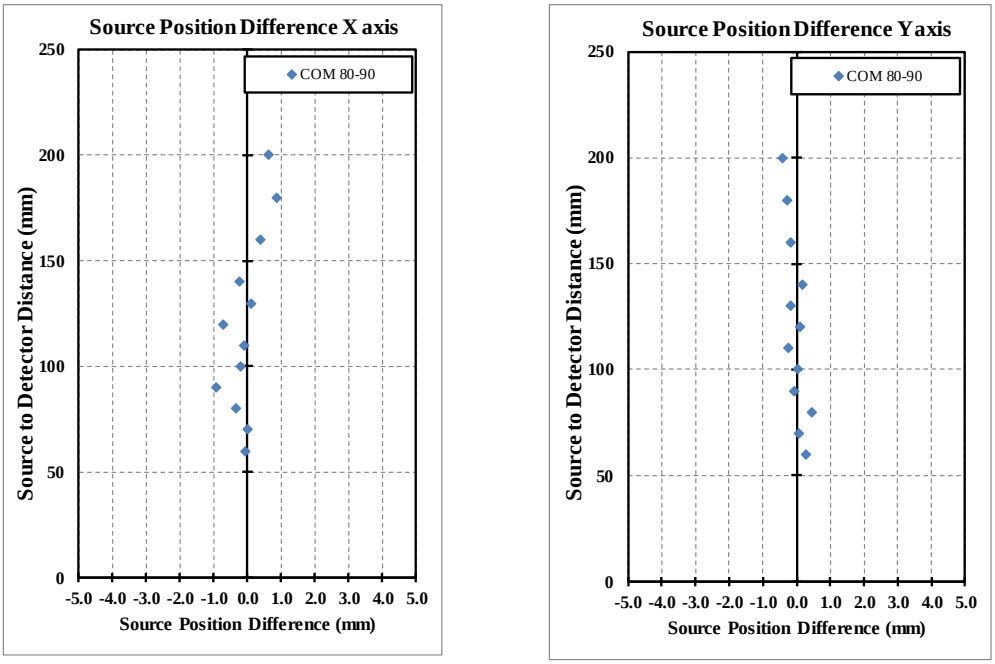

Figure 4.13. The determined source position difference in the FPD *x* and *y* axes, using the COM threshold range 80-90%, as a function of source to detector distance (SDD).

The COM approach for a threshold range of 80% to 90% produced a mean difference of 0.0 and 0.0 mm in the x and y directions respectively. All the calculated source coordinates were within ±1 mm of the expected positions, for both the *x* and *y* axes.

4.2.2.4 Technique 3: Single Profile

The single profile approach produced mean differences of -0.4 and 0.1 mm in the x and y directions respectively. Source coordinates for all images acquired at different SDDs were calculated and compared to the reference source coordinates and the differences are shown in figure 4.14.

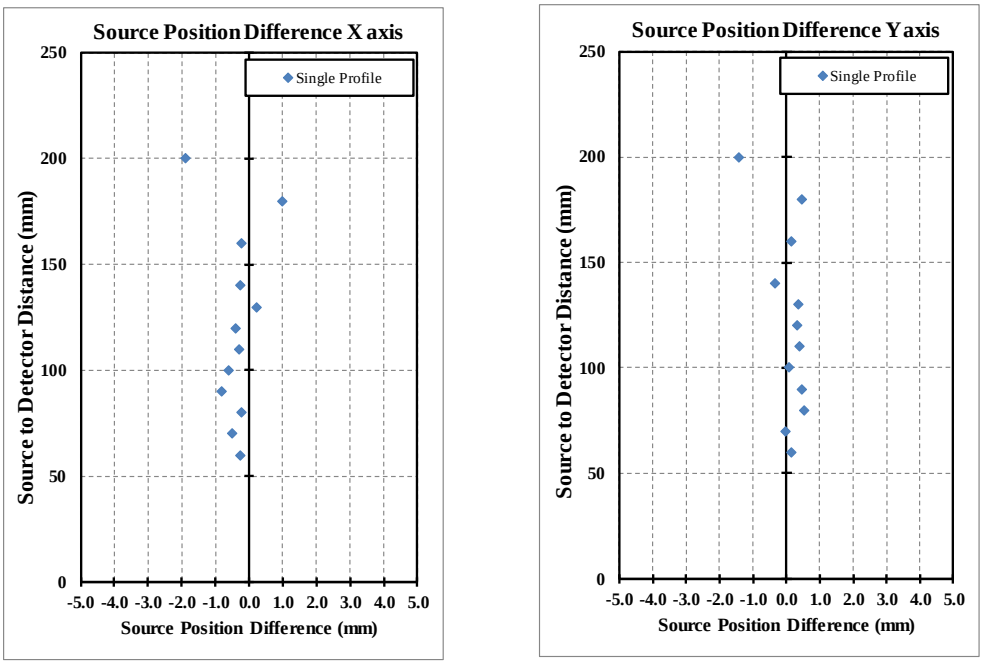

Figure 4.14. The determined source position difference, using the Single Profile approach, in the FPD *x* and *y* axis, as a function of source to detector distance (SDD).

The single profile approach produced an agreement with the reference source coordinate in the *x* and *y* directions to within 1 mm for SDD up to 180 mm. This simple method appears to provide a robust approach to determine the source coordinate.

4.2.2.5 Technique 4: Multiple Profile

The multiple profile approach improved the agreement with the reference source coordinate producing a mean difference of -0.1 and -0.1 mm in the x and y directions respectively. The difference determined at each SDD is shown in figure 4.15.

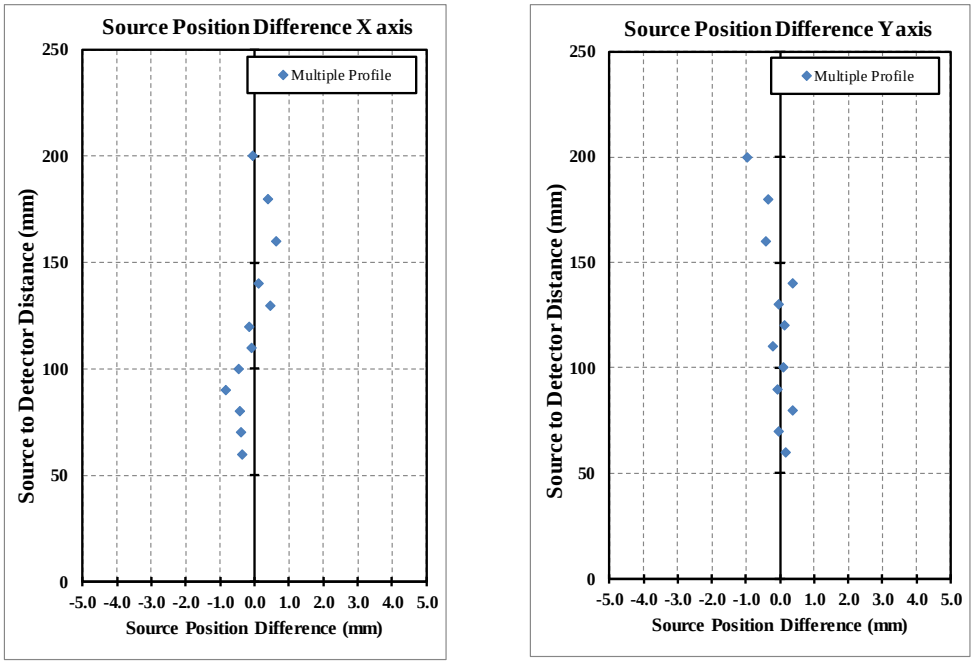

Figure 4.15. The determined source position difference, using the Multiple Profile approach, in the FPD *x* and *y* axis, as a function of source to detector distance (SDD).

The multiple profile approach appears to improve on the single profile approach by determining the source coordinate in the *x* and *y* directions to be within 1 mm of the reference coordinate for SDDs of up to 200 mm.

4.2.2.6 Technique 5: Symmetric Lorentz Single Profile

The difference for each SDD using the symmetric Lorentz fit is shown in figure 4.16.

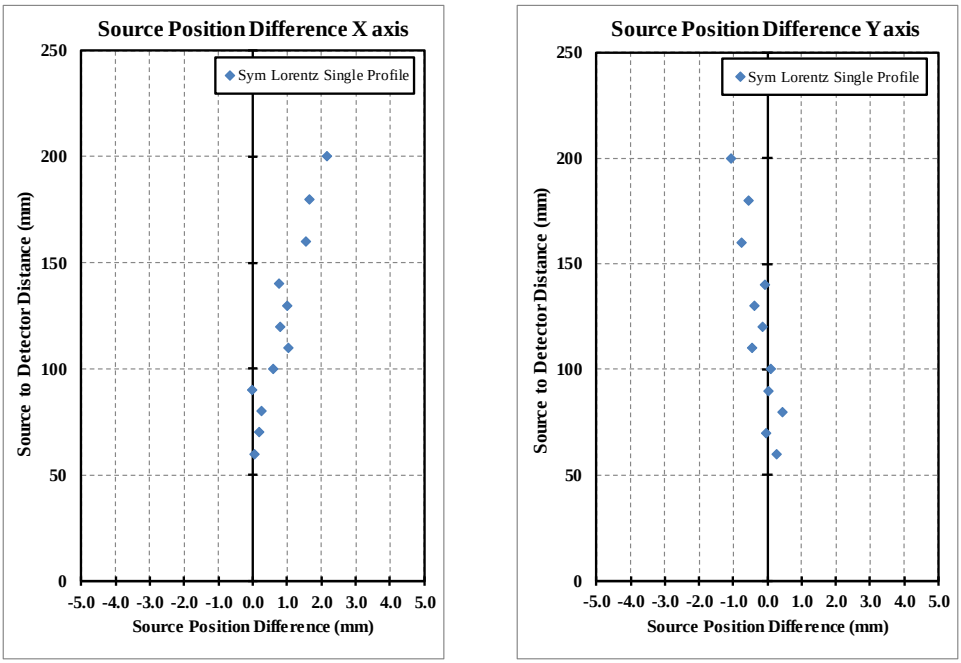

Figure 4.16. The determined source position difference, using the Symmetric Lorentz Single Profile approach, in the FPD *x* and *y* axis, as a function of source to detector distance (SDD).

The symmetric Lorentz data fit shows a systematic drift in the measured source coordinate for the *x* axis. The same is not observed in the *y* axis.

4.2.2.7 Technique 6: Asymmetric Lorentz Single Profile

The difference for each SDD using the asymmetric Lorentz fit is shown in figure 4.17.

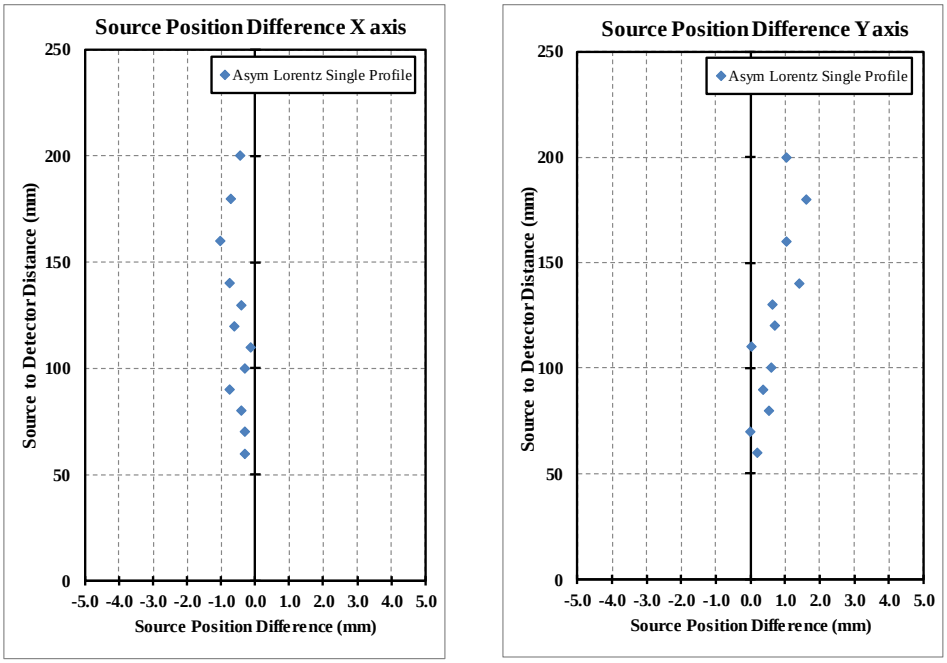

Figure 4.17. The determined source position difference, using the Asymmetric Lorentz Single Profile approach, in the FPD *x* and *y* axis, as a function of source to detector distance (SDD).

The asymmetric approach has improved the agreement with the reference coordinate position in the *x* axis, but shows slightly worse agreement at large SDDs in the *y* axis.

4.2.3 Discussion: Source Coordinate in 2D

4.2.3.1 Summary of 2D Source Position Determination

The six methods investigated to determine the source coordinate for a range of SDDs were compared using the mean difference and maximum difference compared to the reference source coordinate. Table 4.1 is a summary of the results for comparison. Columns 2 and 3 show the mean differences where the numbers in the brackets represent one standard deviation. Columns 4 and 5 show the maximum difference from the reference source and the brackets illustrate the SDD that this maximum difference occurred at.

Table 4.1. The mean difference and standard deviation between the reference source position and the measured position calculated by each algorithm for source to detector distances (SDD) of 60 to 200 mm. The maximum difference (for *x* and *y*) occurred at the SDD shown in brackets.

Method	***x* Mean diff. mm**	***y* Mean diff. mm**	***x* Max. diff. mm**	***y* Max. diff. mm**
Near-Max. Intensity	0.7 (0.5)	0.5 (1.2)	2.0 (110)	2.3 (140)
Centre of Mass	0.0 (0.5)	0.0 (0.3)	0.9 (180)	-0.4 (200)
Single Profile	-0.4 (0.1)	0.1 (0.5)	-1.9 (200)	-1.4 (200)
Multiple Profile	-0.1 (0.4)	-0.1 (0.4)	-0.8 (90)	-1.0 (200)
Symmetric Lorentz	0.8 (0.7)	-0.2 (0.4)	2.1 (200)	-1.1 (200)
Asymmetric Lorentz	-0.5 (0.3)	0.7 (0.5)	-1.0 (160)	1.6 (180)

The near-maximum pixel intensity approach is the most basic attempt at interpreting the image information. The wide distribution of differences in the *y* direction (figure 4.11) suggest that pixel noise in the image, even though an attempt to reduce this was performed, still influences the calculated source coordinate. The algorithm exhibits large individual deviations suggesting it is not robust to image noise variations.

The COM approach has limited value in this application when the defined pixel region for calculation has a large diameter. The source will not necessarily appear in the centre of the FPD and so 60% to 70% and 70% to 80% regions are impractical. The 80% to 90% produces a region diameter that is practical for SDD up to 200 mm. The advantage of this approach is that it appears robust to image noise and is not sensitive to local variations of pixel intensities. The process may be refined by evaluating different percentage ranges. The COM 80-90% approach produced maximum deviations of less than 1 mm at large SDDs.

The single profile approach also produced large maximum differences as seen in figure 4.14, but again at large SDDs which are less likely to be used clinically. The single profile approach is subject to the local deviation in pixel value. The inclusion of more profiles for calculating the source coordinate improved the agreement with the reference source coordinate.

The fitted symmetric Lorentz approach produced a systematic deviation in the *x* axis as the SDD increased, as depicted in figure 4.16. The reason for this deviation is unclear, and possible causes such as the source cable are not in this axis. This method is not likely to be used clinically as the non uniformity of the patients' density will likely produce an asymmetric distribution on the FPD.

The asymmetric fitted Lorentz approach improved on the previous approach by eliminating the systematic drift that was observed. The method produced a mean difference of less than 1 mm for both the *x* and *y* axes, making it a potential option for clinical use.

The techniques evaluated for determining the source coordinate all performed well considering the large SDDs used during this evaluation. For a potential clinical application, it is not expected that the SDD will be greater than 150 mm, based on inspection on assessment of a large number of patient CT images. Almost all techniques (except the near-maximum pixel intensity technique) calculated the source to within 2 mm of the reference coordinate for SDDs up to 160 mm. The COM technique is simple to implement, and therefore possible to automate in a real-time application, it is efficient and exhibits excellent agreement with the reference source coordinate. Considering these characteristics, the COM technique was applied during the source tracking processes described throughout this work.

The following section investigates characteristics of the FPD response that can be used to correlate with the source distance in the *z* axis, i.e. perpendicular from the FPD imaging plane.

4.3 Source Coordinate in 3D

The following sections describe approaches to determine the SDD using metrics extracted from the acquired FPD images. The distance to the source from the FPD is termed the *z* axis and is the perpendicular distance from the FPD imaging plane.

The SDDs used to acquire the FPD images are defined as the reference *z* source coordinate and are used for comparison of each technique defined in the following sections.

4.3.1 Source Coordinate in 3D Methods

The set of measurements acquired using the phantom setup and geometry defined in figure 4.2 is used to evaluate techniques to determine the source position in the *z* axis. The source was positioned at SDDs of 60, 70, 80, 90, 100, 110, 120, 130, 140, 160, 180 and 200 mm for each FPD image capture.

Profiles were acquired at each SDD through the known source (*x*, *y*) reference position and normalised to the profile maximum. The *x* axis profiles are shown in figure 4.18 and illustrate the broadening of the distribution and the noise in the profile as the SDD increases.

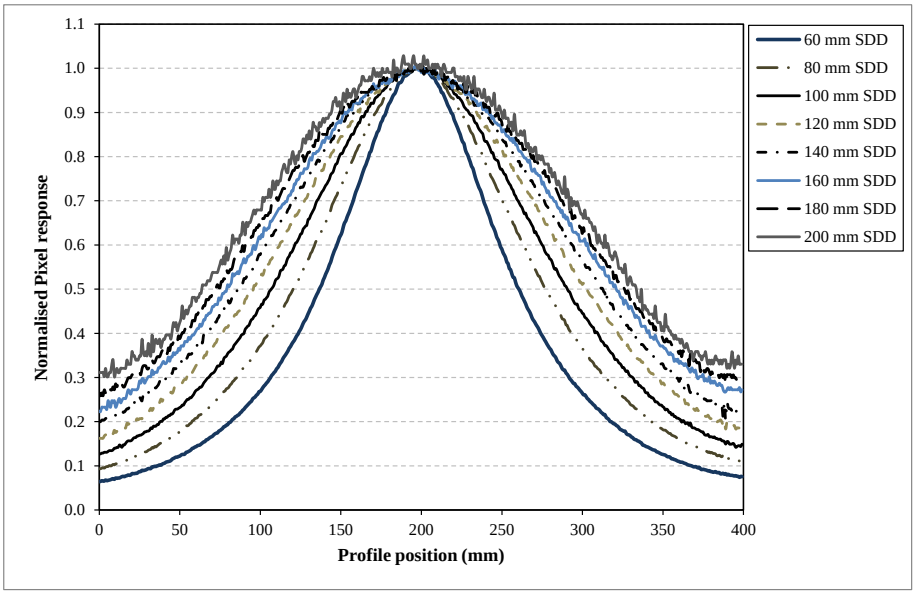

Figure 4.18. The *x* axis profiles, acquired through the known source position, normalised to the maximum value, for the range of SDDs of 60 to 200 mm.

4.3.1.1 Technique 1: Profile Width:

The width of the profiles depicted in figure 4.18 increase as the SDD is increased. This parameter may provide a reliable metric to measure the z source coordinate. The width of the profile is determined for the *x* and *y* profile, and the mean width is calculated, and this is performed at 50% and 80% of the profile maximum value. The full profile width metric at 50% and 80% (FW 80% Max, FW 50% Max) was plotted as a function of SDD and function fitted to the data for evaluation.

4.3.1.2 Technique 2: Threshold Pixel Count:

The COM approach, described in section 4.2.1.3, implements a method to threshold the image across a pixel range of 80% to 90% of the image maximum pixel value. The number of pixels within this threshold range, potentially increases with SDD, as illustrated in figure 4.19, and so was evaluated as a possible z coordinate metric. The number of pixels determined by the threshold range were plotted as a function of SDD.

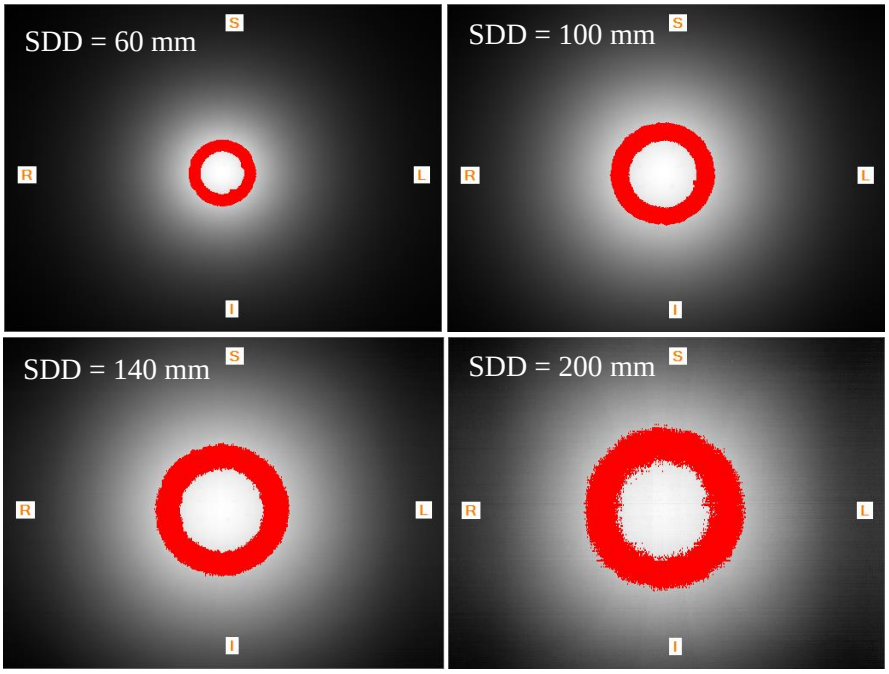

Figure 4.19. An example of the 80% to 90% threshold pixel range for 60, 100, 140 and 200 mm SDD. The pixel count in this threshold range is used as a measure of source distance in the z axis.

4.3.2 Results: Source Coordinate in 3D

4.3.2.1 Technique 1: Profile Width

The calculated mean width for the profiles is shown in figure 4.20 as a function of SDD. The data for the FW 50% max was fitted with an exponential function and shows good agreement up to 160 mm SDD, which is likely to be the typical clinical range for a prostate case.

Due to the shallower gradient of the SDD-profile width relationship, the FW 50% max approach provides a more sensitive measure of source coordinate distance than the FW 80% max approach.

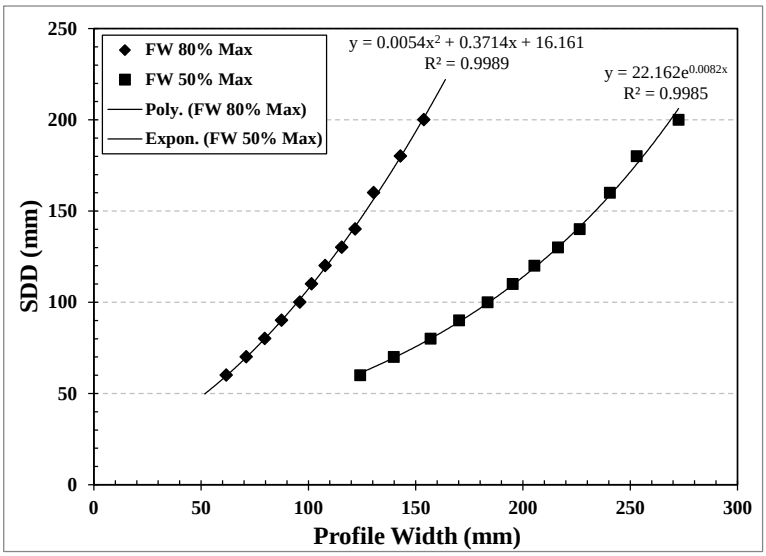

Figure 4.20. The relationship between profile width and SDD for the width at 50% of the maximum (FW 50% max) and width at 80% of the maximum (FW 80% Max).

4.3.2.2 Technique 2: Pixel Threshold Count

The number of pixels determined within the 80% to 90% threshold range is illustrated in figure 4.21. The COM 80%-90% pixel threshold number exhibits a linear relationship between SDD with gradient of approximately 88 pixels per mm.

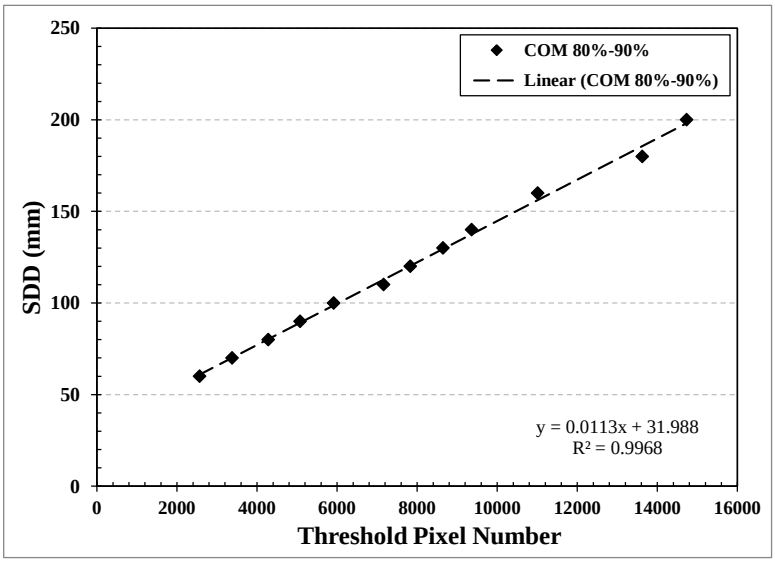

Figure 4.21. The relationship between threshold pixel count for the COM 80%-90% approach and the SDD. A linear fit to the data has been applied to establish a function to determine the z source coordinate for each source image.

4.3.3 Discussion: Source Coordinate in 3D

4.3.3.1 Summary of 3D Source Coordinate Determination

The proposed methods described to determine the z source coordinate provide a metric that can be used as a surrogate for SDD. The COM approach reports a linear correlation with z coordinate distance and therefore provides a constant sensitivity to SDD over the measured range (60 to 200 mm). The FW 80% Max approach represents a less sensitive measure of SDD compared to the FW 50% Max approach, as the width of the profile does not change as rapidly over the measured range. The FW 50% Max profile may suffer from the finite detector size and as illustrated in figure 4.5(d), the large physical dimension of this profile width may not be recorded on the FPD. The COM provides a reliable measure of z coordinate distance and for most cases where the source is not in proximity of the detector edge (see next section), the metric is sensitive to the SDD.

4.4 Discussion

There are a few considerations that add to the complexity of source tracking. In the following sections three key items are discussed; (i) the influence of detector edge, (ii) the influence of phantom size and (iii) extraction of source dwell positions from image sequences.

4.4.1 Influence of Detector Edge on Source Coordinate

Some algorithms used to determine the source coordinate in the plane of the FPD use the captured distribution across the entire image. The bounds of the sensitive region of the FPD may influence the calculated source coordinate result. This may be applicable in a clinical situation when the treatment region of the patient is not centered over the FPD and detector edge effects become relevant.

The solid water phantom was placed on the couch centered above the FPD, 200 mm from the detector edge, as illustrated in figure 4.22(a). The source was driven into the phantom for SDDs of 60, 80, 100, 120, 140 and 160 mm and an image was acquired. The dual exposure method described in section 4.2.1.1 was used to determine the source reference position. The phantom was moved and the image capture process was repeated for the source at 125 mm from the detector edge (figure 4.22(b)) and for the source at 50 mm from the detector edge (figure 4.22(c)).

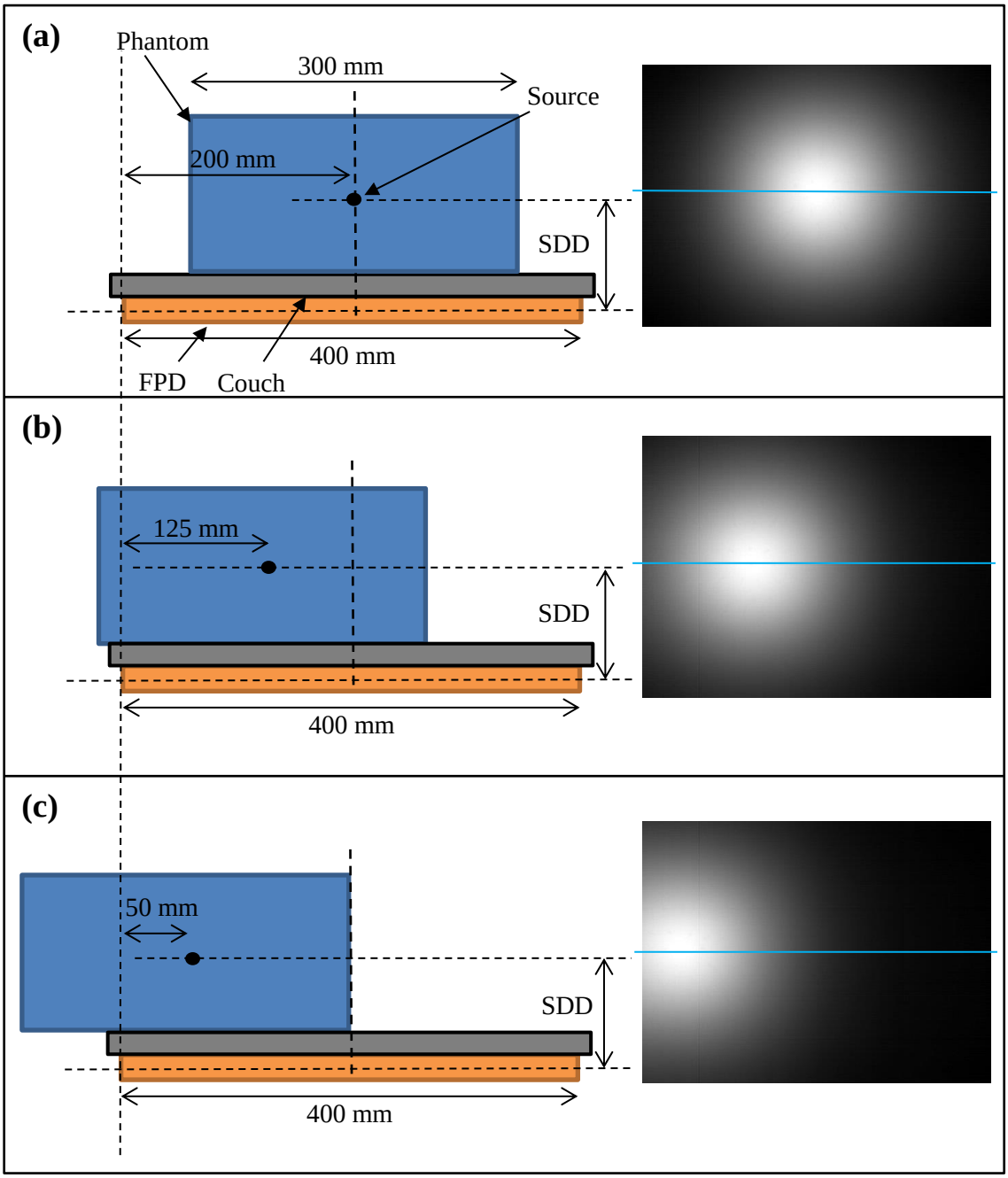

Figure 4.22. The investigation of detector edge effects on the FPD response for the (a) source centered on the panel, (b) the source 125 mm from the edge and (c) the source 50 mm from the detector edge. The blue line in each image represents the position of the response profile shown in figure 4.23.

The acquired images were processed using the COM approach (described in section 4.2.1.3) and the calculated source coordinates were compared to the reference source

position. Profiles were also extracted across the images at 100 mm SDD as illustrated in figure 4.23.

The differences between the reference source position and the calculated position using the COM algorithm is shown in figure 4.24. The agreement for the centered, 125 mm and 50 mm positions are within 2 mm of the reference position for up to 160 mm from the detector. At 180 mm SDD, the 50 mm and 125 mm detector edge datasets deviate from the reference source position by more than 2 mm. This deviation is due to the interaction of the detector edge, distorting the COM 80%-90% calculation as shown in figure 4.25 (d) and (e).

The profiles in figure 4.23 show the detector edge produces an over response. This is probably due to the additional scatter reaching the edge of the detector from the aluminium frame and protection layer around the sensitive region of the detector.

The detector edge effect combined with the missing data points in the threshold annular region degrades the accuracy of the COM method. Up to 50 mm from the detector edge the source coordinate error is up to 2 mm for SDDs up to 160 mm. The proximity of the detector edge skews the measured coordinate away from the detector boundary. The effect appears to be negligible when the distance to the detector edge is greater than the SDD.

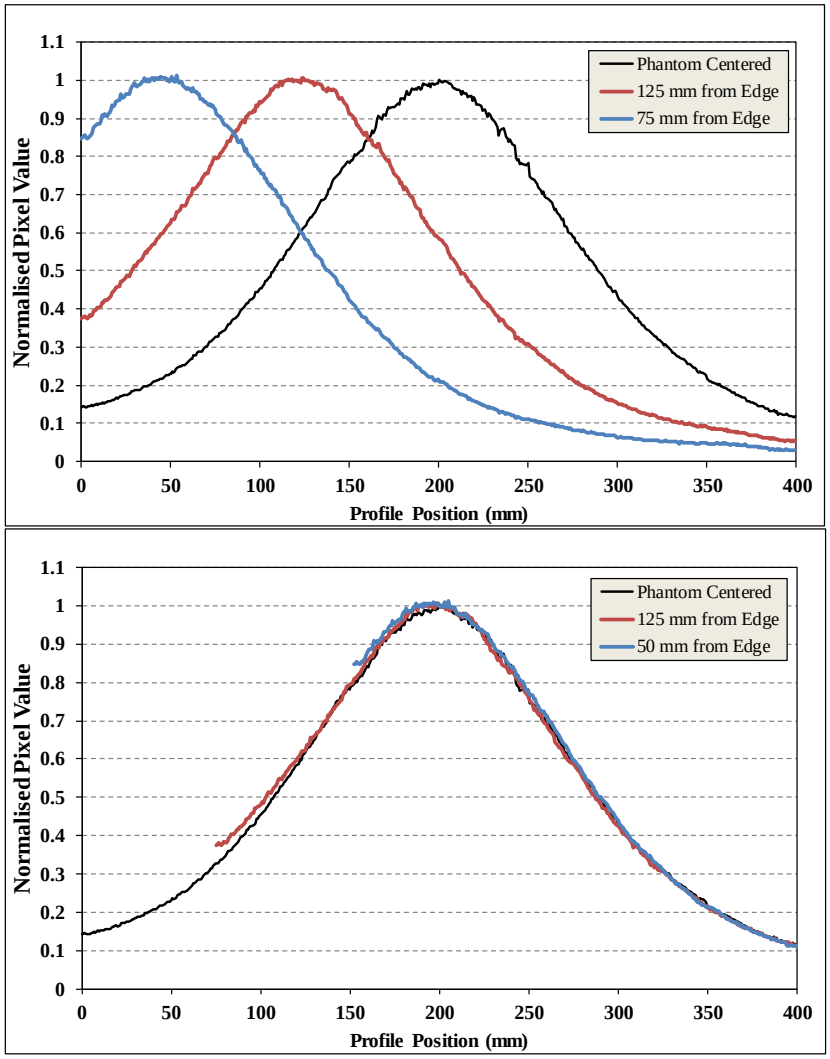

Figure 4.23. The profiles across the images for a SDD 100 mm, showing the distribution acquired by the FPD at each source position and the three profiles overlayed showing the increased response of the detector at the boundaries of the sensitive imaging region.

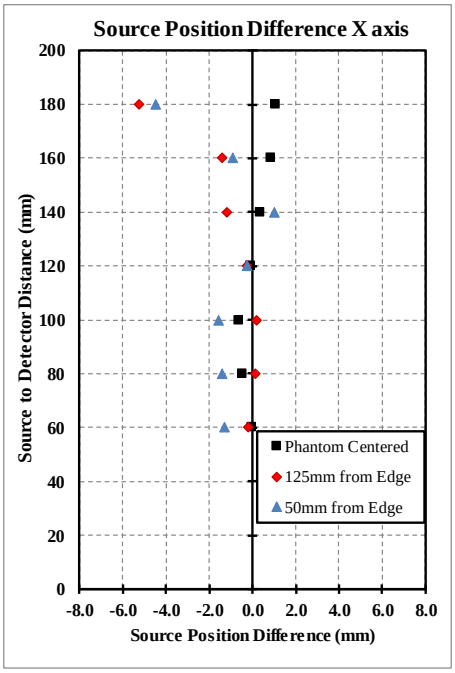

Figure 4.24. The determined source position difference in the FPD x and y axes, using the COM 80%-90% approach, as a function of SDD, to evaluate the influence of detector edge.

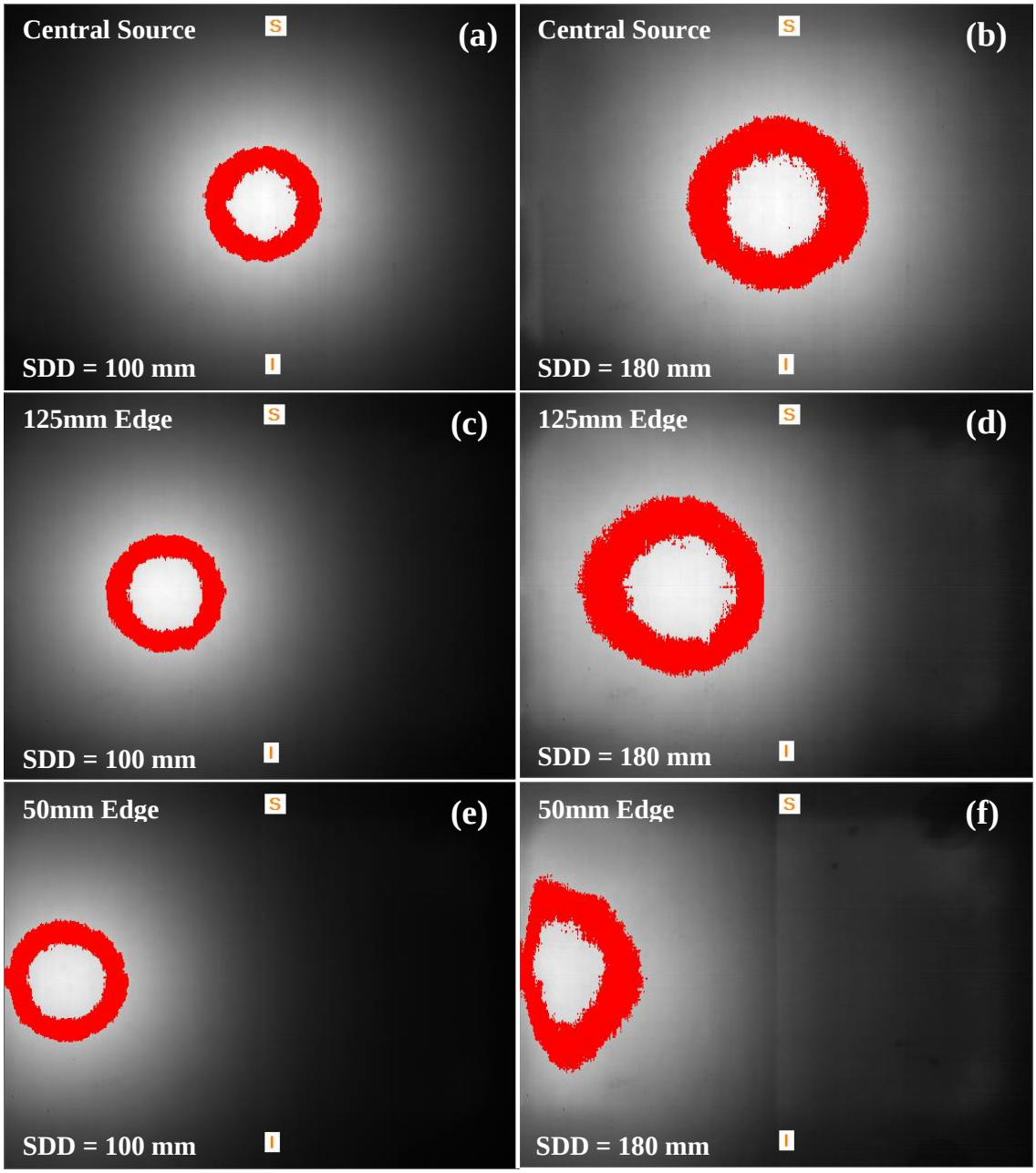

Figure 4.25. The 80-90% COM approach for determining the source coordinate in *x*,*y* and *z*. The red region represents the pixels in the threshold range (80% to 90% of image maximum) that are used as metric for the source coordinate. (a) is the source centered on the FPD at 100mm SDD, (b) is also centered at 180mm SDD, (c) and (d) is the source 125 mm from the edge of the FPD , and (e) and (f) is the source 50 mm from the edge of the FPD.

4.4.2 Influence of Phantom Size on Source Coordinate

The reduced phantom material surrounding the source position was shown to influence the response of the FPD. As described in chapter 3 and shown in figure 3.19, the change in response resulting from this phantom geometry change will potentially influence source coordinate determination. To evaluate this influence, the experimental setup shown in figure 4.26 was used. Phantom slabs were added and images were captured at each increment and the COM algorithm was used to determine the source coordinate. The measured source coordinate was compared to the reference source coordinate determined using the subtraction method previously described.

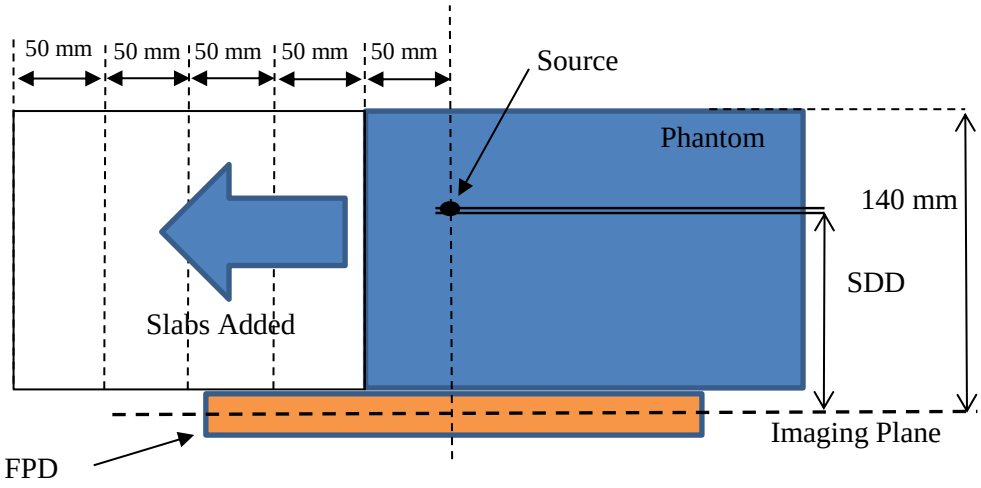

Figure 4.26. The phantom setup for investigating the influence of asymmetric scatter conditions when determining the source coordinate. Slabs of phantom material were added in 50 mm increments.

The orientation of missing phantom material relative to the FPD is shown in figure 4.27. The COM annular region is shown for the 'full' material scenario 4.27(a) and the 'limited' material scenario 4.27(b). The lack of lateral scattering material adjacent to the source position results in an asymmetric 80-90% COM annular region.

The difference between the calculated source coordinates and the reference source coordinates for the FPD *y* axis is shown in figure 4.28.

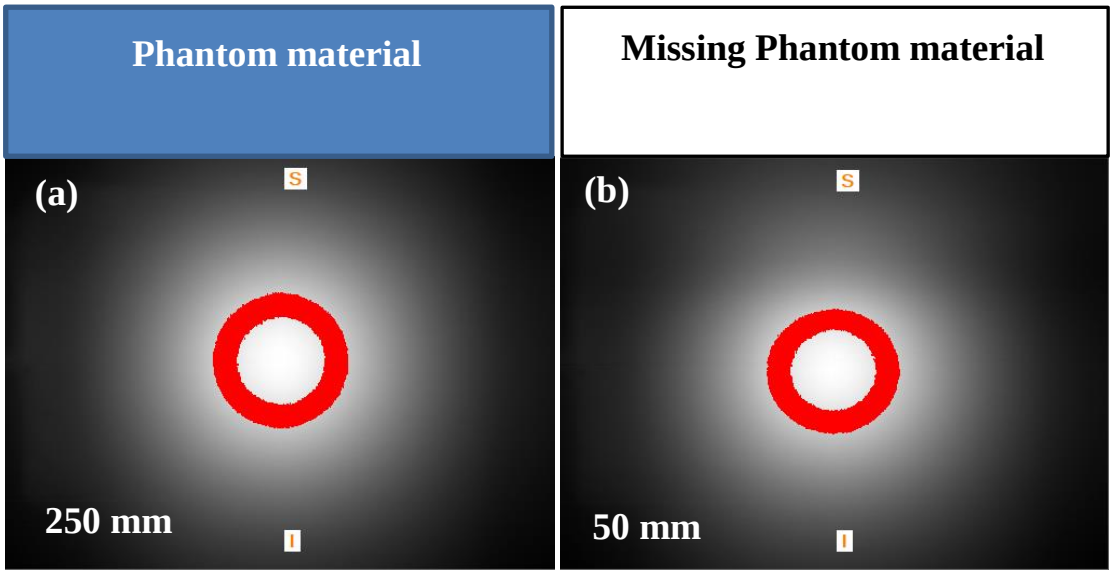

Figure 4.27. The acquired FPD images showing the 80-90% COM approach for determining the source coordinate. (a) The image showing the orientation of the surrounding phantom material and (b) the image showing an asymmetry of the 80-90% annular region and the orientation of the missing phantom material.

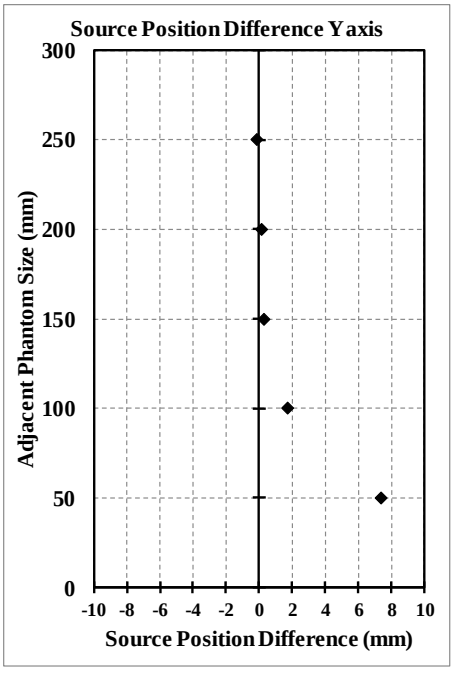

Figure 4.28. The determined source position difference using the COM approach, in the FPD *y* axis, as a function adjacent phantom material size.

The nearby boundary of the phantom influences the source coordinate determination and should be considered in some clinical situations. As determined in section 3.9, approximately 150 mm of surrounding phantom material is required to determined the source coordinate correctly. In some treatment sites, this requirement of surrounding tissue may not be achievable, for example, at the nearby perineum for prostate treatments. One approach to overcome this influence might be to fill the missing tissue region with bolus material to maintain a uniform scatter field. Other approaches may include modelling the geometry and adjusting the COM algorithm to account for the lack of surrounding tissue and therefore reduced scatter contribution.

4.4.3 Source Dwell Position from Image Sequences

The aim of this section is to characterise the capability of the FPD to determine measured dwell positions from a sequence of images as the time at each dwell position is reduced.

4.4.3.1 Method

A treatment plan was created for a single catheter containing 7 dwell positions at 10 mm steps in a catheter 100 mm from the detector (SDD) as illustrated in figure 4.29 All dwell positions were initially programmed with 20 second dwell times. The FPD acquired images in continuous acquisition mode and captured images of the source during the entire treatment sequence. The process was repeated and an image sequence was acquired with dwells 6 to 2 reduced to 15, 10, 5, 4, 3.6, 3, 2, 1 and 0.5 seconds.

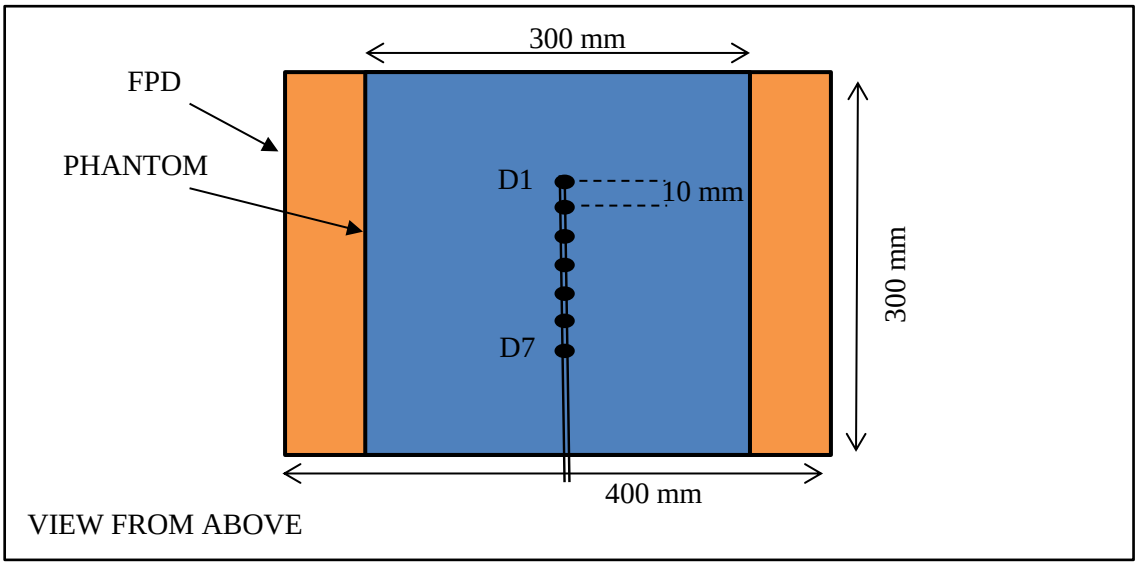

Figure 4.29. The setup of the phantom on the FPD showing a single catheter and the series of 7 dwell positions spaced 10 mm apart.

The COM source approach described in section 4.2.1.3 was used to calculate the source coordinate for each image of the acquired image sequences.

4.4.3.2 Results

The measured source coordinates for each timing sequence are shown in figure 4.30, where the planned dwell locations are shown at 10 mm intervals. The measured source coordinate calculated from each image is represented by a single point. Most of these measured source coordinate points overlap, as the calculated coordinates are almost identical when the source is stationary at a dwell position. However, it can be seen that some image captures occur during source transit between dwell positions (and/or on catheter arrival/departure). The processing of all images in the captured sequence results in apparent measured dwells that do not in fact represent dwell stops of the source. It is also seen that some very short dwells are not captured in any image due to the sampling frequency. Strategies for dealing with these cases are proposed below.

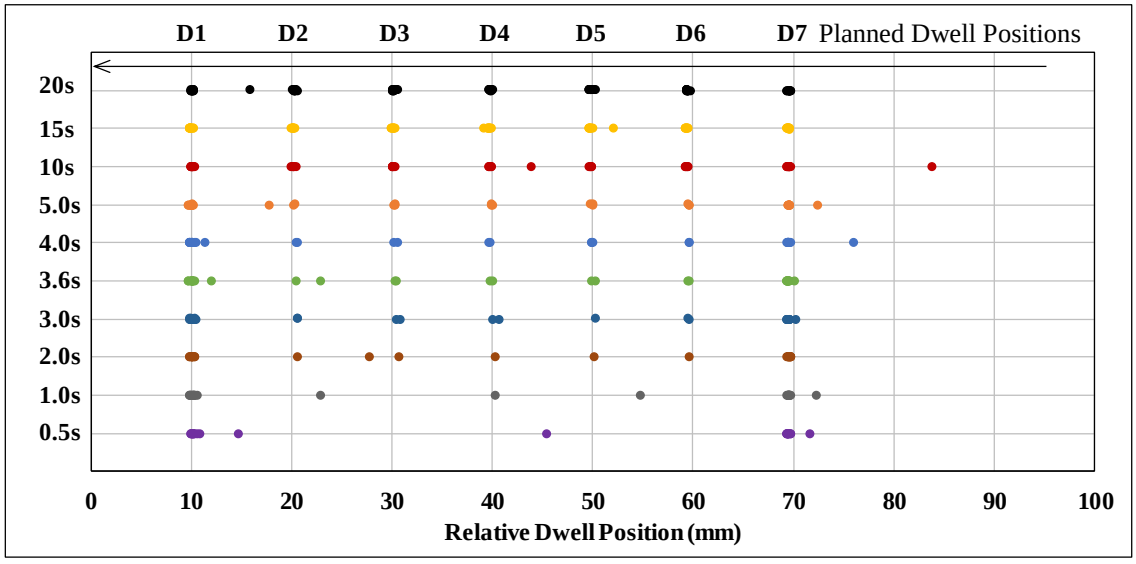

Figure 4.30. The calculated source coordinates along the long axis of the catheter for the series of planned dwells with reducing dwell times. The source progresses through the dwell positions as depicted by the arrow. Data points between the planned dwell positions (D1 to D7) represent measured source coordinate positions while the source was in transit.

The frequency of measured source coordinates at each planned dwell position is shown in figure 4.31 for 20, 5, 3.6 and 1 second timing sequences. At least one measured source coordinate is recorded at dwell positions where the dwell time is greater than or equal to 3.6 seconds.

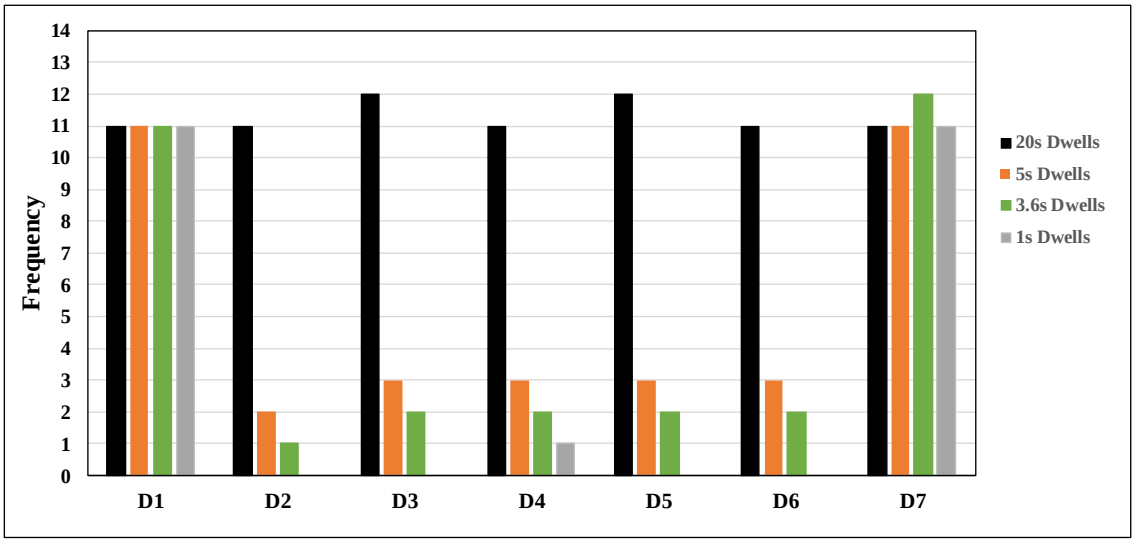

Figure 4.31. The frequency of measured source coordinates corresponding to the planned dwell positions for the 20, 5 3.6 and 1 second sequences. Below the Nyquist sampling time (3.6s) there is no guarantee a source coordinate will be recorded that does not contain motion artifact.

4.4.3.3 Discussion

Two particular challenges are evident in the measurement of the source dwell position: (i) extra recorded dwell positions due to captures occurring during a source transit, and (ii) missing dwell positions due to limited image capture rate.:

As alluded to in the introduction, the acquired sequence of image captures needs to be processed to 'filter out' these additional dwell positions. A possible approach is to filter out the measured coordinates based on the frequency yielding a subset of measured dwell positions that can be evaluated with a higher degree of confidence. This is a function of the time the source dwells at each position, the longer the dwell time the more images acquired at that position, increasing the confidence that this data represents a dwell. In contrast, a recorded single source coordinate may be either a short dwell or a capture of the source in transit. This may be resolved by performing

shape analysis on these captured images and extracting a metric that shows that the source is in transit.

As shown in figure 4.31, reducing the dwell times for dwells 2 to 6 decreased the number of measured source coordinates captured at each planned dwell position. At twice the sampling frequency (Nyquist criteria) of 3.6 seconds, at least one image is acquired at the planned dwell position that does exhibit artefact due to source motion. Below this dwell time (3.6 s) to a dwell time of 1.8 seconds, a measured source coordinate calculated at a planned dwell position is possible but not guaranteed.

Converting measured source coordinates into measured dwell positions requires processing of the data to exclude measured source coordinates that (i) represent the source in transit (between dwell positions, or between the afterloader and the programmed dwell positions), and (ii) coordinates that contain multiple dwell positions with short dwell times exhibiting motion artefact.

4.5 Conclusion

The evaluation of source tracking needed to know the true reference position of the brachytherapy source. This led to the development of the subtraction imaging technique allowing direct imaging of the source capsule. This is in itself novel and is likely to prove useful for a range of quality assurance measurements including applicator commissioning and afterloader quality assurance tests.

After exploring a variety of techniques for extracting the source coordinate a COM approach was adopted. This enabled extracting the source coordinate, from the phantom geometry, in the x and y directions to within 0.5 and 0.3 mm respectively, over the likely clinical range. The COM approach also offers a strategy for deriving the SDD, although to a lesser resolution on the order of 5 mm.

Three complications have been identified that are likely to be important considerations for the clinical implementation. In the next chapter, a pre-treatment imaging component of treatment verification is introduced. It achieves three primary objectives; (i) enables the registration of the source tracking with the anatomy and treatment plan, (ii) assesses the implant geometry immediately prior to treatment geometry delivery and (iii) enables any source tracking differences to be identified as treatment delivery errors or accountable due to catheter displacements.

Chapter 5
Pre-Treatment Verification Imaging

5 Verification Imaging

In the previous chapter we have described the process of locating the position of the HDR brachytherapy source during treatment delivery. In this chapter we focus on the important task of localising the implanted catheters in the patient. The imaging data used for treatment planning of HDR brachytherapy (e.g. CT, MR or US) represents a 'snap shot' in time of the implant geometry, but changes do occur over the time taken from planning to treatment delivery. Swelling and other influences impact the position of the interstitial catheters (or applicator) relative to the surrounding anatomy, and so pre-treatment implant verification using imaging is recommended. Any changes detected in catheter positions relative to the treatment plan influence the interpretation of source tracking results and will represent an upper limit on the agreement that can be expected in the absence of any delivery error.

This chapter describes pre-treatment verification imaging for HDR prostate brachytherapy performed with a flat panel detector and x-ray imaging equipment. The first part of this chapter covers 2D verification techniques, which can be performed with any typical mobile x-ray system. The verification approach is then extended to include a 3D catheter reconstruction method that allows (direct 3D) comparison with the treatment plan derived from the 3D imaging. The 3D approach uses a ceiling-suspended x-ray system, which provides reproducible movements and facilitates oblique shift imaging. Corrections for image divergence are described, a 3D reconstruction approach is given, and a method to register the TPS space with the measurement space enabling direct comparison is provided. A solid water phantom,

described in section 5.1, containing prostate brachytherapy catheters was constructed and is used for both 2D and 3D pre-treatment verification imaging investigations.

5.1 Phantom Construction

A rectangular phantom was constructed from 10 solid water slabs each of 300×300×10mm, containing a simulated brachytherapy implant of 18 plastic catheters (6F Proguide, Elekta, Stockholm, Sweden) spaced at 10 mm intervals, in a grid-like design as depicted in figure 5.1(a). Also embedded in the phantom were three fiducial markers representing prostate anatomical fiducial markers which are typically used for patient positioning in the external beam component of prostate radiotherapy treatment.

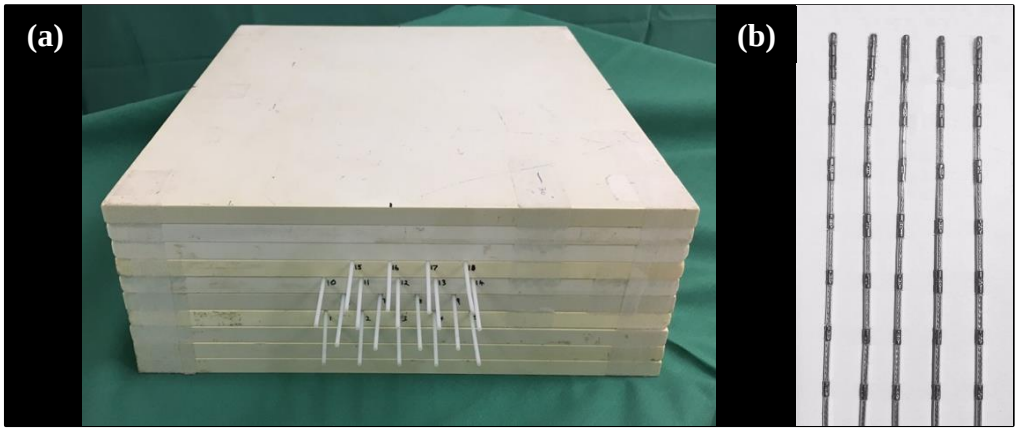

Figure 5.1. (a) The rectangular solid water phantom containing 18 plastic catheters and 3 fiducial markers positioned on the CT couch ready for the planning scan. (b) A sample of the radio-opaque dwell position markers with 10 mm spaced lead markers used during x-ray imaging.

5.2 Treatment Planning Imaging

Radio-opaque CT markers were inserted into each catheter and a CT scan (representing the treatment planning scan) of the phantom was acquired using The Alfred Hospital standard clinical HDR prostate brachytherapy protocol (2.5 mm spaced, 2.5 mm thick slices). The CT images were transferred to the treatment planning system (TPS) (Oncentra v4.3, Elekta, Stockholm, Sweden) and the 'implanted' catheters reconstructed. TPS *patient points* were assigned to the centre of each of the three fiducial markers identified in the CT data.

A plane representing the position of the imaging plane of the flat panel detector (FPD) was created in the TPS. All reconstructed catheter paths and fiducial marker points were projected on to this plane for direct comparison with the 2D measured treatment data acquired in section 5.3.

The 3D coordinates of the reconstructed catheter paths and the identified fiducial marker points were exported for later comparison with the 3D measured treatment data acquired in section 5.4.

5.3 2D Pre-Treatment Imaging

Pre-treatment image verification can be performed with the patient in the treatment position, in the brachytherapy bunker, with a single planar anterior-posterior (A-P) image. Catheter comparison with the treatment plan, performed in the 2D plane of the detector, allows a measure of implant integrity, immediately prior to treatment. Catheters can move independently of each other, with most significant displacements reported in the literature are predominately in the superior-inferior (S-I) direction[31, 33, 37, 75]. In HDR prostate brachytherapy, if the anatomy (prostate) has fiducial markers implanted (as a surrogate for prostate position, often used for EBRT image guided radiotherapy), then the catheter positions relative to the surrounding anatomy can be determined and verified against the treatment plan.

In this work, pre-treatment imaging is performed using an external x-ray source and the FPD as the image receptor. The imaging geometry is illustrated in figure 5.2, with the solid water phantom (as described in section 5.1) depicted on the couch top and a ball bearing (BB) array is positioned in the field for x-ray source and detector localisation. The distance from the x-ray source to imaging plane is defined as the focus to imager distance, *FID*, the distance from the source to the top of BB array is defined as *A*, and the distance from the BB array to the imaging plane is defined as *B*.

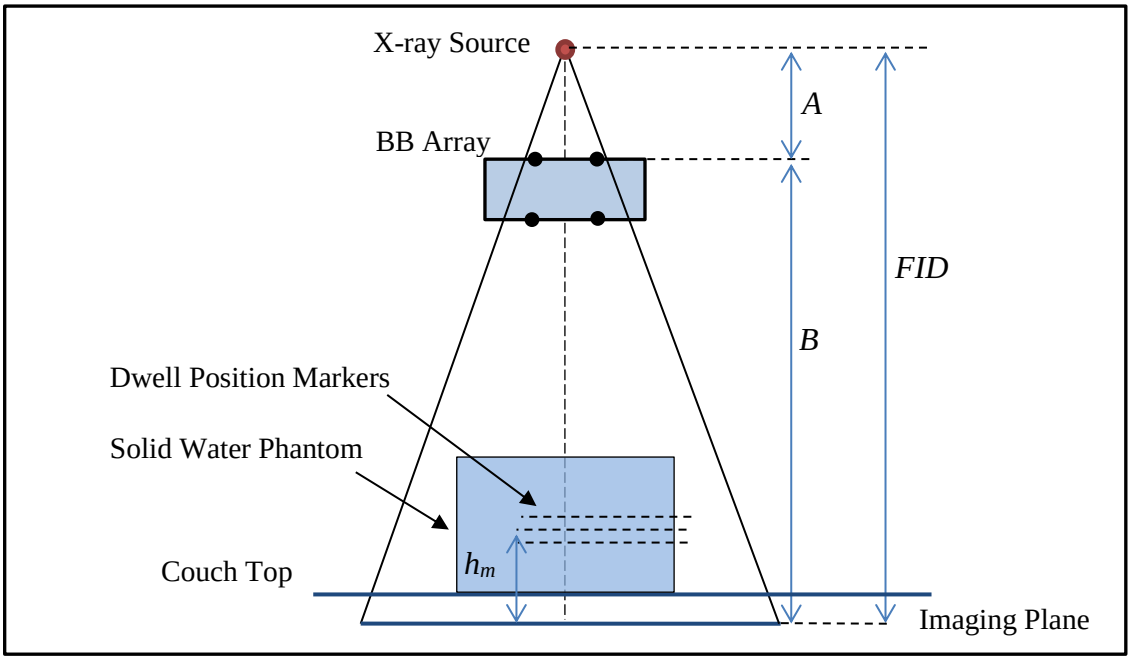

Figure 5.2. An illustration of the geometric arrangement for performing 2D pre-treatment image verification. The solid water phantom containing brachytherapy catheters and dwell position markers, on the treatment couch, with the x-ray source at a distance defined by the focus to imager distance (FID).

The phantom was transferred to the HDR brachytherapy treatment bunker and setup on the couch above the sensitive region of the FPD. Catheter markers (radio-opaque x-ray dwell position markers), different from those used at CT (figure 5.1(b)), were inserted into the 7 selected catheters (catheters 1, 3, 5, 6, 11, 13 and 18) used for this pre-treatment image verification demonstration. The distance from the FPD imaging plane to the catheter (dwell position) marker is defined as the height of the marker, h_m. The h_m for catheters 1, 3, 5 was 80 mm, catheter 6 was 90 mm, catheter 11 and 13 was 100 mm and catheter 18 was 110 mm. The ceiling suspended x-ray system (QRad OTS x-ray suspension system, Carestream Health, Rochester, NY, USA) was positioned above the phantom with a *FID* of 1000 mm. A single A-P image was acquired with the FPD and is shown in figure 5.3. A BB array attached to the x-ray source was used in the radiation field during the image acquisition.

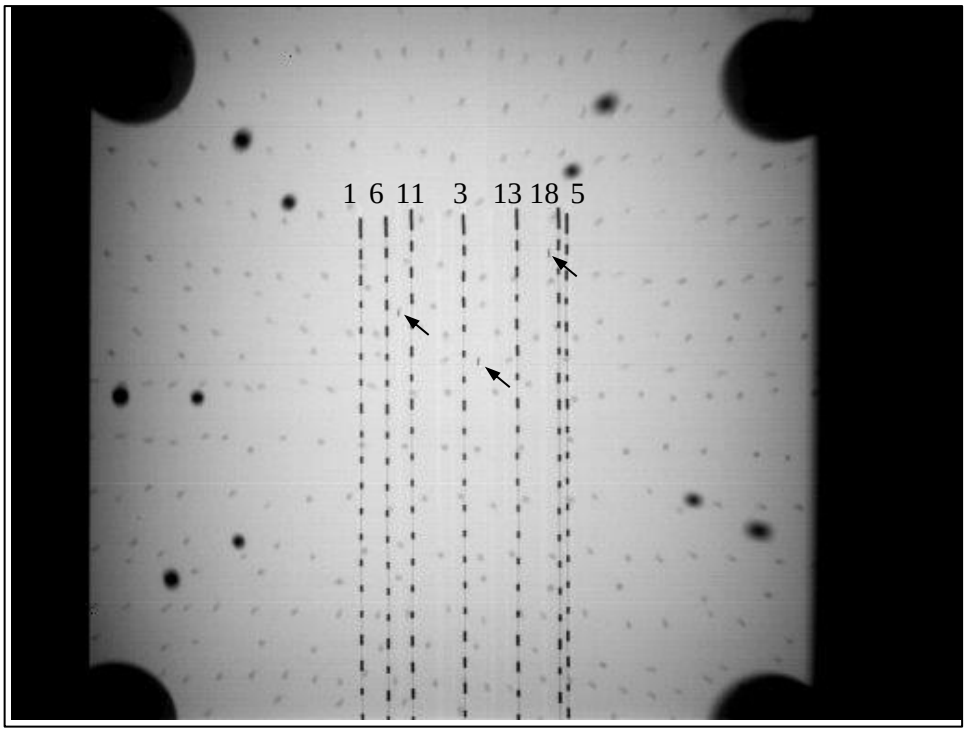

Figure 5.3. The AP x-ray image of the solid water phantom, containing 18 plastic catheters and 3 fiducial markers. The catheter markers inserted into catheters 1, 3, 5, 6, 11, 13 and 18 are also visible. The three fiducial markers are highlighted by the black arrows.

In order to compare the acquired A-P image directly with the TPS data (exported as a 2D plane described in section 5.2), and verify the implanted catheters are correct relative to the surrounding anatomy, the following steps must occur:

- Correction of the image divergence in the acquired A-P image.
- Perform a 2D registration between the TPS and the measurement space.
- Compare the planned catheter paths with the measured catheter paths.

The following sections describe in detail how these steps are accomplished to complete 2D pre-treatment verification.

The treatment room coordinate system is defined to enable registration of the treatment plan (TPS space) to the measured (FPD space) positions. The orientation of the room coordinate system is shown in figure 5.4.

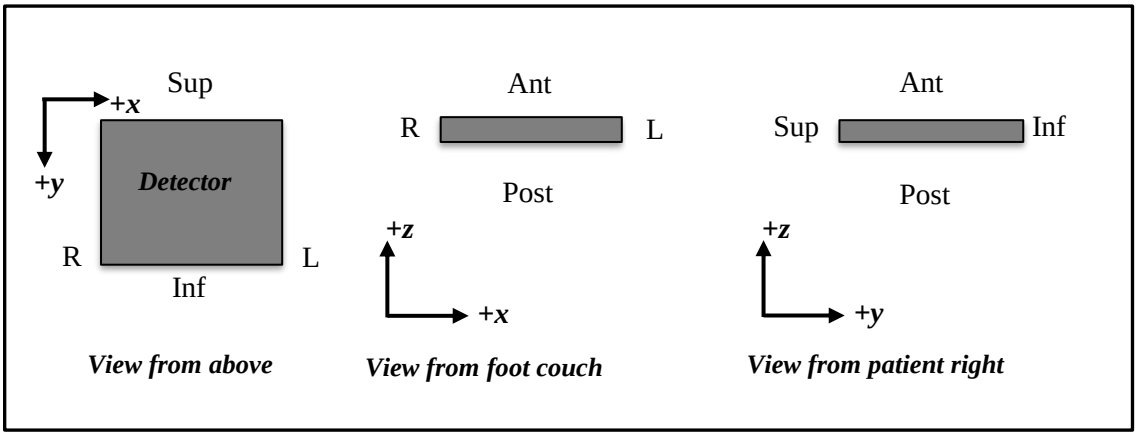

Figure 5.4. The room coordinate system with the origin placed at the top left of the imaging device. The plane of the detector is in the x-y plane and the patient and points above the detector is in the positive z direction.

5.3.1 Image Divergence Correction

The AP x-ray images acquired using the geometry described in figure 5.2 contain geometric distortion resulting from the divergence of the x-ray beam. Features in the AP x-ray image, such as catheter paths and fiducial markers and the distances between them are magnified and corrections need to be applied in order to compare with the TPS data. The x-ray beam central axis position on the A-P image needs to be determined to correct the divergence of each projected feature, transforming the projection to a parallel geometry. The magnification is illustrated in figure 5.5(a), where a catheter marker or a fiducial marker (object) in the patient/phantom is projected on to a plane representing the FPD imaging plane. For a marker at a distance *a* away from the central axis of the x-ray beam, a divergence correction of *d* is applied to produce the orthogonal (parallel) projection for this marker, as illustrated in figure 5.5(b).

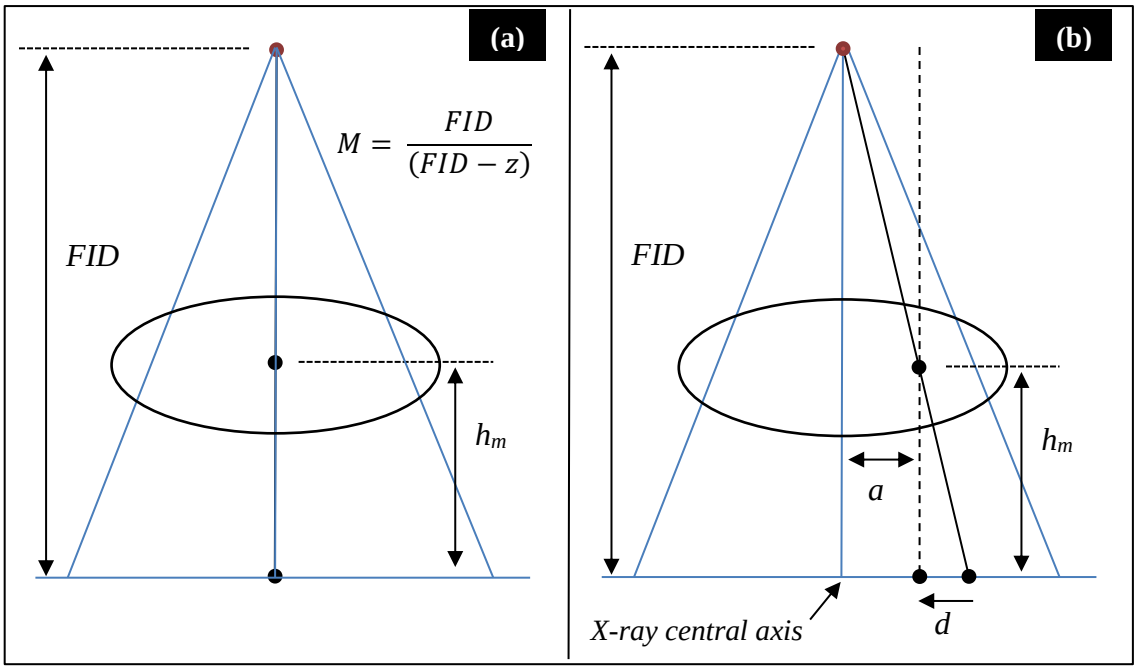

Figure 5.5. (a) The magnification correction for a fiducial marker feature in the patient a height h_m above the imaging plane, for an x-ray source focus to imager distance *FID* and (b) the divergence correction for a fiducial marker in the patient which is height h_m above the imaging plane and a distance *a* away from the central axis of the x-ray beam. A divergence correction of *d* is applied to produce the orthogonal projection for this marker (shown as a dashed line).

A BB array is included in the x-ray field, just below the x-ray collimator, and the design of the BB array used in this work is illustrated in figure 5.6. The BB array provides a mechanism to localise the position of the x-ray source relative to the imaging plane by determining the x-ray central axis position.

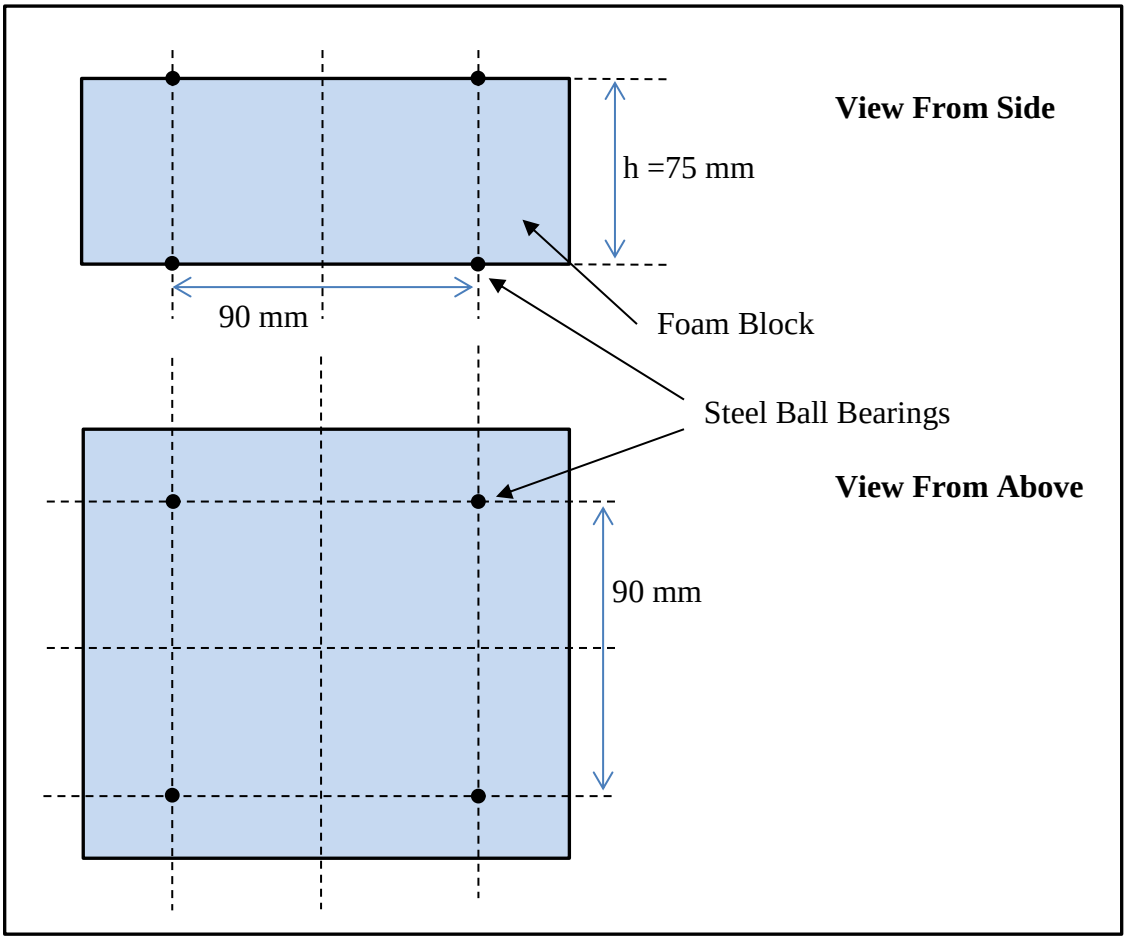

Figure 5.6. The foam block holding the 3mm diameter steel ball bearings (BBs) in a 90 mm square design with each BB plane spaced 75 mm apart. The projected BBs in the AP image are used to localise the FPD with the x-ray imaging focal spot position.

The x-ray central axis position on the AP image was determined by projecting a line through each pair of BBs visible on the image as shown in figure 5.7(a). The intersection point of these projected lines is the x-ray central axis position and represents the perpendicular intersection of the central axis ray from the x-ray source to the imaging plane of the detector. Uncertainties associated with identifying the centre of the projected BB marker on the image can lead to directional discrepancies of the BB projected lines, and so may produce an x-ray central axis region (area) of intersection rather than a point. To account for this measurement variation, the x-ray central axis position is determined by calculating the centre of mass (COM) of all BB line intersection points (4 BB pairs produce 6 possible intersection points).

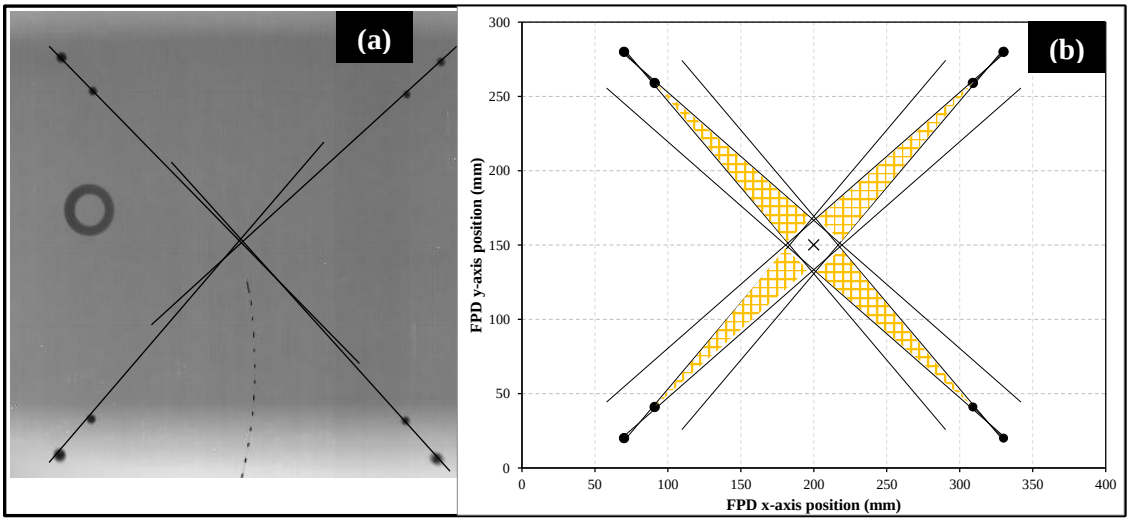

Figure 5.7. (a) The x-ray central axis position determined from the intersection of lines projected between the pairs of BBs. (b) The four sets of BB markers and the projected line spread for a BB marker uncertainty of ±1 pixel. The orange area represents the region where outlier intersection points may occur. The most likely central axis position is shown by the black cross at the centre of the FPD image.

The uncertainty in calculating the x-ray central axis position was determined by performing a simulation to determine the possible region of intersection for all projected lines, based on an individual BB marker point identification uncertainty of ±1 pixel (±0.784 mm). Figure 5.7(b) shows the four sets of projected BB pairs and the range the projected lines can take. The region defined by the central diamond, of size ±16.6 mm, is the region where perpendicular pairs of BB projected lines can possibly intersect, while the long 'wedge shaped' regions, shown as the orange hatched region in figure 5.7(b), represent the area that opposing BB projected lines can possibly intersect. The intersecting lines of opposed BB sets can therefore contribute the greatest uncertainty when determining the x-ray central axis position. Intersection points occurring in this region are outliers, and will skew the centre of mass calculation, influencing the divergence correction applied to the A-P image.

If we ignore outlier intersection points region, determined by the BB opposed projections, the x-ray central axis position divergence correction uncertainty, $\Delta_{DivCorr}$, can be determined for a measured x-ray central axis within the ±16.6 mm diamond. For a *FID* of 1000 mm, and a marker point (in the object) of 50, 100, 150 and 200 mm above the FPD imager plane (h_m), the divergence correction applied, *d*, to the projected

point from the central axis a distance *a*, (as in figure 5.5(b)) has an uncertainty as described in figure 5.8. A marker offset distance of 100 mm from the central axis and 200 mm from the imaging plane, which would be an extreme in a clinical case, produces a divergence correction uncertainty of ±2.8 mm.

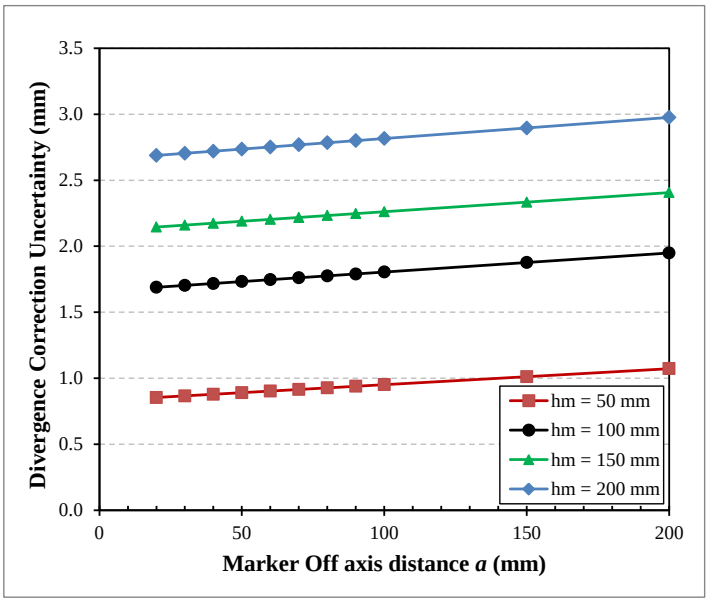

Figure 5.8. The divergence correction uncertainty, $\Delta_{DivCorr}$, for the correction applied to a marker point at distance *a* from the central axis and a height h_m above the imaging plane using the square BB design.

One approach to reduce the uncertainty produced by the BB line projection is to increase the distance between the two BB planes (figure 5.6), resulting in an increased separation between each projected BB pair on the A-P image, therefore reducing the range of the projected 'wedge shaped' region of projected BB intersection lines. The area of the central diamond will also be reduced, but the long 'wedges' due to opposing BB pairs will remain, although narrowed. To eliminate these 'wedges', a new BB array design is proposed, that does not have opposing sets of BB pairs and is described in the next section.

5.3.2 Improving the Ball Bearing Array Design

In order to reduce the event of intersection outlier positions a new BB array design was proposed, and the design is illustrated in figure 5.9(a). The new design distributes 5 pairs of BBs around a 70 mm diameter circle in such a way to avoid opposing BB

projection sets. The BB array was constructed to attach to the accessory tray of the ceiling suspended x-ray system, below the x-ray collimator, as shown in figure 5.9(b), allowing practical use in the clinical environment.

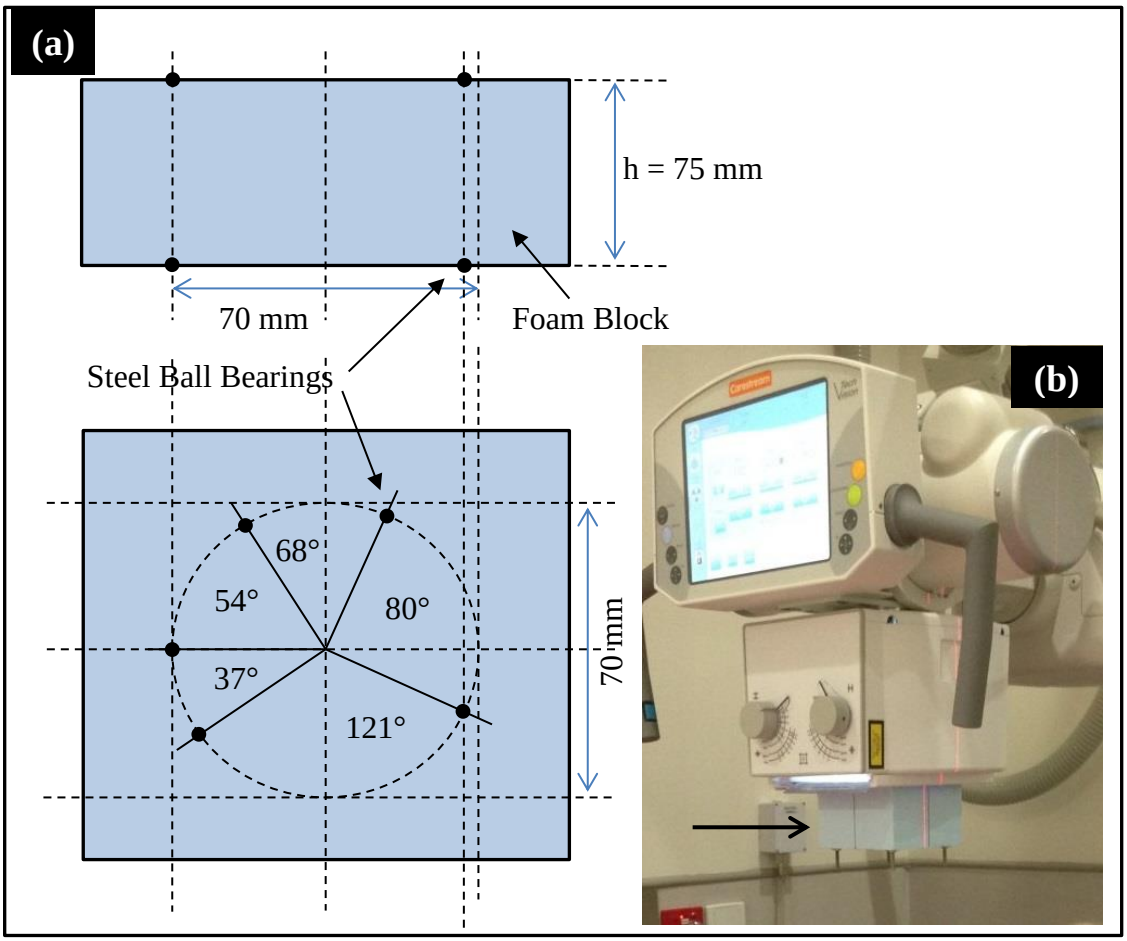

Figure 5.9. (a) The foam block holding the 3 mm diameter steel BBs arranged in a custom design on a 70 mm diameter circle. The positions of the BBs projected on the A-P image are such that when each BB pair is projected they do not meet an opposing BB pair line projection. (b) The BB array attached to the x-ray system collimator accessory tray.

The BB array design also considered the clinical application, in this case HDR prostate brachytherapy. As illustrated in figure 5.10, the projection of the BB pairs avoid the catheter dwell position markers and implant region containing prostate fiducial markers while still projecting on to the FPD imager.

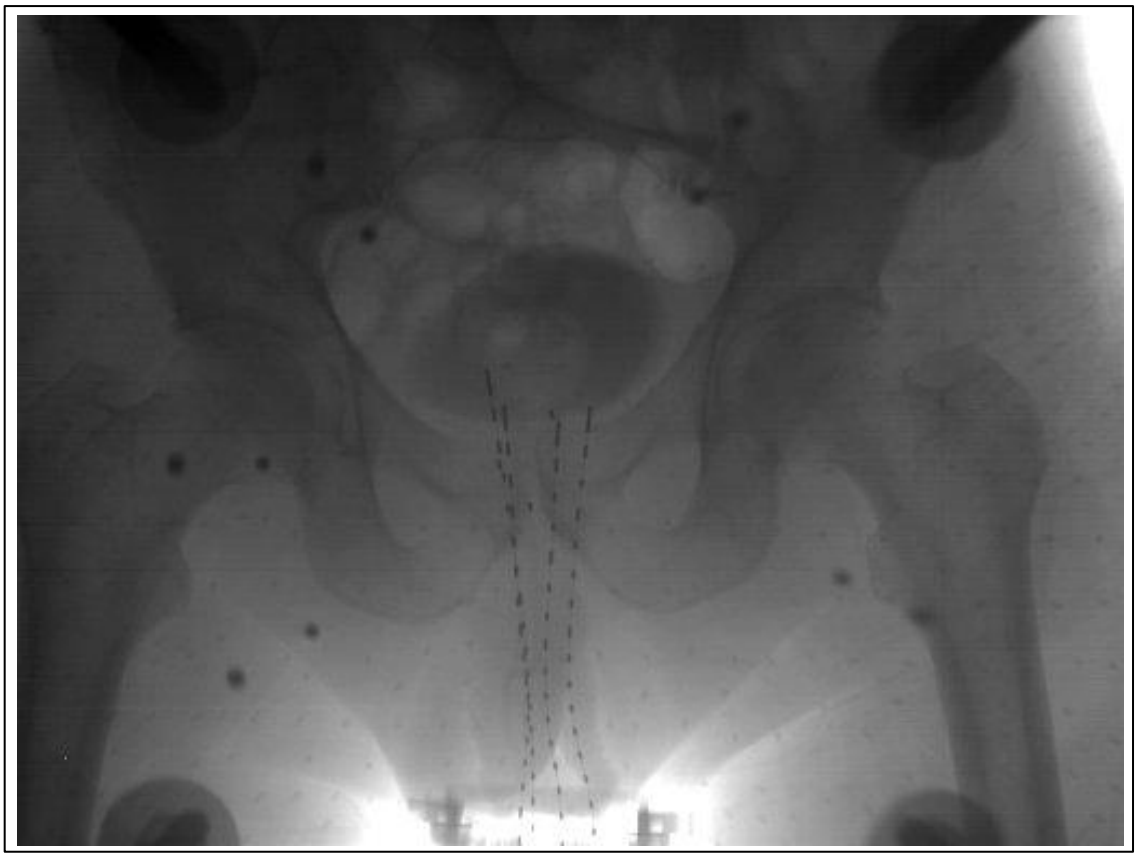

Figure 5.10. An example of the custom designed BB array in a clinical situation. The projected BB pairs are not opposing and they do not obscure the catheter dwell position markers inserted for pre-treatment imaging.

The x-ray central axis position uncertainty was estimated by performing the same simulation described in section 5.3.1, where the possible region of intersection of all lines was determined, based on a BB marker point identification uncertainty of ±1 pixel (±0.8 mm). Figure 5.11 shows the five sets of projected BB pairs and the range the projected lines can take. The central region, where all pairs of BB projected lines can intersect, has a smaller size than the square BB design, with x = ±10 mm and y = ±6 mm. The long 'wedges' observed in the square BB design are eliminated, with only two relatively short regions where intersection outliers can exist, shown as orange hatched regions in figure 5.11.

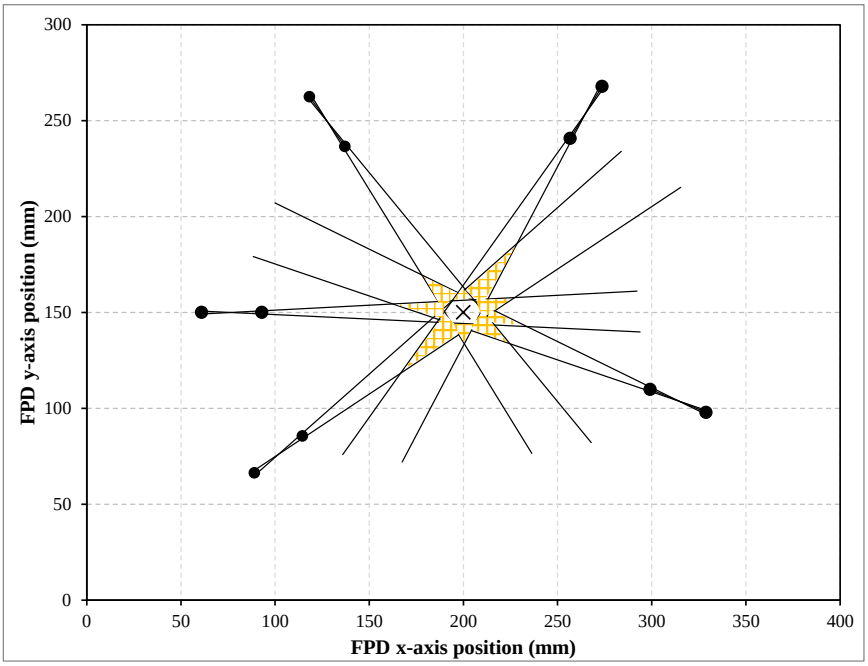

Figure 5.11. The five sets of BB markers and the projected line spread for a BB marker uncertainty of ±1 pixel. The orange area represents the region where outlier intersection points may occur. The 'true' central axis position is shown by the black cross at the centre of the FPD image.

The divergence correction uncertainty, Δd, was evaluated for this circular BB design by considering a measured x-ray central axis within the ±10 mm central region. For a *FID* of 1000 mm, and a marker point (in the object) of 50, 100, 150 and 200 mm above the FPD imager plane (h_m), the divergence correction applied, d, to the projected point from the central axis a distance a, (as in figure 5.5(b)) has an uncertainty as described in figure 5.12.

The divergence correction uncertainty shown in figure 5.12 does not vary strongly with marker off axis distance a, at each marker height h_m. Therefore not aligning the implant directly with x-ray central axis position on the FPD will have only a small (±0.2 mm) influence on total measurement uncertainty, and hence the sensitivity to detect catheter displacements.

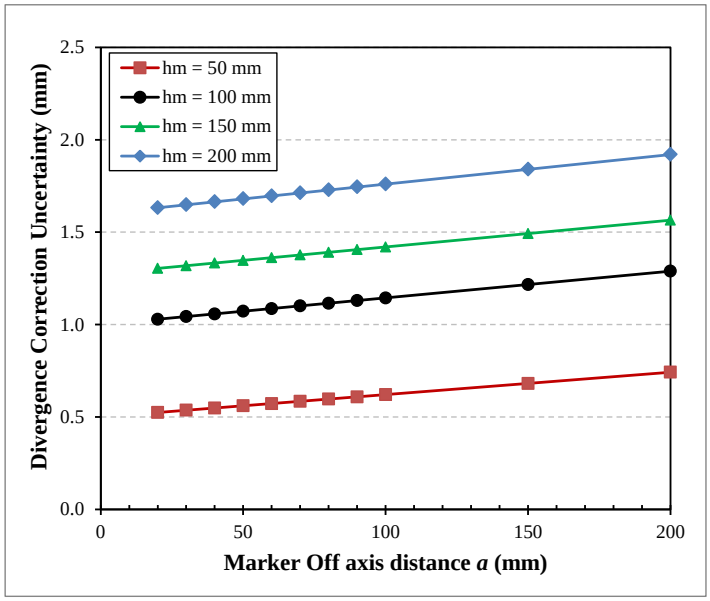

Figure 5.12. The divergence correction uncertainty, $\Delta_{DivCorr}$, for the correction applied to a marker point at distance a from the x-ray central axis and a height h_m above the imaging plane using the circular BB design.

To characterise the performance of the new BB array design, the x-ray central axis position was measured and compared against the performance of the square BB design. The next section describes the procedure to evaluate the two BB designs.

5.3.3 X-ray Central Axis Position Measurement

The uncertainty of x-ray central axis position was evaluated, for each BB design, by calculating one standard deviation of projected BB line intersection points. This was evaluated for a source to imager geometry as illustrated in figure 5.13(a), where the focus to imager distance (FID) was fixed at 1000 mm. The BB array was placed in the x-ray field with the light field cross hairs of the x-ray system set to the centre of the BB array. Each BB array was positioned at a distance from the x-ray source, A, of 650, 500 and 350 mm and an image acquired at each position. Additionally, the circular BB array was placed in the x-ray system accessory tray where A = 250 mm. To evaluate reproducibility, the BB array was rotated by 90 degrees increments (positions of 0°, 90°, 180°, 270°) for each height A, and images also acquired. All 28 central axis position measurements were made without altering the x-ray tube and FPD positions.

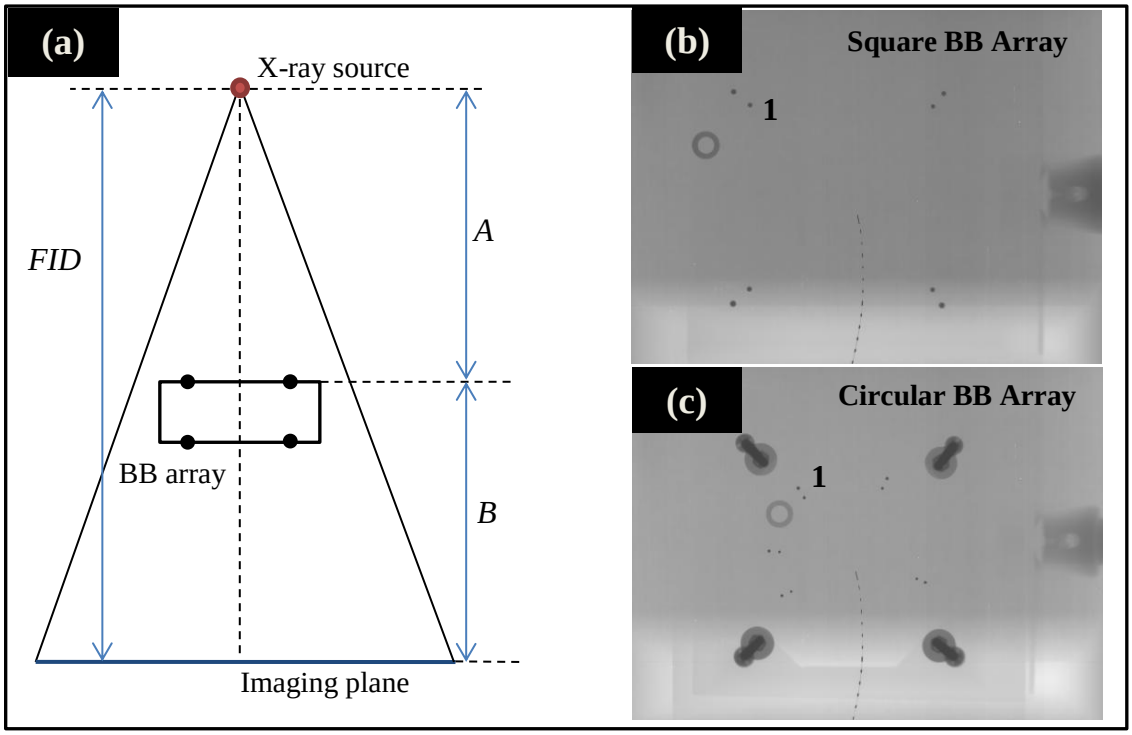

Figure 5.13. (a) The arrangement of the x-ray source, BB array and imaging plane used to measure the x-ray central axis position on the imaging plane. (b) An image of the square BB array with BB pair number 1 marked and (c) an image using the custom BB array. A steel washer, visible in (b) and (c), was attached to the BB array to help define orientation.

A steel washer was attached to the BB array to identify the orientation as it was rotated from 0° to 270°. An x-ray dwell position marker was placed on the surface of the FPD as a reference of patient inferior image orientation. An example of a square BB array image and the circular BB array image is shown in figure 5.13(b) and 5.13(c) respectively.

Each image was processed using in house software shown in figure 5.14, allowing each pair of projected BBs to be identified using a pixel intensity centre of mass (COM) algorithm to determine the centre pixel of the BB marker. The line projection for each BB pair was determined and the intersection points for all lines calculated, as shown by cyan crosses in figure 5.14. The COM calculated centre position is shown by the red cross.

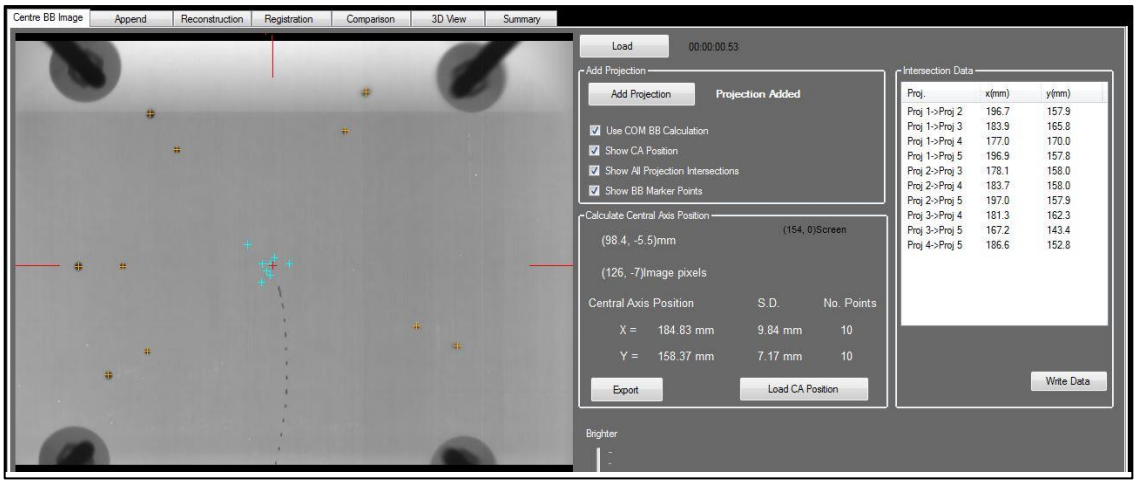

Figure 5.14. The in house software used to process the image to determine the x-ray central axis position. The centre of the projected BBs were identified by using a pixel intensity based centre of mass algorithm, and results are shown as yellow crosses. The intersection point of the projected BB pair lines are shown as cyan crosses and the calculated x-ray central axis position is displayed as a red cross.

The mean and standard deviation of these intersection points was calculated for the square BB and circular BB arrays at each rotated position and the comparison of standard deviation is shown in figure 5.15. It is clear the circular BB array produces less deviation from the calculated x-ray central axis mean position than the square BB array. This reinforces the design concept of eliminating the possibility of outlier intersection points due to BB marker point uncertainty, producing a more precise determination of the x-ray central axis position.

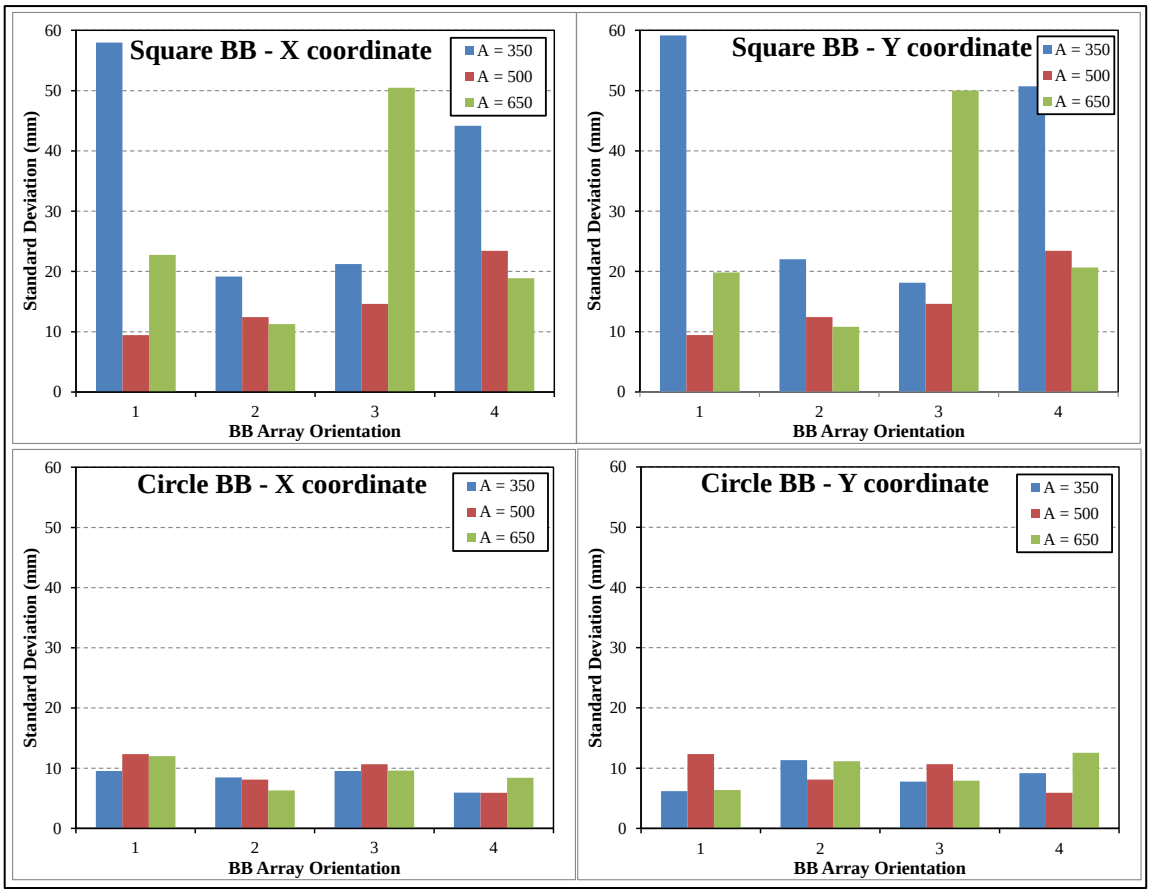

Figure 5.15. The variation of x-ray central axis position for the square BB array and the circular BB array. Each bar represents one standard deviation of BB pair intersection lines, acquired for the three distances of *A*.

The reproducibility results of determining the x-ray central axis is shown in table 5.1 for the square BB array and in table 5.2 for the circular BB array. The mean *x* and *y* coordinates is the absolute mean position of the x-ray central axis position across the four orientations of the BB array. The standard deviation across all distances, *A*, for the circular BB design (column 4 and 5 of table 5.2) is less than the square BB design (column 4 and 5 of table 5.1).

Table 5.1. The calculated x-ray central axis position for the square BB array at a distance *A* from the x-ray source. The x and y coordinate is the calculated mean position for the array in the four orientations (0°, 90°, 180° and 270°) with an uncertainty of 1 standard deviation.

***A* (mm)**	**Mean x (mm)**	**Mean y (mm)**	**S.D. x (mm)**	**S.D. y (mm)**
350	195.1	165.5	12.7	8.7
500	192.8	158.9	7.7	8.2
650	189.1	154.3	4.9	8.7

Table 5.2. The calculated x-ray central axis position for the circular BB array at a distance *A* from the x-ray source. The x and y coordinate is the calculated mean position for the array in the four orientations (0°, 90°, 180° and 270°) with an uncertainty of 1 standard deviation.

***A* (mm)**	**Mean x (mm)**	**Mean y (mm)**	**S.D. x (mm)**	**S.D. y (mm)**
350	189.0	160.7	3.1	1.9
500	188.7	161.1	2.6	1.9
650	185.1	161.4	2.5	1.2
250 (In Tray)	185.4	158.2	0.4	0.1

To further highlight the improved reproducibility of the circular BB design over the square BB, all measured intersection points are shown in figure 5.16, for all distances (*A*) and BB array orientations. The circular BB array design produces a more reproducible result then the square BB which has a greater spread of points and notable outliers.

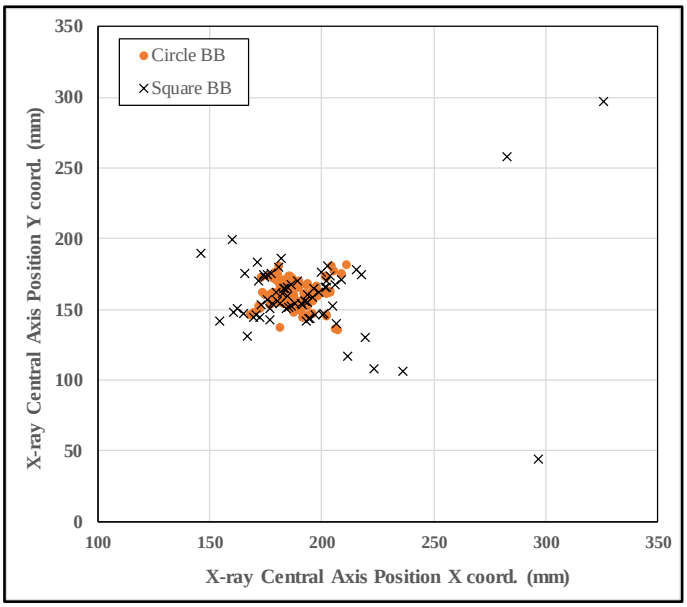

Figure 5.16. The spread of all intersection points used to determine the x-ray central axis position. The circular BB array design produces a more reproducible result then the square BB which has a greater spread of points and notable outliers.

In conclusion, the circular BB array design results in a more reproducible determination of the x-ray central axis position compared with the square BB design. At a distance *A* of 350 mm, the circular BB shows a spread of (*x*) ±3.1 and (*y*) ±1.9 mm, while the square BB is approximately 4 times greater, (*x*) ±12.7 and (*y*) ±8.7 mm. An algorithm using a template based approach could be implemented to automatically segment and identify the BB array pairs in the A-P image.

5.3.4 2D Registration of Planned (TPS) with Measured (FPD) Space

Direct comparison of the treatment plan with the measured catheter positions, for pre-treatment verification, required a relationship between the planned (TPS) space and the measured (FPD) space to be established. The positions of three fiducial markers embedded in the solid water phantom, shown in figure 5.3, were determined in the acquired A-P image. A divergence correction was applied to the measured fiducial marker positions using a correction factor determined by the BB array, as previously described. The measured fiducial marker positions were paired with the corresponding fiducial markers previously identified in the treatment plan. A non-iterative, least squares method of registration was performed [106] (in 2D) to determine the rigid

spatial transformation (rotation and translation) between the planned (TPS) and measured (FPD) spaces.

The reported registration residual from this process, *R*, can be used as a measure of match between the datasets, and is the sum of the squared differences for each registered fiducial marker pair. The registration uncertainty, $\Delta_{Reg.2D}$, is then defined as the mean difference between all fiducial marker pairs in the plane of the FPD, and can be derived from the registration residual by

$$\Delta_{Reg.2D} = \sqrt{\frac{R}{n}} \qquad \text{Eqn. (5.1)}$$

where *R* is the registration residual and n is the number of fiducial marker pairs participating the in the registration.

The registration process is illustrated in figure 5.17 showing the registration between the two corresponding sets of fiducial markers in the TPS and FPD space and the resulting transformation matrix, *T*, which establishes a link between the two frames of reference. The registration uncertainty can be used as a metric for the agreement between the planned and measured geometries and is normalised for the number of fiducial marker pairs used in the registration process. The registration uncertainty therefore represents the geometric uncertainty, in each coordinate, of any point that is transformed using the transformation matrix *T*.

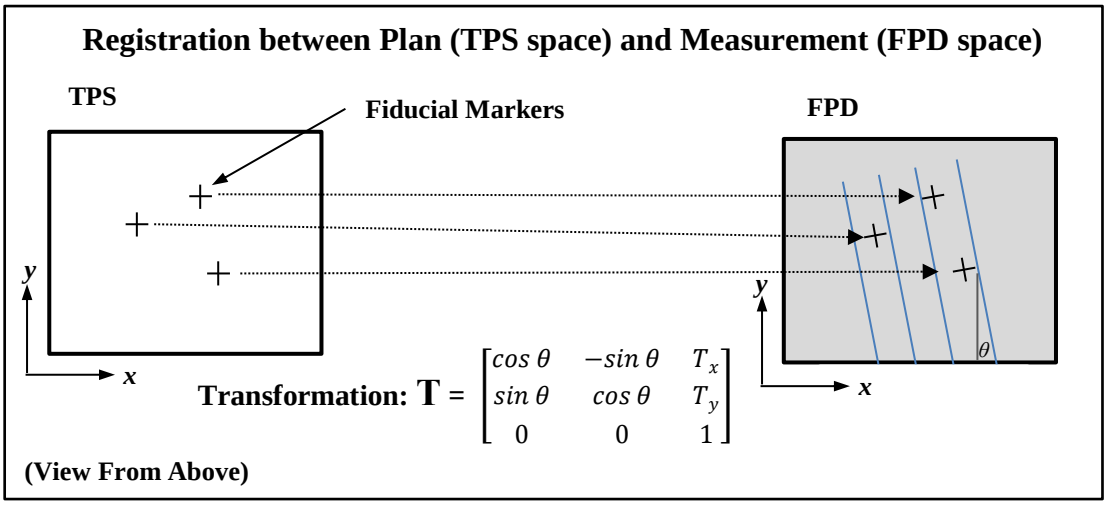

Figure 5.17. An illustration showing the 2D registration process for corresponding fiducial marker points in the treatment plan and the measured image. The resulting transformation matrix, *T*, where θ represents the counter-clockwise rotation of the fiducial markers about the origin, and T_x and T_y represent a translation in the *x* and *y* directions respectively.

Establishing a geometric transformation between the two frames of reference then allows information to be passed in either direction. In this application of pre-treatment verification, the brachytherapy staff require a comparison at the treatment console and so it is logical to map the planned data to the measurement frame of reference.

To illustrate the reproducibility of the process, the phantom was repositioned on the treatment couch two additional times and the A-P image acquired. The sensitivity to catheter displacement from the planned positions was evaluated by shifting the inserted catheter markers out of the plastic catheters (inferiorly), to simulate catheter displacement in the S-I direction. All 7 catheters were displaced by 2, 3, 5 and 10 mm and an A-P image was acquired at each position.

To evaluate the registration robustness under rotation, the solid water phantom was rotated 10.0° in the plane of the FPD (Yaw about the z-axis) to simulate patient setup differences from CT. The phantom was also rotated about the x-axis (tilt out of the plane of the FPD), to simulate patient pelvic tilt. The phantom was rotated by 1.9°, 3.8° and 5.7°, representing rotational deviations from the original planned position, and an A-P image was captured at each position. The fiducial markers were identified in all acquired A-P images and registration performed with the fiducial markers previously

identified in the TPS data. The registration uncertainty, $\Delta_{Reg.2D}$, and the reported rotations for these datasets are shown in table 5.3 and 5.4.

Table 5.3. The reported registration uncertainty, $\Delta_{Reg.2D}$, and rotation, θ, after the 2D registration of the measured fiducial markers with the TPS fiducial markers.

Dataset	**$\Delta_{Reg.2D}$ (mm)**	**Rotation θ**
Initial	0.3	-0.1
Repeat 1	0.5	0.5
Repeat 2	0.4	0.5
2 mm Shift	0.4	-0.5
3 mm Shift	0.3	-0.5
5 mm Shift	0.3	-0.2
10 mm Shift	0.3	-0.2
Mean	0.4	-0.1

The registration uncertainties, presented in table 5.3, for all datasets produce an average registration uncertainty of 0.4 ±0.1 mm, suggesting the registration procedure is highly reproducible.

Simulated rotation of the phantom at treatment, to a position different from that at treatment planning imaging, produces fiducial markers projected on to a plane, that have a different marker position inter-spacing from that at planning. This deviation of projected marker pattern will limit the registration agreement possible, increasing the registration uncertainty indices, while also influencing the catheter agreement.

The rotations applied to the phantom (Tilt about x-axis) caused only a minor increase of the registration uncertainty. The average registration uncertainty recorded for 7 datasets was 0.4 mm, and when a tilt of 5.7° is applied the registration uncertainty increases to 1.0 mm (table 5.4). The rotation recorded in the third column of table 5.4 is the rotation result calculated from the registration process in the plane of the FPD (rotation about the z-axis).

Table 5.4. The reported registration uncertainty, $\Delta_{Reg.2D}$, and calculated rotation, θ, for the datasets with applied phantom tilt to simulate patient pelvic tilt.

Dataset	$\Delta_{Reg.2D}$ (mm)	Rotation θ
10.0° Yaw	0.7	10.5
0.0° Tilt	0.6	0.4
1.9° Tilt	0.3	0.3
3.8° Tilt	0.8	-0.5
5.7° Tilt	1.0	-0.8

In a clinical scenario, when the patient is set up on the couch for treatment, any patient pelvic tilt present, different from the setup at treatment planning imaging, would increase the registration uncertainty. Catheter position comparisons would therefore have larger tolerances applied, as the overall measurement uncertainty is increased, and so would reduce the confidence in detecting small catheter displacements. To combat this, the introduction of a reproducible patient setup protocol to clinical practice would be beneficial. This approach could range from a simple set of lines drawn on the patient skin using the CT laser system as a reference to a more advanced pelvic support (vac-bag) device.

5.3.5 Catheter Path Comparison

Any geometric changes that may have occurred between treatment planning and treatment delivery can be quantified by evaluating the position of the implanted catheters relative to the expected planned positions. Using the spatial transformation established in the previous section, the planned catheter paths can be mapped to the measurement (FPD) space and can be directly compared with the catheter paths identified in the acquired image, as illustrated in figure 5.18.

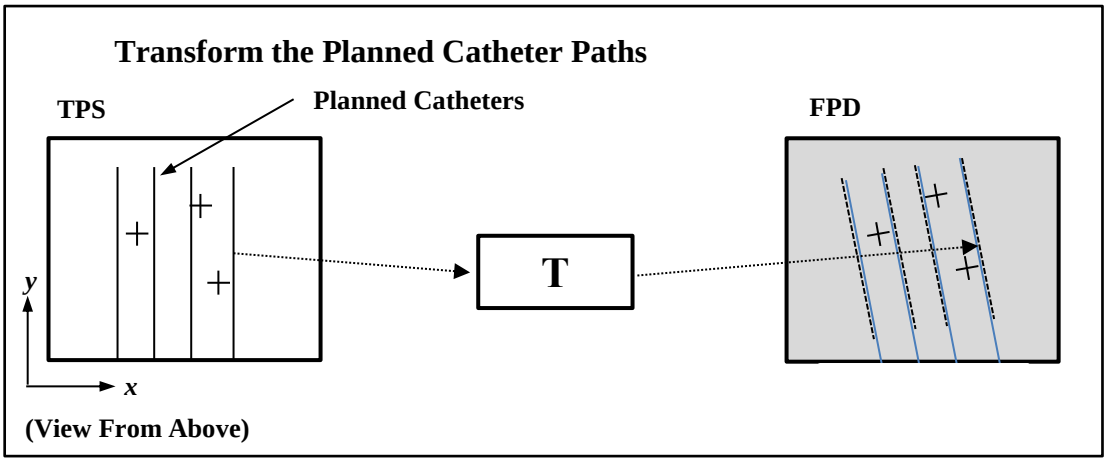

Figure 5.18. The transformation of planned catheter paths into the measurement frame of reference for direct comparison with catheter paths immediately prior to treatment.

The path of each catheter in the A-P image was identified manually by assigning the centres of the 10 mm spaced x-ray dwell position markers, using in-house software. The planned catheter paths, previously exported from the TPS (section 5.2), were transformed to the measurement (FPD) frame of reference, and overlayed on the acquired A-P image. This is illustrated in figure 5.19 for the 5 mm shift dataset, showing the identified catheter marker positions in red and the transformed planned catheter points overlayed on the A-P image in white.

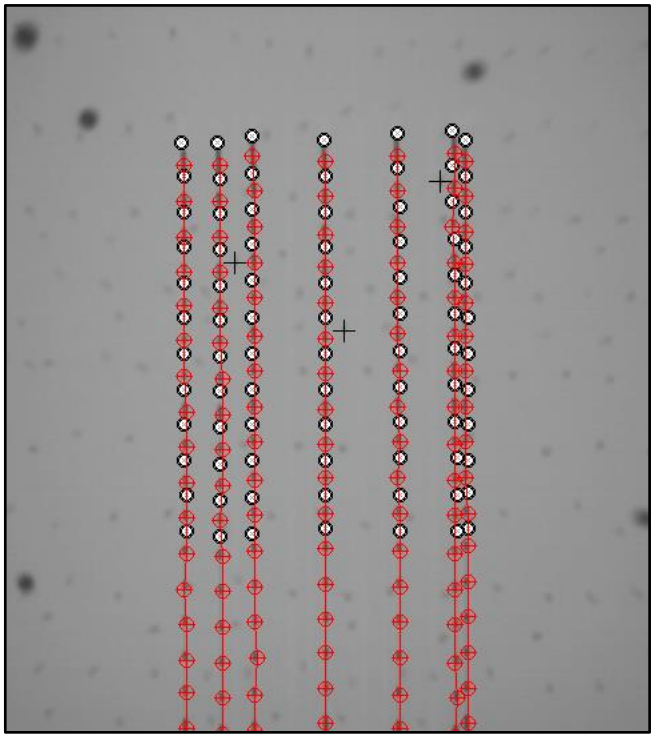

Figure 5.19. The measured (red crosses) and planned (white dots) catheter paths overlayed on the pre-treatment A-P image. A shift of 5mm was applied to the catheter dwell position markers to simulate catheter displacement.

The agreement between planned and measured catheters positions was determined by evaluating the difference between each individual catheter marker point. The quantified differences observed are reported in several ways:

- The mean *x* and *y* (vector) difference for all catheter marker points calculated in the image.
- The mean absolute (scalar) difference for all catheter marker points calculated in the image.
- The maximum mean absolute (scalar) catheter difference. This quantity is determined by calculating the mean absolute difference for each catheter. The maximum value across all calculated catheters is then reported.
- A graphical representation of the absolute difference of catheter marker points per catheter

The mean *x* and *y* differences report the directional implant changes that have occurred between the planning and treatment. The absolute differences reported represent the

overall implant changes from the plan. The maximum absolute catheter difference reports the greatest absolute deviation by a single catheter in the implant.

The reported catheter agreement quantities described are shown in table 5.5 for the measurements performed on the solid water phantom, including the shifted catheter sets and the phantom rotation.

Table 5.5. The mean directional differences between all planned and measured catheter marker points (*x* and *y*), the mean absolute difference and the maximum mean catheter difference. The values in the brackets represent one standard deviation.

Dataset	**x (σ_x) mm**	**y (σ_y) mm**	**Abs. (σ_{abs}) mm**	**Max. Catheter mm**
Initial	-0.5 (0.4)	0.2 (0.6)	0.9 (0.4)	1.3
Repeat 1	0.0 (0.4)	0.2 (0.5)	0.6 (0.3)	0.9
Repeat 2	0.0 (0.5)	0.4 (0.6)	0.8 (0.3)	1.1
2 mm Shift	-0.4 (0.5)	2.3 (0.5)	2.4 (0.5)	2.9
3 mm Shift	-0.2 (0.4)	3.2 (0.5)	3.3 (0.5)	3.8
5 mm Shift	0.1 (0.4)	5.3 (0.6)	5.3 (0.6)	6.1
10 mm Shift	0.2 (0.4)	9.8 (0.5)	9.9 (0.5)	10.6
10.0° Yaw	0.0 (0.4)	0.2 (0.4)	0.5 (0.3)	1.1
0.0° Tilt	-0.1 (0.4)	-0.1 (0.5)	0.6 (0.3)	0.9
1.9° Tilt	-0.3 (0.3)	0.3 (0.5)	0.6 (0.3)	1.1
3.8° Tilt	-0.1 (0.6)	0.5 (0.8)	1.0 (0.5)	1.5
5.7° Tilt	-0.7 (0.9)	0.8 (1.2)	1.6 (0.9)	2.5

The datasets with simulated inferior catheter displacement were correctly identified to within ±0.5 mm in the S-I direction. The rotation datasets have larger reconstruction uncertainty and therefore show a greater average marker disagreement.

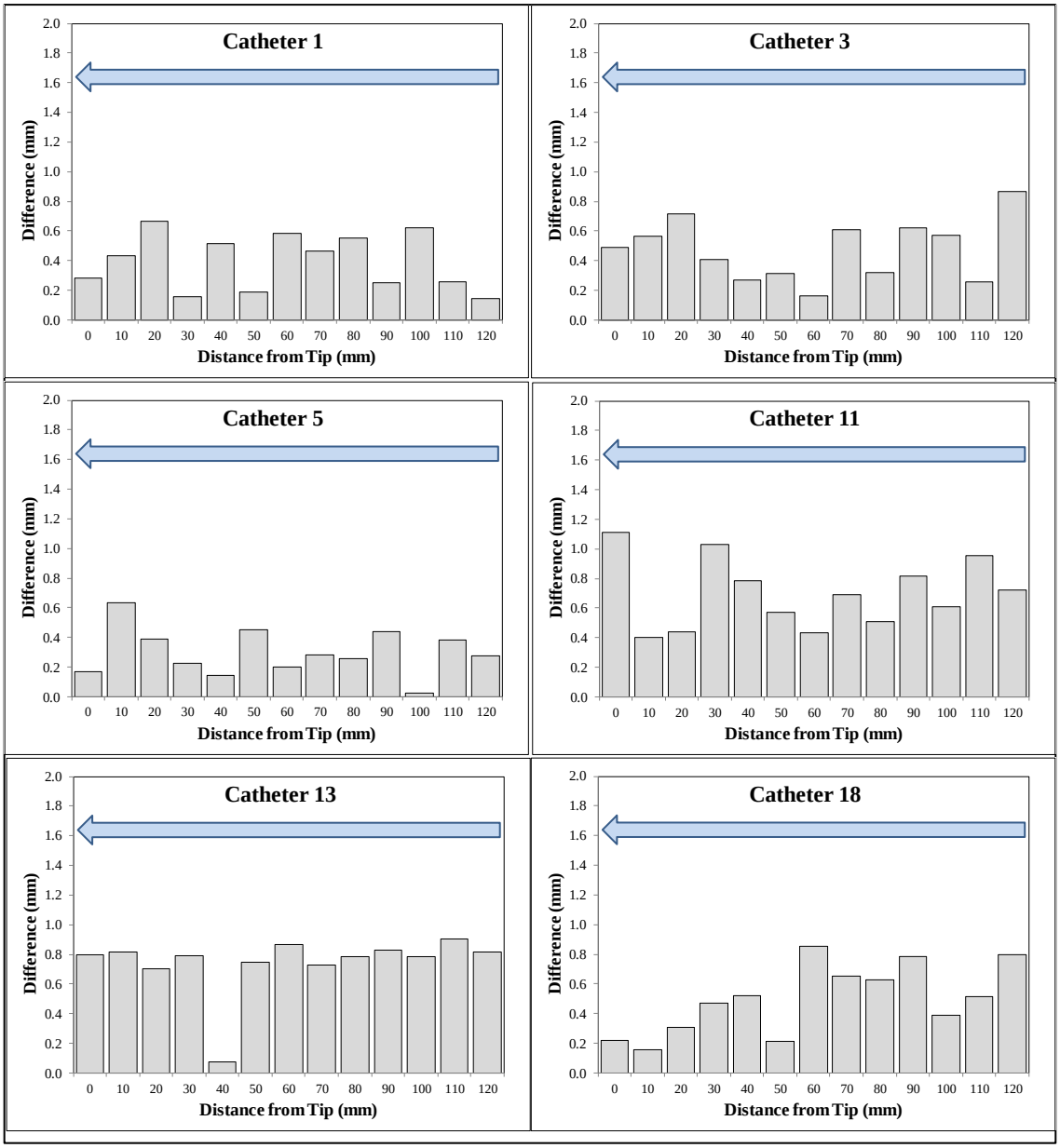

Figure 5.20. The absolute catheter marker difference for the Yaw 10.0 dataset showing the difference at each 10 mm spaced catheter marker point from the catheter tip for all 6 catheters used. The arrow represents the orientation of the catheter tip to connector end.

The absolute marker difference was calculated along each catheter and these are displayed from the catheter tip for each 10 mm spaced marker point, as shown in figure 5.20. This measure can be used to identify individual catheter displacement or highlight differences along the length of the catheter. Note that when prostate catheters are inserted into the bladder, the agreement at the catheter tip may be poor, while still

potentially having acceptable agreement near the PTV. Thus it can be useful to have access to this analysis along the length of the catheters.

5.3.6 Measurement Uncertainty

The measurement uncertainties for performing 2D pre-treatment image verification are; the divergence correction uncertainty applied to correct the A-P image, the TPS and measurement space registration uncertainties, the uncertainty of identifying catheter marker points in the A-P image, and the uncertainty of identifying marker points in the TPS (CT) image data.

The divergence correction uncertainty, $\Delta_{DivCorr}$, for the circular BB array, as described in section 5.3.2, demonstrates a small dependence with off axis marker distance, a. The divergence correction uncertainty does vary as a function of marker height above the FPD, h_m, and this is illustrated in figure 5.12.

The average registration uncertainty for the 7 datasets in table 5.3 is 0.4 mm, and represents the geometric uncertainty of a TPS catheter marker point transformed into the measurement space for comparison. Equation 5.1 indicates that the registration uncertainty, $\Delta_{Reg.2D}$, can be reduced by increasing the number of fiducial markers participating in the registration process.

The catheter marker point identification uncertainty, $\Delta_{APMarker}$, when the catheter marker point is localised in the A-P image, is defined as ±1 pixel (±0.784 mm).

The TPS imaging uncertainty, Δ_{TPS}, in localising a marker point, in the S-I direction, is due to the finite CT slice thickness (2.5 mm), and can be expressed as a measurement uncertainty of ±1.25 mm to account for partial volume effects.

The total 2D pre-treatment imaging measurement uncertainty presented in figure 5.21, is calculated by summing the above components in quadrature as shown by equation 5.2.

$$\Delta_{Total.2D} = \sqrt{{\Delta_{DivCorr}}^2 + {\Delta_{Reg.2D}}^2 + {\Delta_{APMarker}}^2 + {\Delta_{TPS}}^2} \qquad \text{Eqn. (5.2)}$$

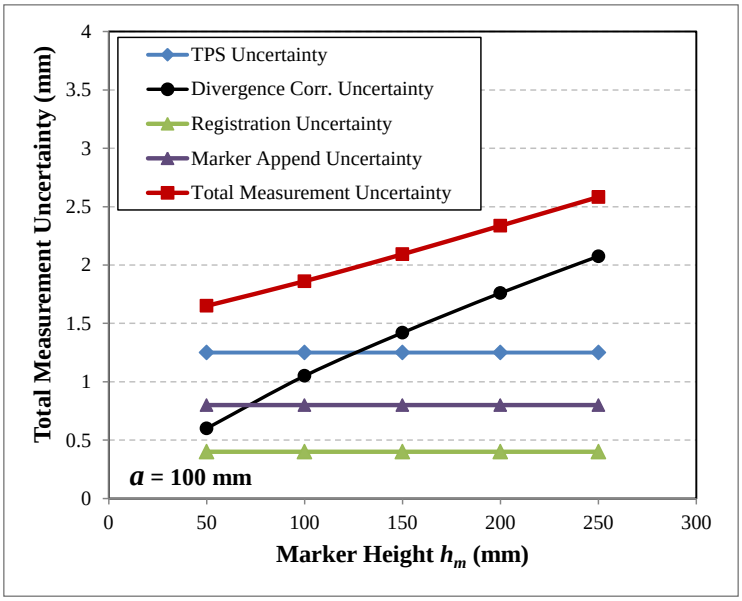

Figure 5.21. The total measurement uncertainty as a function of marker height, h_m, above the FPD, showing the TPS imaging uncertainty in localising a marker point, the divergence correction uncertainty (for a = 100 mm) and the registration uncertainty.

The total measurement uncertainty for catheter path comparison defines the catheter displacement detection threshold, which is the capacity of the verification imaging system to detect a difference in measured catheter marker position from the planned position, and is described in the next section.

5.3.7 Catheter Displacement Detection

The sensitivity to catheter displacement in the S-I direction was determined for this 2D pre-treatment imaging approach. A catheter displacement detection threshold (D_t) was defined as the minimum magnitude a measured and planned catheter point (transformed into measurement space) are required to differ by, before it can be considered a 'true' displacement and not unlikely to be simply due to the measurement uncertainty. The measurement uncertainties described in section 5.3.6 are combined to calculate the D_t, as a function of marker height h_m, for an imaging geometry with a FID of 1000 mm and using the circular BB array.

To illustrate the D_t dependence on the height of the marker h_m, D_t is shown in figure 5.22 as a function of registration uncertainty for marker heights of 50, 100, 150, 200 and 250 mm. This figure combines the total measurement uncertainties present in the pre-treatment verification imaging process to determine a catheter displacement detection threshold for any given registration uncertainty reported.

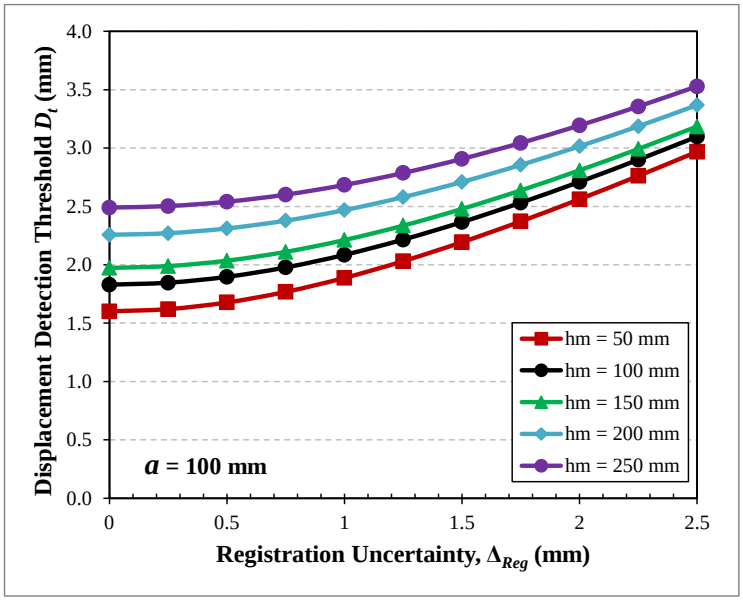

Figure 5.22. The catheter displacement detection threshold, D_t, as a function of registration uncertainty, for a marker height, h_m, above the FPD for 50, 100, 150, 200 and 250 mm, for a marker off axis distance, a, of 100 mm.

When applied clinically, it is expected that the registration uncertainty, $\Delta_{Reg.2D}$, will be greater than the value measured for these phantom studies, due to patient internal organ movements. The increased registration uncertainty only slightly increases the D_t. For example, a registration uncertainty of 0.4 mm will produce a D_t of 1.7 mm for a catheter marker height of 100 mm above the FPD. For a relatively poor registration, $\Delta_{Reg.2D}$ of 1.0 mm, the D_t is 2.0 mm, which is still clinically useful.

5.3.8 2D Pre-Treatment Imaging Conclusion

Pre-treatment image verification, using an A-P image acquired with the FPD, provides a method to verify the implant geometry relative to the anatomy. With knowledge of the imaging geometry, as defined by the BB array, the divergence present in the A-P

image can be corrected. Improving the BB array design for this application allowed the divergence correction uncertainty to be reduced from ±2.8 mm to ±1.7 mm for a marker point 200 mm from the FPD imaging plane and 50 mm off axis. The new circular BB design calculates a more reproducible x-ray central axis position when compared to the classic square BB array.

The 2D registration between the TPS and the measurements space is reproducible, with an average registration uncertainty of 0.4 ±0.1 mm for 7 datasets. When rotation of the phantom is applied (simulating patient pelvic rotation), the 2D registration uncertainty increases for large rotations and the catheter agreement degrades.

With this 2D pre-treatment verification approach, a registration uncertainty of 0.4 mm can identify a catheter displacement of 1.7 mm for a marker 100 mm above the FPD. This detection capability is sensitive enough to identify clinically relevant catheter displacements.

The following section extends the pre-treatment imaging capability from 2D to 3D, using the same FPD, by applying a shift image approach to reconstruct the brachytherapy catheters in 3D.

5.4 Extension to 3D Pre-Treatment Imaging

A HDR brachytherapy implant has the potential for displacement in all three dimensions after treatment planning imaging. To completely evaluate possible changes of the catheter positions (relative to the surrounding anatomy) volumetric imaging is necessary, in the treatment bunker, immediately before treatment delivery. This section of chapter 5 presents a more comprehensive imaging technique that enables direct comparison of the pre-treatment implant geometry with the treatment plan in 3D.

The 3D pre-treatment imaging approach presented follows the subsequent steps:

- Capture two shift images of the implant using the FPD
- Use a back projection approach to reconstruct the catheter paths
- Perform 3D registration with the TPS
- Compare the planned and measured catheter paths in 3D

The following sections describe in detail each of these steps, including examples using the solid water phantom defined earlier in section 5.1.

5.4.1 Shift Imaging

A shift imaging approach is performed to acquire two oblique x-ray images of the object, by moving an x-ray source above the object. The apparent shift of features between the two images, are used to reconstruct the object in 3D. The use of multiple image projections has previously been applied to the reconstruction of brachytherapy catheters, applicators[107-110] and implanted low dose rate seeds[111-114] for treatment planning purposes, but not for HDR brachytherapy pre-treatment verification, as performed in this work. In this section an approach using the flat panel detector (FPD) under the patient and an x-ray source moving laterally above the patient is described. The imaging geometry used to acquire the two shift images is illustrated in figure 5.23, showing the FPD under the brachytherapy treatment couch and the x-ray source on a ceiling-suspended rail.

Two shift images are captured with the x-ray source at position P1, and position P3 as shown in figure 5.23. The implanted marker, $P_m(x_m, y_m, z_m)$, has an apparent 'shift' of position in the two corresponding images ($P_2 \rightarrow P_4$), and with knowledge of the acquisition geometry, the 3D position of the marker can be reconstructed. The use of multiple image projections has been applied to the reconstruction of brachytherapy applicators, implanted catheters and implanted low dose rate seeds for treatment planning purposes, but not for HDR brachytherapy pre-treatment verification. This approach is novel for HDR brachytherapy, enabling reconstruction of the implant, in the treatment bunker, for comparison with the treatment plan immediately before treatment commences.

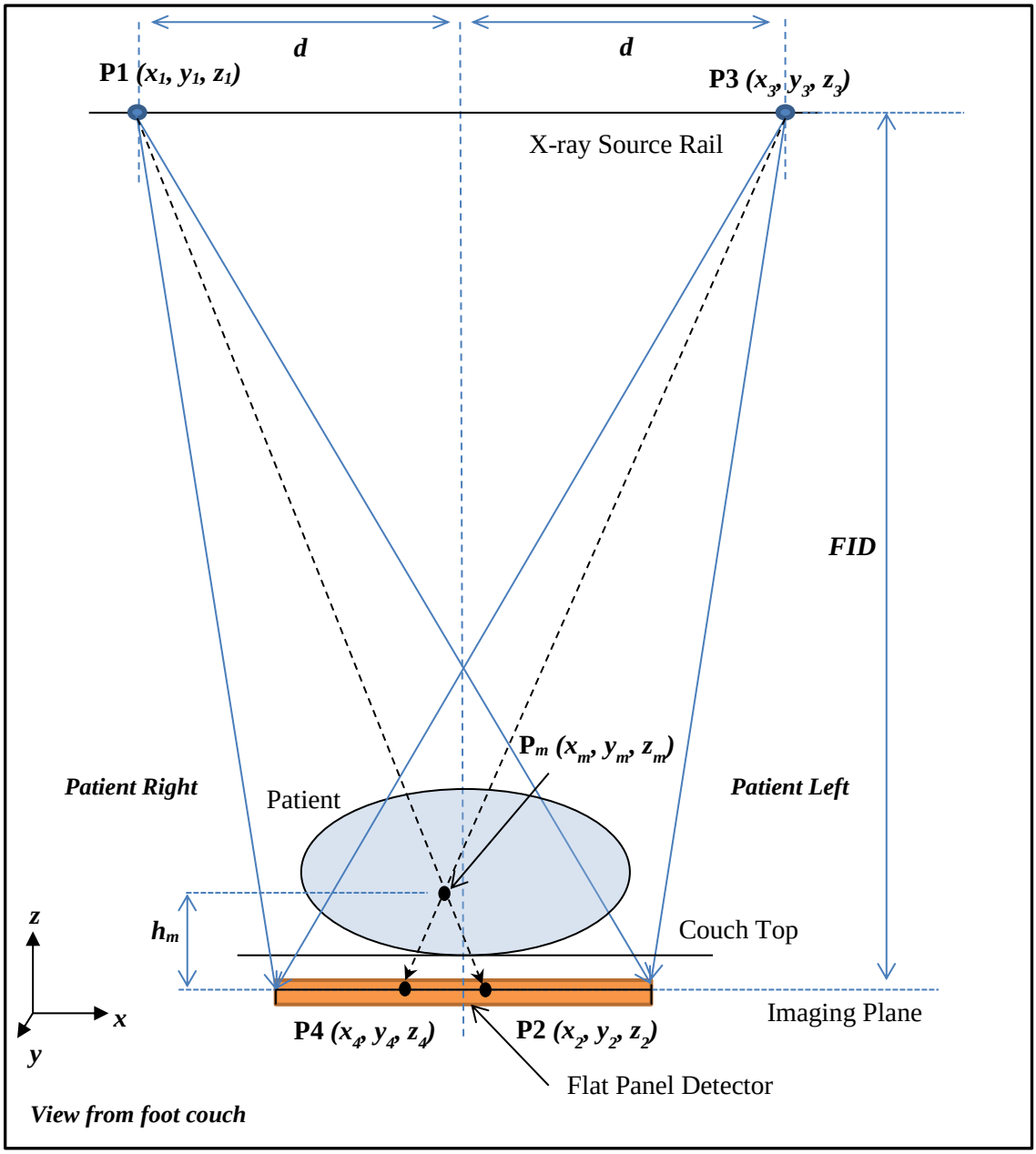

Figure 5.23. The imaging geometry to acquire the two shift images for catheter position reconstruction. The x-ray source is shifted by a distance *d*, *FID* is the focus to imaging plane distance and h_m represents the distance of a marker point above the FPD imaging plane.

5.4.2 Shift Image Reconstruction

The reconstruction of a brachytherapy catheter is achieved by identifying the path of the catheter in each of the acquired shift images. The 2D catheter path defined in each shift image is then back projected toward the position of the x-ray source, as shown in

figure 5.24, where the reconstructed 3D path of the catheter appears at the intersection of the back-projected catheter paths.

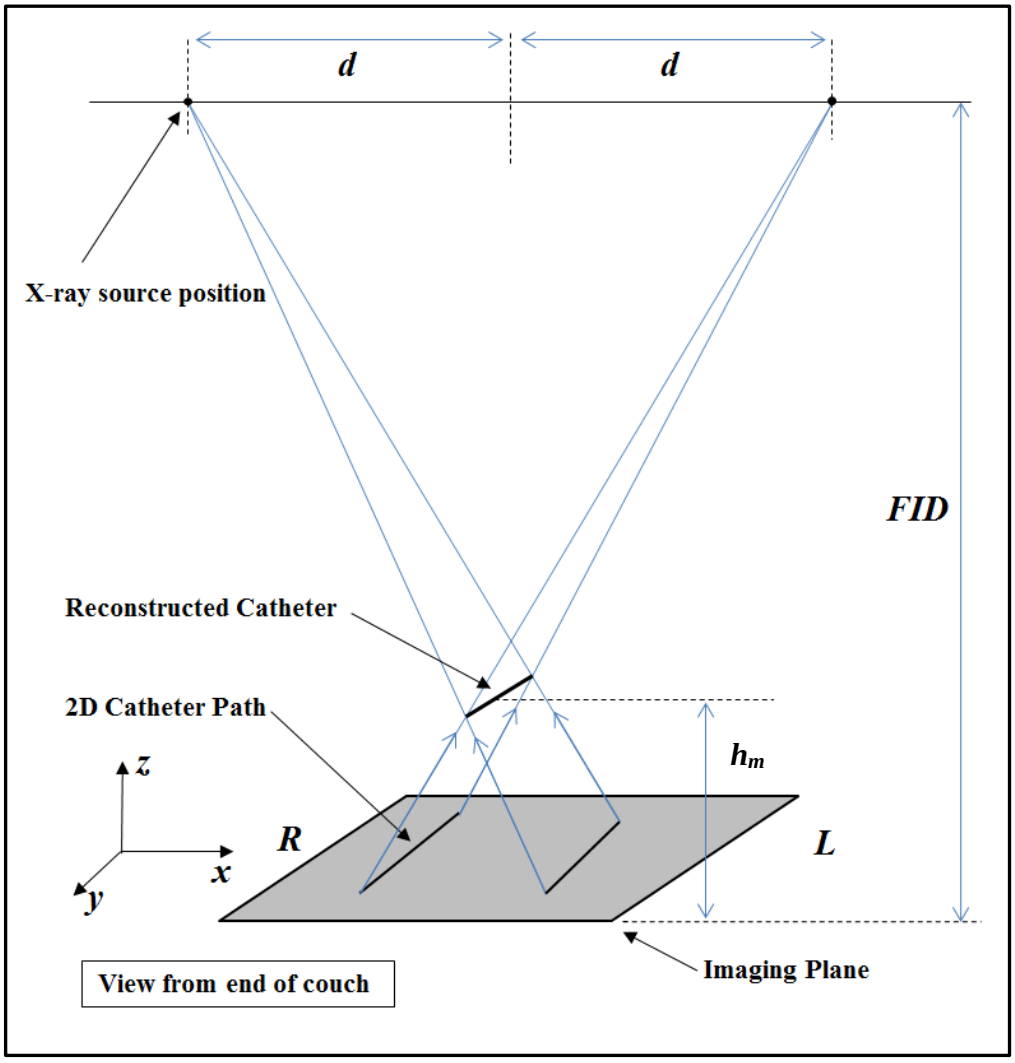

Figure 5.24. An illustration of the catheter reconstruction method showing the 2D catheter paths from each acquired image. The 2D catheter paths are back projected to the x-ray source positions, at 1000 mm above the imaging plane (FID) and shifted off-axis by a distance *d*. The path of the catheter in 3D, at a distance h_m above the imaging plane, is determined by the intersection of these back projections.

This process can be expressed mathematically by determining the point of intersection for the vectors $\overrightarrow{V_1}$ and $\overrightarrow{V_2}$ as illustrated in figure 5.25. This intersection point exists if the imaging geometry is ideal, but in reality the uncertainty associated with the localisation of the x-ray source and the position of the projected marker in the image may not guarantee that these two vectors will intersect. In 3D space it is expected the vectors

will pass close to each other, and so the mid-point of the shortest segment between them, P_m, as illustrated in figure 5.25, is used as the reconstructed position of the implanted marker.

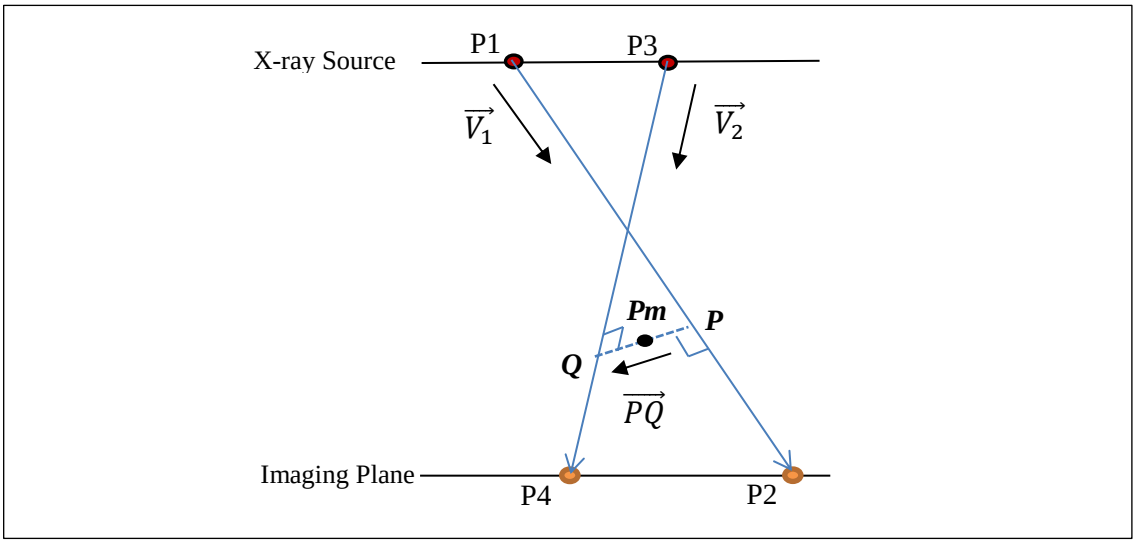

Figure 5.25. The 3D vectors $\overrightarrow{V_1}$ and $\overrightarrow{V_2}$, connecting the x-ray source to the projected point on the imaging plane. If the vectors in 3D space do not intersect due to position uncertainty, the mid-point P_m of the shortest segment between the two vectors represents the intersection point and is used as the reconstructed position of the marker.

The process to reconstruct the marker position requires knowledge of the x-ray focal spot positions, P1 and P3, and localising the projected marker positions in each image, P2 and P4. To determine the reconstructed marker position, P_m, the following process is followed:

The two projection vectors are defined as the lines connecting P1 to P2 and P3 to P4:

$$\overrightarrow{V_1} = \overrightarrow{P12} = \begin{pmatrix} x_2 - x_1 \\ y_2 - y_1 \\ z_2 - z_1 \end{pmatrix} \qquad \text{Eqn. (5.3)}$$

$$\overrightarrow{V_2} = \overrightarrow{P34} = \begin{pmatrix} x_4 - x_3 \\ y_4 - y_3 \\ z_4 - z_3 \end{pmatrix} \qquad \text{Eqn. (5.4)}$$

The points that exist on each line that represent the shortest distance between the two vectors are defined as P and Q, where these points are determined by:

$$\begin{aligned} P_x &= x_1 + (x_2 - x_1)t \\ P_y &= y_1 + (y_2 - y_1)t \\ P_z &= z_1 + (z_2 - z_1)t \end{aligned} \qquad \text{Eqn. (5.5)}$$

and

$$\begin{aligned} Q_x &= x_3 + (x_4 - x_3)s \\ Q_y &= y_3 + (y_4 - y_3)s \\ Q_z &= z_3 + (z_4 - z_3)s \end{aligned} \qquad \text{Eqn. (5.6)}$$

$$\begin{aligned} P_x &= x_1 + \overrightarrow{V_{1x}}t \\ P_y &= y_1 + V_{1y}t \\ P_z &= z_1 + V_{1z}t \end{aligned} \qquad \text{Eqn. (5.7)}$$

and

$$\begin{aligned} Q_x &= x_3 + \overrightarrow{V_{2x}}s \\ Q_y &= y_3 + V_{2y}s \\ Q_z &= z_3 + V_{2z}s \end{aligned} \qquad \text{Eqn. (5.8)}$$

where *t* and *s* are scalar coefficients.

The vector $\overrightarrow{PQ}$ can then be defined as:

$$\overrightarrow{PQ} = \begin{pmatrix} Q_x - P_x \\ Q_y - P_y \\ Q_z - P_z \end{pmatrix} \qquad \text{Eqn. (5.9)}$$

The vector $\overrightarrow{PQ}$ represents the shortest distance between the vectors $\overrightarrow{V_1}$ and $\overrightarrow{V_2}$ if $\overrightarrow{PQ}$ is perpendicular to both. In the case where the vectors do intersect, the vector $\overrightarrow{PQ}$ will equal zero. To constrain $\overrightarrow{PQ}$ to be perpendicular to both, the scalar (dot) product should be zero as shown:

$$\overrightarrow{PQ} \cdot \overrightarrow{V_1} = 0 \qquad \text{Eqn. (5.10)}$$

and

$$\overrightarrow{PQ} \cdot \overrightarrow{V_2} = 0 \qquad \text{Eqn. (5.11)}$$

expanding this gives:

$$\begin{pmatrix} Q_x - P_x \\ Q_y - P_y \\ Q_z - P_z \end{pmatrix} \cdot \begin{pmatrix} x_2 - x_1 \\ y_2 - y_1 \\ z_2 - z_1 \end{pmatrix} = 0 \qquad \text{Eqn. (5.12)}$$

and

$$\begin{pmatrix} Q_x - P_x \\ Q_y - P_y \\ Q_z - P_z \end{pmatrix} \cdot \begin{pmatrix} x_4 - x_3 \\ y_4 - y_3 \\ z_4 - z_3 \end{pmatrix} = 0 \qquad \text{Eqn. (5.13)}$$

$$(Q_x - P_x)\vec{V}_{1x} + (Q_y - P_y)\vec{V}_{1y} + (Q_z - P_z)\vec{V}_{1z} = 0 \qquad \text{Eqn. (5.14)}$$

and

$$(Q_x - P_x)\vec{V}_{2x} + (Q_y - P_y)\vec{V}_{2y} + (Q_z - P_z)\vec{V}_{2z} = 0 \qquad \text{Eqn. (5.15)}$$

$$\begin{aligned}(\vec{V}_{1x}\vec{V}_{2x} + \vec{V}_{1y}\vec{V}_{2y} + \vec{V}_{1z}\vec{V}_{2z})s - \left(\vec{V}_{1x}{}^2 + \vec{V}_{1y}{}^2 + \vec{V}_{1z}{}^2\right)t \ldots \\ + \vec{V}_{1x}(x_3 - x_1) + \vec{V}_{1y}(y_3 - y_1) + \vec{V}_{1z}(z_3 - z_1) = 0\end{aligned} \qquad \text{Eqn. (5.16)}$$

and

$$\begin{aligned}\left(\vec{V}_{2x}{}^2 + \vec{V}_{2y}{}^2 + \vec{V}_{2z}{}^2\right)s - (\vec{V}_{1x}\vec{V}_{2x} + \vec{V}_{1y}\vec{V}_{2y} + \vec{V}_{1z}\vec{V}_{2z})t \ldots \\ + \vec{V}_{2x}(x_3 - x_1) + \vec{V}_{2y}(y_3 - y_1) + \vec{V}_{2z}(z_3 - z_1) = 0\end{aligned} \qquad \text{Eqn. (5.17)}$$

Equations 5.16 and 5.17 are simultaneous equations and solving for the parameters *s* and *t* will allow the position of point *P* and *Q* to be determined.

These simultaneous equations can be expressed in matrix notation as:

$$\begin{bmatrix} a & b \\ c & d \end{bmatrix} \begin{bmatrix} s \\ t \end{bmatrix} = \begin{bmatrix} e \\ f \end{bmatrix} \qquad \text{Eqn. (5.18)}$$

where from Eqn. 5.16 and Eqn. 5.17

$$\begin{aligned} a &= (\vec{V}_{1x}\vec{V}_{2x} + \vec{V}_{1y}\vec{V}_{2y} + \vec{V}_{1z}\vec{V}_{2z}) \\ b &= -\left(\vec{V}_{1x}{}^2 + \vec{V}_{1y}{}^2 + \vec{V}_{1z}{}^2\right) \\ e &= -(\vec{V}_{1x}(x_3 - x_1) + \vec{V}_{1y}(y_3 - y_1) + \vec{V}_{1z}(z_3 - z_1)) \end{aligned} \qquad \text{Eqn. (5.19)}$$

and

$$\begin{aligned} c &= \left(\vec{V}_{2x}{}^2 + \vec{V}_{2y}{}^2 + \vec{V}_{2z}{}^2\right) \\ d &= -\left(\vec{V}_{1x}\vec{V}_{2x} + \vec{V}_{1y}\vec{V}_{2y} + \vec{V}_{1z}\vec{V}_{2z}\right) \\ f &= -(\vec{V}_{2x}(x_3 - x_1) + \vec{V}_{2y}(y_3 - y_1) + \vec{V}_{2z}(z_3 - z_1)) \end{aligned} \qquad \text{Eqn. (5.20)}$$

Solving for *s* and *t* using an inverse matrix approach is:

$$AX = B \qquad \text{Eqn. (5.21)}$$

$$X = A^{-1}B \qquad \text{Eqn. (5.22)}$$

$$\begin{bmatrix} s \\ t \end{bmatrix} = \frac{1}{k}\begin{bmatrix} d.e - (b.f) \\ -(c.e) + (a.f) \end{bmatrix} \qquad \text{Eqn. (5.23)}$$

where

$$k = \left[\frac{1}{ad - bc}\right] \qquad \text{Eqn. (5.24)}$$

and so the parameters *s* and *t* are:

$$s = \frac{1}{k}[d.e - (b.f)] \qquad \text{Eqn. (5.25)}$$

and

$$t = \frac{1}{k}[-(c.e) + (a.f)] \qquad \text{Eqn. (5.26)}$$

inserting *s* and *t* into Eqn. 5.7 and Eqn. 5.8 gives the coordinate of points *P* and *Q*. The position of the reconstructed marker, P_m, is the mid-point between points *P* and *Q* which is determined by:

$$\begin{aligned} P_{mx} &= \frac{(P_x + Q_x)}{2} \\ P_{my} &= \frac{(P_y + Q_y)}{2} \\ P_{mz} &= \frac{(P_z + Q_z)}{2} \end{aligned} \qquad \text{Eqn. (5.27)}$$

The reconstruction procedure described is applied practically by using in-house software that allows corresponding catheter marker points in each image to be assigned,

an example of this is shown in figure 5.26. The back projection reconstruction is then performed for each pair of marker points and the 3D position of the reconstructed marker P_m is determined.

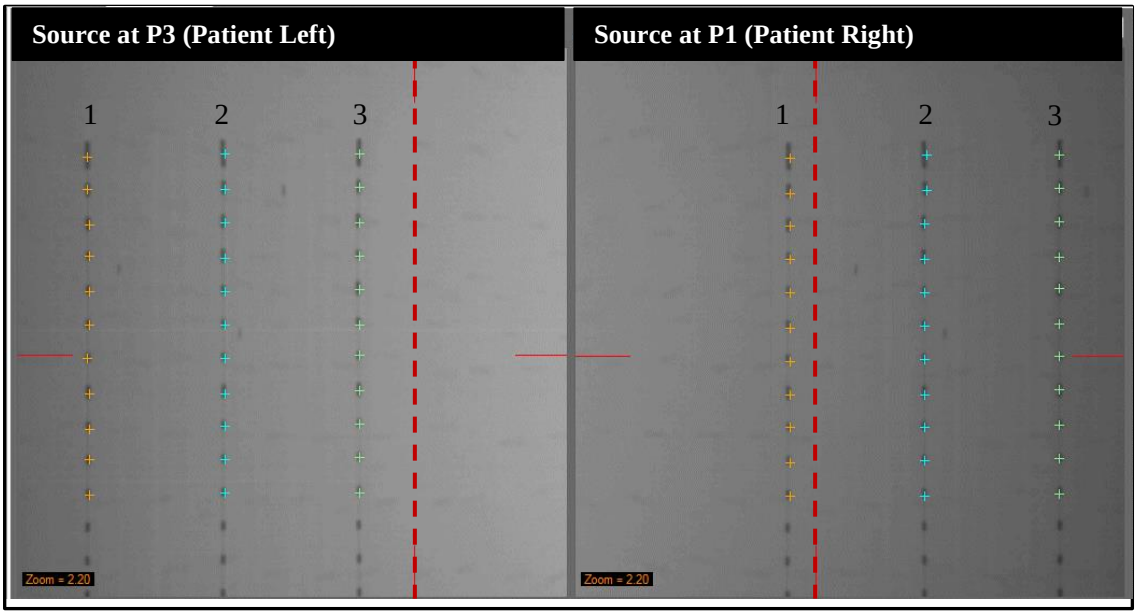

Figure 5.26. An example of assigning corresponding catheter marker points to define the catheter path in each shift image. The apparent shift of each catheter can be seen relative to the central axis reference, shown as the red dashed line.

To demonstrate the shift image reconstruction process, images were acquired of the solid water phantom (described in section 5.1), with catheter markers inserted into catheters 1, 3, 5, 6, 11, 13 and 18. The images were acquired using the imaging geometry defined in figure 5.23, with a FID = 1000 mm and a d = 400 mm and an example of the acquired shift images is shown in figure 5.27. To illustrate the reproducibility of the reconstruction process, the phantom was placed on the treatment couch two more times and shift images acquired at each instance.

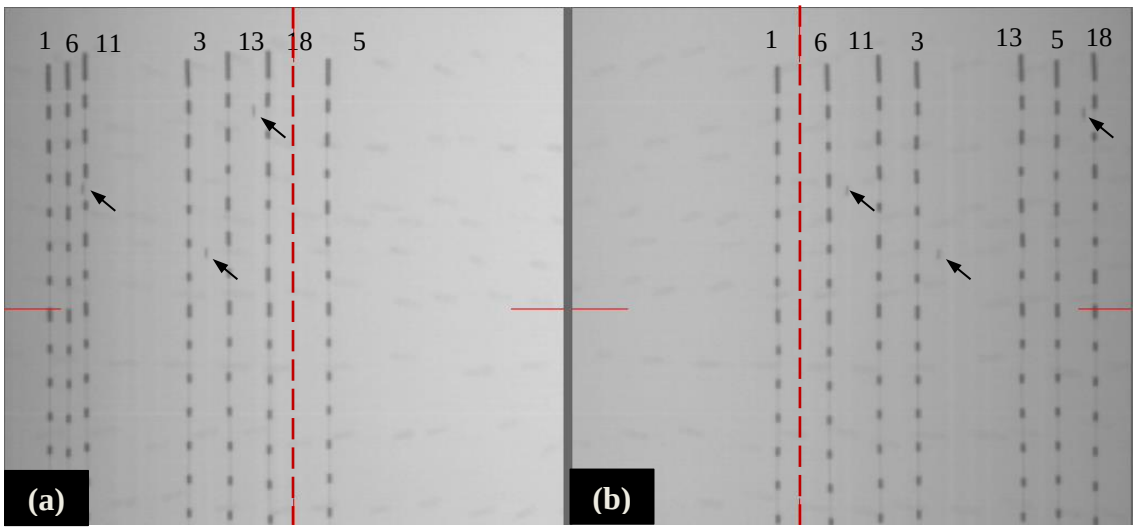

Figure 5.27. The two shift images acquired with the x-ray source shifted to the patient left (a) and then shifted to the patient right (b). The x-ray central axis is shown as the red dashed line. The corresponding fiducial markers in the phantom are highlighted by the black arrows. The dwell position markers for each catheter are identified in each shift image to define the 2D path of the catheter. The catheter numbers (labelled) are identified by the coded sequence of dots and dashes.

For the three acquisitions, the catheter paths were reconstructed in 3D using the back projection method described. To verify the geometric quality of the reconstruction result (not introducing systematic distortions), the agreement between reconstructed and known (model) catheter marker positions was determined for all catheter marker points in the implant. To determine the reproducibility of the shift image reconstruction method, the solid water phantom was re-positioned on the treatment couch 2 additional times, and the 3D reconstruction was repeated.

The differences for the initial and repeat datasets are shown in table 5.6, where the mean absolute error of 0.8 mm (s.d. 0.4 mm), and featured a 3D root mean square error (RMSE3D) of 0.9 mm. This is the radius of the sphere centred at the true position, containing the reconstructed point with a probability of 68%. This was calculated using 13 catheter marker positions, in each of 7 catheters and 3 repetitions (n=273 marker points). This is a measure of the implant reconstruction integrity achievable in the control case where there are no changes to the implant geometry i.e. the relative positions of all markers and catheters.

Table 5.6. The reported absolute and RMSE difference between the reconstructed and known catheter marker positions to verify the geometric integrity of the reconstruction process. The bracket values represent 1 standard deviation.

Dataset	Absolute Error (mm)	$RMSE_{3D}$ (mm)
Initial (n= 91)	0.9 (0.4)	0.9
Repeat 1 (n=91)	0.8 (0.3)	0.9
Repeat 2 (n= 91)	0.8 (0.4)	0.9
Mean	0.8	0.9

5.4.3 Shift Image Reconstruction Field of View

The application of shift imaging for reconstruction requires that the brachytherapy implant be captured in both images. Corresponding features are then identified in each image and reconstructed as described in the previous section. The size of the implant that can be reconstructed depends on the imaging geometry and detector size used. This section characterises the size of a brachytherapy implant that can be reconstructed using this shift image method, for FPD widths, D_w, and for a range of x-ray shift distances, d.

To quantify the size of a brachytherapy implant that can be captured, an imaging field of view width parameter, FOV_w, was defined, and is illustrated in figure 5.28. The FOV_w, is defined as the imaging field width at a height of 150 mm above the FPD imaging plane for an x-ray shift distance, d, and a detector width, D_w. The parameter is defined at a height of 150 mm which represents an approximate distance from the FPD imaging plane to a distal source dwell position in a typical prostate implant.

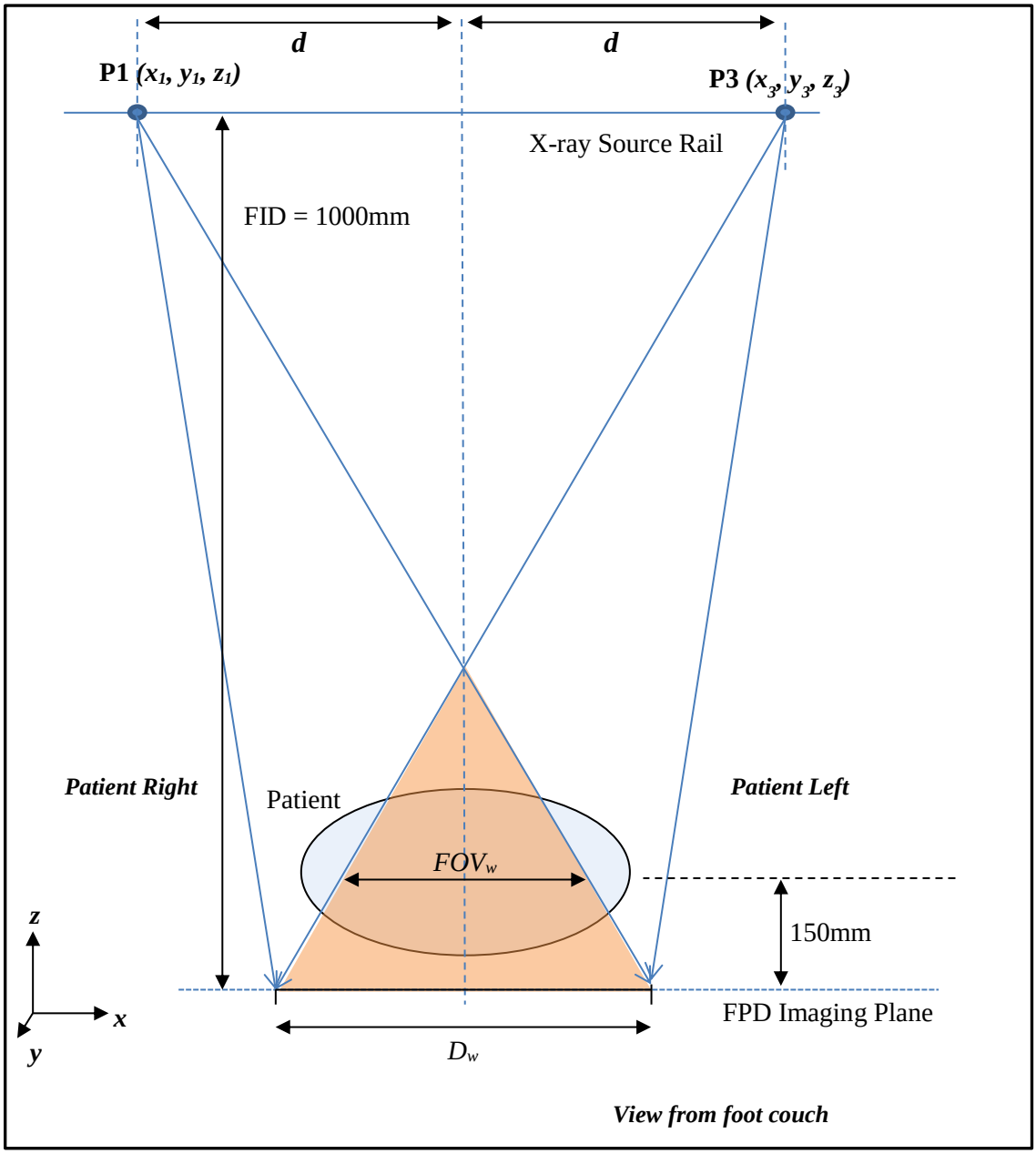

Figure 5.28. An illustration showing the shift image area (orange region) achieved with an x-ray source shift distance *d*, focus imager distance *FID* =1000 mm and with a detector width, D_w. The imaging field of view parameter, FOV_w, is defined as the imaging field width at a height of 150 mm above the FPD imaging plane.

The FOV_w was evaluated over a range of x-ray source shift distances, *d*, for a detector width, D_w, of 400, 300 and 200 mm. It can be seen in figure 5.29 the FOV_w increases as the x-ray shift distance *d* decreases, for all detector widths. A smaller x-ray shift, *d*,

may provide a greater imaging FOV_w, but the trade-off is an increased reconstruction uncertainty in the *x* axis (patient L-R direction), as described later in section 5.3.4.

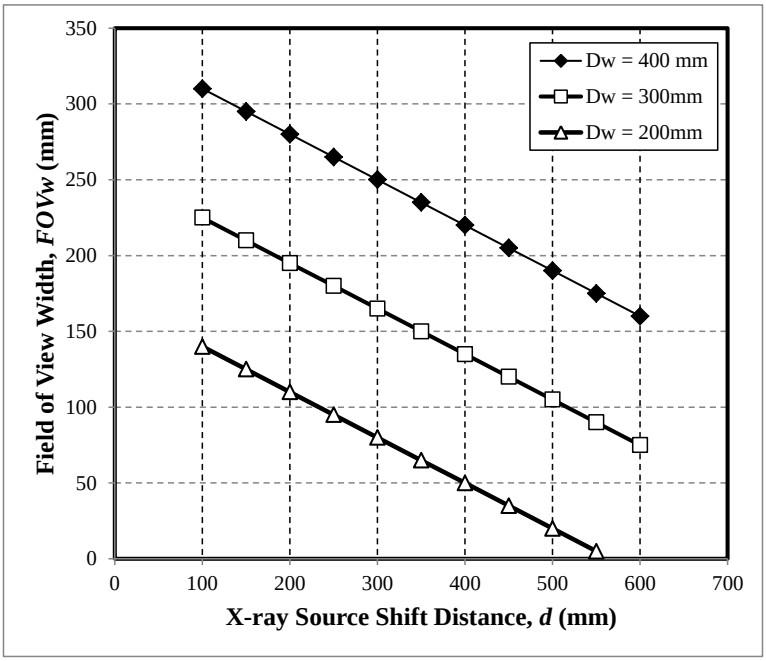

Figure 5.29. Imaging field of view width w at 150mm above the treatment couch as the x-ray source shift is increased. The height of 150mm above the couch is typical of catheter positions implanted in a patient and the width w represents an available view to include the entire template. Smaller shifts *d* produce greater field of view but as seen later increase the reconstruction uncertainty.

The FOV_w is expressed as a function of D_w, d, h_m and FID in equation 5.26.

$$FOV_w = D_w - \frac{h_m D_w}{FID} - \frac{2h_m d}{FID} \qquad \text{Eqn. (5.26)}$$

The expression can be used to define the applied imaging geometry based on the available FPD width.

5.4.4 3D Registration with TPS

The measurement (FPD) space and the planning (TPS) space have distinct frames of reference. A registration between the two is required to compare the planned catheter paths with the measured catheter paths immediately prior to treatment. The registration applied in this work is a rigid registration using corresponding landmark points that can

be identified in each space. In this application fiducial markers implanted into the prostate, visible in both imaging sets, are used as the registration landmark points. The fiducial markers are routinely implanted into the prostate for EBRT treatment position verification and were not specifically included for this exercise.

The registration algorithm used in this work follows the method described by Arun *et al*[106], and performs a non-iterative least squares based rigid registration between corresponding pairs of landmark points, producing a geometric transformation between the two frames of reference.

The goal of pre-treatment verification imaging is to evaluate possible displacement of the implant from the intended (planned) position, relative to the surrounding anatomy, immediately prior to treatment. It is therefore practical to visualise the planned catheter positions in the measurement (FPD) frame of reference, as the patient is in treatment delivery position awaiting confirmation.

In terms of the registration algorithm, the reference geometry (static) will be the FPD space and the registration process will transform the TPS geometry to the FPD frame of reference. This transformation is given by

$$P_{FPD_i} = R.P_{TPS_i} + T \qquad \text{Eqn. (5.27)}$$

where P_{FPD_i} and P_{TPS_i} are 3x1 column matrices representing the (*x*,*y*,*z*) coordinates of each corresponding pairs of fiducial points *i*, *R* is the 3x3 rotation matrix and *T* is the 3x1 translation matrix.

A non-iterative least squares fitting method of the two data sets is performed, based on a singular value decomposition of a 3x3 matrix, which aims to find *R* and *T* to minimise the difference between the data sets as described by

$$E^2 = \sum_{i=1}^{n} \left\| P_{FPD_i} - \left(P_{TPS_i} + T\right) \right\|^2 \qquad \text{Eqn. (5.28)}$$

where *E* can be used as measure of the match between the data sets.

The resulting rotation matrix is a 3x3 matrix in the form:

$$R = \begin{bmatrix} r_{11} & r_{12} & r_{13} \\ r_{21} & r_{22} & r_{23} \\ r_{31} & r_{32} & r_{33} \end{bmatrix} \quad \text{Eqn. (5.29)}$$

Decomposing the rotation matrix into the three components gives:

$$R = ZYX \quad \text{Eqn. (5.30)}$$

where

$$X = \begin{bmatrix} 1 & 0 & 0 \\ 0 & \cos(\theta_x) & -\sin(\theta_x) \\ 0 & \sin(\theta_x) & \cos(\theta_x) \end{bmatrix} \quad \text{Eqn. (5.31)}$$

and

$$Y = \begin{bmatrix} \cos(\theta_y) & 0 & \sin(\theta_y) \\ 0 & 1 & 0 \\ -\sin(\theta_y) & 0 & \cos(\theta_y) \end{bmatrix} \quad \text{Eqn. (5.32)}$$

and

$$Z = \begin{bmatrix} \cos(\theta_z) & -\sin(\theta_z) & 0 \\ \sin(\theta_z) & \cos(\theta_z) & 0 \\ 0 & 0 & 1 \end{bmatrix} \quad \text{Eqn. (5.33)}$$

The three Euler rotations can then be calculated by

$$\theta_x = \tan^{-1}(r_{32}.r_{33}) \quad \text{Eqn. (5.34)}$$

$$\theta_y = \tan^{-1}\left(-r_{31}.\sqrt{r_{32}^2 \times r_{33}^2}\right) \quad \text{Eqn. (5.35)}$$

$$\theta_z = \tan^{-1}(r_{21}.r_{11}) \quad \text{Eqn. (5.36)}$$

These Euler rotations can be used to describe the movements applied between treatment imaging and treatment delivery. This result may be useful for reporting possible internal rotation of the implant that may be clinically relevant. The orientation of the reported rotations is depicted in figure 5.30.

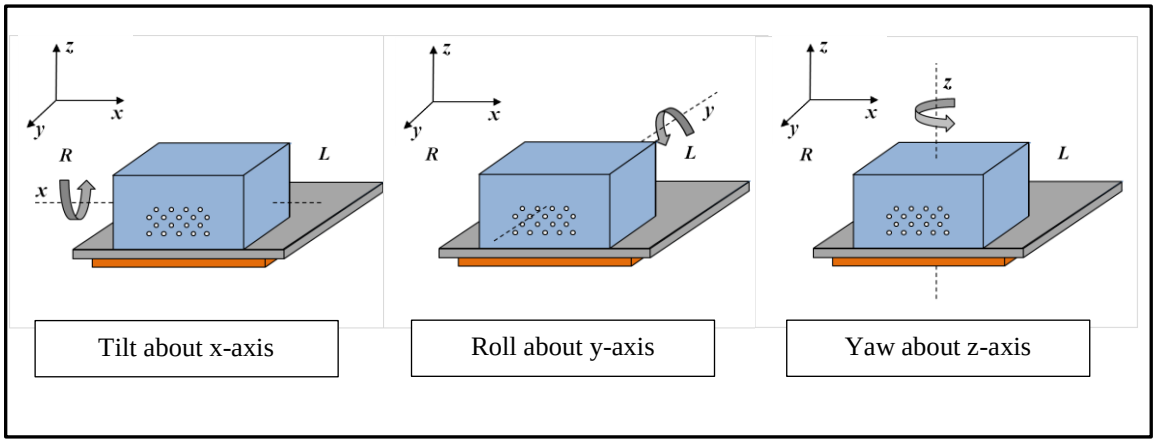

Figure 5.30. An illustration defining the orientation and direction of the reported rotations (tilt, roll, yaw) from the registration process.

The registration process reports a registration residual value, *E*, defined by equation 5.27. The residual value reports a measure of the registration quality, for all corresponding fiducial marker pairs participating in the registration. This is a poor metric for comparing registration quality across data sets as the value increases with the number of fiducials used in the process.

The registration uncertainty ($\Delta_{Reg.3D}$) represents the uncertainty of the geometric transformation between the two spaces (TPS and measurement), and is derived from the reported registration residual as shown in equation 5.37:

$$\Delta_{Reg.3D} = \sqrt{\frac{E}{n}} \qquad \text{Eqn (5.37)}$$

where *n* is the number of fiducial marker pairs participating in the registration. $\Delta_{Reg.3D}$ may be interpreted as the square-weighted average residual error per marker, and is an indicator of the consequential error likely to be observed in other points under the same transformation. The registration uncertainty contributes to the total measurement uncertainty and is therefore later included in the evaluation of catheter displacement detection.

The three sets of shift image reconstructions performed on the phantom in section 5.4.2 was registered with the TPS data using the three sets of corresponding fiducial markers.

The reported residual, registration uncertainty and the reported rotations for the three datasets are shown in table 5.7.

Table 5.7. The reported residual, registration uncertainty and the reported rotation after registration between the TPS data and reconstructed fiducial markers for the three datasets.

Dataset	Residual (mm)	$\Delta_{Reg.3D}$ (mm)	Tilt x-axis (°)	Roll y-axis (°)	Yaw z-axis (°)
Initial	0.9	0.6	0.6	-0.5	-0.1
Repeat 1	0.6	0.5	-0.6	-0.9	0.1
Repeat 2	1.1	0.6	0.6	-0.6	0.3

5.4.5 Reconstruction and Registration Robustness

To evaluate the robustness of the 3D reconstruction and registration process, in the presence of possible patient setup variations, a pelvic rotation of the patient was simulated by elevating the inferior edge of the solid water phantom. Clinically this would represent the difference in pelvic tilt at CT (legs down), compared with legs elevated (lithotomy position) at treatment. The inferior edge of the phantom was elevated by 10, 20 and 30 mm producing phantom tilt (about *x*-axis) of 1.9°, 3.8° and 5.7° respectively. Images were captured at each rotational tilt position using the shift image acquisition method described, reconstruction was performed, and registration with the TPS was achieved.

The agreement between reconstructed and known (model) catheter marker positions was determined for all catheter marker points in the implant, to verify the geometric quality of the reconstruction result, and the results for the three rotation datasets are shown in table 5.8.

Table 5.8. The reported difference (and S.D.) between the reconstructed and known catheter marker positions for the 3 rotation datasets to verify the geometric integrity of the reconstruction process.

Dataset	Absolute Error (mm)	$RMSE_{3D}$ (mm)
1.9° rotation	0.7 (0.3)	0.7
3.8° rotation	0.6 (0.3)	0.7
5.7° rotation	0.6 (0.2)	0.7

The residual, registration uncertainty and reported rotations is shown in table 5.9 for the three rotation datasets. The derived transformation matrix provided a measure of rotations which was then compared to the known applied rotations. The rotations reported by the registration algorithm were 1.0°, 3.9° and 5.5° for the 1.9°, 3.8° and 5.7° applied rotations respectively.

Table 5.9. The measured residual, registration uncertainty and the reported rotation after registration between the TPS data and reconstructed fiducial markers for three datasets.

Dataset	Residual (mm)	Δ_{Reg} (mm)	Tilt x-axis (°)	Roll y-axis (°)	Yaw z-axis (°)
1.9° rotation	0.3	0.3	1.0	-0.3	0.2
3.8° rotation	0.9	0.5	3.9	0.6	0.7
5.7° rotation	0.3	0.3	5.5	-1.0	0.1

5.4.6 Measurement Uncertainty Analysis

The total measurement uncertainty has three sources, the 3D marker reconstruction uncertainty, the registration uncertainty, and the TPS marker identification uncertainty. The following sections describe each measurement uncertainty and how it contributes to the overall measurement uncertainty budget.

5.4.6.1 Reconstruction Uncertainty

The 3D reconstruction uncertainty of the fiducial markers will influence the quality of registration between the planned and measurement space, and therefore will also influence the agreement between the measured and planned catheter paths. An analysis was performed to establish the 3D reconstruction uncertainty ($\Delta_{Recon.3D}$) of a marker point (fiducial marker or catheter marker) determined from the two shift images. The reconstruction uncertainty was evaluated for marker points at 50, 100, 150, 200 and 250 mm above the FPD imaging plane (h_m), and for the imaging geometry defined in figure 2 (d = 400 mm , FID = 1000 mm). Uncertainties of x-ray shift (Δd), marker identification ($\Delta pixel$), and x-ray source-to-imaging plane (ΔFID) of ±2.0 mm, ±0.8 mm (1 pixel) and ±3.0 mm respectively was applied to calculate the total 3D reconstruction uncertainty.

The parameters contributing to the total 3D reconstruction uncertainty, for the imaging geometry defined in figure 5.24 (d = 400 mm , FID = 1000 mm), is shown in figure 5.32. The reconstruction uncertainty is the same for the x and y direction (figure 5.32(a)) and is greater in the z direction (figure 5.32(b)). The contribution of each imaging parameter in the reconstruction process is shown. The x, y and z uncertainties are combined in quadrature to establish the total reconstruction uncertainty which is shown in figure 5.32(c).

The imaging geometry parameters used to perform the reconstruction in this study (FID = 1000 mm, d = 400 mm) produce a reconstruction uncertainty for catheter marker points up to 150 mm from the imaging plane of approximately ±0.9 mm in the A-P direction (z axis) and ±0.4 mm in the S-I, L-R directions (x, y axis). Figure 5.32(a) shows that generally the process of assigning the coordinates of catheter marker points on each shift image contributes the greatest to the overall reconstruction uncertainty, except where catheters are furthest from the FPD whereupon the geometric uncertainty dominates. Reducing the detector pixel size will further improve the overall reconstruction uncertainty, although the current pixel resolution of 0.8 mm allows identification of clinically relevant catheter displacements.

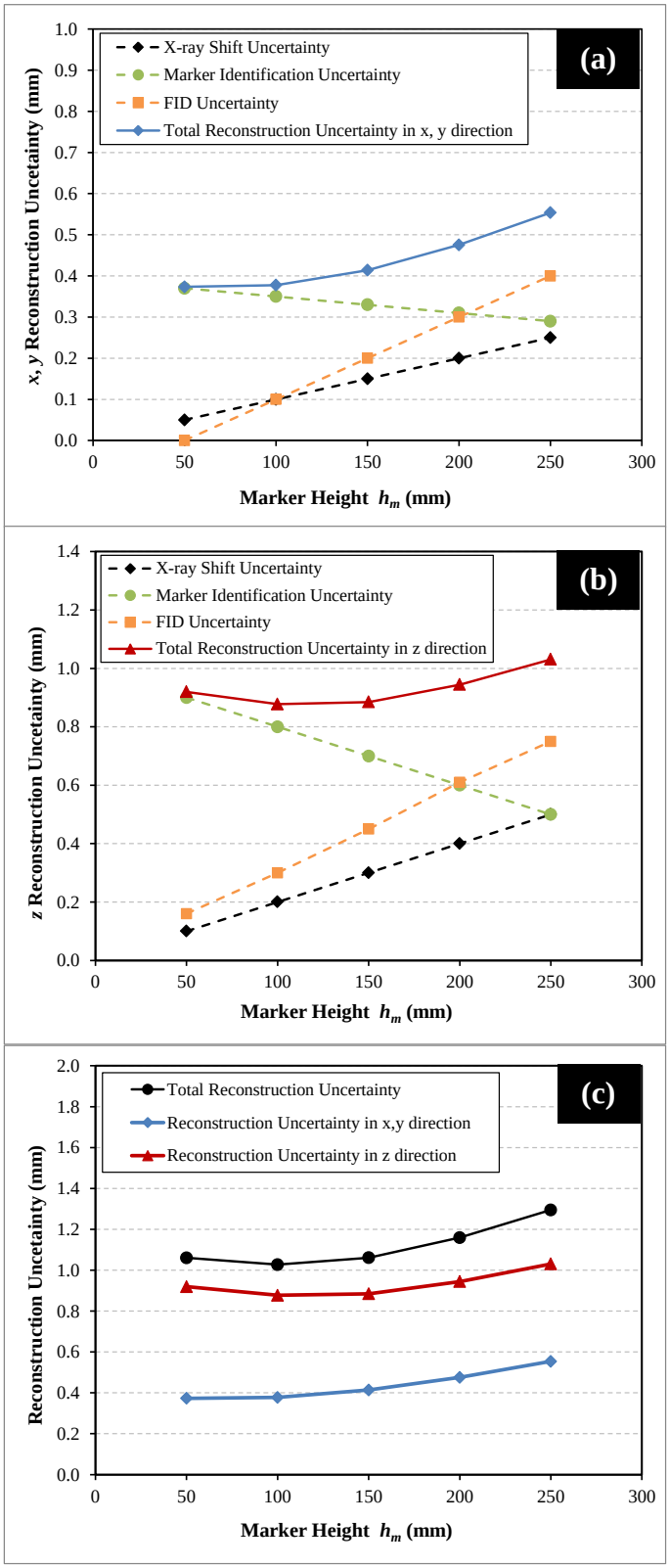

Figure 5.32. (a) The uncertainty of marker reconstruction in the *x* and *y* axes as a function of marker height h_m from the detector plane, and (b) in the *z* axis (or distance from the detector plane). (c) The total combined 3-D reconstruction uncertainty.

5.4.6.2 Registration Uncertainty

The registration uncertainty ($\Delta_{Reg.3D}$) represents the uncertainty of the geometric transformation between the two spaces (TPS and measurement), and is derived from the reported registration residual as shown in equation 5.33:

$$\Delta_{Reg.3D} = \sqrt{\frac{R}{n}} \qquad \text{Eqn (5.33)}$$

where n is the number of fiducial marker pairs participating in the registration. $\Delta_{Reg.3D}$ may be interpreted as the square-weighted average residual error per marker, and is an indicator of the consequential error likely to be observed in other points under the same transformation.

5.4.6.3 TPS Marker Identification Uncertainty

Finally, the uncertainty of identifying catheters and fiducial markers in the TPS (Δ_{TPS}) was considered. In this study, CT imaging was performed on the phantom using 2.5 mm contiguous slices. The uncertainty of identifying marker points in the axial plane of the images is related to the CT reconstruction pixel size, and the uncertainty in the couch long axis, which is typically half the CT slice thickness (±1.25mm) to account for possible partial volume effects.

5.4.7 Measure of Catheter Agreement

In a similar approach to that used in section 5.3.5, the agreement between planned and measured catheters positions was determined by evaluating the difference between each individual 10 mm spaced catheter marker points, in 3D. The quantified differences observed are reported in several ways:

- The mean *x*, *y* and *z* (vector) difference for all catheter marker points calculated in the image.

- The mean absolute (scalar) difference for all catheter marker points calculated in the image.
- The maximum mean absolute (scalar) catheter difference. This quantity is determined by calculating the mean absolute difference for each catheter. The maximum value across all calculated catheters is then reported.
- The 3-D root mean square error ($RMSE_{3\text{-}D}$). This quantity is the radius of the sphere centred at the true (planned) position, containing the reconstructed (measured) point with a probability of 68%.

The mean *x*, *y* and *z* differences report the directional implant changes that have occurred between planning and treatment. The absolute differences reported represent the overall implant changes from the time of planning imaging (CT). The maximum absolute catheter difference reports the greatest absolute deviation by a single catheter in the implant.

The reported catheter agreement quantities described are shown in table 5.10 for the measurements performed on the solid water phantom and the phantom rotation datasets. Using the coordinate system illustrated in figure 5.24, a positive marker point difference value represents a shift toward patient left, patient inferior and patient anterior.

Table 5.10. The mean vector difference between all planned and measured catheter marker points, the mean absolute difference for all points and the maximum mean catheter difference. The absolute difference for all catheters and the maximum individual catheter difference is also shown. The bracket values are 1 standard deviation.

Dataset	x (σ_x) mm	y (σ_y) mm	z (σ_z) mm	Abs. (σ_{abs}) mm	Max. Catheter mm	$RMSE_{3D}$ mm
Initial	-0.1 (0.3)	0.0 (0.4)	0.1 (0.6)	0.7 (0.3)	1.0	0.8
Repeat 1	-0.4 (0.3)	-0.2 (0.5)	0.3 (0.6)	0.9 (0.4)	1.5	1.0
Repeat 2	0.0 (0.3)	-0.1 (0.5)	0.7 (0.7)	1.0 (0.5)	1.4	1.2
1.9° rotation	-0.1(0.4)	-0.2(0.4)	1.0(0.8)	1.3(0.7)	1.7	1.4
3.8° rotation	0.0(0.5)	-0.1(0.5)	0.4(0.5)	0.9(0.3)	1.1	0.9
5.7° rotation	-0.3(0.4)	0.1(0.3)	0.7(0.9)	1.1(0.7)	1.8	1.3

Figure 5.33 illustrates the individual catheter vector differences for the 'Initial' dataset acquired. All vector differences reported in figure 5.33 have no apparent systematic deviation.

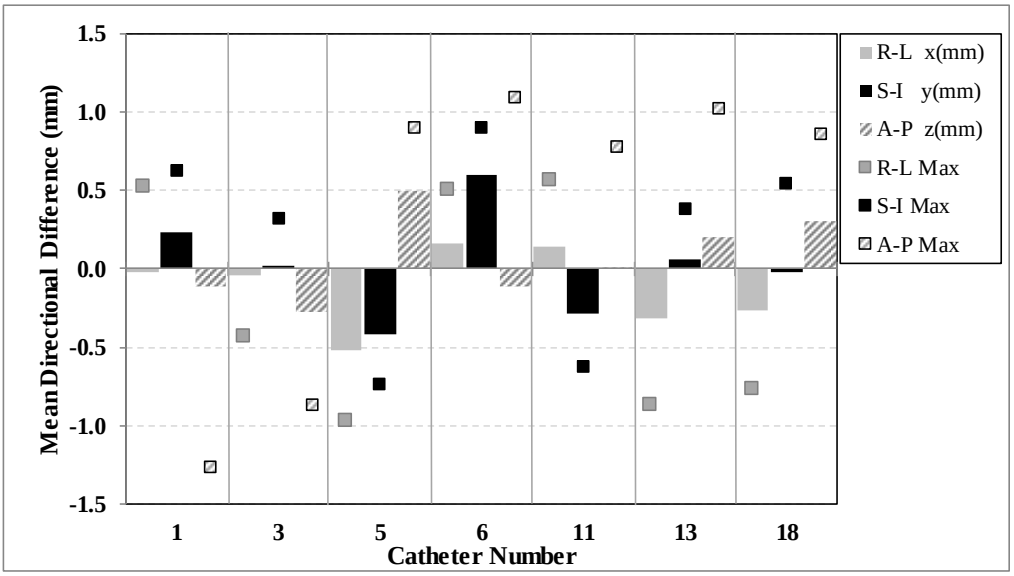

Figure 5.33. The mean and maximum vector difference per catheter for the 'Initial' dataset, showing the Left-Right (*x*), Superior-Inferior (*y*) and Anterior-Posterior (*z*) orientations. Positive measured difference are Left, Inferior and Anterior.

The common approach to measure catheter agreement in prostate brachytherapy is to evaluate the catheter tip position (only) relative to the fiducial markers[32-34, 37, 78], often using 2D planar imaging. Such an approach provides limited information and lacks detail of the catheter path agreement, especially through the prostate region, where geometric accuracy of the catheter positions is important. This measure of catheter agreement of reporting the directional differences provides an assessment of implant deviation in the S-I, A-P and L-R orientations throughout each catheter. This information is especially important for clinical staff who evaluate geometric deviations at the treatment delivery console immediately prior to treatment. A visual representation of deviations, as shown in figure 5.33, depicts the average vector difference per catheter, which can immediately inform the treatment staff of corrections that may need to be applied.

5.4.8 Catheter Displacement Detection

The uncertainties described in the preceding uncertainty analysis sections were combined in quadrature to estimate a displacement detection threshold (D_t) for any point in a catheter. This was defined as the minimum magnitude of shift that can be detected with a confidence > 95% (i.e. 2σ) and is shown in equation 5.34:

$$D_t = \sqrt{{\Delta_{Recon.3D}}^2 + {\Delta_{Reg.3D}}^2 + {\Delta_{TPS}}^2} \qquad \text{Eqn (5.34)}$$

An assumption was made that the registration discrepancies were normally distributed with a standard deviation described by the registration uncertainty, $\Delta_{Reg.3D}$ (Equation 5.33). The variances for geometric uncertainties and discretised image uncertainties (pixel dimensions) were calculated from triangular and rectangular probability distributions respectively.

The geometric imaging uncertainty is a function of the height (h_m) of the point above the imaging plane (see figure 5.23). The detection threshold was calculated for a broad range of h_m expected to span the practical range (50-250 mm). To provide a clinical perspective, the CT data of 33 consecutive clinical HDR prostate cases were examined to measure the distance from the imaging plane to the most anterior catheter path (in each patient). This distance represents the range of h_m likely to be observed at treatment, and allows the determination of the typical clinical detection threshold, D_t. The dependence of the detection threshold on the registration uncertainty – expected to be somewhat variable in the patient case – was also explored.

The sensitivity to catheter displacement was investigated by simulating inferior catheter shifts by displacing all radio-opaque dwell position markers by 2, 3, 5 and 10 mm out of the catheters (toward the +*y* direction). Shift images were acquired for each displacement and the 3D catheter paths were reconstructed, registered with the TPS data for comparison, and displacements calculated. The registration results of the reconstructed fiducial points with the TPS fiducials for the displaced catheter datasets are shown in table 5.11, and are consistent with the values reported for the static case of table 5.7.

Table 5.11. The reported residual, registration uncertainty and the reported rotation after registration between the TPS data and reconstructed fiducial markers for three datasets.

Dataset	Residual (mm)	$\Delta_{Reg.3D}$ (mm)	Tilt x-axis (°)	Roll y-axis (°)	Yaw z-axis (°)
2 mm Shift	0.9	0.5	0.9	-0.7	0.3
3 mm Shift	0.4	0.4	-0.7	-0.8	-0.6
5 mm Shift	0.3	0.3	-0.6	-0.6	-0.3
10 mm Shift	0.4	0.4	-0.7	-0.8	-0.6

The differences between planned and measured catheter locations are summarised in table 5.12, for all applied catheter shifts. The measured shifts in the S-I direction, the direction of the applied shifts, are highlighted in bold. The measured displacement of each catheter is defined to be the mean across all markers in that catheter, and is given in each of the Cartesian directions. The absolute length of the net vector is given, along with the maximum individual catheter displacement. The latter is expected to be useful for identifying individual catheter bending or movement.

Table 5.12. The mean vector difference between planned and measured catheter marker points for all catheters when a known catheter displacement is applied. (Applied shift uncertainty ±1.0 mm). The absolute difference for all catheters and the maximum individual catheter difference is also shown.

Dataset	x (σ_x) mm	y (σ_y) mm	z (σ_z) mm	Abs. (σ_{abs}) mm	Max. Cath mm
2mm Shift	-0.1(0.5)	**2.1**(0.5)	0.3(0.9)	2.4(0.5)	3.1
3mm Shift	-0.2(0.5)	**3.5**(0.4)	0.9(0.8)	3.7(0.5)	4.4
5mm Shift	-0.1(0.4)	**5.3**(0.4)	0.8(0.7)	5.4(0.5)	5.9
10mm Shift	-0.2(0.5)	**10.0**(0.5)	0.7(0.9)	10.1(0.5)	10.9

The displacement detection threshold, D_t, of any point in the catheter, was calculated from the reconstruction, registration and TPS localising uncertainties described in the preceding sections. As seen in Figure 5.32(c), the total reconstruction uncertainty has a geometric dependence on h_m but in practice, this dependence becomes negligible over the clinically relevant range (from 50-150 mm above the imaging plane) when the uncertainties are combined as a quadrature sum, due to competing influences. The

registration quality achieved will also influence the threshold for detection of catheter movements. A total uncertainty budget for displacement detection D_t was calculated with a 95% confidence interval, using the reconstruction uncertainties shown in figure 5.32 and the TPS imaging uncertainty as a function of the registration uncertainty and is shown in figure 5.34.

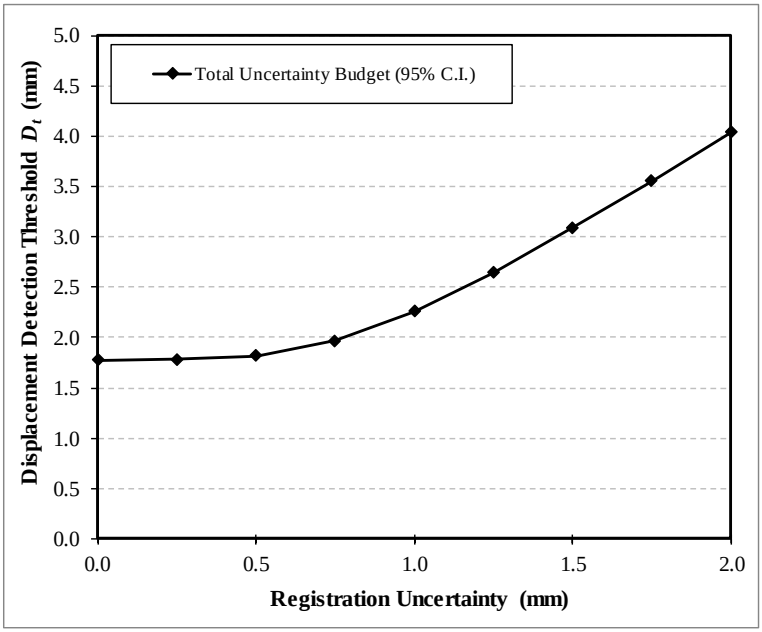

Figure 5.34. The catheter displacement detection threshold (D_t) for a catheter marker point as a function of the registration uncertainty. The detection threshold is weakly dependent on marker height h_m and more strongly dependent on registration uncertainty.

It can be seen from figure 5.34 that the uncertainty, and hence D_t, is weakly dependent on h_m, and is more strongly influenced by the registration uncertainty. Of the 33 sample clinical cases evaluated, the maximum measured height of the furthest catheter from the couch (h_m) was 157.1 mm (mean 140.1 mm, s.d. 9.9 mm) and from figure 5.34, for a registration uncertainty of 0.4 mm, the displacement detection threshold, D_t, is 1.8 mm and would be detected with a confidence of 95%.

The detection threshold for a S-I catheter shift is better than the uncertainty for an individual point due to the contribution of all markers in the catheter which will all move in approximately the same direction by the same amount. Thus the uncertainty is defined in equation 5.35 as

$$\Delta_{S-I} = \frac{RMSE_{3D}}{\sqrt{m}} \approx \frac{\sigma_y}{\sqrt{m}} \qquad \text{Eqn (5.35)}$$

where m=13 is the number of markers in the catheter.

Adopting the $RMSE_{3D}$ of 1.1 mm observed experimentally over the 6 experiments (Table 5.10, n = 507) as our *a priori* pointwise uncertainty, the detection threshold for a S-I whole catheter displacement is given by

$$D_{t,S-I} = 2 \times \frac{RMSE_{3D}}{\sqrt{m}} = \frac{2 \times 1.1}{\sqrt{13}} = 0.6\ mm \qquad \text{Eqn (5.36)}$$

Figure 5.35 shows the measured mean inferior displacement of each catheter for the four datasets with applied catheter shifts. Each data point represents one catheter and the error bars denote one standard deviation of marker point differences in each catheter. The S-I catheter displacement detection threshold, $D_{t,S-I}$, is shown by the dashed line.

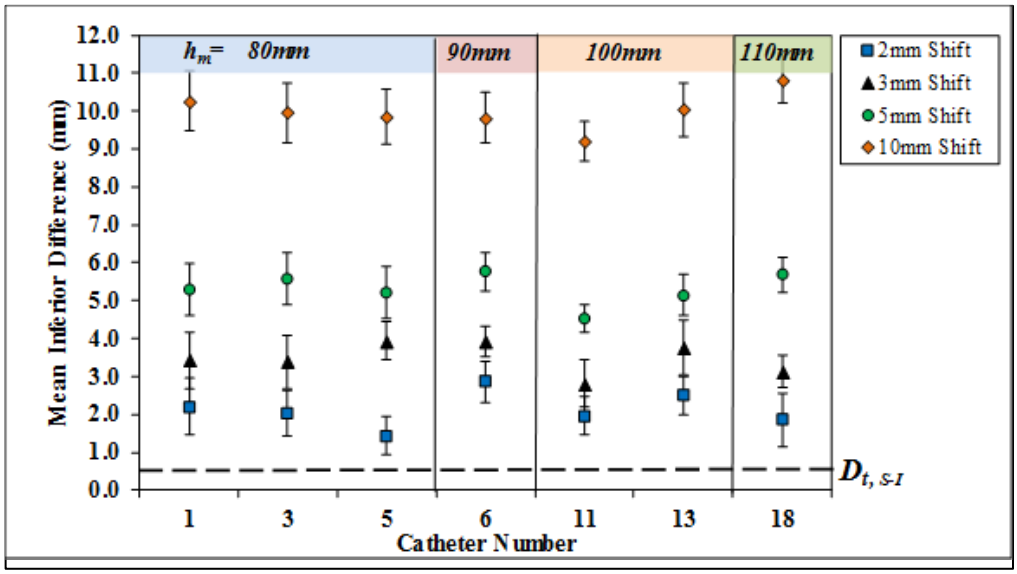

Figure 5.35. The average inferior difference per catheter for the applied shifts of 2, 3, 5 and 10 mm. The height above the imaging plane h_m is 80 mm for catheters 1,3 and 5, 90 mm for catheter 6, 100 mm for catheters 11 and 13, and 110 mm for catheter 18 and is separated by the vertical lines in the figure. The $D_{t,S-I}$ (0.6 mm) for these values is shown by the dashed line.

The catheter displacement detection threshold is determined from the measurement uncertainties, with the largest contribution being from the TPS imaging CT slice thickness. The identification of the catheter marker points and fiducial markers in the TPS has the greatest uncertainty in the S-I orientation. Reducing the CT slice thickness will reduce the catheter displacement detection threshold, and in this study, halving the CT slice thickness to 1.25 mm, would reduce D_t from 1.8 to 1.3 mm. The additional patient CT imaging dose and management of a larger image data set also needs to be considered.

5.4.9 Optimising the Imaging Geometry

An evaluation of the imaging geometry (*d*, *FID*, h_m) was performed to determine an optimal geometry that produces a minimal marker point reconstruction uncertainty. The reconstruction uncertainty for a catheter marker point 150 mm above the imager was determined while varying the *FID* and the x-ray shift parameter *d*.

The reconstruction uncertainty in the *x, y* and *z* directions was evaluated as a measure of changing imaging geometry used to perform the catheter reconstruction. The variation is shown in figure 5.36. Increasing the ceiling x-ray shift distance (*d*) reduced the *z* reconstruction uncertainty, without significant change to the *x, y* uncertainty. But for a reduced *FID*, the *x, y* uncertainty increases with increasing x-ray shift distance. Increasing the *FID* had only minor reduction on the *x, y* uncertainty.

The data presented in figure 5.36 suggests an increased x-ray shift distance *d*, will result in a minimal marker point reconstruction uncertainty in the A-P direction (*z* axis), as this produces a greater apparent movement of the marker across each shift image. The *x, y* reconstruction uncertainty can be reduced for a large x-ray shift *d*, by increasing the *FID*. For a relatively poor imaging geometry setup with the *FID*= 500 mm and a ceiling x-ray shift distance *d*= 500 mm, the reconstruction uncertainty in *x,y* and *z* is less than ±2.0 mm.

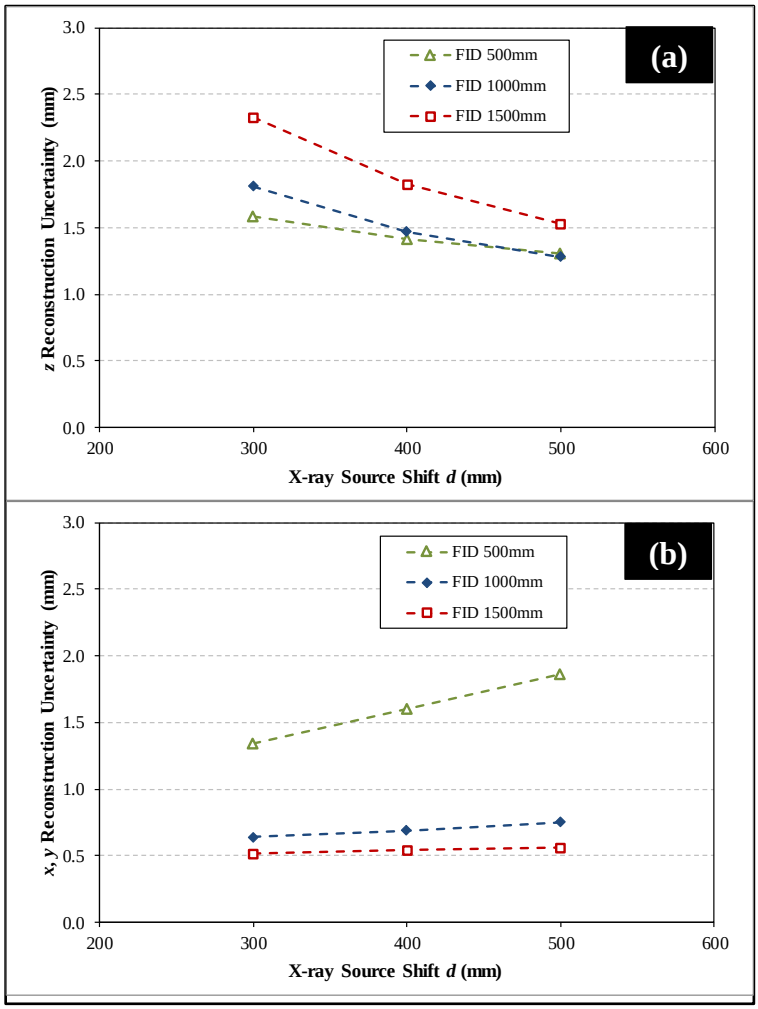

Figure 5.36. The reconstruction uncertainty of a marker at h_m = 150 mm, as a function of x-ray shift distance *d*, for FID of 500, 1000 and 1500 mm, (a) in the *x* and *y* and (b) in the *z* direction.

Other factors will also influence the imaging settings used, such as the brachytherapy treatment room size (limiting the x-ray shift *d*) and the physical dimensions of the FPD. For example, a small detector used with a large ceiling x-ray shift, may result in some of the catheter marker points (implant features) being projected beyond the imager and not captured in the shift image reconstruction process. This imaging geometry would restrict the capability to perform pre-treatment verification imaging.

5.4.10 3D Pre-Treatment Imaging Conclusion

The approach to perform shift image reconstruction of the catheter positions to enable 3D comparison with the treatment plan enables a more comprehensive comparison verification of implant position. The demonstrated 3D catheter reconstruction, using a

shift image technique, was applied in the treatment bunker, to perform pre-treatment implant position verification. Although the shift image technique is not new, this is a novel application of the approach to provide valuable pre-treatment catheter verification information, desirable immediately before treatment.

Assessment of catheter displacement can be performed throughout the implant volume, and not just at the catheter tip as typically performed with 2D verification approaches. Integration with a TPS would enable dosimetric evaluation relative to the current state of the implant geometry.

At present all catheter marker points are considered with the same importance when reporting the catheter agreement values. But (for example) a discrepancy at the catheter tip, which is often beyond the prostate (or even in the bladder), will not impact the treatment delivered because it is not loaded with a source dwell, and could therefore be excluded from the agreement criteria. We foresee that a weighting factor could be applied to catheter marker positions within the prostate or some proximity to the defined organs at risk.

The pre-treatment verification approach described in this work can be applied to CT (or MRI) based treatment planning, permitting a method to verify catheter positions in the treatment room.

This approach could be applied to gynaecological brachytherapy, but would require fiducial markers implanted to establish a reference to the surrounding anatomy. Pre-treatment imaging may also identify unwanted changes in the applicator configuration due to unlocked or loose applicator assembly mechanism.

5.5 Conclusion

Pre-Treatment verification imaging is an important process in the quality assurance process for treatment delivery and this chapter has described a 2D and 3D approach to achieve this in the treatment bunker. Both methods achieve registration with the TPS enabling direct comparison with the treatment plan in the same frame of reference.

The 2D verification approach has the following advantages:

- Simple hardware requirements (no ceiling suspended x-ray), only needs a mobile x-ray system

- Faster and simpler analysis and processing of the image
- Clinical workflow benefits
- Easy initial implementation to achieve verification
- Sensitive to many errors

The 3D verification approach requires additional hardware, but provides a more comprehensive reconstruction of the implanted catheters for comparison.

This chapter has demonstrated the capacity to evaluate catheter positions from the catheter tip and along the catheter path. In a clinical case, this approach may overstate implant differences, as catheter differences outside the treatment region are not necessarily clinically relevant. For example, a prostate case where catheters are inserted into the bladder, evaluation of catheter agreement at the tip is less important than focussing attention on the treatment sub-region. To provide a more clinically relevant assessment of the implant agreement, the evaluations can also be performed for only catheter marker points that occur within the treatment region volume.

Pre-treatment evaluation of the catheter positions is useful for evaluating the results of the source tracking process, especially for detecting treatment delivery errors. With the acquired knowledge of the actual catheter positions immediately before treatment, the source tracking method can compare measured dwell positions to the expected positions defined by the pre-treatment imaging, not just by the treatment plan. This pre-treatment imaging agreement must be taken into account when setting tolerance limits for error detection during source tracking.

In the following chapter, the combination of source tracking and pre-treatment imaging is shown to be extremely valuable for identifying a range of possible errors that can occur in treatment delivery.

Chapter 6
Error Trapping

6 Introduction

The role of treatment verification is to ensure the treatment is delivered correctly to the patient, as intended by the treatment plan, and to identify errors if they occur. The use of a flat panel detector as a treatment delivery verification device provides a range information that can be interpreted in many ways to verify treatment delivery parameters.

The source tracking and pre-treatment imaging capability of the FPD has been demonstrated in chapters 4 and 5 respectively. The aim of this chapter is to demonstrate the capability of this system to identify an error during the treatment delivery, typically difficult to detect with other approaches. This chapter investigates approaches to interpret the data provided by the combination of pre-treatment imaging with source tracking to establish metrics that can identify treatment errors. Erroneous treatment delivery to a solid water phantom for a variety of treatment errors was performed to evaluate the measurement metrics used to identify such errors.

6.1 Treatment Delivery Errors

Partly due to the high degree of manual involvement in the treatment process, HDR brachytherapy has a high relative risk of error, when compared to other radiotherapy treatment approaches. The causes of incorrect treatment delivery may include (i) human errors, (ii) unaccounted catheter (or applicator) displacement relative to the patient's anatomy and (iii) afterloader malfunction.

Some of the more common human errors, which can occur during treatment planning, patient set up and during treatment delivery are listed below.

- Incorrect patient plan selection at the treatment console
    - Selection of the wrong patient
    - Selection of the correct patient but incorrect treatment fraction
- Incorrect channel (indexer) length selected for the applicator
- Incorrect source step size
- Incorrect connection of source transfer tubes from the afterloader to the patient

The geometric changes of the implant that occur between imaging for treatment planning and the treatment delivery can impact the correct delivery of the plan. These errors are:

- Movement of the catheters (applicator channels) relative to the surrounding anatomy
- Movement of the catheters (applicator channels) relative to each other

and these are due to:

- Swelling of the surrounding tissue
- Organ filling and/or displacements
- External mechanical influence (e.g. pressure on the applicator/ bumping when transferring patient)

Afterloader malfunction is an unlikely occurrence, and the resulting event may be unpredictable, but the result is likely to be a deviation from the intended treatment.

The challenge of a comprehensive treatment verification system is to be capable of identifying all types of treatment delivery events. The FPD acquires data prior to and during treatment delivery, and this information can be evaluated to identify specific treatment errors described above. Certain combinations of errors flagged by each metric suggest the concept of ‘error signatures’ that are evident across multiple data analyses. The identification of an error signature may help guide the operator to the cause of the error and allow investigation and corrective action to be taken.

6.2 Error Detection Metrics – 'Error Signatures'

The information acquired by the FPD can be analysed in various ways to confirm the treatment was delivered as expected or to identify a treatment error. The following sections provide a breakdown of the analysis performed on the data provided by the FPD in order to establish metrics that can be used to flag an error event.

The FPD provides information on the current geometry of the implant obtained during pre-treatment imaging. Using the methods described in chapter 5, this treatment geometry can be directly related to the treatment plan, establishing a reference of where the planned source dwell positions are expected to occur (be delivered).

As the treatment is delivered to the patient, and each source dwell position is measured in sequence by the FPD, analysis of the measured source dwell positions can occur in principle in real-time, immediately flagging an error. This real-time approach is not currently implemented in this analysis but is discussed in the future directions of this work. The approach taken here is to retrospectively analyse the measured source dwell positions post treatment and to report correct delivery or error events.

The analysis performed compares the positions of the planned and measured source dwells in the plane of the FPD. The evaluation is currently a 2D approach as this is the intended initial clinical implementation of the system. Challenges associated with the 3D application of this verification system are discussed in the conclusion of this thesis. The following sections describe the metrics reported and how they validate treatment delivery parameters. A single reported metric will not necessarily define which error event is occurring, but combinations of these metrics will narrow down the possibilities.

6.2.1 Visual Comparison

The measured dwell positions can be overlaid on the A-P image acquired during the pre-treatment imaging process. The TPS data is also registered with the FPD frame of reference and so the planned dwell positions can also be displayed on the A-P image. A visual representation of the agreement between planned and measured dwell positions provides a method to identify a treatment error. Visual inspection can be supplemented by several useful quantitative metrics.

6.2.2 Individual Dwell Position Difference

The 2D difference vector is determined for each measured dwell position relative to its expected (or planned) position. The dwell position difference vector is defined in equation 6.1 as

$$\tilde{\delta}_i = p_{meas,i} - p_{plan,i} \qquad \text{Eqn. (6.1)}$$

where p_{meas} is the measured coordinate position of the source dwell and p_{plan} is the expected (or planned) position of each source dwell *i*, in the FPD frame of reference. For each difference vector, the signed *x* and y components representing the L-R and S-I directional differences respectively, are extracted as defined in equation 6.2.

$$\tilde{\delta} = \tilde{\delta}_{LR} + \tilde{\delta}_{SI} \qquad \text{Eqn. (6.2)}$$

The L-R direction represents the x-axis of the FPD and the A-P is the y-axis, as defined by the coordinate system definition in figure 5.4. The length of the difference vector, the absolute individual dwell difference (δ) is also calculated.

These individual dwell position difference metrics on their own may not identify an error, but can inform the operator of local dwell position deviations that have occurred post treatment planning.

6.2.3 Mean Difference

The mean ($\bar{\delta}$) and standard deviation (σ) are calculated across all dwell positions and represents the mean value of the absolute individual dwell difference (δ). This metric will be sensitive to errors affecting the whole implant or all dwells, e.g. whole implant displacements or indexer length error. For a multiple catheter (channel) treatment, where a single catheter exhibits a deviation, the magnitude of the deviation may be obscured by the averaging process performed. Another metric, maximum mean catheter difference, is presented below to catch these occurrences.

6.2.4 Mean Directional Difference

The mean ($\overline{\tilde{\delta}_{LR}}$) ($\overline{\tilde{\delta}_{SI}}$) and standard deviation (σ_{LR}) (σ_{SI}) directional differences for signed *x* and *y* components are calculated across all dwells delivered for the treatment.

These metrics can provide directional information about deviations and inform the user of any systematic displacement of dwell positions. For example, a small mean difference in the S-I direction and a large standard deviation suggests individual catheter displacement within the implant, such as catheter slip at the template.

6.2.5 Absolute Mean Directional Difference

The absolute mean directional difference ($\overline{|\tilde{\delta}|}$) is calculated for all dwell positions from the mean directional components ($\overline{\tilde{\delta}_{LR}}$) ($\overline{\tilde{\delta}_{SI}}$). This metric can be used to identify the systematic shift component of an implant. For example, a large absolute mean directional difference and a small standard deviation would suggest an entire implant displacement.

6.2.6 Maximum Mean Catheter Difference

The mean catheter difference ($\overline{\delta_j}$) can be calculated for each catheter, *j*. The maximum mean catheter difference ($\overline{\delta_{max}}$) across all catheters can be used to highlight individual catheter deviations. For example a large maximum mean catheter difference ($\overline{\delta_{max}}$) and a small mean difference ($\bar{\delta}$) would suggest a swapped channel connection error or an incorrectly defined channel (indexer) length for a single catheter in the implant. This metric will identify which catheter exhibits the observed error.

6.2.7 Histogram of Absolute Individual Dwell Difference

The distribution of differences reported by the absolute individual dwell difference (δ) can be represented as a histogram. This provides a representation of the spread of differences of all the dwell positions, and will also identify any outliers that may represent single dwell positions that have been incorrectly delivered. The histogram distribution may also be used to define an error action threshold, when a percentage of the total number of dwells deviate from their expected positions.

6.2.8 Histogram of Individual Directional Difference

These histograms illustrate the distributions reported by the signed components representing the L-R ($\tilde{\delta}_{LR}$) and S-I ($\tilde{\delta}_{SI}$) directional distributions. The distribution will show any systematic differences such as all dwells delivered inferior of their expected planned positions. These metrics could suggest an incorrect indexer length

(shorter/longer) or catheter displacements due to swelling or swapped channel connection error.

6.2.9 Absolute Dwell Difference Profile

The absolute individual dwell differences (δ) can be reported with a bar graph showing the absolute difference at each dwell position along the catheter path. This is reported for each catheter in the implant and allows interrogation of individual dwell differences and the position along the catheter they occur. The results may suggest differences due to geometric changes of the implant from anatomical displacements.

6.2.10 Individual Dwell Time

The individual dwell time can also be measured by the FPD by integrating the image time stamps for determined dwell positions that occur in the same location. The difference between the measured and planned dwell times can be evaluated and discrepancies can be highlighted at particular dwell positions along the catheter path.

6.2.11 Catheter Treatment Time

The per catheter treatment time can also be measured by integrating the FPD image time stamps as described above. A bar graph representing the catheter time profile for the whole treatment fraction can be created to verify the per catheter treatment times and identify individual catheter discrepancies. This metric can be useful in identifying incorrect treatment plan selection where the time profiles are different. It can also be used to identify swapped catheter errors, in the unlikely event where the catheter paths are overlaid on the 2D A-P image, and the dwell positions of each channel are identical.

6.2.12 Overall Treatment Time

The total treatment time can be measured by integrating the time stamps of the FPD images acquired that contain a brachytherapy source response. This is described in section 4.2.11, and has an uncertainty relative to the image acquisition frame rate. This value can be directly compared to the planned treatment time (corrected for current source AKR) and used as an additional metric for correct treatment delivery.

The metrics defined in the previous sections are used within the following section to provide examples of how the FPD system can be used as an error trapping device.

6.3 Error Trapping Investigations

The solid water phantom described in section 5.1 is used to perform a series of treatment delivery error events. The treatment is initially delivered correctly (without errors) to demonstrate a reference (or baseline) set of error trapping metrics. Treatment error events are then introduced and the acquired data evaluated to demonstrate error identification.

6.3.1 Method

The solid water phantom containing 18 plastic catheters and three fiducial markers was placed on the CT couch, radio-opaque CT markers were inserted, and a CT scan performed. The CT data was transferred to the Oncentra TPS and for demonstration purposes only a treatment plan was created using 6 of the 18 available catheters (as illustrated in figure 6.1). When the treatment plan was complete it was sent to the treatment console computer, where it was loaded ready for treatment delivery.

The phantom was transferred to the HDR brachytherapy treatment bunker and placed on the treatment couch in preparation for treatment delivery. Radio-opaque x-ray dwell position marker wires were inserted into the 6 catheters used for treatment and a pre-treatment A-P image was acquired using the imaging geometry previously defined in figure 5.2.

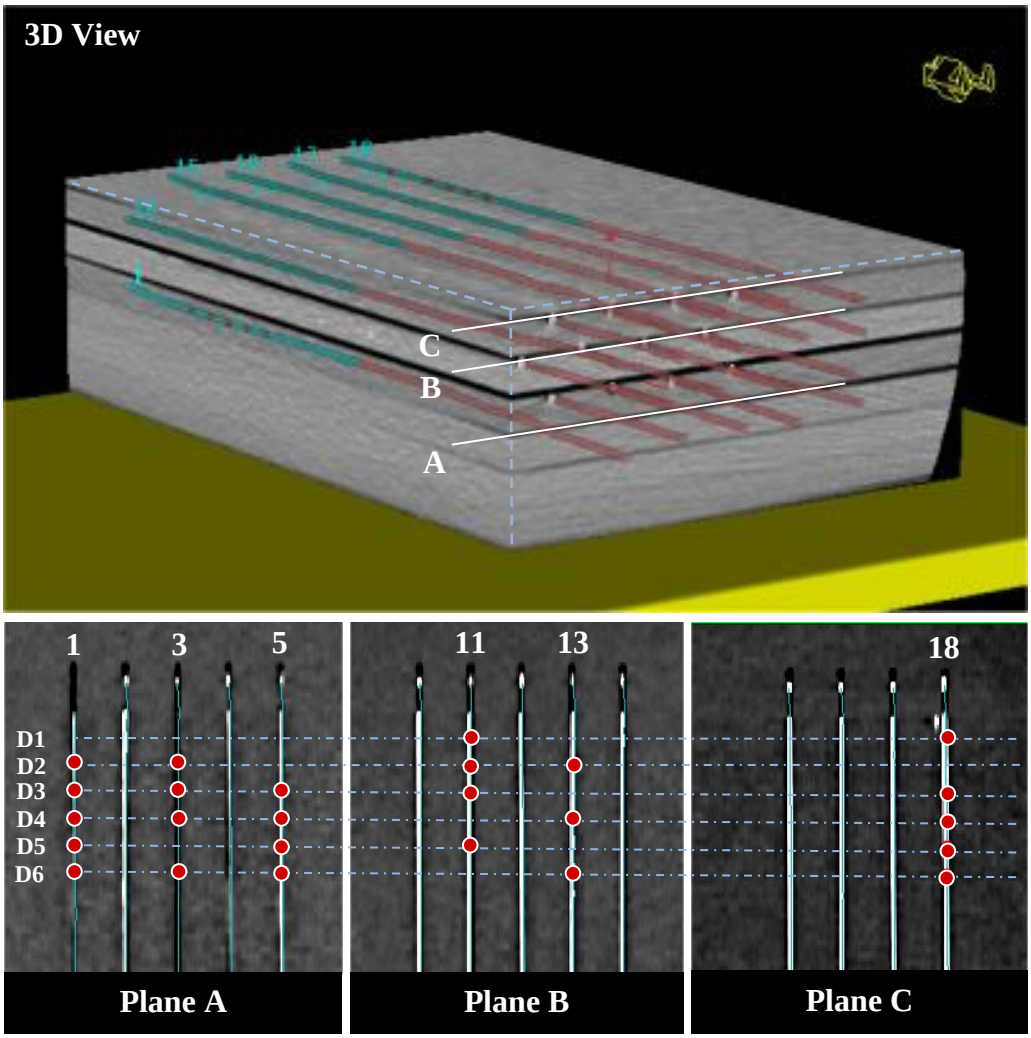

Figure 6.1. The simple treatment plan created to demonstrate the error trapping capability of the FPD system. Six catheters were used and these were selected across three separate rows (A, B and C) providing a range of source to detector distances.

The three fiducial markers were identified in the pre-treatment A-P image and a 2D rigid registration was performed as described in section 5.3.4. The paths of the planned catheters were transformed into the measurement frame of reference using the transformation established by the registration process. Analysis was performed to determine the agreement between the planned and measured catheter positions. The planned dwell positions were also transformed into the measurement space for comparison with the delivered dwell positions.

The marker wires were removed from the catheters, the transfer tubes were connected between the catheters and the afterloader and the treatment started. During the treatment delivery, the FPD was operated in continuous capture mode acquiring images of the phantom exit radiation as the treatment was delivered to each catheter.

The agreement between planned and measured source dwell positions was determined by evaluating the 2D difference, in the plane of the FPD, between each individual measured dwell position. The quantified differences observed are reported using the metrics defined in section 6.2:

- Visual comparison
- The mean difference for all dwell positions calculated, ($\bar{\delta}$)
- The mean L-R and S-I differences for all dwell positions calculated, ($\overline{\tilde{\delta}_{LR}}$) ($\overline{\tilde{\delta}_{SI}}$)
- The absolute mean directional difference for all dwell positions calculated, ($\overline{|\tilde{\delta}|}$)
- The maximum mean catheter difference, ($\overline{\delta_{max}}$)
- A graphical representation of the absolute differences of dwell positions per catheter.
- Histograms of the distribution of absolute difference and directional differences for all dwell positions.
- Total Treatment time, individual catheter times and individual dwell time profiles.

The analysis of the measured dwell positions delivered by each of the treatment plans can be performed in two ways:

(i) The entire set of measured dwell positions are compared to the planned set of dwell positions and the above measures of agreement are performed. This approach does not consider the sequence the dwells are delivered, and in some instances of errors (swapped channels, incorrect treatment plan), as will be illustrated later, the order the dwells are delivered are important for identifying an error.

(ii) The error trapping analysis is performed with knowledge of the programmed sequence of catheter channels. For each planned catheter, the planned dwell positions for that catheter are used for comparison with each successive measured dwell. Each measured dwell is compared to a corresponding

planned dwell and this comparison is performed per catheter. The overall histogram distributions and the calculated mean and standard deviation values are then a summation of these results. This approach provides a dwell by dwell comparison and is more sensitive to identifying errors than comparing all delivered dwells with all planned dwells.

The measured dwell positions delivered for each of the following plans were evaluated on a per catheter basis as described in (ii) above.

6.3.1.1 Correct Delivery

The plan was loaded on the treatment console without any modifications and the transfer tubes were connected to the phantom and independently confirmed to ensure no errors were introduced.

6.3.1.2 Incorrect Plan Selection

To produce an incorrectly loaded treatment plan error, an alternative treatment plan was created and sent to the treatment console. This 'incorrect' plan used the same treatment catheters but consisted of different dwell positions, was loaded and delivered to the phantom.

6.3.1.3 Incorrect Channel Length

The treatment plan was modified on the TPS by reducing the defined indexer length of each treatment channel by 5 mm. At the TPS (Oncentra BPS v4.3, Elekta), this error is difficult to identify as the isodose distributions relative to the patient's anatomy remain unchanged, but the result at treatment is a systematic shift of the dose.

6.3.1.4 Swapped Channel Connection

The treatment plan was loaded on the treatment console without modification. The transfer tube channels 1 and 5 were swapped so that transfer tube 1 was connected to catheter 5 and vice versa for transfer tube 5.

6.3.1.5 Incorrect Plan Dwell Times

The treatment plan was modified with all dwell times increased to represent an incorrect calculation of dwell times at the treatment console, possibly due to a

systematic error of the afterloader system performing time calculations. This error represents a failure of the afterloader or possibly a discrepancy of source AKR specification between TPS and the afterloader.

6.3.2 Results

The data collected for the 5 treatment deliveries was processed and the metrics defined in section 6.2 were calculated. A summary of some of these values is given in table 6.1 which shows the agreement between the planned and the delivered dwell positions for a correct delivery and each introduced error event.

Table 6.1. The table shows the absolute mean difference, the mean directional differences, and the mean difference between planned and measured dwell positions for all dwells in the implant. The maximum mean catheter difference is also shown and the values in the brackets represent one standard deviation.

Dataset	$\lvert\bar{\delta}\rvert$ **mm**	$\overline{\tilde{\delta}_{LR}}$ **mm**	$\overline{\tilde{\delta}_{SI}}$ **mm**	$\bar{\delta}$ **mm**	$\overline{\delta_{max}}$ **mm**
Correct Plan	0.2	-0.1 (0.4)	-0.2 (0.4)	0.6 (0.2)	0.8
Incorrect Plan Selection	12.2	-0.1 (0.4)	12.2 (9.6)	14.1 (6.5)	19.8
Incorrect Channel Length	4.8	-0.2 (0.4)	4.8 (0.5)	4.8 (0.5)	5.3
Swapped Channel Conn.	3.1	3.1 (48.8)	-0.2 (0.5)	29.1 (38.8)	80.0
Incorrect Dwell Times	0.3	-0.1 (0.4)	-0.3 (0.5)	0.6 (0.3)	0.8

A visual comparison of the measured and planned dwell positions is shown in figure 6.2 where the red dots are the planned dwell positions and the blue circles are the measured dwell positions.

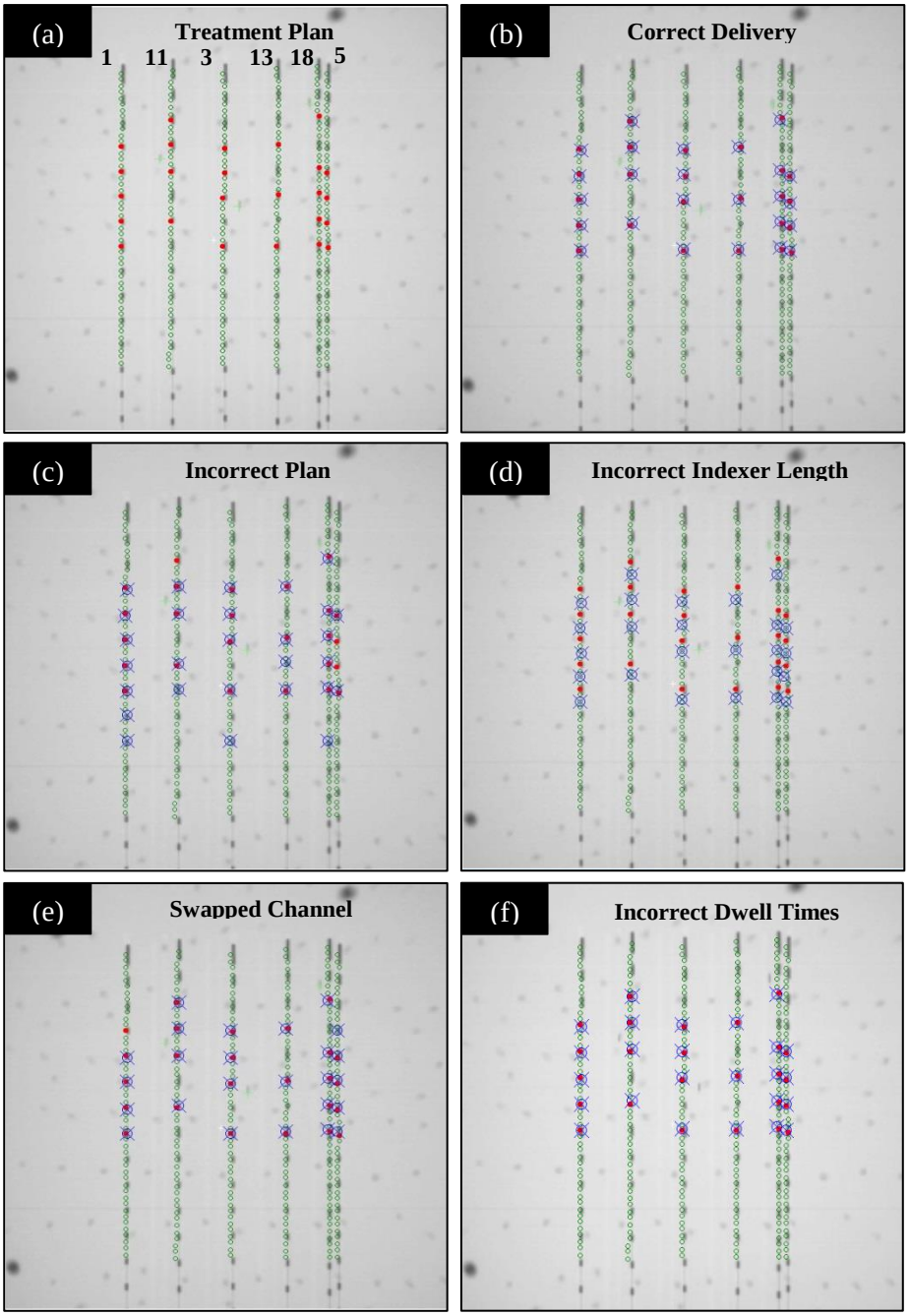

Figure 6.2. (a) The pre-treatment AP images showing channel numbers, the planned inactive (green circles) and active (red dots) dwell positions mapped on to the pre-treatment image. (b) The correctly delivered plan showing the measured source dwell positions as blue circle-cross. (c) The incorrect plan delivered. (d) The incorrect indexer length plan delivered. (e) The swapped channel connections plan delivered and (f) the incorrect dwell times plan delivered.

The following sections show the results for each delivered treatment plan, reporting the calculated error detection metrics described in section 6.2.

6.3.2.1 Correct Delivery

The treatment was delivered correctly and the distribution of dwell position differences is shown in the histograms of figure 6.3, showing the absolute (a) and the directional dwell differences (b) and (c). The measured dwell positions agree to within 1.0 mm of the planned positions for all of the dwells. The visual comparison (d) of the measured dwell positions is also shown along with a summary of the calculated measures of agreement (e). The absolute individual dwell differences (δ) are illustrated with the bar graphs shown in figure 6.4, showing the dwell positions along the catheter path, that contained a programmed dwell stops. The circle-cross indicate a dwell position that did not have a programmed dwell position and therefore no comparison is performed at this position.

The comparison of planned total catheter time with measured catheter time of each catheter is shown in figure 6.5, where the error bars are twice the sampling interval of the FPD. All measured catheters agree with the planned time within the measurement uncertainty. The total treatment time is compared with the measured treatment time, which is a summation of all measured catheter times.

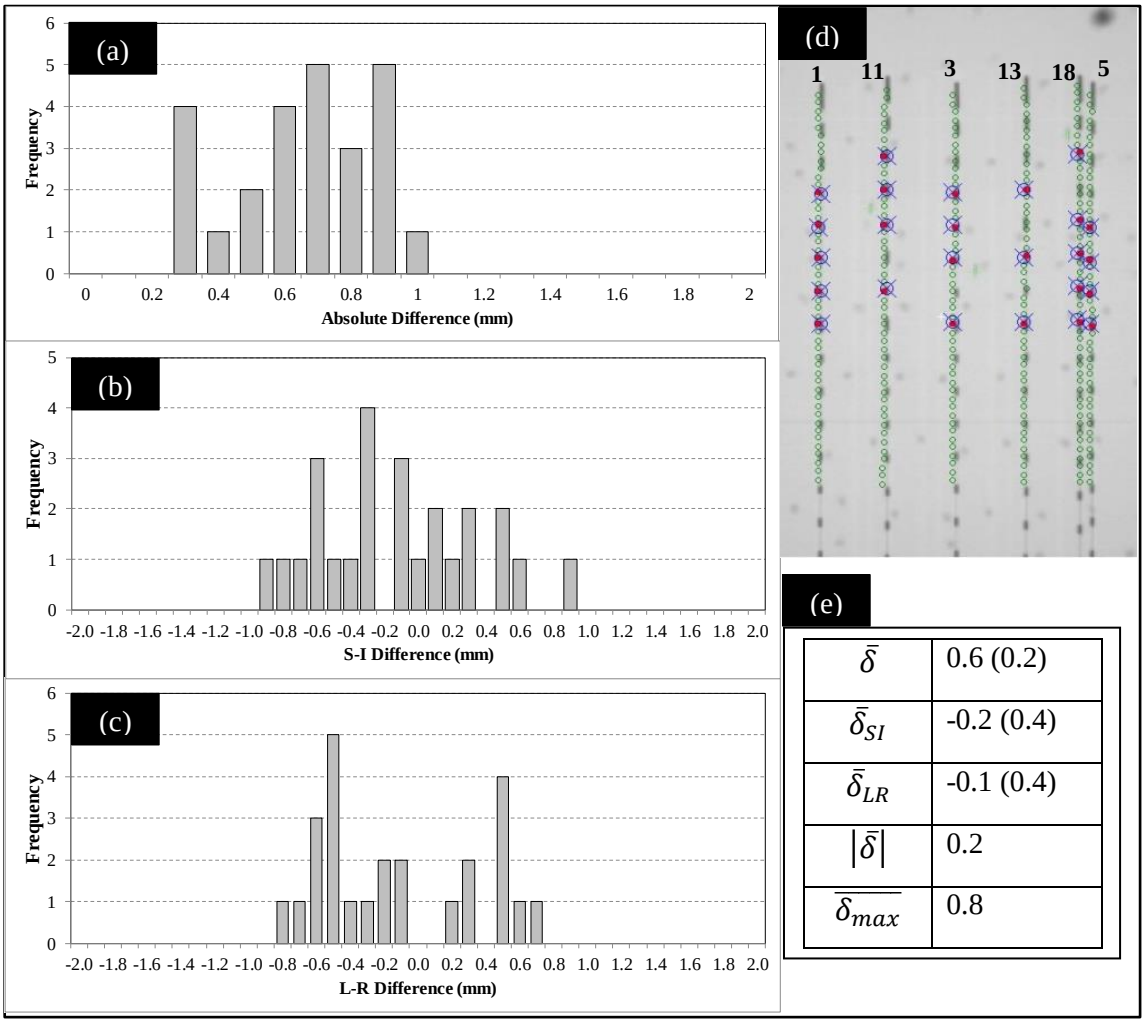

Figure 6.3. Histograms showing the distribution of dwell position differences for the correctly delivered treatment plan with (a) the absolute dwell difference (δ), (b) the S-I directional dwell difference (δ_{SI}), (c) the L-R directional dwell difference (δ_{LR}), (d) the visual comparison of dwell positions and (e) the summary of agreement metrics.

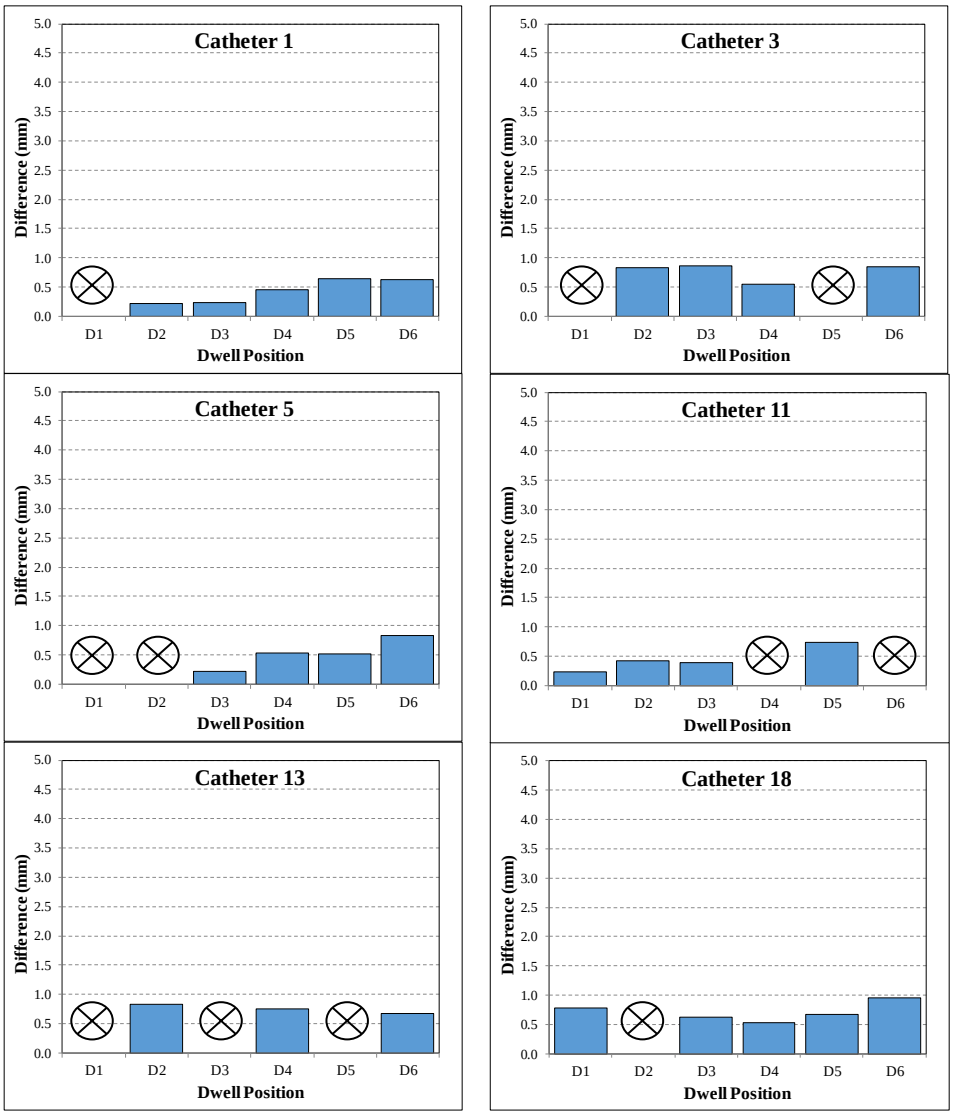

Figure 6.4. The absolute difference (δ) of each dwell position for each catheter for the correctly delivered treatment plan. The circle-cross indicates that a source dwell was not programmed for that position (refer to treatment plan in figure 6.1).

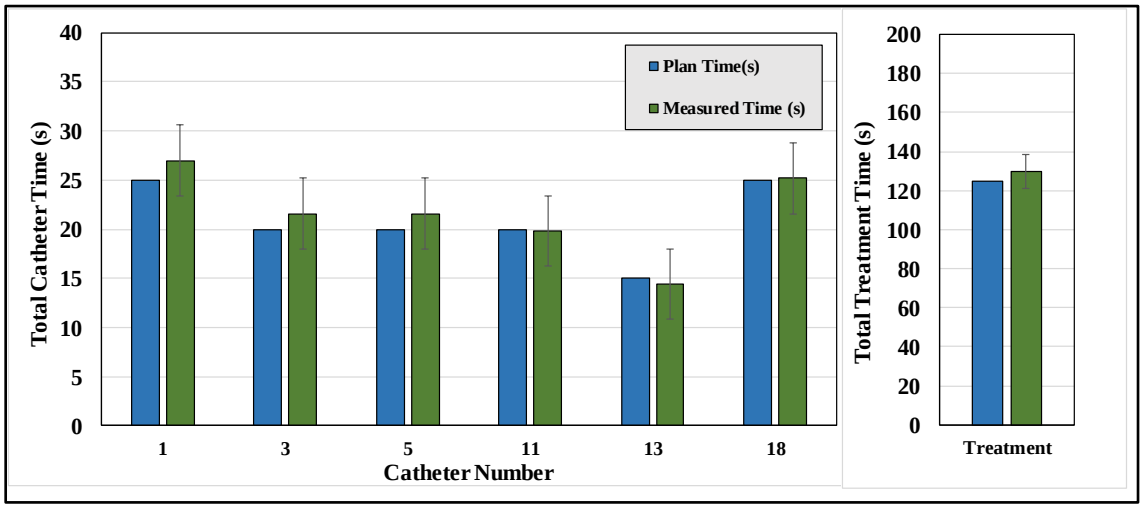

Figure 6.5 The comparison of planned total catheter time with measured catheter time of each catheter for the correctly delivered treatment plan, where the error bars are twice the sampling interval of the FPD. The total treatment time is compared with the measured treatment time, which is a summation of all measured catheter times.

6.3.2.2 Incorrect Plan Selection

The incorrect plan was delivered as the treatment and the distribution of source dwell position differences is shown in the histograms of figure 6.6, showing the absolute dwell differences and the directional dwell differences. Large discrepancies are seen in the absolute difference histogram and the S-I directional histogram indicating incorrectly delivered dwell positions.

The visual comparison (figure 6.6(d)) shows that all the catheters were used by this 'incorrect' plan, but some catheters received incorrect number of dwells and/or incorrect spacing relative to the expected plan. A visual evaluation of the delivered dwells does not clearly expose the significance of this treatment error. The summary of metrics (figure 6.6(e)) highlights that almost all values indicate an error. In this case the L-R directional histogram shows good agreement with the expected plan, and this is due to the 'incorrect' plan using the same set of catheters.

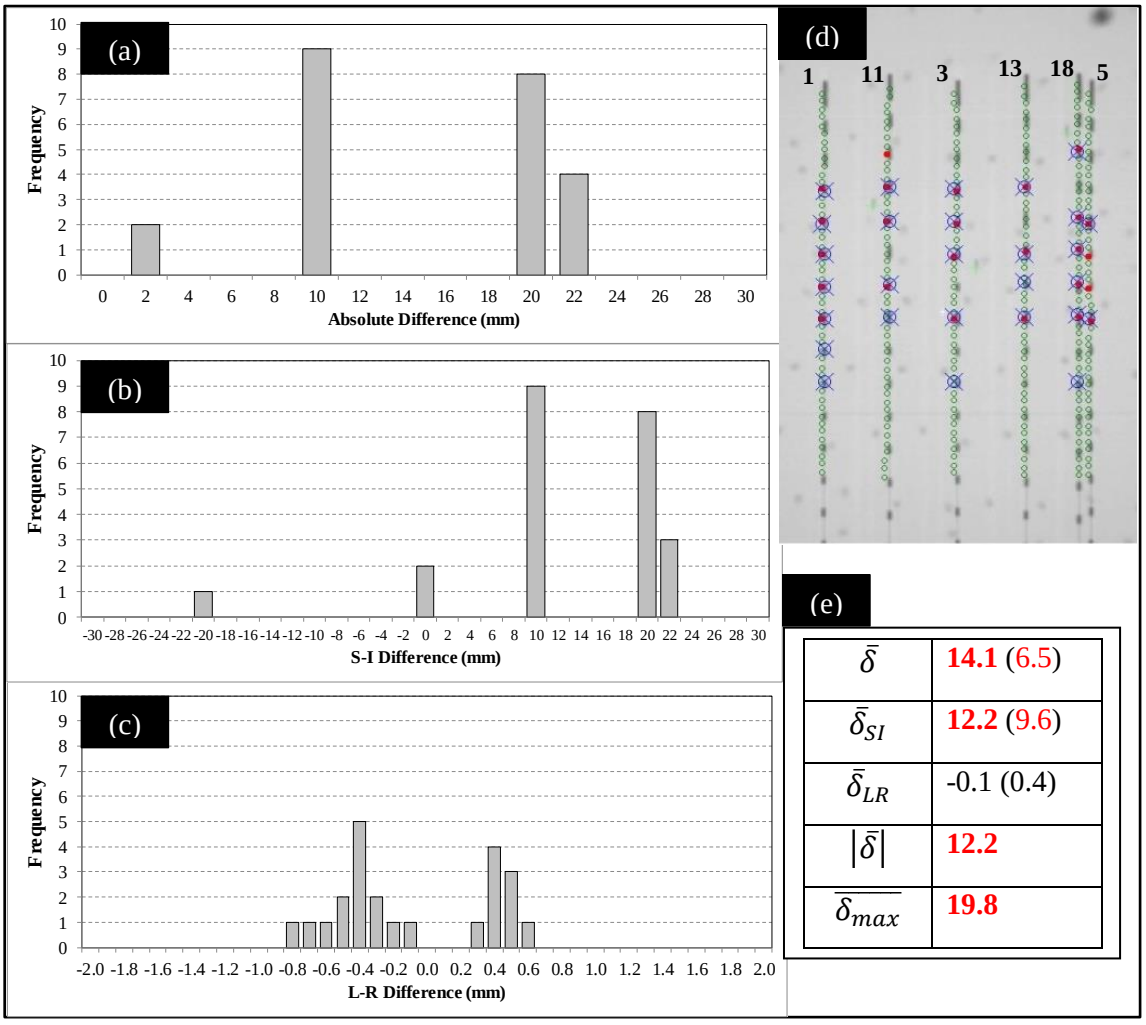

Figure 6.6. Histograms showing the distribution of dwell position differences for the incorrect plan selection delivered treatment plan with (a) the absolute dwell difference (δ), (b) the S-I directional dwell difference (δ_{SI}), (c) the L-R directional dwell difference (δ_{LR}), (d) the visual comparison of dwell positions and (e) the summary of agreement metrics, where red indicates disagreement.

The sequence of active dwell positions for the incorrect plan did not necessarily match the expected plan and this can be seen for each absolute individual dwell difference (δ) illustrated by the bar graphs shown in figure 6.7, showing dwell positions along the catheter path, that contained programmed dwell stops. The triangles at dwell positions D3 and D4 of catheter 5 represent planned dwell positions that did not record a measurement, as this 'incorrect' plan only had 2 active dwell positions in catheter 5. A dwell position comparison at D3 and D4 was not performed. The incorrect plan also

delivered additional dwells to some catheters (e.g. catheters 1, 3, 13 and 18) further complicating the process of error identification.

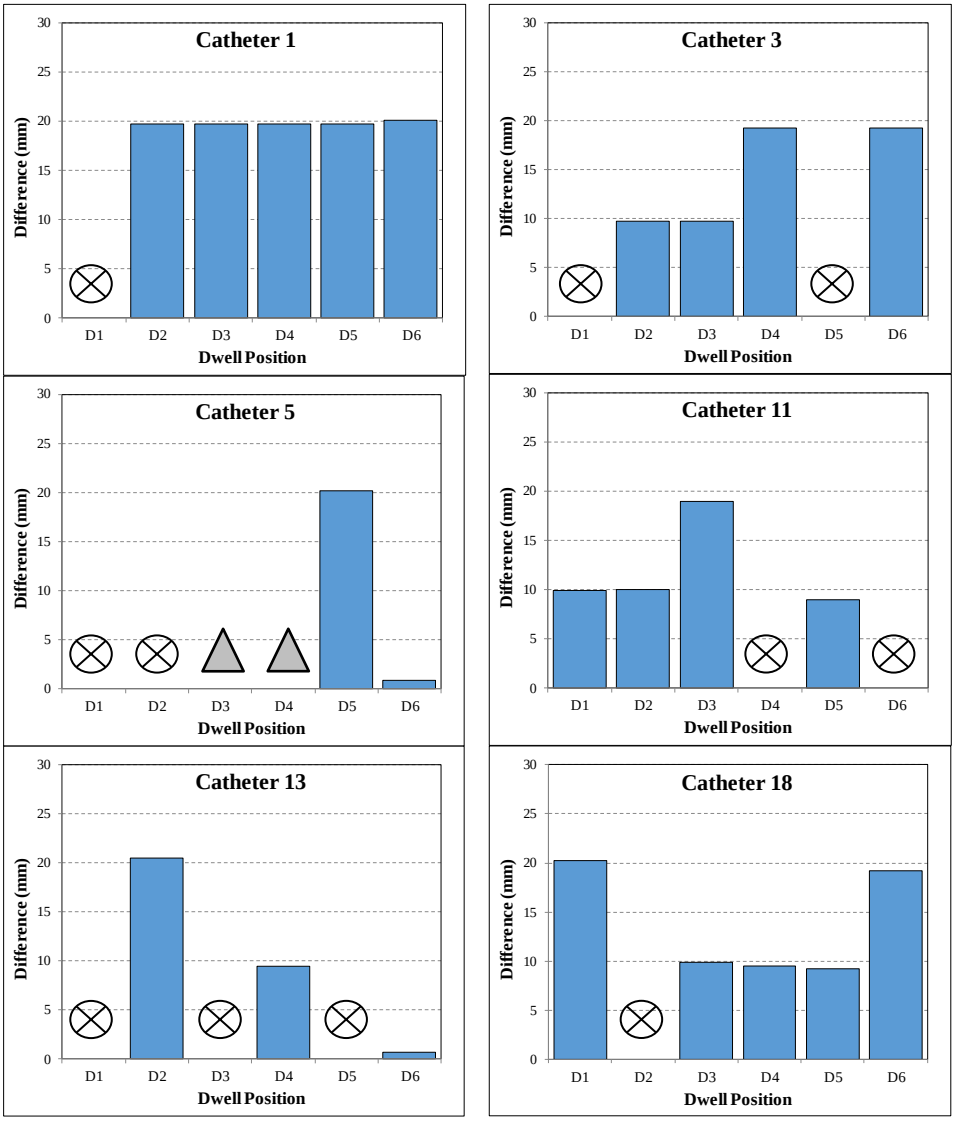

Figure 6.7. The absolute difference (δ) of each dwell position for each catheter for the incorrect plan selection delivered treatment plan. The circle-cross indicates that a source dwell was not programmed for that position (refer to treatment plan in figure 6.1). The triangles at dwell positons D3 and D4 of catheter 5 represent planned dwell positions that did not record a measurement, as this 'incorrect' plan only had 2 active dwell positions in catheter 5. A dwell position comparison at D3 and D4 was not performed.

The comparison of planned total catheter time with measured catheter time of each catheter is shown in figure 6.8, where the error bars are twice the sampling rate of the FPD. The green columns are measured catheters where the times agree with the planned time within the measurement uncertainty, red indicates disagreement. The total measured treatment time does not agree with the planned treatment time, as many of the individual catheters times are incorrect.

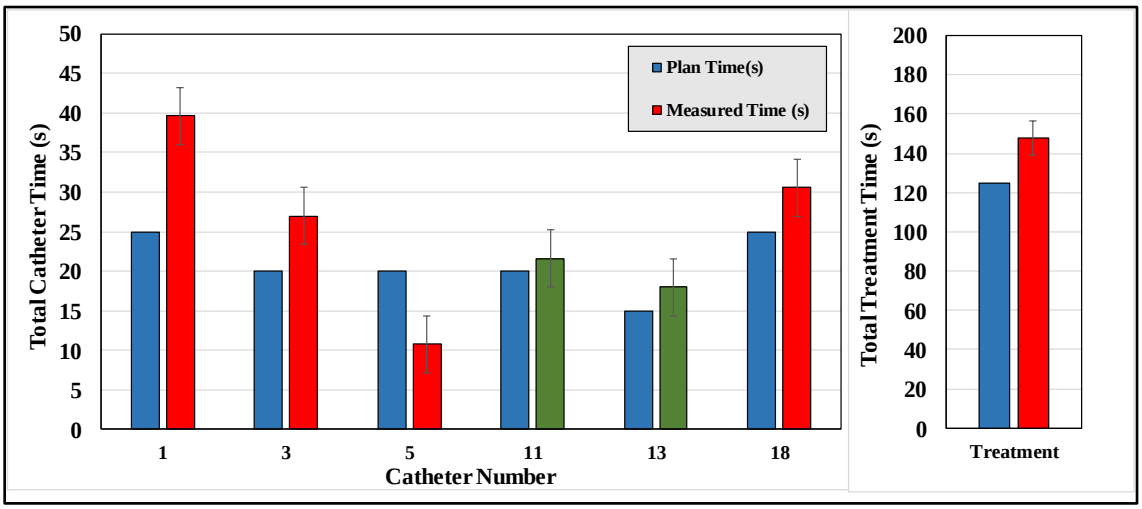

Figure 6.8 The comparison of planned total catheter time with measured catheter time of each catheter for the incorrect delivered treatment plan, where the error bars are twice the sampling rate of the FPD. The green columns are measured catheters where the times agree with the planned time within the measurement uncertainty. The total treatment time is compared with the measured treatment time, which is a summation of each measured catheter time.

6.3.2.3 Incorrect Channel Length

The treatment was delivered with an incorrect channel length of 5 mm toward the inferior direction. The distribution of source dwell position differences is shown in the histograms of figure 6.9, showing a spread of the absolute dwell differences centered at 5 mm. The directional dwell differences also confirm this systematic displacement of all dwells, with the S-I directional histogram showing the dwells at approximately +5 mm. The L-R directional histogram confirms the dwell positions are correct to within 1mm of the expected position.

The visual comparison of the measured dwell positions clearly shows a systematic displacement of all dwells in the inferior direction. The summary of the calculated

measures of agreements further highlight the systematic nature of this error showing an absolute and directional displacement (S-I direction) and both having small standard deviations indicating all dwells have been displaced by approximately the same magnitude.

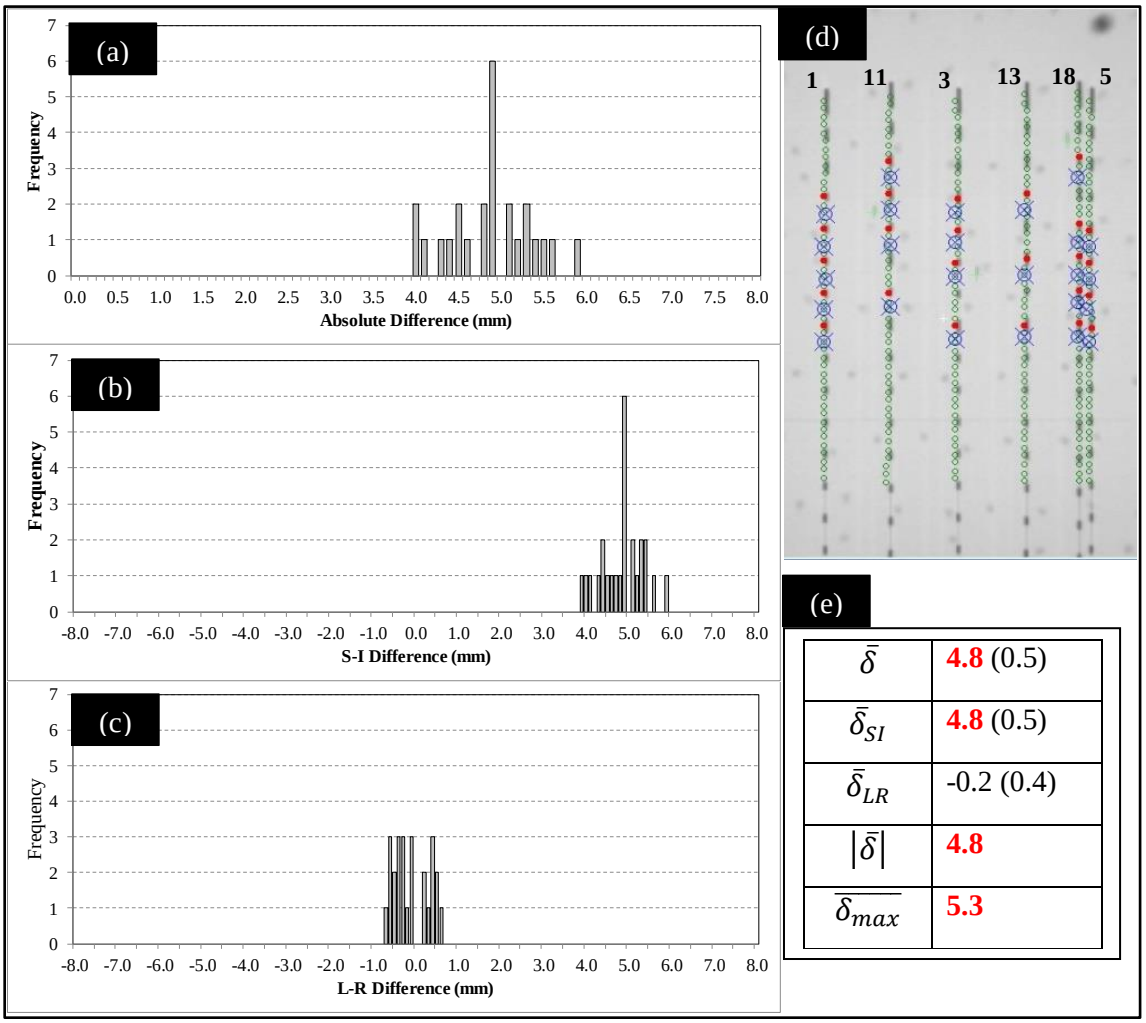

Figure 6.9. Histograms showing the distribution of dwell position differences for the incorrect indexer length delivered treatment plan with (a) the absolute dwell difference (δ), (b) the S-I directional dwell difference (δ_{SI}), (c) the L-R directional dwell difference (δ_{LR}), (d) the visual comparison of dwell positions and (e) the summary of agreement metrics, where red indicates disagreement.

The absolute individual dwell differences (δ) are illustrated with the bar graphs shown in figure 6.10, showing the dwell positions along the catheter path, that contained

programmed dwell stops. The circle-cross indicate a dwell position that did not have a programmed dwell position and therefore no comparison is performed at this position.

The total catheter time histograms (not shown) do not feature any discrepancies, and appear as in figure 6.5 within the measurement uncertainty.

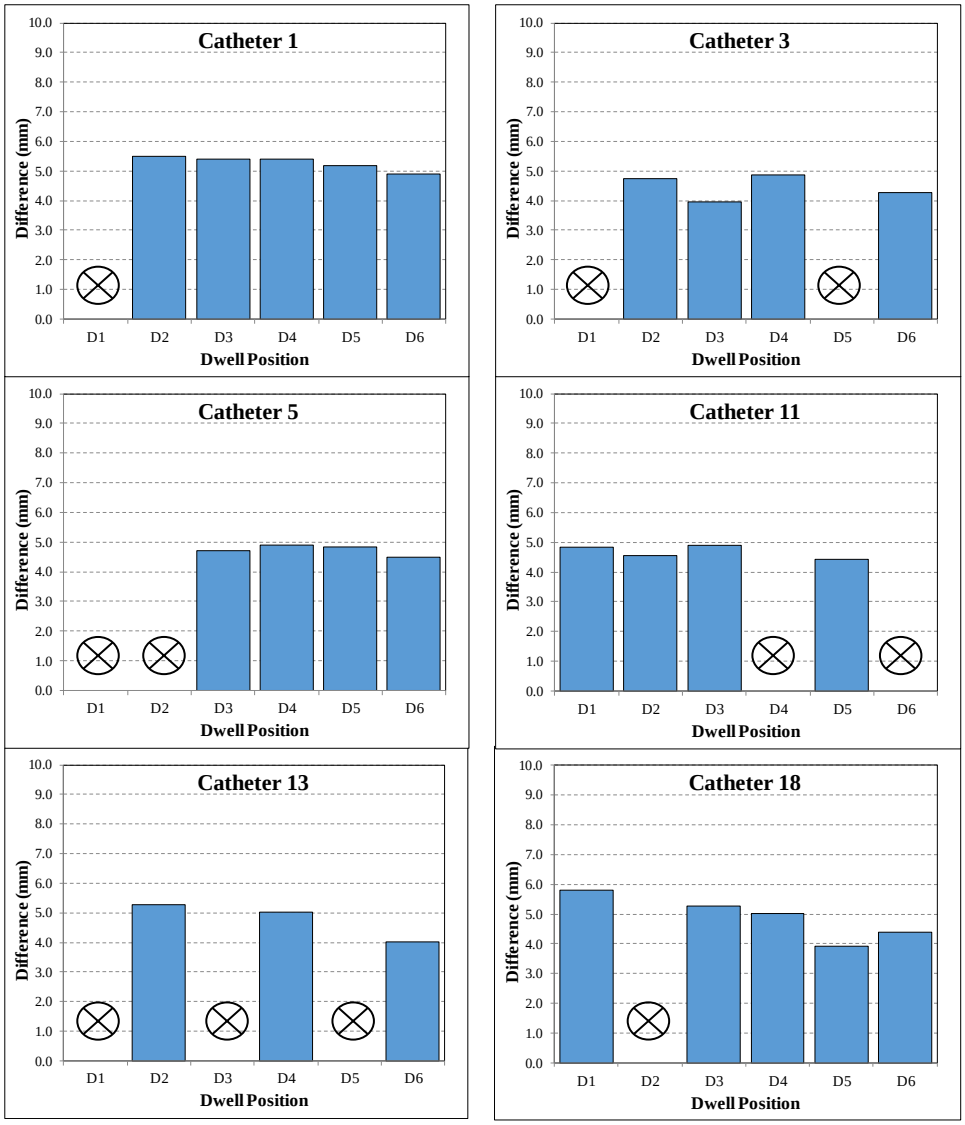

Figure 6.10. The absolute difference (δ) of each dwell position for each catheter for the incorrect indexer length delivered treatment plan. The circle-cross indicates that a source dwell was not programmed for that position (refer to treatment plan in figure 6.1).

6.3.2.4 Swapped Channel Connection

The treatment was delivered with the transfer tubes of channel 1 and 5 swapped. The distribution of source dwell position differences is shown in the histograms of figure

6.11, showing many of the absolute dwell differences are less than 1 mm, but with a group of dwells with an absolute error of approximately 80 mm. The directional dwell differences show a S-I distribution around zero, but the L-R distribution exhibits dwell differences of +80 mm and -80 mm. This 'bimodal' signature suggest two sequences of dwells that were delivered at opposite L-R positions in the implant, i.e. a catheter connection swap event.

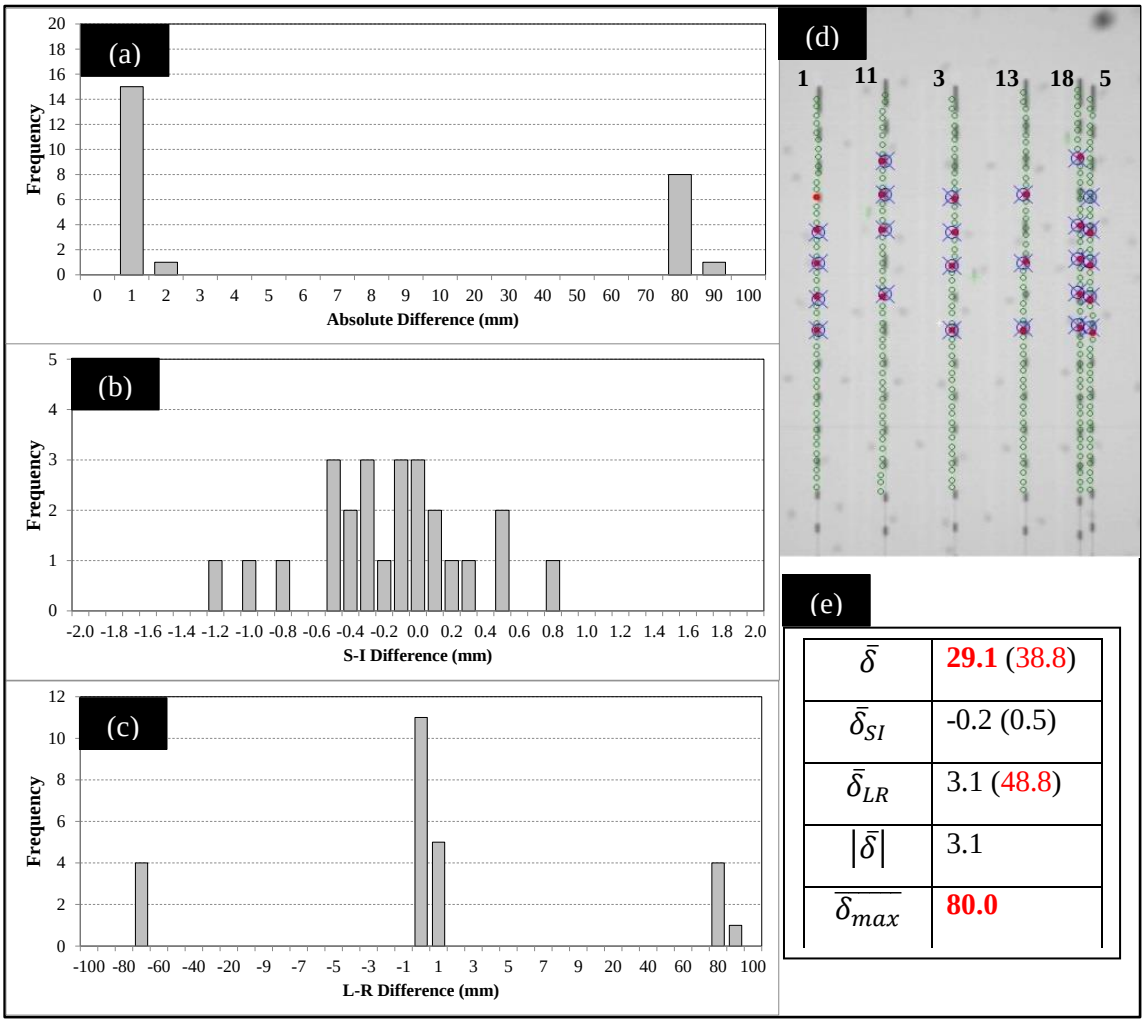

Figure 6.11. Error metric reporting for swapped channel connection error (Details are as per figure 6.9)

The visual comparison of the measured dwell positions is shown in figure 6.11(d), and due to the nature of this error, it is not easily visualised as dwells are delivered in corresponding swapped channels. But the summary of the calculated measures of

agreement highlight this error, where the mean difference and the standard deviation of the mean L-R directional difference clearly indicate a discrepancy.

The absolute individual dwell differences (δ) are illustrated with the bar graphs shown in figure 6.12, showing the dwell positions along the catheter path, that contained programmed dwell positions.

The total catheter time histograms (not shown) do not show any deviations from expectation, as in the case of incorrectly programmed channel length.

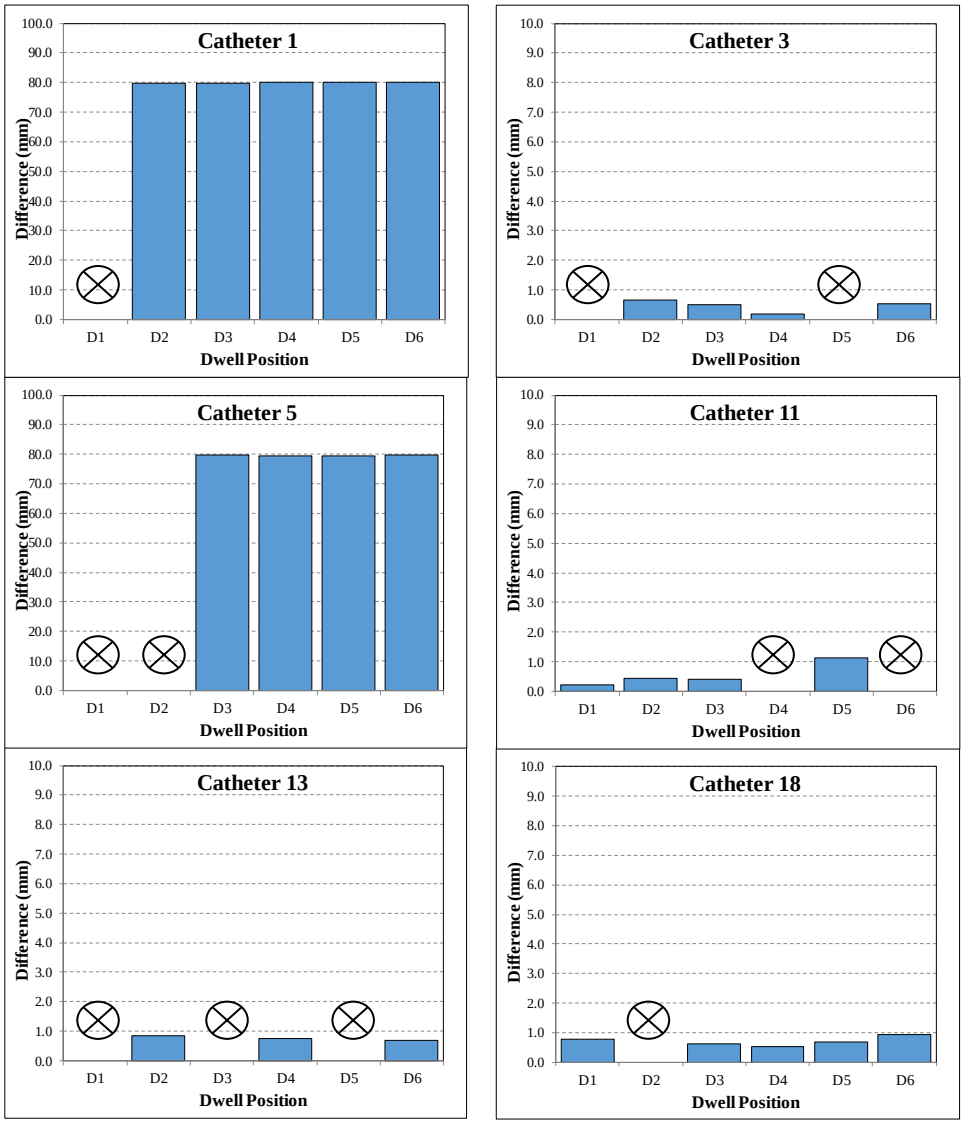

Figure 6.12 The absolute difference (δ) of each dwell position for each catheter for the swapped channel connection delivered treatment plan. The circle-cross indicates that a source dwell was not programmed for that position (refer to treatment plan in figure 6.1).

6.3.2.5 Incorrect Plan Dwell Times

The treatment plan was delivered with all dwell times increased by a factor of 2. The distribution of dwell position differences is shown in the histograms of figure 6.13, showing the absolute (a) and the directional dwell differences (b) and (c). The measured dwell positions agree to within 1.0 mm of the planned positions for 92% of the dwells. The visual comparison (d) of the measured dwell positions is also shown along with a summary of the calculated measures of agreement (e). The absolute individual dwell differences (δ) are illustrated with the bar graphs shown in figure 6.14, showing the dwell positions along the catheter path, that contained programmed dwell positions.

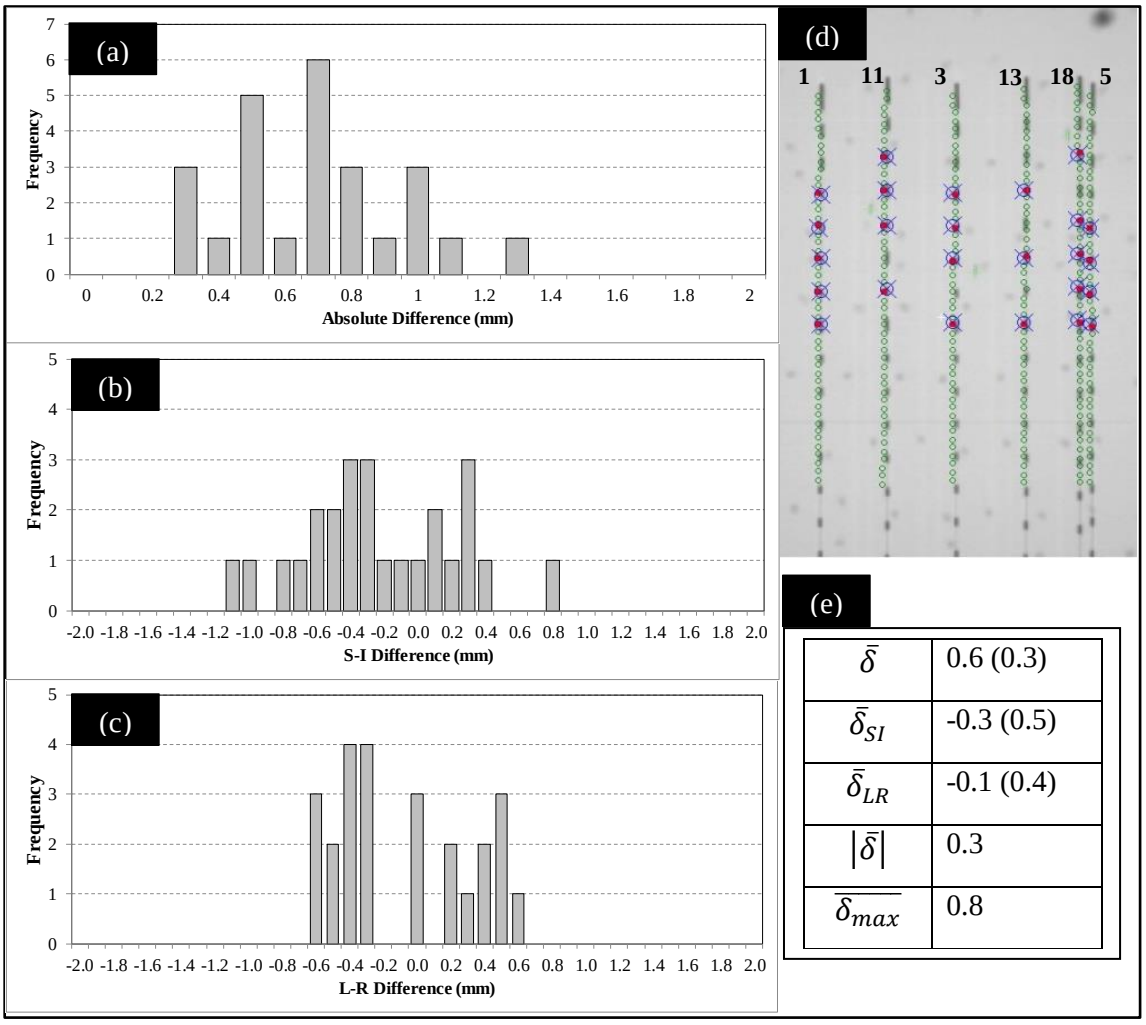

Figure 6.13. Histograms showing the distribution of dwell position differences for the incorrect dwell time treatment plan with (a) the absolute dwell difference (δ), (b) the S-I directional dwell difference (δ_{SI}), (c) the L-R directional dwell difference (δ_{LR}), (d) the visual comparison of dwell positions and (e) the summary of agreement metrics.

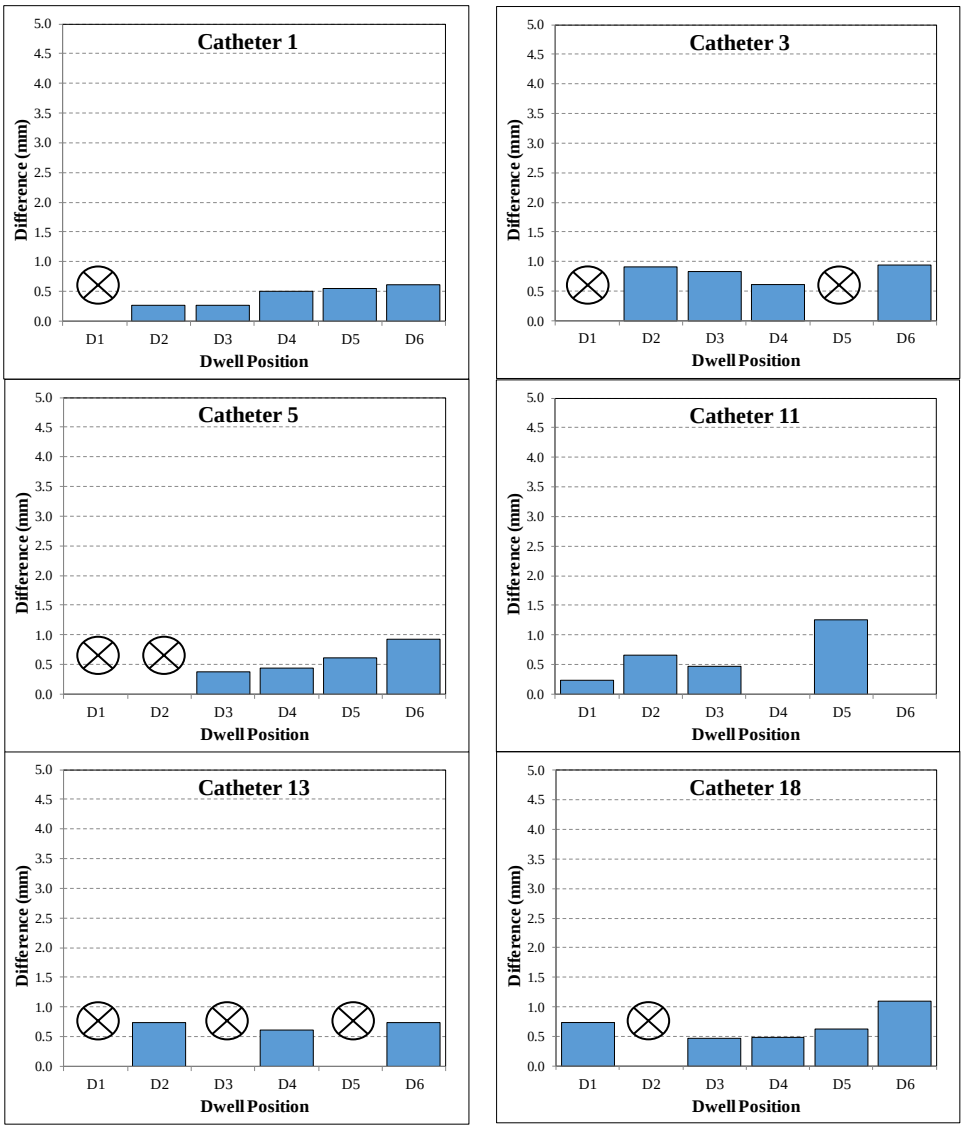

Figure 6.14 The absolute difference (δ) of each dwell position for each catheter for the swapped channel connection delivered treatment plan. The circle-cross indicates that a source dwell was not programmed for that position (refer to treatment plan in figure 6.1).

In this case figure 6.15 exhibits large catheter time errors and a large total treatment time error. To further illustrate these observed time differences, the per dwell time difference for each catheter is shown in figure 6.16, where all measured dwells are approximately twice as long as expected – in this case 5 seconds larger than the planned dwell time.

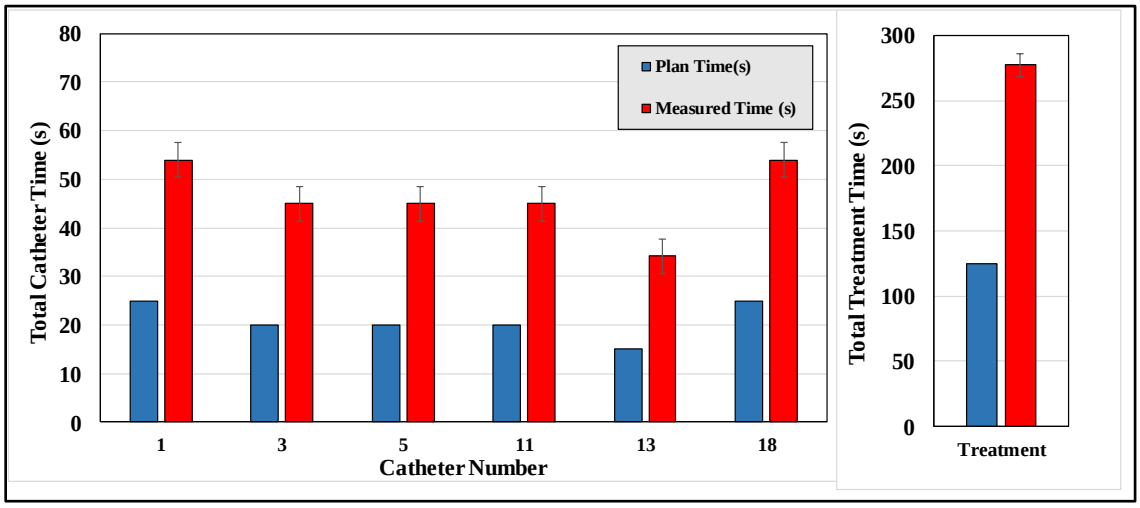

Figure 6.15 The comparison of planned total catheter time with measured catheter time of each catheter for the incorrect dwell times delivered treatment plan, where the error bars are twice the sampling interval of the FPD. The total treatment time is compared with the measured treatment time, which is a summation of each measured catheter time.

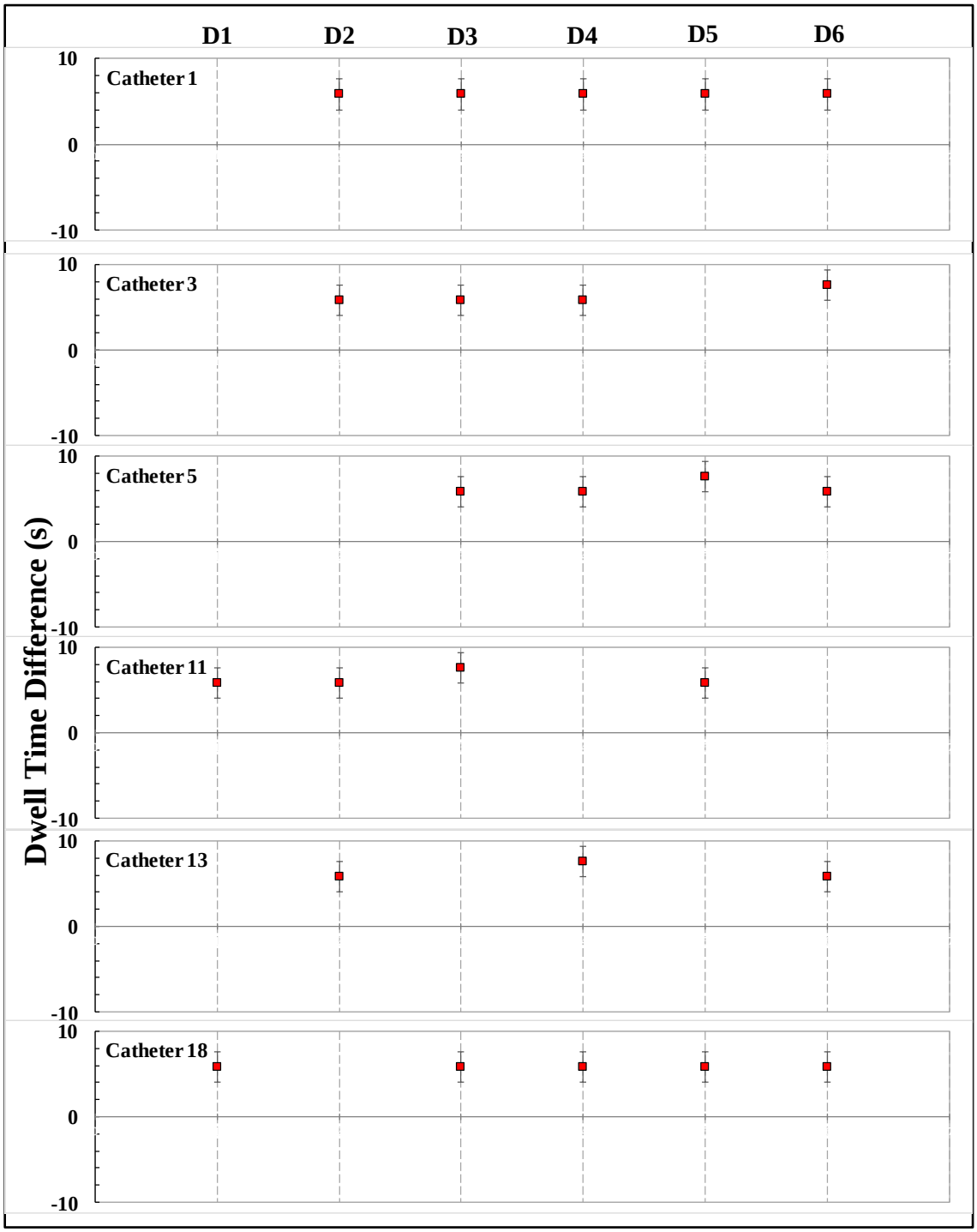

Figure 6.16 The difference of dwell time for each programmed dwell position in each catheter. The error bars shown for each data point represent the sampling interval of the FPD (±1.8 seconds).

6.3.3 Discussion

The four errors introduced into the treatment plans are intended to illustrate error events that may occur and are difficult to identify with existing approaches. Error trapping is not performed blindly, and knowledge of the treatment delivery as it proceeds is available. In this work, the treatment order of the planned catheters is used to establish the sequence of planned dwell positions for comparison with each measured dwell position. The approach is important for generating per dwell metrics that can provide absolute and directional difference metrics.

6.3.3.1 Correct Delivery

The treatment plan was delivered with no introduced errors to illustrate the comparison metrics with deviation due only to measurement uncertainties. The mean absolute dwell position difference was 0.6 mm and a maximum mean catheter difference was 0.8 mm. The spread of the directional difference histogram comparisons were less than 1.0 mm suggesting all dwell positions were delivered as expected.

6.3.3.2 Incorrect Plan Selection

Treatment of a patient with an incorrect plan is an event that can have significant consequences. Depending on the magnitude of difference between the correct and incorrect plan the treatment error may be difficult to detect. For example, a multi-fraction prostate treatment, where each treatment fraction is determined with a CT and optimised treatment plan, successive treatment fraction plans may be similar. The active catheter and the location of the dwell positions within each catheter may only be slightly different as the treatment plan optimisation deals with anatomical changes between fractions. Delivery of the incorrect treatment plan (fraction) may be difficult to identify and the target may be under-dosed and OARs over-dosed.

Another challenge for an error trapping system is how to manage an incorrect plan delivery when the number of dwells in each catheter does not match the planned number of dwells. In this approach, the system is measuring dwells per catheter, and when the dwell count is incorrect an error will be indicated. Error trapping during treatment delivery would ideally flag this as a potential error by the end of the first catheter. Investigation would still be required to distinguish this error from the case of one or more dwells that were in fact delivered, but not captured for some reason such as

very short dwell times. In the example used, catheter 5 was delivered with only 2 dwells out of an expected 4 dwells. The sequence of measured dwells, as shown in figure 6.7, confirmed the first delivered dwell (D6) was in the correct position, but the second measured dwell (D5) was incorrect by approximately 20 mm. The next two planned dwells, D4 and D3 were not measured as the 'incorrect' plan did not have any more programmed dwells in this catheter. In this case these dwells were flagged for no comparison as there was no corresponding measured dwell for comparison. The other catheters shown in figure 6.7 exhibit a 10 or 20 mm absolute difference for almost all dwell positions, confirming that the sequence the dwells were delivered is important in highlighting this type of error. In contrast, visual inspection of the dwell position agreement shown in figure 6.6(d) shows that many of the measured dwell positions appear to correspond with planned dwell positions. A broad comparison of all planned and measured points in this instance may down-grade the severity of the error suggesting only a few dwell positions were mis-aligned with the expected positions. Clearly the time profile information becomes an important component of the error signature in this case.

6.3.3.3 Incorrect Channel Length

The definition of channel length (or indexer length) is a parameter which has the potential to introduce an error if it is incorrectly specified. In at least one TPS it is possible for an operator to unwittingly accept a default channel length or enter an incorrect length for a given applicator type or channel. The error introduced to the treatment plan involved all channels exhibiting an incorrect channel length definition 5 mm toward the inferior of the implant.

The approach used here could clearly identify this systematic error due to the relationship established between the measurement frame of reference and the TPS. This enables absolute verification of measured dwell positions relative to the treatment plan and therefore the systematic offset in the treatment plan was identified. A relative verification of all dwell positions in this case would not identify this error type.

The error 'signature' associated with this error type is unique, with the metrics exhibiting mean values of displacement (e.g. the absolute mean difference) with relatively small standard deviations, showing all dwells have been displaced by approximately the same amount. In addition, the maximum mean catheter displacement

is approximately equal to the reported absolute mean difference also showing that no single catheter has been displaced by significantly more than the others.

6.3.3.4 Swapped Channel Connection

One of the most likely, and difficult to detect, treatment delivery errors to occur in HDR prostate brachytherapy is swapped channel connection error due to the large number of catheters used and the manual process of connecting the transfer tubes. The identification of this error event can occur by interrogating the metrics provided in figure 6.11. The absolute difference histogram shows many of the dwell positions were delivered correctly with differences less than 1 mm. The distribution also shows 9 dwells that were delivered to the incorrect position by approximately 80 mm. It is not immediately clear where this discrepancy is from as a visual comparison of the delivered dwells in figure 6.11(d) shows only 2 dwells delivered incorrectly. The L-R direction difference histogram (figure 6.11(c)) provides further detail, showing that 4 dwells were delivered -80 mm from their planned position and 5 dwells were delivered approximately +80 mm from their planned position. The absolute difference per catheter dataset shown in figure 6.12 illustrates that catheter 1 and catheter 5 have had the correct number of dwells delivered, but the channels have been swapped. The distance between these two catheters is 80 mm, hence the reported discrepancies.

This swapped catheter error event also has a specific signature that can identify what type of error has occurred. In this case, the histograms provide the indication that a swapped channel error has occurred. The two distinct clusters in the absolute histogram, one at zero and one at the magnitude of distance between the swapped channels. This similar distribution is observed in the L-R directional histogram.

6.3.3.5 Incorrect Plan Dwell Times

The treatment plan delivered with incorrect plan dwell times was included in this work to highlight the capability of this verification system to validate dwell time as well as dwell position. The time profile histograms form a useful component of the verification system by helping in two ways: to detect errors and also to identify the types/cause of errors when detected. The times for all dwells was increased by a factor of 2 to simulate a more likely error of time calculation that would impact all dwells rather than individual dwells.

The results obtained from the source tracking process show the treatment plan was delivered without any dwell position errors. The metrics shown in figures 6.13 and 6.14 report position distributions similar to figures 6.2 and 6.3, for the correctly delivered treatment plan. The per catheter time comparison of figure 6.15 immediately shows a discrepancy from the planned catheter times and this is also reflected by the difference in total treatment time. The measurement system using the FPD to record dwell times provides an additional dimension to this error trapping system. The time difference comparison per dwell, as shown in figure 6.16, allows the individual dwells to be verified. The FPD frame rate is relatively slow, so dwell timing resolution is quite limited, however even this low resolution data is extremely valuable in diagnosing error types.

6.3.4 Error Trapping Investigations Conclusion

The metrics described in this section have been used successfully to identify all introduced treatment delivery errors. A notable advantage of this system is the capability to perform absolute dwell position verification and not just a relative verification measurement. This enables certain error types to be identified, that would otherwise go undetected.

6.3.5 Comparison with other Error Trapping Systems

There are several other treatment verification systems proposed in the literature, as described in chapter 2, but none has the capacity to comprehensively detect all of the known classes of error (table 6.2). The power of the present system is the combination of pre-treatment imaging and source tracking. This combination enables the system to perform both relative and absolute treatment verification allowing the system to monitor and account for geometric changes in the implant that will influence the level of treatment delivery agreement observed. Furthermore, this system is equally sensitive to any dwell position error, anywhere in the implant, independent of location relative to the detector. The limitations of these other verification systems hinder their ability to identify certain classes of treatment error and the detectable errors vary across these systems.

The most directly comparable verification system is electromagnetic (EM) tracking, which performs mapping of the catheter paths immediately prior to treatment. The system described by Poulin *et al* [85] captures implanted catheter paths in a phantom,

where catheter trajectories are identified within a uncertainty of 0.7 mm, where each catheter reconstruction time is approximately 10 seconds. The reconstruction uncertainty for the 3D reconstruction approach described in this thesis is 1.0 mm (for a point 100 mm from the detector imaging plane) which is only slightly greater than the EM system, and is clinically equivalent. The obvious extension of EM tracking technology would be to integrate a sensor into the clinical source capsule to perform real time source tracking, but this is yet to be demonstrated. EM tracking in the clinical environment will require some calibration efforts to be included in the overall workflow. A proposed clinical workflow illustrated by Beaulieu *et al* [86], describes a calibration procedure to ensure all reference sensors are correctly calibrated and the imaging system is correctly registered with the EM tracking frame of reference. For the system described in this thesis, the registration of the imaging system to the tracking system occurs during the pre-treatment imaging step therefore no additional pre-calibration steps are required. EM tracking has the potential to identify treatment errors such as catheter displacement due to implant geometry changes and incorrectly defined channel length, but would not identify a swapped channel connection error.

While the present system actually tracks the source throughout the treatment delivery, others infer correct treatment delivery by comparison of a point dose with an expectation. The dose measurement uncertainty of many of these point dosimeters have been shown to be relatively small, but when used to perform in vivo measurements often large discrepancies relative to the expected value are reported. As discussed previously, these IVD approaches have limited value for treatment error detection due to a large proportion of the measurement uncertainty being due to the position uncertainty of the dosimeter. Mason *et al* [46] reported a position measurement uncertainty for a single MOSFET dosimeter of 4.1% (k=1) which results in a total plan measurement uncertainty of 12.3% (k=2). This value was used as the error detection threshold, but this is highly dependent on the location of the dosimeter and is insensitive to errors occurring far from the dosimeter position which contribute only a small percentage to the total measured dose. For 40 patients measured, only one patient measurement was identified above the error detection threshold and this was justified by likely needle reconstruction errors. Carrara *et al* [64] also quoted a large uncertainty due to detector position uncertainty (3.5%, k=1) which results in a total measurement uncertainty of 5.7% (k=1). If used as an error detection threshold, approximately 45%

of patients would have been flagged as having a treatment error. Only after re-imaging of the volume (post treatment) to verify the catheter (source) to detector distances, was the error detection rate reduced to approximately 18%. Both of these recent publications, where integrated measured dose is used as a surrogate to identify treatment delivery errors, are examples of how limited this approach is as a real time error detection mechanism. To overcome these limitations Johansen *et al* [115] describe a time resolved in vivo dosimetry system for performing source tracking during HDR prostate brachytherapy. A single radioluminescent crystal dosimeter was used inside a dedicated catheter, additional to the implanted clinical catheters, and acquired readings of dose rate every 50ms. The measured dose rate at each dwell position was then used to reconstruct the likely position of each dwell position relative to the dosimeter. This approach was then used to identify catheter displacements with an uncertainty of approximately 1mm. The approach also can catch some swapped catheter connection and incorrect indexer length treatment delivery errors. But currently these discrepancies are only relative to the dosimeter and not to the surrounding patient anatomy. The system described in this thesis combines imaging and source tracking, therefore discrepancies relative to the patient anatomy are possible.

One key advantage of IVD over source tracking is to perform measurements that can be used to monitor organ at risk dose. The exact position of the dosimeter in this approach is not critical, as the dosimeter is likely to move with the organ as the patient geometry changes. But the resulting monitored dose value can be used as a safety system to monitor and limit organ total dose. Improved detector design, incorporating fiducial markers in the detectors has produced improved confidence in localising detector position during pre-treatment imaging, as illustrated by the Urethral dose measurements performed by Suchowerska *et al* [50]. The addition of detector localisation improved the agreement of measured to predicted dose to be less than 10% for all patients.

Small detector measurement volumes and angular and energy independence, such as the PSD [43], provide reduced uncertainty in dose measurements, but only sample the treatment volume at a single point. This approach limits the ability to identify treatment errors that have a spatial ‘signature’, (swapped catheter connection, incorrect channel length) as described in this chapter. IVD may flag a swapped catheter connection error, but would be incapable of identifying what type of error caused the IVD measurement discrepancy. Furthermore, in certain geometries where the incorrect source to detector

distance is similar to the correct source to detector distance (mirrored swapped catheter error), an error is unlikely to be identified.

The concept of real time treatment verification using a C-arm operated in fluoroscopic mode was demonstrated by Nose *et al* [73]. Although this is real time, the approach is limited to only detecting gross errors, as there is no indication of where the expected dwell position is located relative to the observed patient anatomy. Without an absolute reference to the treatment plan, the identification of treatment errors is subjective by performing a visual comparison between the fluoroscopic screen and a plan printout, which limits the effectiveness of this approach. The system proposed in this thesis has the potential to identify errors in real time, establishes a direct reference between the treatment geometry and the treatment plan by performing pre-treatment imaging, and uses an algorithm to determine if an error has occurred.

This verification system produces large amounts of data that can be interpreted to not only flag that an error has occurred, but also to suggest the potential source of the error. The identification of the error type occurs due to the signatures that different error types produce across the measured data. These error signatures are further explored in the next section where specific detection metrics are summarised for their sensitivity to particular error events.

6.4 Summary of 'Error Signatures'

This verification system produces large amounts of data that can be interpreted to not only flag that an error has occurred, but also to suggest the potential source of the error. The identification of the error type occurs due to the signatures that different error types produce across the measured data. These error signatures are further explored in the next section where specific detection metrics are summarised for their sensitivity to particular error events.

The detection of a treatment error involves evaluation of many metrics in parallel that support an error event and can direct the operator to the likely cause of the error. Table 6.2 summarises the error event and the likely detection by each defined metric. M^x represents that the error may be detected but is particular to the characteristics of the error and is further quantified in the text below the table.

Table 6.2. The summary of error events and detection metrics, showing the sensitivity of each metric to an error event. Y = sensitive, N = not sensitive and M^x = maybe -with a description of the signature below.

Error Events	Visual Comparison	Mean Diff. ($\bar{\delta}$)	S.D. Mean Diff. (σ)	Mean Dir.Diff.($\overline{\delta_{LR}}$) ($\overline{\delta_{SI}}$)	S.D.Mean Dir.Diff. (σ_{LR})(σ_{SI})	Abs. Mean Dir. Diff. ($\overline{\lvert\delta\rvert}$)	Max. Mean Cath. Diff. ($\overline{\delta_{max}}$)	Histo. Abs. Dwell Diff.	Histo. Dir. Dwell Diff.	Abs. Dwell Diff. Profiles	Dwell / Cath. / Tmt. Times
Incorrect Plan	M^1	**Y**	**Y**	M^2	M^3	**Y**	**Y**	**Y**	**Y**	**Y**	M^4
Incorrect Channel Length	**Y**	M^5	M^6	M^7	M^8	**Y**	**Y**	**Y**	**Y**	**Y**	**N**
Swapped Channel Connection	M^9	**Y**	**Y**	**N**	M^{10}	**N**	**Y**	**Y**	**Y**	**Y**	**N**
Incorrect Dwell Times	**N**	**N**	**N**	**N**	**N**	**N**	**N**	**N**	**N**	**N**	**Y**

Incorrect Plan

- M^1 – The visual comparison of the dwells may not necessarily indicate a treatment error has occurred. If the incorrect treatment plan contains dwell positions that are very similar to the desired plan (possibly a successive fraction), then the overlay of dwell positions may not be significantly different.
- M^2 & M^3 – The distribution of the measured dwells of the incorrect plan may not vary significantly from the correct plan. There is a possibility that the L-R direction distribution is similar to the original plan and so this metric on its own may not flag an error event.
- M^4 – It is not likely that the dwell time of the incorrect plan with be the same as the correct plan. There is a possibility that the total catheter times may resemble the planned times and so in this case these metrics on their own may not flag an error event.

Incorrect Channel Length

- M^5 – If all the catheter channels have been assigned an incorrect channel length, then the mean difference metric will be a strong indicator of an error and will resemble the incorrect offset applied to the channels. If only one or a few channels have been assigned incorrectly then this metric on its own may not necessarily flag an error event.
- M^6 – The standard deviation of the mean difference metric will flag an error in combination with the mean difference metric. A small value will suggest all channels have been assigned the incorrect channel length.
- M^7 – The mean directional difference metrics are likely to be valuable in the SI direction. If all the catheter channels have been assigned an incorrect channel length, then the metric will resemble the incorrect offset magnitude and direction, where a positive value represents an inferior offset.
- M^8 – The standard deviation of the mean directional difference metrics in combination with the mean directional difference will provide additional support of an error event in the case where all catheters have been assigned incorrectly.

Swapped Channel Connection

- M^9 – The visual comparison of dwell positions may not clearly define a swapped channel connection event. The measured dwell positions will appear along the corresponding swapped catheter path and so may not be apparent to the operator.
- M^{10} – The standard deviation of the mean directional difference metrics will identify an error in the LR direction. The magnitude of this reported value, in conjunction with a small value for the mean directional difference metric, will be a strong indicator of an error and represent approximately half the distance between the catheter paths of the swapped channels.

6.5 Extension to Real-Time Error Detection

The error detection investigated throughout this chapter has used a retrospective evaluation of the data. During this developmental phase, the system was used in a non-interventional (retrospective) mode to improve the understanding of the system's

capabilities, and to develop ways of presenting data to the operators/treating staff. All dwells were measured by the verification system and, after the treatment delivery, analysis was performed to verify correct delivery. As shown, this retrospective approach is comprehensive but it does not enable immediate action to be taken on an identified error to minimise the potential harm to a patient.

The natural progression of a system is to perform the dwell position evaluation in real-time, as the treatment is delivered, and using the range of error detection metrics available, establish if the treatment is proceeding according to the plan. The 5 treatment plans delivered to the phantom in section 6.2 were re-analysed in the dwell delivery order (to mimic real-time evaluation) and the sequential error detection metrics were calculated.

The goal of error trapping clinical implementation is to continually monitor these metrics and when a metric reaches an investigation threshold, the operator could be notified of the discrepancy. If the metric reaches the action level threshold, the HDR brachytherapy afterloader could be triggered to halt treatment while the source of the identified error is determined. Some of the error trapping metrics described in section 6.2 could be plotted in 'real-time' (dwell delivery sequence) as the treatment progresses. For example, the absolute individual dwell difference (δ) metric is shown in figure 6.17 for the correctly delivered plan and for each introduced error event. Potential investigation and action levels are also shown.

In the case of swapped catheter channels, as illustrated in figure 6.17, the first delivered dwell position is incorrect by 80 mm, this metric would flag an error and halt treatment. The human error could be corrected, the plan my need to be modified to account for the incorrectly delivered dose, and the potential damage to the patient is minimised. The combination of other error metrics in real-time will allow identification of the potential error source, similar to the errors that are flagged in table 6.2.

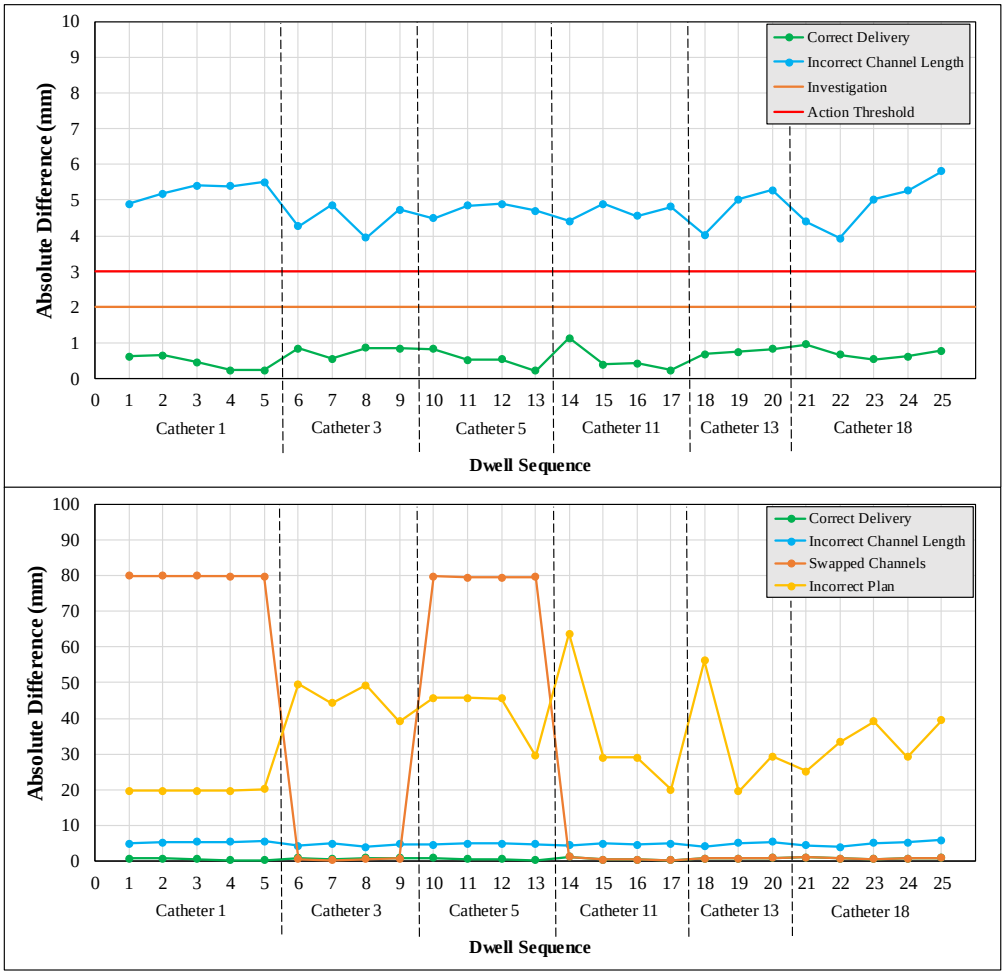

Figure 6.17. A concept for error metric presentation for real-time treatment verification. The absolute difference of each individual dwell is presented as each dwell is delivered in sequence. The correct plan and the 4 introduced error types are shown.

6.6 Conclusion

This chapter has illustrated the capability of this system as an error trapping device in HDR brachytherapy. A key advantage of this system is the rich source of data that can inform the treatment staff of treatment delivery status. The combination of information from data visualisation tools and metrics can aid in the identification and source of errors. The interpretation of the error 'signatures' are possibly amenable to automation, or at least algorithmic guidance. Expert interpretation is still recommended for evaluation of the information presented, for example the 'incorrect plan' demonstrates the complexity of interpretation.

The error trapping concepts explored in this chapter will apply even to other treatment verification systems, for example electromagnetic source tracking implementations. One of the greatest challenges will be to refine the techniques used to present the information to the operators in a meaningful, clear, efficient and unambiguous way. It is expected this will evolve with experience. Another significant factor in making such a system useful to clinical staff is a smooth integration into the treatment procedures. The integration into a clinical environment is explored in the next chapter.

Chapter 7
Clinical Implementation

7 Introduction

The aim of the final part of this work was to transfer the methods and knowledge obtained in the previous chapters into the clinical environment where it will provide a direct benefit to patients. The translation of a phantom based study to the clinical environment can be a difficult process. Integration of new processes into an existing treatment workflow, without significantly adding to treatment procedure time is challenging. This chapter describes the steps taken to implement this treatment verification system in a HDR brachytherapy clinical environment. Modifications made to the treatment couch to accommodate the FPD and the x-ray equipment added to the treatment bunker to perform pre-treatment imaging is also covered. The clinical workflow was slightly modified, establishing a straight-forward approach, permitting verification to be performed routinely. Clinical results are presented for an example patient using the pre-treatment imaging and source tracking verification process.

7.1 Introducing Treatment Verification to the Clinical Environment

HDR prostate brachytherapy has been performed since 1998 at Alfred Health Radiation Oncology (AHRO), Alfred Health, Melbourne, Australia, as a boost to the EBRT schedule. CT data is used for treatment planning and the HDR brachytherapy prescription dose is delivered in two treatment fractions. The patient is transferred from the hospital ward bed onto the CT couch for treatment planning imaging using an air driven hover mattress. Moving the patient between the bed and the CT imaging couch

increases the risk of disturbing the brachytherapy implant geometry. To further reduce this risk at treatment, the patient remained on the hospital ward bed in the HDR brachytherapy bunker, as shown in figure 7.1. Only an external check of the catheters positions relative to the template was performed, no verification of the catheter positions using imaging was done.

Figure 7.1. The connection of afterloader transfer tubes in preparation for treatment delivery in the HDR brachytherapy bunker. The patient remains on the hospital ward bed for treatment.

Establishing treatment verification in this clinical environment, which is similar to most CT based HDR brachytherapy clinics, was challenging as the treatment procedure does not easily lend itself to verification using the system described in this work. Although treating the patient on a hospital ward bed eliminated another movement that may potentially disturb the implant geometry, the uncertainty of the implant position due to the non-reproducible patient setup on a soft mattress was of greater concern. Furthermore, even if the FPD could be integrated into the ward bed patient setup, implant position verification imaging would be extremely difficult as the patient geometry does not reflect the reference geometry used for treatment planning.

A change of clinical practice was introduced and the patient was transferred from the ward bed on to the brachytherapy treatment couch, containing the FPD, using a hover mattress. Any deviation of the implant geometry after the treatment planning CT (either due to swelling or patient movements) is identified and accounted for during image verification.

The following sections in this chapter describe the development of a treatment couch to contain the FPD, additional x-ray equipment installed in the bunker (to provide 3D implant position verification), patient setup, pre-treatment imaging and the source tracking procedure.

7.1.1 Treatment Couch Design

A treatment verification couch was designed which allowed integration of the FPD into the couch and permits the patient to be set up, in a position that closely matches that at treatment planning imaging (CT), in the HDR brachytherapy treatment bunker. An existing brachytherapy treatment couch, shown in figure 7.2, was previously used for treatment of other anatomical sites. This treatment couch (Betastar, Maquet Getinge Group, Sweden) is very typical of an operating theatre couch, has a modular design, allowing end sections to be removed if required.

Figure 7.2. The HDR brachytherapy couch at AHRO used for treatment of other anatomical sites. The couch can be tilted and couch ends can be removed for various setup requirements.

A couch end attachment was designed that could host the FPD and support the pelvis of the patient above the detector imaging region and this design is shown in figure 7.3. The FPD was mounted below the patient allowing source tracking and pre-treatment imaging to occur. Positioning the FPD below the patient (rather than above the patient) produced the shortest brachytherapy source to detector distance for a prostate patient, and reduced possible air gaps limiting the influence of inhomogeneities during the source tracking process. The patient's weight was also supported by a low density

carbon fibre couch top, protecting the sensitive region of the FPD, while not interfering with imaging.

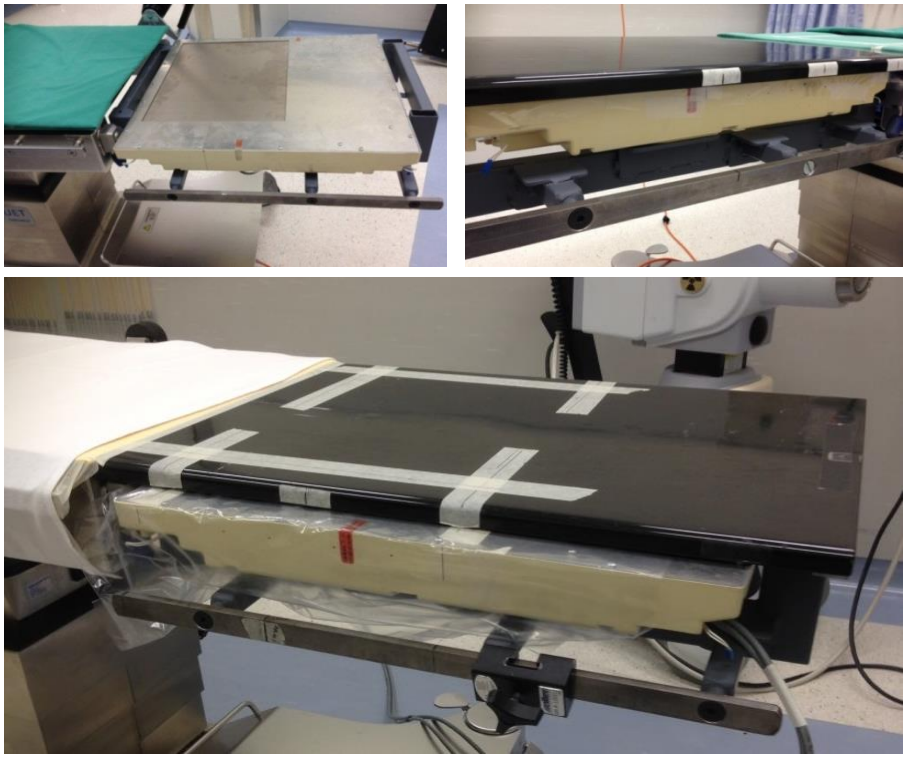

Figure 7.3. The treatment verification couch design incorporating the FPD below the patient and a carbon fibre couch top to support the patient. The side rails allow attachment of leg support stirrups allowing the patient to be set up in a position that closely matches treatment planning imaging.

Side rails were also added to the couch end attachment allowing patient leg support stirrups to be mounted. This provided a method to support and lower the patient legs to approximately horizontal, again to reproduce the CT imaging setup.

7.1.2 Treatment Room Modifications

HDR brachytherapy treatment bunkers are not typically designed with treatment verification in mind and therefore lack components that assist with the verification clinical workflow.

Moving the patient on to the treatment couch is swift using the hover mattress system, but aligning the brachytherapy implant (pelvis) above the sensitive region of the FPD

can be challenging due to the hover mattress and other hospital bedding obscuring the imager localisation marks on the treatment couch. To overcome these potential problems, a laser system was installed in the HDR bunker, similar to a LINAC bunker laser system. Two lateral cross lasers and one sagittal laser was installed, so the couch could be aligned to the laser isocentre at the centre of the FPD imaging device (L-R & S-I). In addition to positioning the patient, the lateral cross lasers also enabled replication of the patient pelvic rotation at CT imaging using skin marks (See figures 7.7 and 7.9(a)).

To perform pre-treatment imaging, using the FPD as the image receptor, an in room x-ray source was required. This was initially achieved by using a mobile x-ray system (AMX-4, GE Medical Systems, Milwaukee, Wisconsin, USA), on loan from the hospital Radiology department, and is shown in figure 7.4.

This mobile x-ray system was used during our initial clinical work, but it became clear that positioning the x-ray source at a known distance (*FID*) was a challenge, as the system is not designed for such accurate positioning. The mobile device is quite bulky and in a relatively small brachytherapy bunker, the device was difficult manoeuvre and position. This type of system does not lend itself to perform shift imaging (as described in section 5.4.1), and so only 2D pre-treatment imaging was possible.

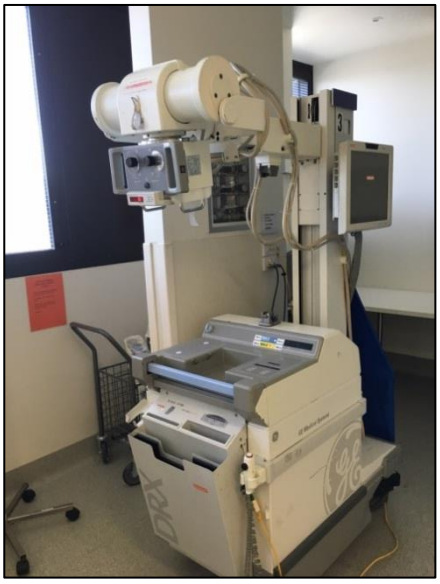

Figure 7.4. The mobile x-ray system GE AMX-4 model from Radiology department used initially for 2D pre-treatment image verification.

To overcome these limitations, AHRO installed a ceiling suspended x-ray system (QRad OTS x-ray suspension system, Carestream Health, Rochester, NY, USA) in the HDR brachytherapy bunker, as shown in figure 7.5(a). The ceiling suspended x-ray system moves in all directions by rolling along perpendicular rails suspended below the ceiling. The height of the x-ray head can be moved via a telescopic extension and the x-ray head can also be rotated. Mechanical stops were added to the rails, relative to the central axis position of the FPD, to provide reference stop positions left and right (laterally) of the patient. These stop positions provide swift positioning movements during the pre-treatment imaging process, reducing the procedure time. When the system is not in use during a clinical case, it can be parked in the corner of the room, as shown in figure 7.5(b), providing access to move around the treatment room.

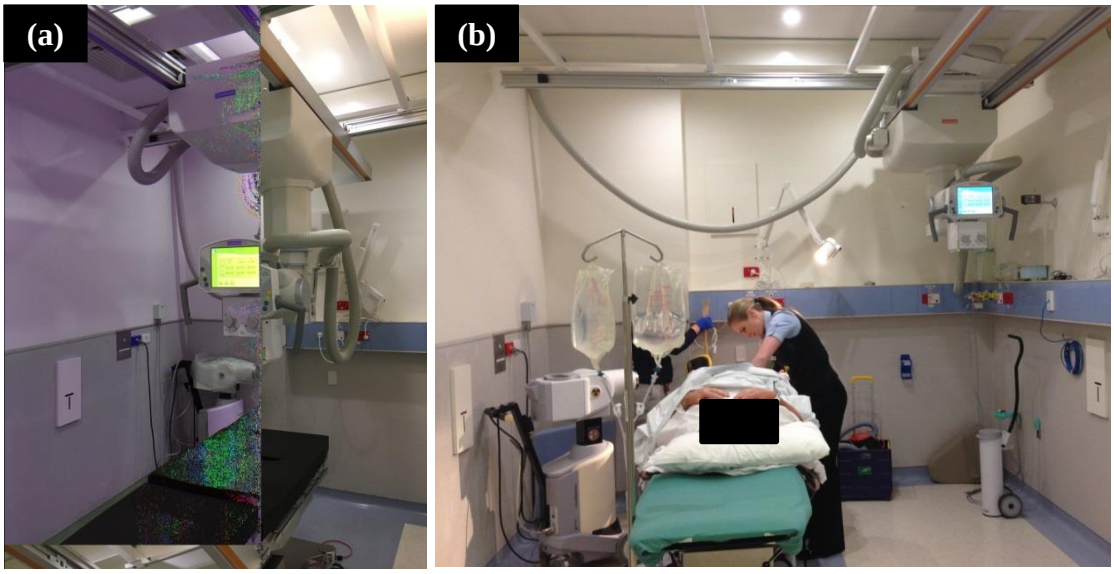

Figure 7.5. (a) The treatment room ceiling suspended x-ray system used for pre-treatment imaging and (b) the system parked out of the way during a clinical case.

7.1.3 Clinical Workflow Changes

The clinical workflow was modified to accommodate the addition of pre-treatment imaging and source tracking verification. The additions to the clinical workflow are shown in green, as illustrated in figure 7.6. The flowchart indicates the steps taken to implement treatment verification and the approximate time frame from patient arrival at the treatment bunker to the start of treatment delivery.

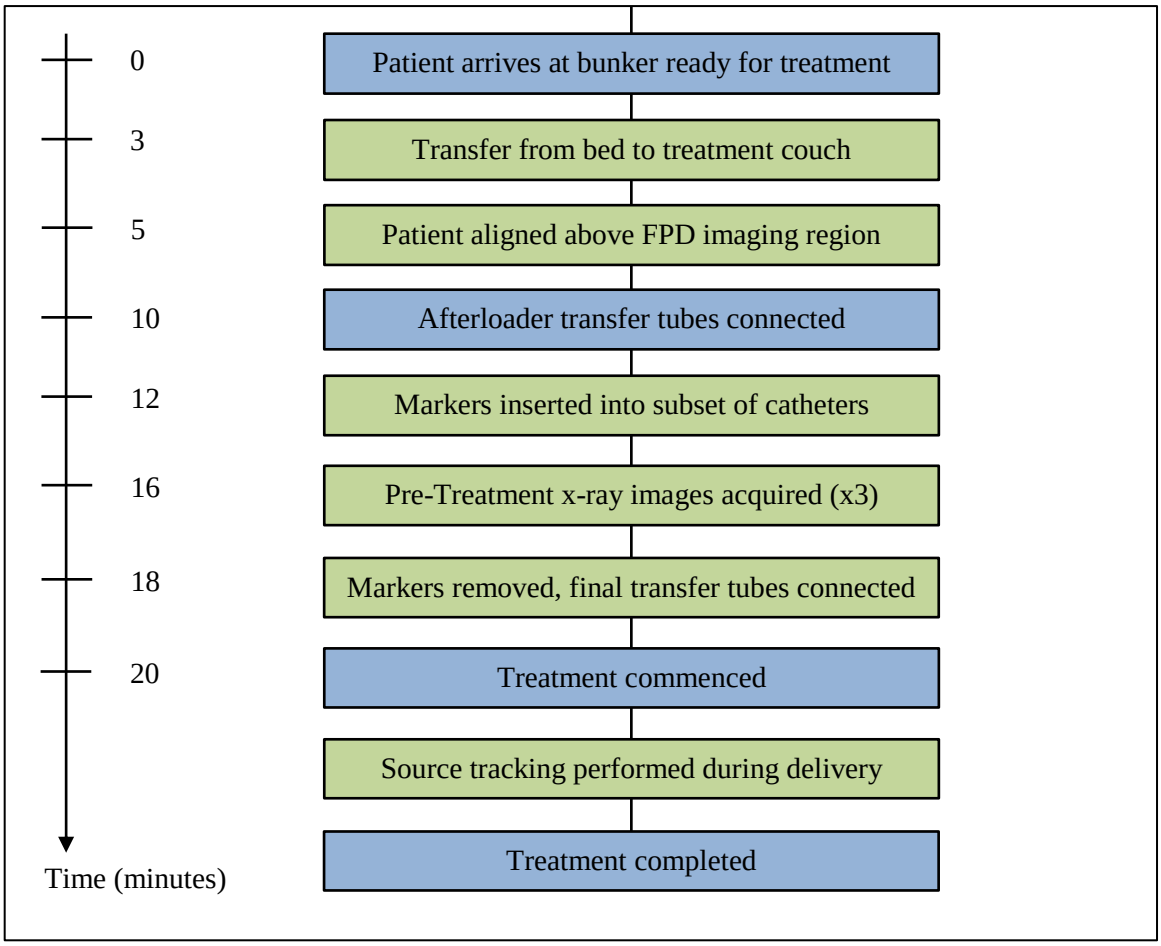

Figure 7.6. The HDR prostate brachytherapy treatment verification workflow performed at AHRO. The green boxes represent additional steps included in the workflow to implement treatment verification.

The only workflow change that occurs prior to the patient arriving at the treatment bunker (not described in figure 7.6) occurs at the CT imaging step. Skin marks are drawn on the patient's pelvis, as shown in figure 7.7, using the CT lasers to capture the observed pelvic rotation.

Figure 7.7. Skin marks drawn on the patient at CT imaging to capture the observed pelvic rotation. The skin marks are then used to align the patient at treatment using the treatment bunker lasers.

At treatment, the patient is transferred to the treatment couch using the hover mattress. The patient legs are placed in the stirrups attached to the couch and lowered to a horizontal position. The skin marks on the pelvis are aligned with the treatment room lasers to centre the implant over the FPD and to replicate the set up seen at CT imaging.

The afterloader transfer tubes are connected to the brachytherapy implant, except for 5 catheter channels that have been designated to be used for imaging. Radio-opaque x-ray dwell position markers are inserted into these channels in preparation for imaging. An A-P image and two ‘shift’ (oblique) images are acquired using the process described in chapter 5 (and illustrated in figure 5.23).

The A-P image is registered against the treatment plan (as described in section 5.3.4) and the planned catheter positions are directly compared with the measured catheter positions. A decision based on any measured catheter displacement is then made by the Radiation Oncologist and treatment proceeds if determined to be below some clinical threshold. The two captured ‘shift’ images are evaluated offline. The x-ray markers are removed, the final few transfer tubes are connected, and the treatment commences.

During treatment delivery source tracking is performed, with the FPD operated in 'continuous image acquisition' mode, capturing images of the source radiation exiting the patient. The source tracking images are then processed and evaluated offline.

Once treatment is completed, the patient is disconnected from the brachytherapy afterloader, and returned to the hospital ward bed using a hover mattress.

7.2 Example Clinical Case

This section describes in detail the end-to-end verification process performed for an example case and illustrates the analysis of the data obtained using the methods described in the previous chapters of this thesis.

7.2.1 Method

The initial implementation of this verification system in the clinical environment was performed as a passive study, and no intervention was performed, unless gross errors were observed. Visual comparison of the A-P image and plan was done online, but further analysis of the acquired verification data was performed post-treatment.

7.2.1.1 Treatment Protocol

The Alfred Health Radiation Oncology department currently performs HDR prostate brachytherapy boost along with an external beam component. Our technique is similar to that of many modern HDR prostate brachytherapy programmes, where up to 18 plastic catheters (Proguide^{TM}, Elekta AB, Stockholm, Sweden) are inserted into the prostate, and HDR brachytherapy treatment is delivered with a remote afterloader (microSelectron^{TM}, Elekta AB, Stockholm, Sweden) in two fractions of 8.5 Gy. Treatment planning with the Oncentra TPS (Oncentra, v4.3, Elekta AB, Stockholm, Sweden) is based on CT imaging which is performed at each treatment fraction[116].

7.2.1.2 Treatment Procedure

While the patient was anaesthetised in the operating theatre, the plastic catheters were inserted into the prostate and guided into position using trans-rectal ultrasound (TRUS) imaging. Three gold fiducial markers were implanted into the prostate and placed in the anterior, mid and base regions of the prostate. A CT scan was performed for treatment

planning purposes and skin marks were added for reproducible patient set up at treatment, as previously shown in figure 7.7. The treatment plan was created using the TPS following our departmental protocol.

Figure 7.8. The patient transfer process from the ward bed to the brachytherapy treatment verification couch performed with a hover mattress. The patient lies on a flat couch replicating the setup at treatment planning imaging (CT) and the legs are supported with stirrups.

At the time of treatment, the patient was transferred on to the treatment couch containing the FPD as shown in figure 7.8. The patient was aligned such that the target (implant) region was centered over the sensitive imaging area of the FPD. The position of the patient on the treatment couch, specifically the hip rotation, was adjusted to replicate the supine position of the patient during the planning CT scan. This was achieved by aligning the patient skin marks to the in room lasers (figure 7.9(a)) and supporting the patient's legs in stirrups (Yellow Fins^{TM}, Allen Medical, Acton, MA, USA), attached to the treatment couch, as depicted in figure 7.9(b).

Figure 7.9. (a) Alignment of the patient over the sensitive region of the FPD using the treatment room lasers and replicating the pelvic rotation with skin marks. (b) The patient in treatment position in preparation for pre-treatment imaging, replicating the legs down position at CT.

A subset of the total number of implanted catheters (5 catheters) were designated to be used for pre-treatment imaging. A subset of catheters was used for pre-treatment imaging for three reasons: (i) to avoid excessive marker overlap in the pre-treatment images, (ii) to consider the workflow timeline and limit additional work and (iii) minimise the time between pre-treatment imaging and source tracking. These catheters are selected to represent the extent of the implant geometry, and so catheters are idealy selected from the posterior template row, left and right positions and the anterior template row. Using the information obtained from the CT data, an informed selection of these catheters was possible, minimising potential projection overlap on the A-P image.

Radio-opaque x-ray dwell position markers were inserted into the selected catheters, as shown in figure 7.10(a). The ceiling suspended x-ray system was moved into position above the patient as shown in figure 7.10(b). A single A-P image was acquired using the FPD as the image capture device and the imaging geometry defined in figure 5.2. To correct for divergence in the image and to localise the x-ray source with the FPD, a BB array was included in the image capture (Section 5.3.2).

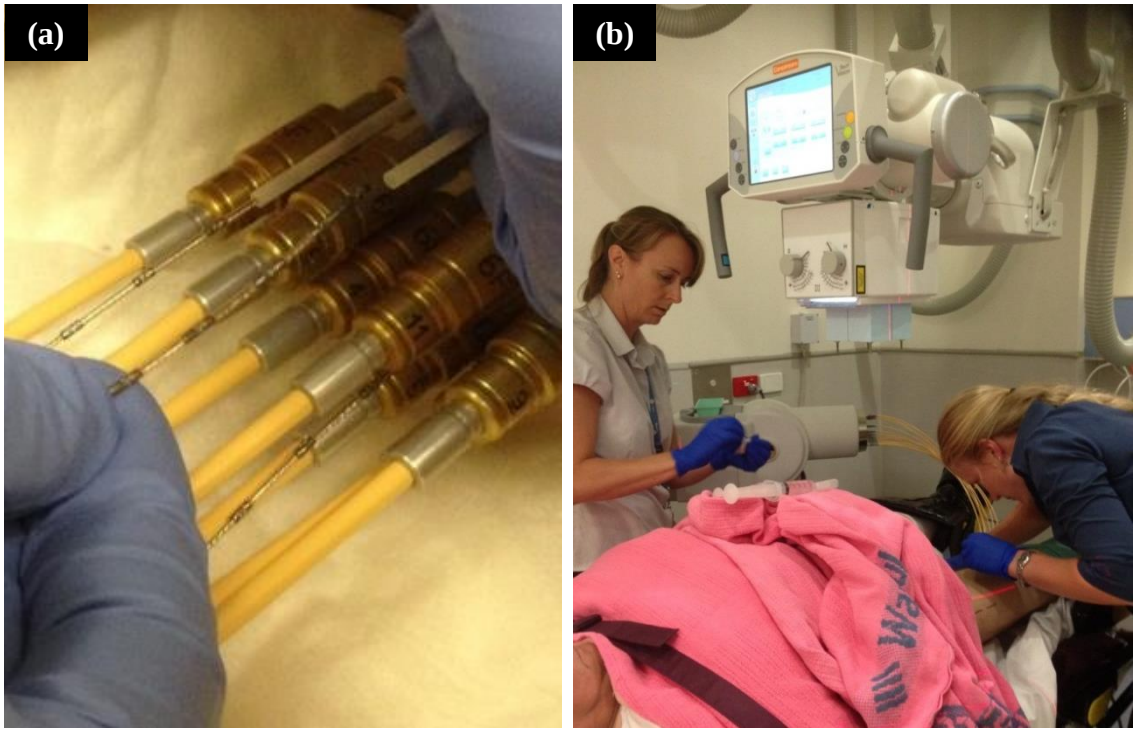

Figure 7.10. (a) The x-ray markers being inserted into the selected subset of catheters in preparation for pre-treatment imaging. (b) The ceiling suspended x-ray system above the patient ready for imaging. The BB array is mounted below the x-ray collimator and is included in the A-P x-ray image.

The BB array was removed and the shift imaging was performed according to the procedure previously described in section 5.4.1. The x-ray dwell position markers were removed from the catheters, and the few remaining transfer tubes were connected and the HDR brachytherapy treatment commenced.

For source tracking during treatment delivery, the FPD was operated in 'continuous acquisition' mode as described in section 3.13. The capture process acquired a sequence of 'images' of patient exit radiation, as the source progressed through the programmed dwell positions, at a rate of 1 image every 1.8 seconds, where each image consists of 1 reset frame and 4 frame averages. The source tracking frame rate (0.625 fps) limits the acquisition of very short programmed dwell positions. Planned source dwell positions with dwell times greater than 3.2 seconds (2× acquisition period) were captured with at least one image (at each dwell position) containing no artifact due to source motion.

Once treatment was completed, the sequence of images was processed to determine the source coordinate in the plane of the FPD. The measured dwell positions were then calculated from the sequence of source coordinates using the methods described in section 4.5, and these were then directly compared to the treatment plan for verification.

The following sections describe the various comparisons of measured data with the treatment plan, each providing confirmation of aspects of treatment parameters, in order to achieve overall treatment delivery verification.

7.2.1.3 2D Pre-Treatment Image Verification

The A-P image acquired immediately before treatment was used to evaluate the current catheter positions immediately prior to treatment and identify any displacements. The image was processed using methods previously described in chapter 5. For clarity, the process is summarised by the following points:

- Projected BB marker pairs were identified and are used to correct for image divergence
- The fiducial markers visible in the image were identified and positions marked
- The catheter paths observed in the image were identified and positions marked
- Registration with the TPS was performed (described in section 5.3.4)
- Planned catheter paths were projected onto the A-P image
- Comparison of planned and measured catheter positions was performed using the methods established in section 5.3.2

The 2D pre-treatment image processing described above was performed using in-house software enabling comparison of the catheter positions to be performed at the treatment console (Appendix C: Pre-Treatment Verification 2D). The projected BB pairs were manually selected by the user, and the centres of the BBs were calculated by performing a pixel threshold on a ROI surrounding each selected BB. A COM algorithm was then applied to determine the centre pixel position of each BB. The intersection point of the BB array was calculated using the method described in section 5.3.3 to determine the x-ray CAX. The three fiducial markers were identified by the user selecting the centre of each marker visible on the A-P image. Each of the 5 catheters were identified in the A-P by using the unique ‘dot-dash’ labelling of the

markers. The user then selected the centre of each catheter marker along its path to define the absolute position for comparison with the TPS. The treatment plan was exported from the TPS and imported into the in-house software, and a registration performed (section 5.3.4) using the 3 fiducial markers also specified in the treatment plan. The planned catheter paths imported from the treatment plan were then transformed into the measurement frame of reference using the transformation determined by the registration and these transformed planned catheter paths were overlaid on the A-P for direct comparison with the measured catheter paths.

7.2.1.4 3D Catheter Reconstruction Image Verification

The two 'shift' images acquired prior to treatment delivery were processed post treatment due to treatment time constraints. The images were used to establish a 3D representation of the catheter positions using the back projection reconstruction approach previously defined in section 5.4.2. A summary of this method is as follows:

- The corresponding catheter marker points for each catheter are identified and marked in each image
- The corresponding fiducial marker points in each image are identified and marked.
- Using the known image acquisition geometry, the catheter points and the fiducial marker points are back projected to create a 3D representation of the implant geometry (see figure 5.2.4)
- 3D registration of the reconstructed fiducial markers with the TPS is performed (see section 5.4.4)
- Comparison of planned and measured catheter positions was performed using the methods established in section 5.4.7

The shift images acquired during the pre-treatment imaging process were processed post-treatment using in-house software (Appendix C: Pre-Treatment Verification 3D). Each corresponding catheter is identified in each image using the 'dot-dash' marker labelling. The user manually selects corresponding marker points of each catheter until the path of each catheter is defined. The user also manually selects the corresponding fiducial markers in each image. The software performs the back projection of the catheters and fiducial markers as described in section 5.2.4 to calculate the 3D definition of the catheter paths and fiducial marker positions. The treatment plan is

imported and the software performs a 3D registration with the defined fiducial markers. The planned catheter paths are then transformed into the reconstructed implant (measurement) frame of reference and the catheter positions were then compared in 3D.

7.2.1.5 Source Tracking

The images acquired during source tracking were processed post-treatment to verify the positions of the source dwells. The sequence of images acquired for each catheter were processed using the COM approach defined in section 4.2.1.3 to calculate the 2D coordinate of the source in the plane of the FPD. The sequence of calculated source coordinates (one per image) for each catheter were further processed to establish the measured dwell position. Each measured dwell position is derived from a collection of calculated source coordinates, that are within a spatial threshold (as described in section 4.5) where the dwell position co-ordinate is the mean of the source coordinates collection.

The aim of this processing is to filter (a) measured dwell positions that are calculated from images that are a summation of multiple short dwells, and (b) calculated dwell positions that have almost identical coordinates, but differ due to measurement uncertainties.

The measured dwell positions were then compared to the planned positions for each catheter using the software developed in-house (Appendix C - 'Patient Analysis').

The measured positions were compared to the planned positions as defined by the TPS. Therefore, possible agreement achievable between measured and planned positions was limited by the implant changes observed at pre-treatment imaging. The error detection metrics used to describe the agreement are defined in section 6.2

7.2.1.6 Individual Catheter Treatment Times

During the source tracking process the verification system is continuously acquiring images. For each catheter, the acquisition starts before the source leaves the afterloader safe and continues until the source returns to the afterloader safe. The resulting set of images therefore contains a period of blank images at each end of the sequence. The total catheter treatment times were measured by using an algorithm to extract the timestamp from the start and end images containing a brachytherapy source response.

7.2.2 Results

The following sections provide a detailed description of the results obtained for this example patient and the analysis performed.

7.2.2.1 2D Pre-Treatment Image Verification

The acquired A-P image, shown in figure 7.11, depicts the catheter positions derived from the radio-opaque x-ray dwell position markers, immediately prior to treatment, the three fiducial markers (black arrows) and the sets of BB projections (orange ellipses) from the BB array. The A-P image provides the geometric relationship between the implant, anatomy, x-ray source and the FPD required to perform quantitative pre-treatment image verification.

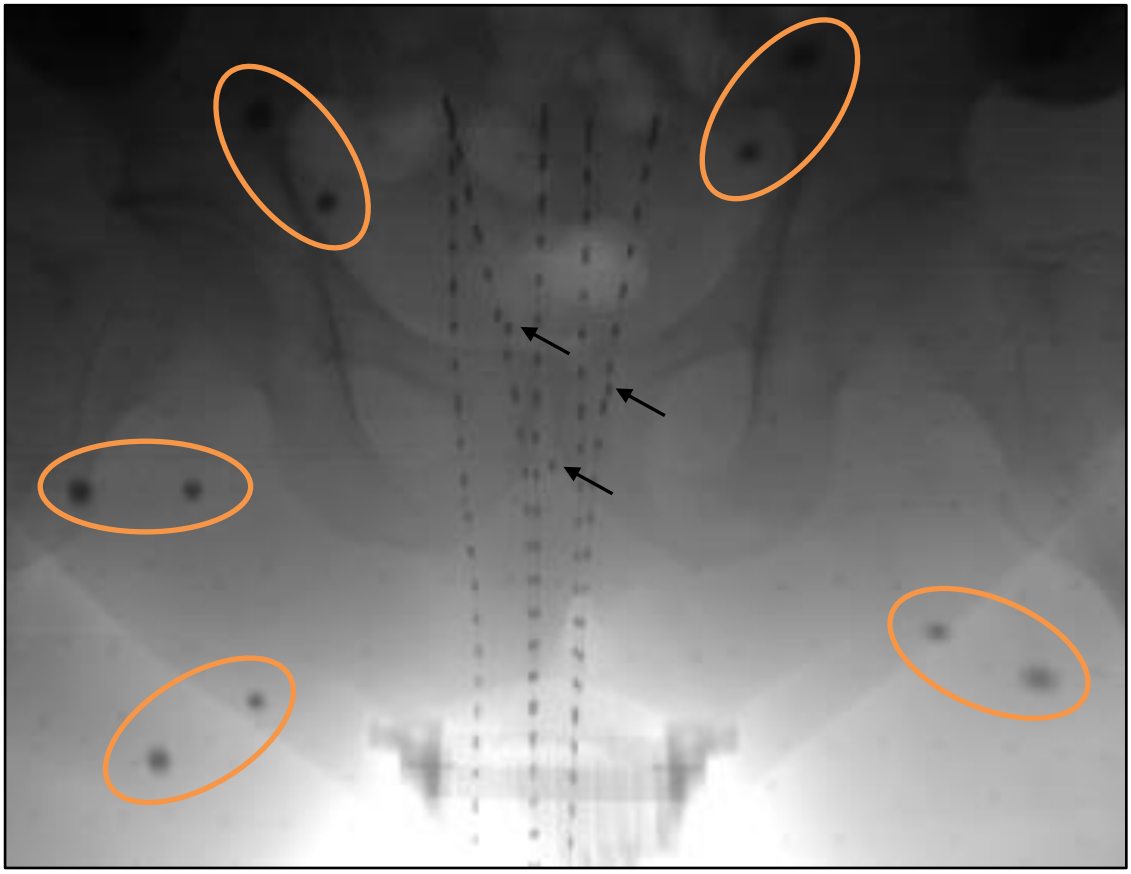

Figure 7.11. Pre-treatment A-P image acquired with the x-ray dwell position markers inserted into the specified catheters and the 5 BB array pairs (orange ellipses) in the field. The three fiducial markers implanted into the prostate are also visible (black arrows).

The catheters selected for pre-treatment imaging (4, 5, 7, 16 and 17) identified in the A-P image are shown in figure 7.12(a), where each catheter marker point defined by the user is shown as a red circle. The three fiducial markers were also identified in this image and are shown as green crosses (highlighted by black arrow). For comparison, figure 7.12(b) shows the TPS A-P view of the implant with the same 5 selected catheters and 3 fiducial marker positions.

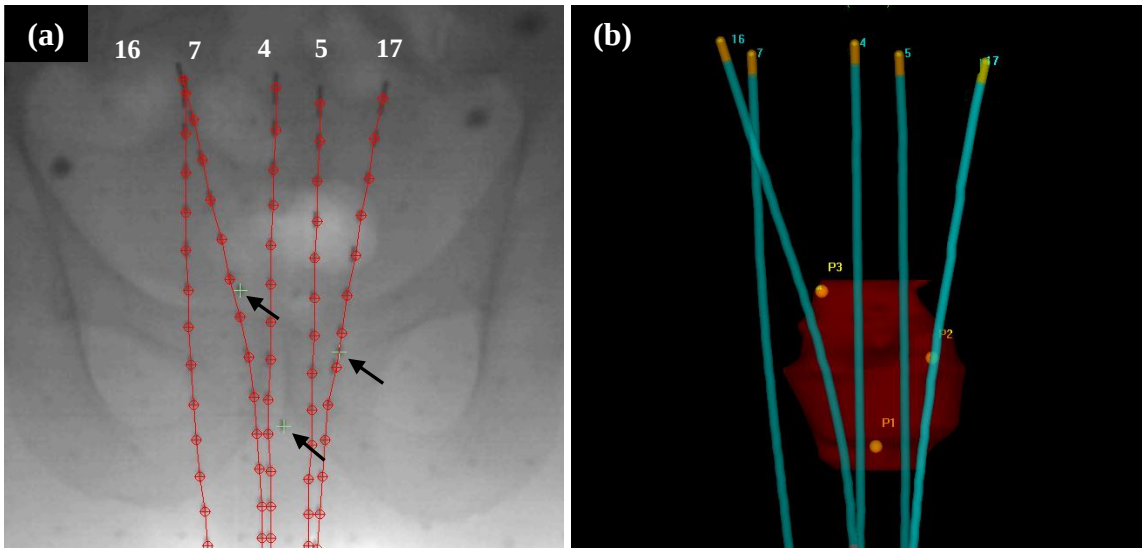

Figure 7.12. (a) The measured catheter paths are identified in red along with the 3 fiducial markers (green crosses). (b) For comparison with the A-P image, the TPS A-P view of the implant showing the catheters used for pre-treatment imaging and the 3 fiducial markers identified in the CT data.

The TPS catheter paths mapped to the FPD space are shown overlaid on the A-P image in figure 7.13(a). The agreement between the measured and planned catheters can be observed along the length of the catheter path.

The difference in measured and planned catheter positions was calculated for all catheter marker points for 120 mm along the path of each catheter. For a more clinically relevant assessment of the differences in catheter marker points, the subset of points that exist within the treatment region was also evaluated. The treatment region was identified by using the active source dwell positions for each catheter shown as solid red dots in figure 7.13(b). As previously mentioned in chapter 5, this evaluation

excludes points that exist in the bladder, that have the potential for large movements, but do not contain active source dwell positions.

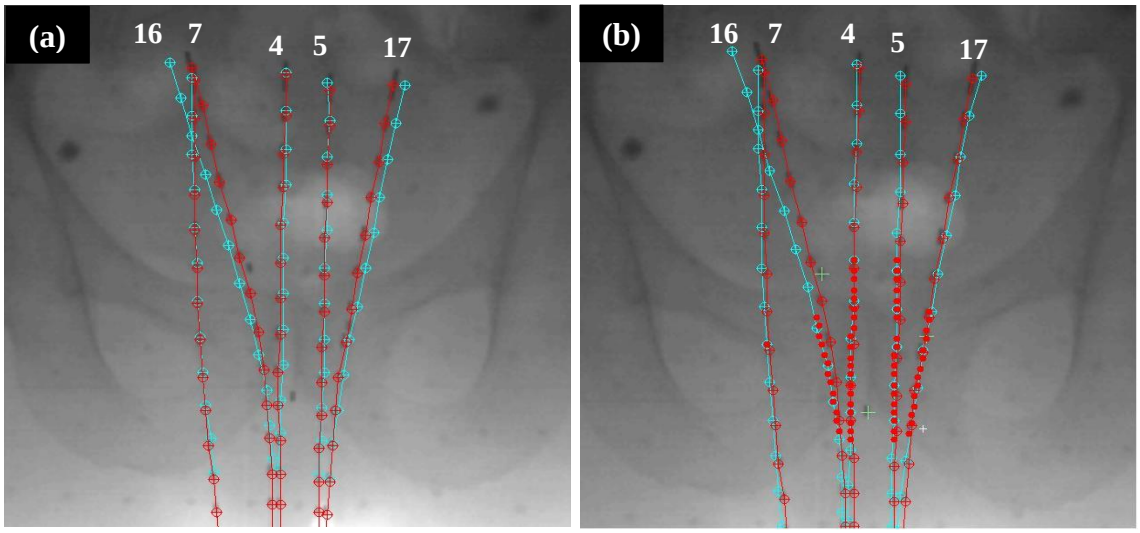

Figure 7.13. (a) The pre-treatment image showing the measured catheter paths (red) with the TPS catheter paths (cyan) mapped on to the image, for direct comparison immediately prior to treatment delivery. (b) The addition of the active source dwell positions (solid red circles) showing the 'treatment region', defining the region where catheter agreement is critical because this is where the dose will be delivered to the patient.

Histograms showing the distribution of absolute catheter differences for all catheter marker points and the directional catheter difference in the S-I direction are presented in figure 7.14. The 2D registration uncertainty and the resulting rotation is shown in column 2 and 3 of table 7.1. The absolute catheter marker differences, L-R and S-I difference for all points and the treatment region subset were calculated and the results are shown in column 4, 5 and 6 of table 7.1. The maximum mean catheter displacement is also reported.

Table 7.1. The reported registration uncertainty, $\Delta_{Reg.2D}$, and rotation, θ, after the 2D registration. The mean directional difference between all planned and measured catheter marker points (*L-R* and *S-I*), the mean difference and the maximum mean catheter difference. The subset data for points only in the treatment region is also presented. The values in the brackets represent one standard deviation.

Dataset	$\Delta_{Reg.2D}$ (mm)	Rotation θ	L-R (σ_x) mm	S-I (σ_y) mm	Abs. (σ_{abs}) mm	Max. Catheter mm
Patient 1	0.6	1.2	0.4 (1.4)	-0.3 (0.9)	1.3 (1.1)	2.9
Subset			-0.1 (0.7)	0.0 (1.2)	1.1 (0.7)	2.1

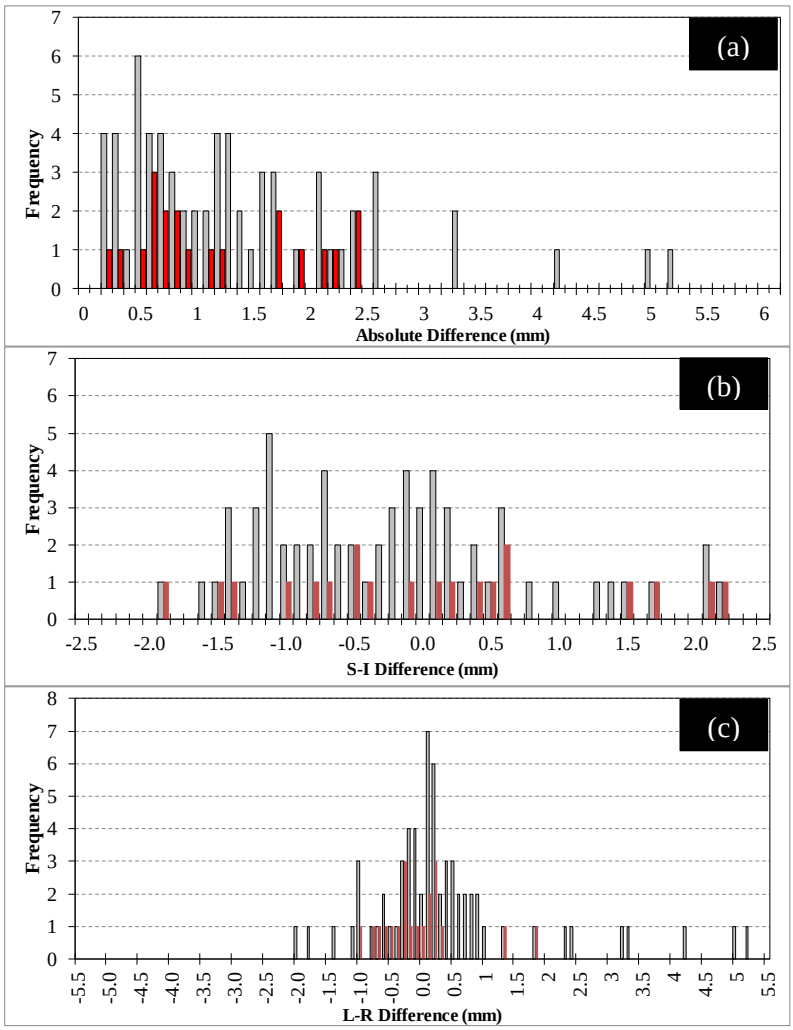

Figure 7.14. The distribution of catheter marker point difference for all points (grey) and for the points in the treatment region (red) for (a) the histogram of absolute catheter marker differences (b) The histogram of superior-inferior (S-I) catheter marker difference and (c) the histogram of left-right (L-R) catheter marker difference. For (b) and (c) the positive axis represents a shift of the measured catheter markers to the patient inferior and the patient right direction relative to the planned position.

The absolute catheter marker difference profile for each of the 5 catheters used for pre-treatment imaging is shown in figure 7.15. The absolute difference is presented for each catheter at each 10 mm spaced marker from the catheter tip to 120 mm along the catheter path.

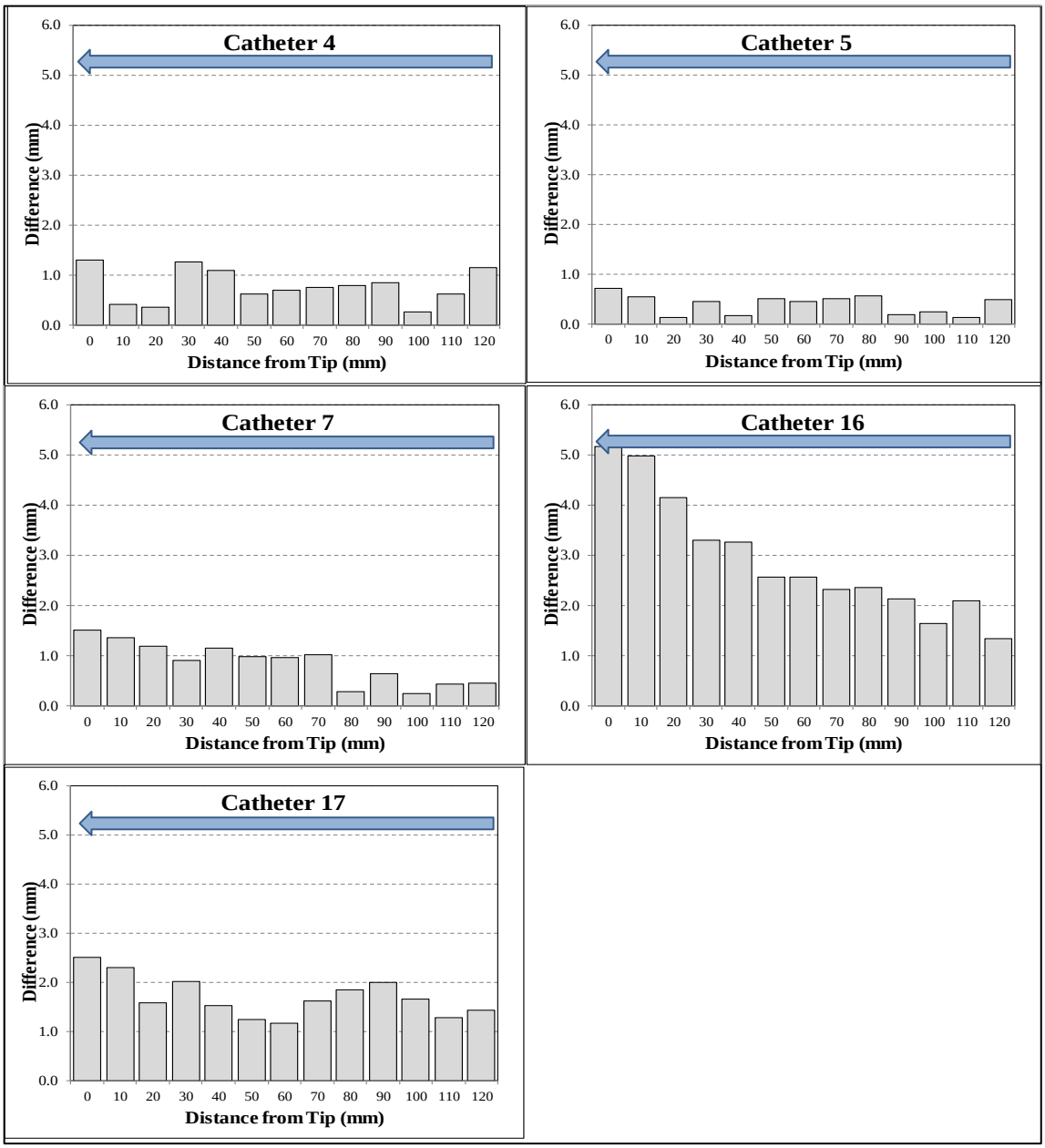

Figure 7.15. Absolute catheter marker difference profiles showing the difference at each 10 mm spaced catheter marker point for all 5 catheters inserted into the patient for pre-treatment imaging. The blue arrow provides orientation of the catheter tip and connector end.

7.2.2.2 Measurement Uncertainty

The measurement uncertainty analysis for this patient, using the approach defined in section 5.3.6, results in the following total measurement uncertainty:

- Reported registration uncertainty ($\Delta_{Reg.2D}$) = 0.6 mm
- Divergence correction uncertainty ($\Delta_{DivCorr}$) = 1.4 mm (average h_m = 150 mm)
- Marker identification uncertainty ($\Delta_{APMarker}$) = 0.784 mm (±1 pixel)
- TPS marker identification uncertainty (Δ_{TPS}) = 1.25 mm (½ CT slice thickness)

The total calculated measurement uncertainty using equation 5.2 is 2.1 mm. This total uncertainty value can also be determined by using figure 5.22, with a registration uncertainty of 0.6 mm and an average marker height of 150 mm. The total measurement uncertainty value defines the 2D catheter displacement detection threshold and in this example patient case only one catheter (catheter 16) exhibits displacement that is identified above this threshold.

7.2.2.3 3D Catheter Reconstruction Verification

The acquired 'shift' images are shown in figure 7.16(a) depicting an observed shift relative to the FPD at each 'LEFT' and 'RIGHT' image acquisition position. The corresponding fiducial marker points and catheter marker points, that were identified by the user in each image, are shown in figure 7.16(b). To distinguish each catheter channel number, each corresponding catheter path is identified with a different colour. The corresponding fiducial markers are shown in figure 7.16(b) as red crosses.

The 3D registration results between the reconstructed fiducial markers and the TPS fiducial marker is shown in table 7.2. The registration residual, registration uncertainty and the reported rotations (as described in section 5.4.4) are shown for this patient.

Table 7.2. The reported residual, registration uncertainty and the reported rotation after registration between the TPS data and reconstructed fiducial markers for the three datasets.

Dataset	Residual (mm)	$\Delta_{Reg.3D}$ (mm)	Tilt x-axis (°)	Roll y-axis (°)	Yaw z-axis (°)
Patient 1	2.0	0.8	-2.3	6.8	3.8

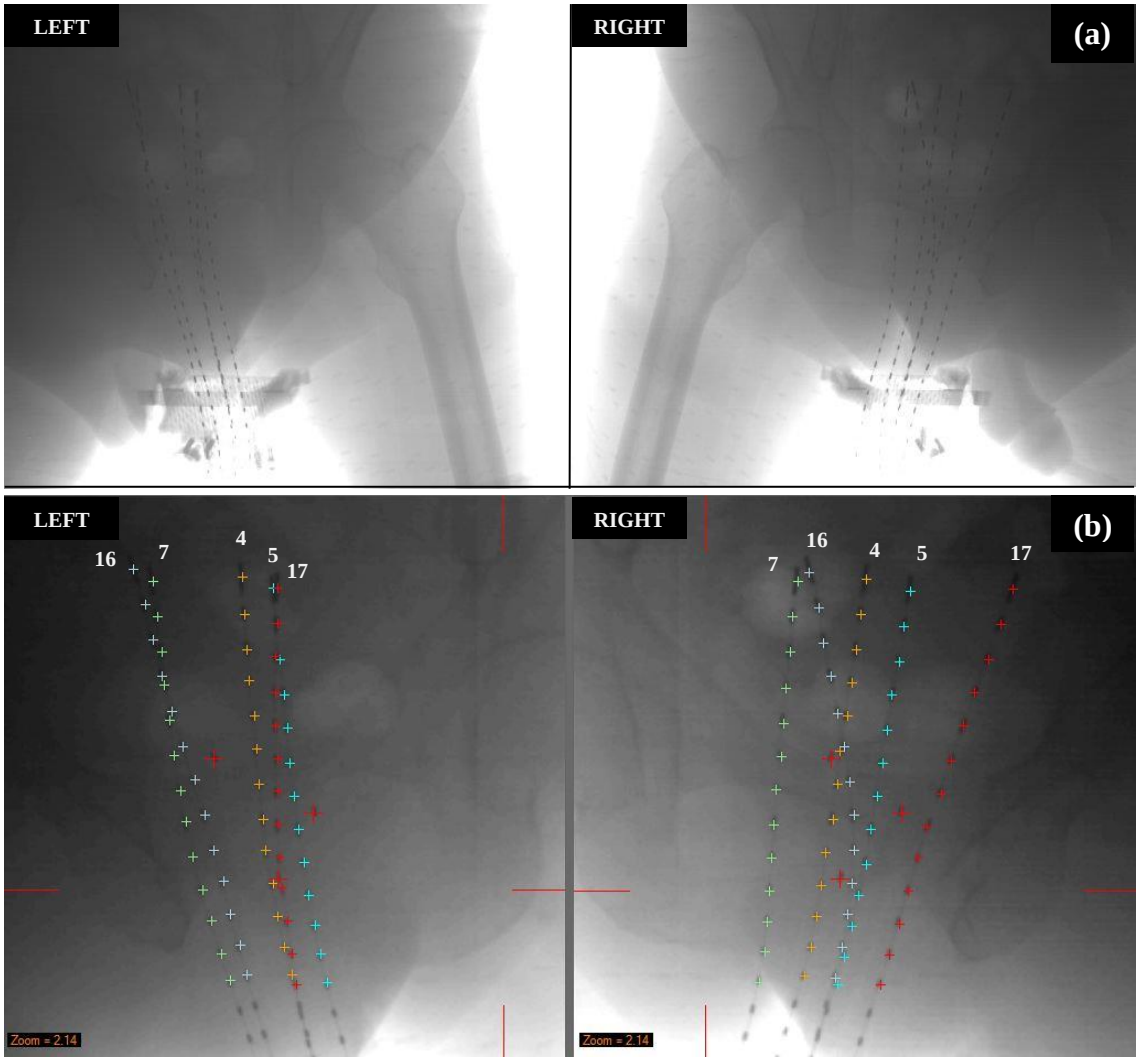

Figure 7.16. (a) The acquired 'shift' images of the patient prior to treatment captured with the x-ray source moved to the 'LEFT' and then 'RIGHT' of the patient. (b) The corresponding catheter marker points identified in each 'shift' image in preparation for 3D reconstruction. The fiducial marker points are also identified (large red crosses) in each image.

The calculated difference between the 3D reconstructed catheter paths and the TPS catheter paths is summarised in Table 7.3. The distribution of absolute differences between the two datasets is represented as a histogram as shown in figure 7.17. The 3D directional difference is also provided in figure 7.18.

Table 7.3. The mean vector difference between all planned and measured catheter marker points, the mean absolute difference for all points and the maximum mean catheter difference. The absolute difference for all catheters, the maximum individual catheter difference and the RMSE3D is also shown. The bracket values are 1 standard deviation.

Dataset	L-R (σ_x) mm	S-I (σ_y) mm	A-P (σ_z) mm	Abs. (σ_{abs}) mm	Max. Catheter mm	$RMSE_{3D}$ mm
Patient 1	0.9 (2.2)	1.6 (1.4)	-1.4 (3.5)	4.3 (2.3)	7.2	4.9

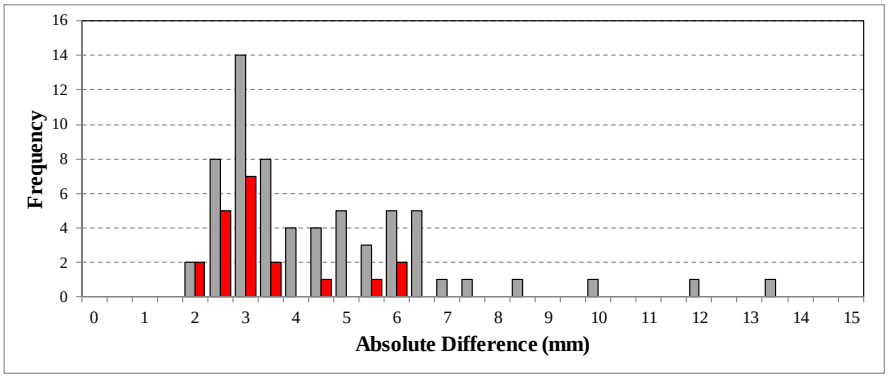

Figure 7.17. The histogram of 3D absolute catheter marker difference for all 5 catheter marker wires inserted into the catheters for all catheter marker points (grey) and for the subset of points within the treatment region (red).

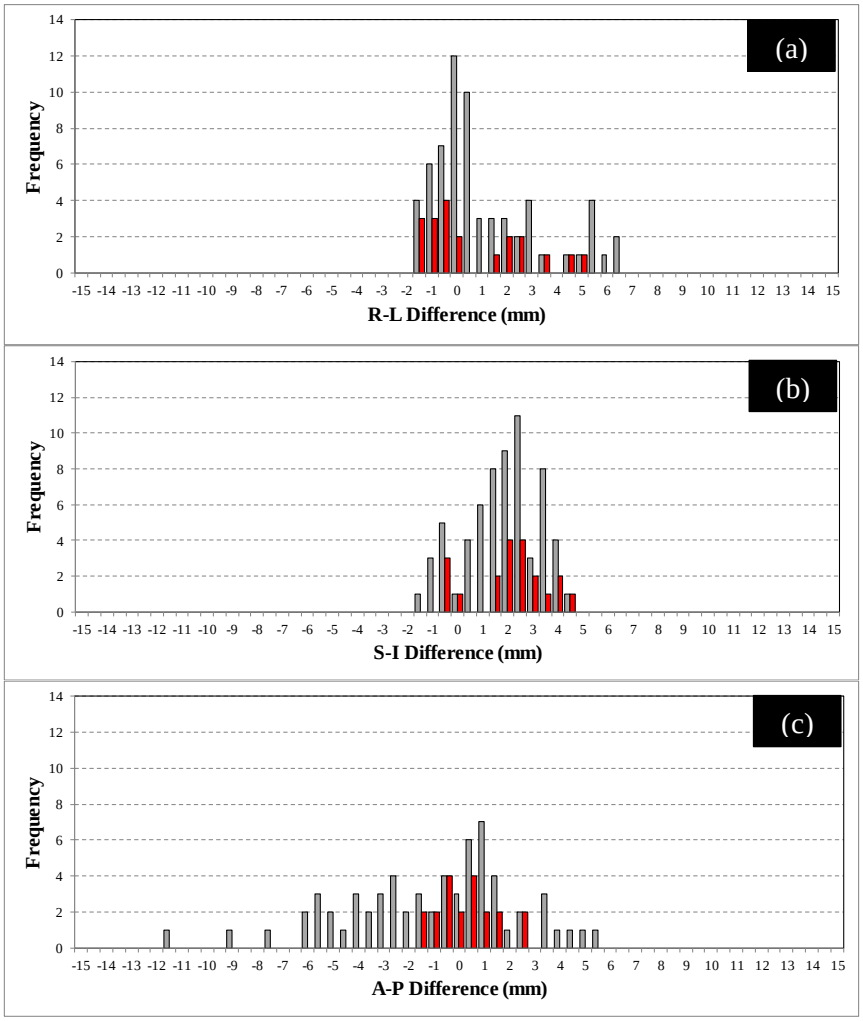

Figure 7.18. For all 5 catheters used for pre-treatment imaging the distribution of differences is shown for all catheter marker points (grey) and for the points within the treatment volume (red) for: (a) the histogram of the right-left (R-L) catheter marker difference, (b) the histogram of superior-inferior (S-I) catheter marker difference and (c) the histogram of anterior-posterior (A-P) catheter marker difference.

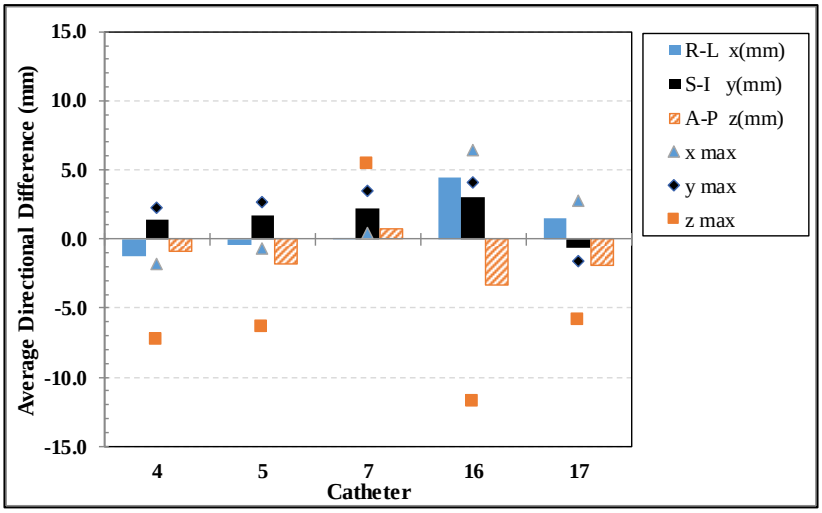

Figure 7.19. The mean and maximum vector difference per catheter, showing the Left-Right (*x*), Superior-Inferior (*y*) and Anterior-Posterior (*z*) orientations. Positive measured differences are Left, Inferior and Anterior.

7.2.2.4 Source Tracking

The source tracking data can also be presented overlaid on the A-P image by virtue of the combined imaging system using the same detector. Figure 7.20(a) shows the planned dwell positions (red circles) of the 5 catheters used for pre-treatment imaging and are compared with the measured source coordinates (blue circles-cross). The planned dwell positions do not incorporate any geometric implant changes that may have been identified since treatment planning imaging. Figure 7.20(b) shows modified planned dwell positions (orange circles) accounting for geometric changes determined during pre-treatment imaging.

The measured source coordinates in figure 7.20(b) represent the calculated positions of the source (in 2D), for each image in the sequence acquired as the treatment was delivered to each catheter. These measured positions are not necessarily dwell positions, due to the image capture rate of the FPD, and so extraction of the dwell positions from the sequence of measured source coordinates was performed using the approach described in section 4.5. A subset of measured dwell positions for comparison with the treatment plan were then determined by initially combining source coordinate measured positions that were within 1 mm of each other. All positions that consisted of only one source coordinate were excluded. The resulting distribution of measured dwell

positions are shown in figure 7.21. The matching planned dwell positions are shown in figure 7.21 as magenta dots.

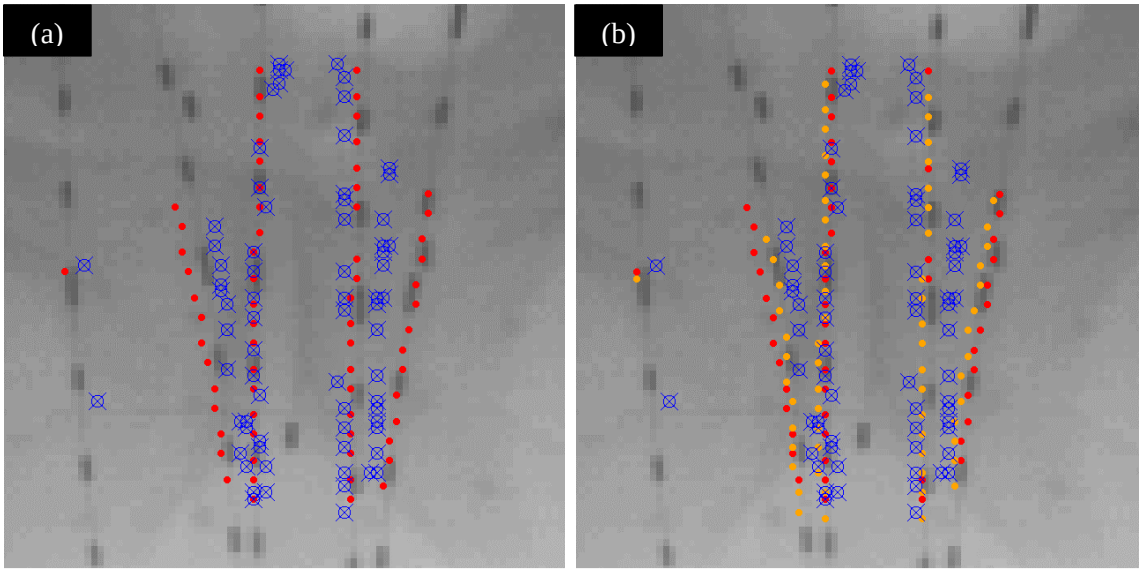

Figure 7.20. (a) The measured source co-ordinates shown as blue circles-cross and the planned dwell positions (solid red circles) from the treatment plan overlaid on the pre-treatment A-P image. (b) The planned dwell positions modified to account for the implant geometry changes (orange circles) determined during the pre-treatment imaging immediately prior to treatment.

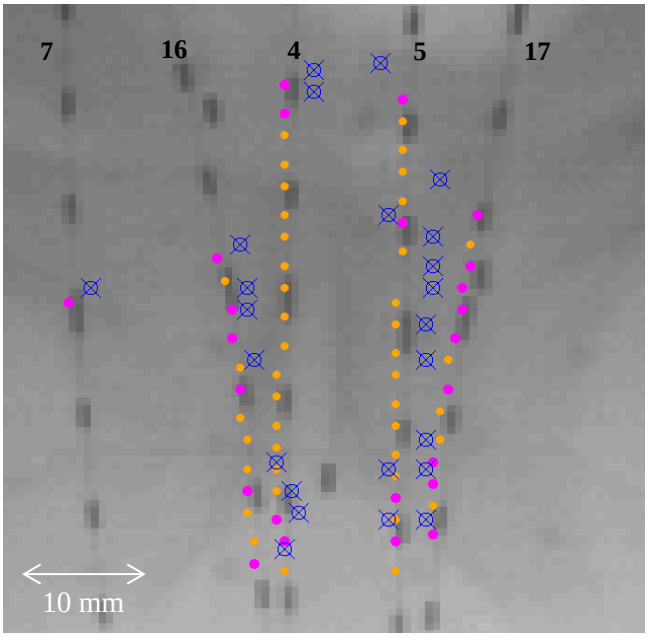

Figure 7.21. The filtered dwell position distribution showing the planned dwell positions with dwell time of at least 3.2 seconds (Magenta dots). The measured dwell positions, for comparison with the planned dwells, are shown as blue circle-crosses and contain at least 2 source coordinate measurements.

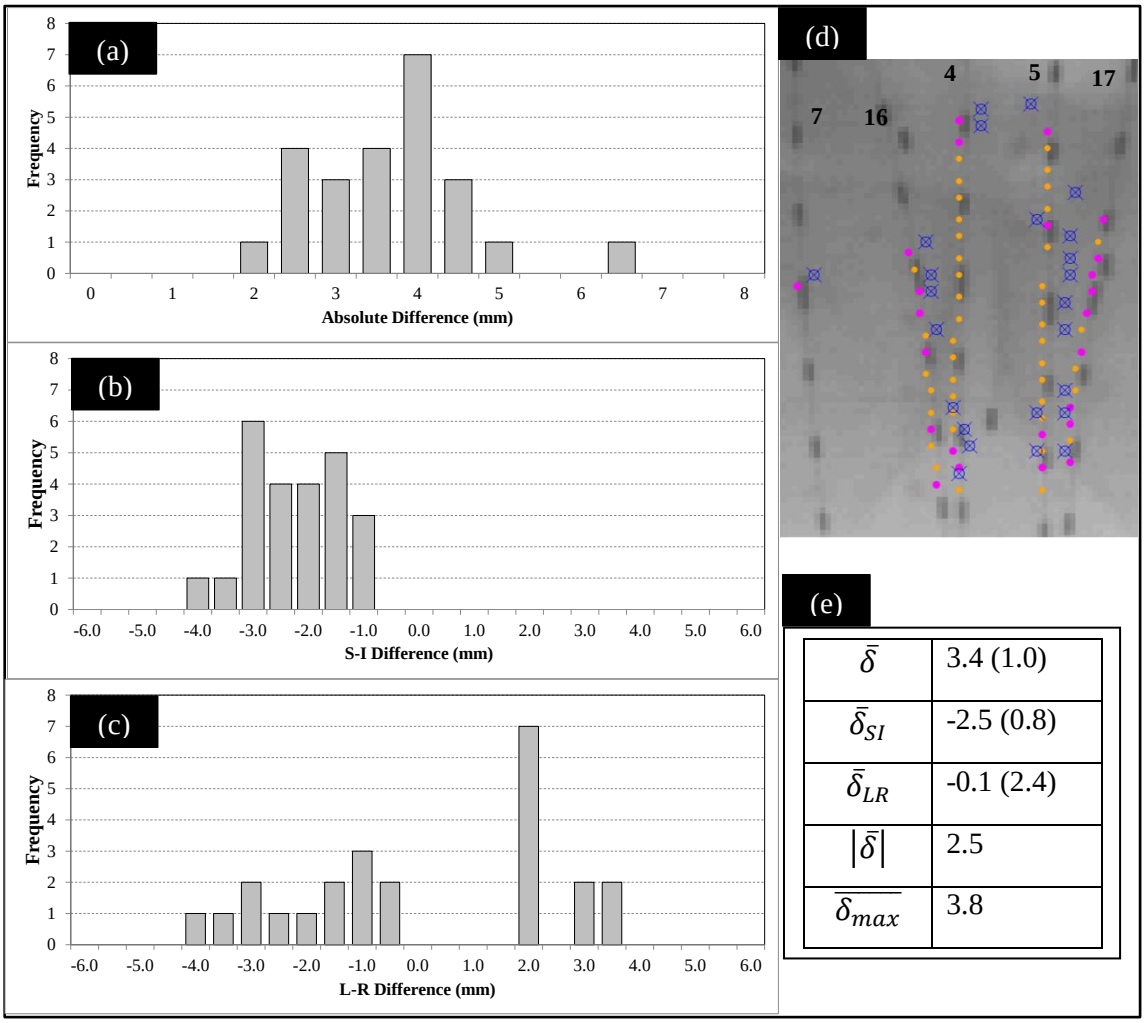

Figure 7.22. Histograms showing the distribution of dwell position differences for the patient treatment plan with (a) the absolute dwell difference (δ), (b) the S-I directional dwell difference (δ_{SI}), (c) the L-R directional dwell difference (δ_{LR}), (d) the visual comparison of dwell positions and (e) the summary of agreement metrics.

7.2.2.5 Individual Catheter Treatment Times

The total treatment time was measured by using the time stamps for each FPD image containing the brachytherapy source. The comparison with the TPS data for each of the 17 treatment catheters is shown in figure 7.23.

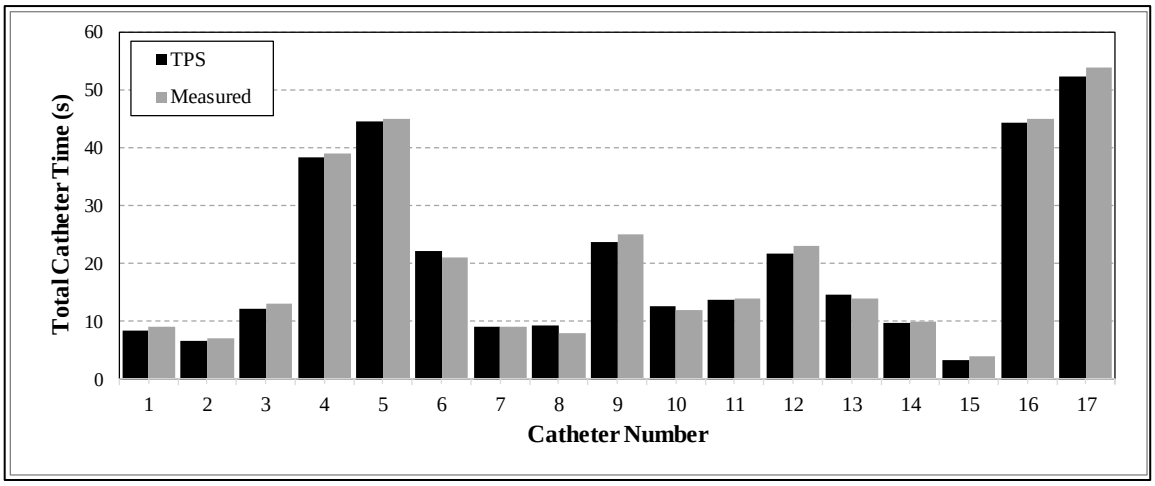

Figure 7.23. The treatment time profile showing the measured total time for each catheter (grey) compared with the time derived from the TPS (black).

7.2.3 Discussion

The treatment verification process described here for this sample patient case illustrates the additional workflow changes that have been implemented within AHRO brachytherapy program. These workflow additions, shown in figure 7.6, are each only minor changes, but together they build a strong program of verification not possible with previous work practices. The additional overall time added to the process is minimal, typically less than 15 minutes, but this is easily justified by the benefits. These gains all relate directly to improving the quality of the treatment provided, decreasing the risk of error and adding to the patient safety net.

7.2.3.1 2D Pre-Treatment Image Verification

The 5 catheters used for pre-treatment imaging were selected to span the extent of the implant geometry (L-R and A-P) and so their projections on the A-P image would not overlap, as seen in figure 7.12(a). Catheter number 16 exhibits a left to right bend and shows slight overlap with catheter number 7 toward the superior end of the implant. The visual comparison of the implant immediately prior to treatment with the TPS (figure 7.12(b)) shows good agreement and possibly suggests that no significant movement has occurred post treatment planning. This visual evaluation can be misleading and only registration using the fiducial markers can provide the mathematical relationship between the TPS and measurement space, allowing quantitative evaluation of the implant position relative to the treatment plan.

In this patient example, a registration uncertainty of 0.6 mm is calculated which is on the order of magnitude observed with the phantom cases explored in chapter 5. This result suggests the relative position of each fiducial marker has not changed significantly since planning. This registration uncertainty is considered small and not likely to produce are large catheter displacement detection threshold (section 5.3.7). The TPS catheter paths are therefore mapped into the FPD space with greater confidence.

The overlay of the TPS and measured catheter paths shown in figure 7.13 generally shows good agreement with the paths of the catheters agreeing well near the fiducial markers and agreeing less toward the tips of the catheters. The fiducial markers are a surrogate for the prostate and so agreement in this region of the image is desirable. Observed displacement toward the catheter tip has less clinical relevance as this is in the bladder and not likely to contain active source dwell positions.

The average displacement of catheter points in the left-right and superior-inferior directions are 0.4 and -0.3 mm respectively, suggesting that for the 5 catheters measured the overall average displacement is not clinically significant. The maximum average absolute displacement is 2.9 mm and suggests that one catheter (catheter 16) has displacements that require further investigation.

The histogram of absolute displacement for all catheter marker points (figure 7.14(a)) shows only a few outliers that have displacements greater than 2.9 mm. The actual locations of these larger displacements can be determined by investigating each individual catheter marker points displacement as provided by figure 7.15 and it is observed that catheter 16 has these larger displacements toward the catheter tip. This is also visible figure 7.13, showing the separation of the measured and TPS paths of catheter 16 in the bladder region of the implant.

The capability of this approach to provide information on the magnitude, direction and location of displacements is a key advantage over catheter tip only based approaches that only provide a magnitude of displacement relative to some reference point and may over (or under) estimate the catheter displacement present.

The 2D approach to pre-treatment verification of course has its limitations, but these can be justified to provide substantial verification information that can be practically

achieved in real time in a clinical scenario. The imaging of a subset of catheters is indeed a compromise as imaging all catheters (up to 18 for example) would be time consuming and the resulting A-P image would contain many overlapping catheter markers. A catheter not measured may move separately from the entire implant, but most likely only due to a mechanical slip of a catheter at the template. External visual inspection (or measurement) is likely to identify this event. The subset provides a sample of the implant, and with knowledge of the implant geometry from the CT data, strategic catheter selection occurs to minimise the possibility of overlap. The catheter displacements measured by the system are also only in the 2D plane, representing a L-R and S-I shift. The implant and anatomy is 3D and possible catheter displacements out of plane (in the A-P direction) are not be detected using this 2D approach.

7.2.3.2 3D Catheter Reconstruction Verification

Shift imaging is performed to achieve a 3D representation of the implant geometry in the treatment bunker immediately prior to treatment delivery. The two images captured by the FPD are shown in figure 7.16(a) where the relative shift of the catheter paths relative to the image can be seen. The catheter paths and fiducial markers in each image were identified and this process can be seen in figure 7.16(b). The reconstructed 3D geometry of the fiducial markers were registered with the TPS fiducial markers resulting in a 3D registration uncertainty of 0.8 mm. This value is on the order of the magnitude calculated with the 2D registration, further suggesting the stability of the relative positions of the fiducial markers. In this particular case, the calculated rotations resulting from the registration are relatively small.

A summary of comparison of the planned and measured catheter paths are listed in table 7.3. The average L-R, S-I and A-P catheter marker point displacements are shown, with the average L-R and S-I displacements larger than reported by the 2D approach as the additional dimension (A-P axis) is now accounted for. (different transformation matrix). The average absolute catheter displacement of 4.3 mm and the maximum average catheter displacement are also larger than reported by the 2D approach.

The histogram of absolute displacement shown in figure 7.17 also shows most points displaced by approximately 4 mm with a few outlier points 10 mm or greater. Figure 7.18(c) shows that many of these outlier points are displaced in the A-P direction. The

magnitude of these displacements may only be clinically significant if the displacements have occurred in the target (prostate) region and not in the bladder. Similar to the 2D approach, a further breakdown of these catheter displacement per catheter shows that all of the calculated displacements occur toward the tip (in the bladder) and away from the treatment region of the implant.

The 3D pre-treatment imaging approach provides many pieces of information that report on the agreement of the implant with the treatment plan. The challenge is to provide this information to the clinical staff in such a way to identify a problem if it occurs, highlight an item that may require additional investigation, or that the data sets agree. One useful approach is to show the agreement on a per catheter basis. Figure 7.19 shows the average catheter marker points displacement in each L-R, S-I and A-P direction for each catheter. Also provided is the maximum marker points displacement in each direction per catheter flagging possible larger individual catheter displacements.

7.2.3.3 Source Tracking

The measurement of source dwell positions during treatment delivery allows for confirmation that the dose is being delivered to the correct location relative to the implanted fiducial markers, where these can be interpreted as a surrogate for patient anatomy. It also allows confirmation that the geometric arrangement of the set of dwell positions relative to each other is consistent with the plan.

Figure 7.20(a) shows that the number of dwell positions determined by the source tracking system is less than the planned number. This is a direct result of the poor time resolution of the FPD. When operating in continuous acquisition mode, the FPD captures one image every 1.8 seconds and therefore limits its capability to uniquely capture source dwell positions with dwell times less than 1.8 s. The result may be (but not limited to) multiple dwell positions (with short dwell times) being captured in a single image or an image of a single dwell position containing source movement artefact as the source arrives and/or departs that dwell.

Additionally, the challenge of assigning each measured dwell position with the corresponding planned dwell becomes more difficult if multiple dwell positions are blurred into a single captured image. This creates a challenge of registering each measured dwell to a corresponding planned point for a difference calculation, i.e. if the

number of dwells in the two lists differ, then it is not as simple as comparing each measured coordinate to the next on the list from the plan. Although not all measured dwells have corresponding planned dwells, the information is still extremely valuable, proving information about the source travel path during treatment.

One approach to overcome the timing resolution limitation of the FPD is to utilise planned dwells that exhibit relatively large dwell times for comparison with measured dwells. The catheter dwell time profile is known from the treatment plan and therefore the measured dwells, corresponding to the large dwell times, can be identified by processing the sequence of calculated source position coordinates. For this patient example a planned dwell time threshold of 3.2 seconds (figure 7.21) produced the same number of measured dwell positions.

The distribution of measured dwell positions, shown in figure 7.21, agree with the general shape of the planned dwell position distribution. The generated subset of dwell positions enabled a quantitative analysis to be performed to calculate the metrics of agreement, as described in section 6.2. The data for this patient is presented in the same format as illustrated by figure 6.3, to provide an overview of the source tracking results. For the 24 dwell positions analysed, the mean difference was 3.4 mm. The distribution of absolute and directional differences is shown in figure 7.22(a), (b) and (c) respectively. These histograms indicate a mean displacement of the measured dwell positions toward the superior of the patient and with an approximate even distribution of measured dwell differences to the patient left and right. These observed differences are likely to arise from combinations of (i) sub-degree rotations of the couch and FPD caused by patient weight induced couch sag and (ii) possible movement of the patient after pre-treatment imaging and (iii) the asymmetric scatter field caused by the finite geometry of the patient. The catheters that are at a greater distance from the FPD (catheters 16 and 17) exhibit a larger discrepancy due to the reduced detector signal, decreasing primary-scatter ratio, and greater geometric effect of any couch rotation. As the observable consequences are quite systematic, they are likely to be amenable to further improvement. Future versions of our system will incorporate more information on couch position, and asymmetric scatter compensation.

There is considerable interest in interpreting the measurement uncertainty in terms of dosimetric uncertainty to answer the question: “What is the clinical significance?” It is

important to appreciate that this form of treatment verification addresses the source dwell position and time, rather than a direct dose measurement, and therefore the uncertainty will be specific to the patient plan, the patient geometry, each individual source dwell position and the location of the measured dwell position within the entire implant. The same is true of a dose measurement: the dose discrepancy at the detector is not necessarily representative of the clinically significance of dose discrepancies elsewhere in the patient or treatment volume. Ongoing work includes the development of a dose assessment tool to make this evaluation on a plan by plan basis.

At present the data extracted from the system is used to watch for gross discrepancies or obvious errors. We anticipate adopting a 2σ or 3σ investigation level on source position deviations based on the 3-dimensional position uncertainty of that system. The source-tracking system is currently employed in a non-interventional or 'record and verify' capacity, so source tracking data is processed after completion of the treatment. When the full capability of the system is established, real-time analysis will facilitate interruption decisions in the event of a significant error being observed.

7.2.3.4 Individual Catheter Treatment Times

The measurement of total treatment time for each catheter provides a further verification that the treatment was delivered correctly. All total catheter times measured agree with the expected TPS times (figure 7.23), within measurement uncertainty due to the FPD timing limitation when operating in continuous acquisition mode. As described in section 6.4, certain delivery errors would be visible in this total catheter time profile data, such as interchanged transfer tubes and incorrect treatment plan (or fraction) selection by the operator. For instances where the treatment times are the same (or very similar) delivery errors will be flagged if source dwell positions do not agree.

The FPD used in this work has a long acquisition time compared to some possible short dwell times delivered in a clinical treatment plan, making some individual dwell time verification difficult. One approach to overcome this is to limit the shortest dwell time allowed by the TPS, but this may restrict the optimisation algorithm achieving a clinically acceptable plan, especially so when the treatment source is 'hot'. The other alternative is to overcome this technology limitation and purchase a new and faster FPD especially selected to meet the criteria of this verification purpose. This is the option presently being pursued in ongoing work.

These clinical workflow changes have established a routine treatment verification process, providing a quantitative method to perform pre-treatment imaging, allowing verification of catheter positions to be directly compared to the treatment plan. The novel approach of using the imaging FPD for source tracking allows verification of the delivered dwells to be compared to the plan and relative to the surrounding anatomy.

7.3 Clinical Implementation Conclusion

This chapter has described the steps taken to implement this treatment verification system in a HDR brachytherapy clinical environment. The addition of a couch mounted FPD, ceiling suspended x-ray system and in-room lasers established a platform to perform treatment verification routinely. The clinical workflow was modified to accommodate the introduction of treatment verification and only increased the overall treatment time by approximately 15 minutes. The example patient case presented showed that the verification procedure developed was practical and achievable in a clinical environment.

This approach using in room imaging, with a well-defined geometry enables registration with the treatment plan and therefore verification of the catheter positions relative to the prostate against the treatment plan itself. For this patient case, the pre-treatment imaging provided the clinical staff with information of how the catheters had deviated between treatment planning imaging and treatment delivery. It was determined from the AP image that the mean catheter displacement in the S-I direction was 0.4 mm INF, for the 5 catheters selected for imaging.

The combination of pre-treatment imaging with source tracking enabled absolute verification of the delivered dwell positions against the treatment plan. In this patient case, the measured set of dwell positions differed from the planned positions by a mean of 3.4 mm. A systematic displacement of 2.5 mm to the patient superior direction of the implant was observed. The error detection metrics displayed in figure 7.22 provide a clear summary of the treatment delivery status. The visual representation of the dwells overlaid on the AP image in conjunction with the other error trapping metrics allows the system to identify possible errors introduced into the treatment process and provides the staff with an opportunity to evaluate and address an error where required.

Treatment verification in HDR prostate brachytherapy is challenging and potentially treatment errors occur without the treatment staff having any knowledge of the event. This approach of combining pre-treatment imaging and source tracking in a clinical environment is novel and provides information that is not easily achievable using other approaches.

All verification comparisons were made directly against the treatment plan and not against the data on the treatment delivery console. This approach enables further treatment errors to be identified such as TPS to treatment console data transfer error, discrepancies of specified source activity between the TPS and treatment console, incorrect plan selection by the operator at the treatment console and incorrect manual changes to the plan made by the operator.

This chapter illustrates the use of this system in a clinical environment. The relatively simple integration into the clinical workflow has enabled the process to become routine. It provides an increased level of safety for the patient and improves the quality of treatment delivered.

Chapter 8
Conclusion and Recommendations

8 Summary

The aim of this thesis was to develop a treatment verification system for HDR brachytherapy that could be used to verify the planned treatment, detect a treatment delivery error and potentially improve patient safety. A novel approach was developed, using a FPD, to perform pre-treatment imaging immediately prior to treatment and implement source tracking during the treatment delivery.

An available FPD was evaluated for its suitability for the proposed application, and characterised for its response to two radiation sources. The FPD responded to the ^{192}Ir source, for a range of clinically relevant distances (20 to 200 mm) away from the FPD despite the low dose rates and the changing photon spectrum. The pixel resolution of the FPD (0.784 mm) and the detection region (300 x 400 mm) provided a suitable detector to perform pre-treatment imaging. The image acquisition time of the FPD when operating in continuous acquisition mode for source tracking was one image capture every 1.8 seconds. Although not designed for source tracking, the FPD was found to be adequate to perform this proof of principle work.

Pre-treatment imaging, using the ceiling suspended x-ray system, allowed the position of the catheters to be verified relative to the treatment plan. The approach that was established enabled imaging to occur in the treatment bunker, immediately prior to treatment delivery, potentially detecting changes in the implant geometry that would otherwise go unnoticed and unaccounted for. A key benefit of this system is the relationship established between the FPD and the TPS. This allowed a direct quantitative comparison of the catheter positions with the treatment plan, permitting useful position verification metrics to be established. The system is capable of identifying catheter displacements (in 3D) of the order of 2.0 mm with a confidence of

95%. Pre-treatment imaging was able to detect changes in the implant prior to treatment, which are not necessarily errors, but when identified and accounted for improve the quality of the treatment delivered to the patient.

Source tracking provided further challenges as the source is moving and stationary during the treatment delivery period. The source tracking acquisition was not synchronised with the afterloader source movements and so methods were developed to deal with moving and stationary source captures. The source coordinate could be determined to within 0.9 mm of the expected position in a phantom geometry, for distances of up to 200 mm away from the FPD. The differences between expected and measured source positions in a patient were larger due to the irregular patient geometry and other influences.

The novel combination of pre-treatment imaging and source tracking allowed the development of error trapping regimes. A significant advantage of this system is the multitude of information it can provide about the treatment. The evaluation of these data streams from the system, enabled error signatures to be identified, and therefore flag an error when it occurred and predict the likely source of the error type. The error trapping capability was demonstrated and showed it could identify clinically relevant errors (incorrect plan selection, swapped channel connection, incorrect channel length, incorrect dwell times), as highlighted by the ICRP 97 report into prevention of HDR brachytherapy accidents[15], which are difficult to detect with other verification approaches.

The integration into a clinical environment showed that the proposed verification approach could be applied in a typical clinical setting. Various modifications to workflow were required to accommodate treatment verification, but added only approximately 15 minutes to the overall treatment time. Some modifications were made to the treatment room to aid with patient set up, including a laser system for patient alignment. The clinical verification process was shown to be non-invasive, time economical and potentially sensitive to clinically relevant errors. In this instance, the system was used in a passive manor, with all data being evaluated retrospectively.

While the system has already proved to provide valuable information, there are several limitations. The first is that of overlapping catheters in the pre-treatment projection images. This limits the number of catheters that can be verified, but still provides

extremely useful information about the stability of the implant. The source tracking functionality is inherently limited by the image capture rate, in its ability to capture very short dwells. This is readily addressed with improved hardware, and is discussed further below in ongoing work. Even while only able to reliably record the longer dwells, there is sufficient information to provide staff with greater confidence that certain errors have not occurred. In the clinical patient case, the source tracking suffers greater uncertainty than seen in the phantom measurements. The primary cause is likely due to the asymmetric and unpredictable scatter field resulting from the patient geometry. Lastly, the implementation requires considerable work by the attending physicist to perform the pre-treatment imaging and source tracking steps. Many of these tasks can be automated to streamline the process as also mentioned below in future directions. Even with these limitations, the system provides valuable information that has clinical significance, facilitating improvements in the quality of treatment delivered.

8.1 Significance

The verification system incorporating both pre-treatment imaging and source tracking is a novel approach of addressing many of the challenges in treatment verification highlighted by previous publications in this field. Pre-treatment verification has been performed previously, but rarely in the treatment bunker immediately before treatment and with limited quantitative comparison with the treatment plan. The ability to evaluate the geometry of the implant at the time of treatment in 2D and 3D has the potential to enable real time correction and optimisation algorithm to be developed.

Source tracking has been pursued by other authors, but only for the purpose of system quality assurance. To date, to the author's knowledge, no other publication has reported on HDR brachytherapy source tracking in a clinical environment. The challenges of including a treatment verification system into a clinical workflow have been addressed in this work, providing significant benefit to the treating staff, while enabling an approach that can be performed routinely.

Many of the steps described in this thesis to capture and evaluate the data can be automated using intelligent image processing and visual representation of verification data. These automations will further streamline the clinical workflow, reinforcing the routine aspect of the procedure. This will potentially enable wide uptake of the

approach as the verification process can easily be performed by typical medical physicists and radiation therapy staff.

Studies have suggested that dose escalation in HDR prostate brachytherapy will deliver a therapeutic gain while potentially maintaining acceptable rectal and urethral toxicities [117, 118]. Progression to large fractional or single fraction doses leaves no room for error, and so a verification system such as the one demonstrated here could ensure that the treatment is administered correctly, strictly to the plan, avoiding induced toxicities leading to poor patient quality of life or reduced tumour control.

8.2 Ongoing Work and Future Directions

The project has addressed many of the challenges in HDR brachytherapy treatment verification, but there are still aspects that need to be further developed and resolved. Our research group is actively involved in further development of this system.

The pre-treatment imaging data shows the radio-opaque catheter markers inserted for verification against the treatment plan. Currently our research group is developing image processing algorithms to automatically identify and quantify these catheter markers. The auto-identification of each marker can be used to potentially automate the pre-treatment evaluation of catheter displacement.

Major decisions are required when catheter displacement immediately prior to treatment delivery is identified. If the displacement is deemed clinically significant, a protocol of how to manage the discrepancies should be followed. Currently, for prostate HDR brachytherapy, a clinically relevant displacement threshold is yet to be agreed upon. Furthermore, the path to follow to address these displacements is also varied. The novel approach of this system establishes a relationship between the FPD and the TPS, therefore potentially allowing the dosimetric impact of the identified displacements to be immediately evaluated. Development of a new optimisation algorithm is needed to address these catheter displacements, with a focus on adaptive planning routines available at the treatment console.

The limited image acquisition rate during source tracking has recently been addressed by trialling a new detector that is capable of capturing up to 30 frames per second. The improved imaging will enable short dwell times to be sampled correctly allowing verification of all dwell positions.

The new imaging device can be controlled via in-house software, therefore allowing routines to be included that can process the acquired images during treatment delivery. The system could then provide verification metrics to the user in real time potentially allowing treatment interruption to occur when deviations exceed some defined threshold.

A significant advantage of this system over other approaches is the large range of data provided. One of the challenges is to present these data in a sensible, non-ambiguous and clear manor to the clinical staff at the treatment console. Further work is needed to investigate the data management and display to the user during pre-treatment imaging and treatment delivery (source tracking).

The system captures the position of the source and the time it dwells at each position during the treatment delivery. At present these positions are compared to the expected positions for verification. The acquired information can be used to reconstruct the 3D dose distributions for direct comparison with the treatment plan. The delivered dose volume could be used to inform subsequent treatment planning events in order to account for possible underdosed or overdosed regions. The development of a dose reconstruction algorithm from measured dwell positions is the topic of a current project within our group.

As briefly investigated in this thesis, the response of the FPD can be interpreted as dose and hence the treatment delivery can be verified by comparing predicted 'dose response' images with measured images. Further development of this approach is needed as it can provide complimentary information to the data already acquired.

The focus of this work has been primarily for prostate brachytherapy as this is the dominant site treated at Alfred Health Radiation Oncology. Translation of these concepts to other anatomical sites treated with HDR brachytherapy should be readily achievable. Other pelvic treatments, such as cervical cancers, have similar characteristics as prostate treatments, albeit with different applicators, and are the most promising next step.

Other sites, such as breast brachytherapy exhibit additional challenges, such as optimal detector positioning, non-uniform scatter fields and practical implementation that will require investment to resolve.

By developing a novel treatment verification system that is non-invasive, multi-functional, and can be implemented with existing technology this work has the potential to meaningfully improve patient safety.

Appendix A
Publications and Presentations Arising From This Work

A.1 Publications

Smith RL, Hanlon M, Panettieri V, Millar JL, Matheson B, Haworth A, and Franich RD. *An Integrated System for Clinical Treatment Verification of HDR Prostate Brachytherapy combining Source Tracking with Pre-Treatment Imaging* Brachytherapy. 2017 Sep 22. S1538-4721(17)30426-9. doi: 10.1016/j.brachy.2017.08.004.

Smith RL, Haworth A, Panettieri V, Millar JL, and Franich RD *3D catheter reconstruction in HDR prostate brachytherapy for pre-treatment verification using a flat panel detector*, Phys Med. 2017 Jul;39:121-131. doi:10.1016/j.ejmp.2017.06.008.

Smith RL, Haworth A, Panettieri V, Millar JL, and Franich RD *Identification of Catheter Displacements in HDR Prostate Brachytherapy Using a 'Shift Image' Reconstruction Technique*, Brachytherapy, 16(3)Supp., S106, May 2017, DOI: 10.1016/j.brachy.2017.04.204

Smith RL, Haworth A, Hanlon M, Matheson B, Millar JL, Panettieri V, and Franich RD *Clinical Application of Pre-Treatment Image Verification of Catheter Positions for HDR Prostate Brachytherapy*, Brachytherapy, 16(3)Supp., S114, May 2017, DOI: 10.1016/j.brachy.2017.04.223

Beaulieu L, **Smith RL,** Franich RD. Real-Time In-Vivo Dosimetry. In: Song WY, Tanderup K and Pieters B, editors. *Emerging Technologies in Brachytherapy*, CRC Press, Series in Medical Physics and Biomedical Engineering, March 2017, p.408, ISBN 9781498736527; *In Press*.

Venselaar JLM, Beaulieu L, Chen Z, **Smith RL**. *Advances in Brachytherapy Physics*. In: Godfrey DJ, Van Dyk J, Das SK, Curran BH, Wolbarst AB, editors. Advances in Medical Physics, Volume 6. Madison, WI: Medical Physics Publishing; July 2016. p.203. ISBN 9781930524903

Smith RL, Haworth A, Panettieri V, Millar JL, and Franich RD *Treatment Delivery Error Trapping in HDR Brachytherapy*, Brachytherapy, 15:S39, May 2016, DOI: 10.1016/j.brachy.2016.04.040

Smith RL, Haworth A, Panettieri V, Millar JL, and Franich RD. *A method for verification of treatment delivery in HDR prostate brachytherapy using a flat panel detector for both imaging and source tracking.* Med Phys. 2016;43(5):2435.

Smith, R. L., J. Millar, B. Matheson, B. Hindson, M. Taylor, and R. Franich. *"Clinical implementation of in vivo source position verification in high dose rate prostate brachytherapy."* Radiol Oncol 115:S87, 2015.

Smith RL, *High Dose Rate (HDR) Brachytherapy Treatment Verification Using An Electronic Portal Imaging Device (EPID)*, Congress Report, International Congress on Radiotherapy & Oncology, 3rd ESTRO Forum, Barcelona, Spain, p68-69, April 2015.

Ryan L. Smith, Jeremy L Millar, Annette Haworth, Michael L Taylor, Rick D Franich. *In vivo treatment delivery error trapping in HDR prostate brachytherapy* J Contemp Brachy. vol.7,p103, 2015.

Natasha Mason, **Ryan L. Smith**, Vanessa Panettieri, Bronwyn Matheson, Jeremy L. Millar. *Evaluation of HDR prostate brachytherapy catheter displacement between planning and treatment using a flat panel detector*. J Contemp Brachy. vol.7,p104, 2015.

Smith RL, Taylor ML, McDermott LN, Haworth A, Millar JL, and Franich RD. *Source position verification and dosimetry in HDR brachytherapy using an EPID.* Med Phys. 2013;40(11):111706.

Smith RL. *Verifying Brachytherapy Treatment of Prostate Cancer*. Monash Comprehensive Cancer Consortium (MCCC), Annual Research Report 2013-14

Smith RL, *High Dose Rate (HDR) Brachytherapy Treatment Verification Using An Electronic Portal Imaging Device (EPID)*, Post Forum Report, International Congress on Radiotherapy & Oncology, 2nd ESTRO Forum, Geneva, Switzerland, p34-35, April 2013.

Franich RD, **Smith RL**. *Curing cancer with radiation - Safely*. Stories of Australian Science 2011, Science in Public publication.

A.2 Patents

Smith RL and Franich RD, Patent: "*Brachytherapy dose verification apparatus, system and method"*, WO 2012034157 A1, RMIT University, Filing date Sep. 13th, 2010.

Smith RL, Australian Innovation Patent, AU 2008100728 *"A real time treatment dose verification system for afterloader brachytherapy systems"*, 2008.

A.3 Posters

Smith RL, Haworth A, Millar JL, Panettieri V and Franich RD, *In vivo Image Guided Brachytherapy Verification (IGBV) in high dose rate prostate brachytherapy – Initial Clinical Experience*, ABS Annual Meeting, April 2017, Boston, USA.

Smith RL, Haworth A, Hanlon M, Matheson B, Millar JL, Panettieri V and Franich RD, *Clinical Application of Pre-Treatment Image Verification of Catheter Positions for HDR Prostate Brachytherapy*, ABS Annual Meeting, April 2017, Boston, USA.

Smith RL, Taylor ML, McDermott LN, Haworth A, Millar JL and Franich RD, *The influence of inhomogeneities on measurements of source position in high dose rate (HDR) brachytherapy using an Electronic Portal Imaging Device*, ESTRO 33, April 2014, Vienna, Austria.

Smith RL, Haworth A, Taylor ML, Millar JL and Franich RD, *Identifying Common Delivery Errors in HDR Brachytherapy using a Flat Panel Imager*, ABG, February 2014, Adelaide, Australia

Smith RL, Taylor ML, Haworth A, Millar JL and Franich RD, *HDR Brachytherapy Treatment Delivery Error Trapping Using a Flat Panel Imager*, EPSM, November 2013, Perth, Australia

A.4 Presentations

A.4.1 *Invited Presentations*

"HDR Prostate Brachytherapy Treatment Verification – from benchtop to bedside" Alfred Health Radiation Oncology, Department Seminar Series, Mar 2017, Melbourne, Australia

"HDR brachytherapy treatment verification using a flat panel detector" GEC-ESTRO *In Vivo* Dosimetry Seminar, 5th Dec. 2014 Brussels, Belgium

"HDR Brachytherapy Treatment Verification", Australian Radiation Protection and Nuclear Safety Agency (ARPANSA), Department Seminar Series, Oct 2014, Yalambie, VIC, Australia

"Verifying Brachytherapy Treatment of Prostate Cancer" Southern Melbourne Cancer Symposium, 18th Sept 2014, Monash Comprehensive Cancer Consortium (MCCC), Clayton, VIC, Australia

"HDR brachytherapy treatment verification – Necessary but difficult" Department Seminar, February, 2014, Calvary Mater Newcastle, Newcastle, NSW, Australia

HDR Brachytherapy Source Position Verification and Dosimetry using an Electronic Portal Imaging Device [EPID]" William Buckland Radiotherapy Centre, Department Seminar Series, Mar 2013, Melbourne, Australia

Toward routine treatment verification in HDR brachytherapy" EPSM (Australian Medical Physics) Scientific Meeting, Dec 2012, Gold Coast, QLD, Australia

A.4.2 *Conference Presentations*

R.L. Smith, A Haworth, V. Panettieri, J.L. Millar, and R.D. Franich *"A 'Shift Image' 3D Reconstruction Technique for Identification of Catheter Displacement in HDR Prostate Brachytherapy"* EPSM (Australian Medical Physics) Scientific Meeting, Nov 2016, Sydney, NSW, Australia

R.L. Smith, A Haworth, V. Panettieri, J.L. Millar, and R.D. Franich *"Treatment Delivery Error Trapping in HDR Brachytherapy"* World Congress of Brachytherapy, June 2016 San Francisco, U.S.A.

R.L. Smith, A Haworth, V. Panettieri, B. Matheson, S Miller, H Mack, J.L. Millar and R.D. Franich *"An update of clnical treatment delivery verification of HDR prostate brachytherapy at Alfred Health"* Australasian Brachytherapy Group, Annual Scientific Meeting, Mar 2016, Fremantle, WA, Australia

R.L. Smith, J.L. Millar, A Haworth, M.L. Taylor and R.D. Franich *"In vivo Image Guided Brachytherapy Verification (IGBV) in high dose rate prostate brachytherapy - Initial Clinical Experience"* World Congress of Medical Physics, June 2015 Toronto, Canada

"Clinical implementation of in vivo source position verification in high dose rate prostate brachytherapy", 3rd ESTRO Forum, April 2015, Barcelona, Spain.

"In vivo treatment delivery error trapping in HDR prostate brachytherapy" Australasian Brachytherapy Group, Annual Scientific Meeting, Mar 2015, Sydney, Australia

"Clinical implementation of in vivo source position verification for high dose rate (HDR) prostate brachytherapy using a flat panel imager" Combined Scientific Meeting (CSM), Sept 2014, Melbourne, Australia

"High dose rate (HDR) brachytherapy treatment verification using an electronic portal imaging device (EPID)" Highlights: Best of Brachytherapy 2013, 2nd ESTRO Forum, April 2013, Geneva, Switzerland

"HDR Brachytherapy Source Position Verification and Dosimetry using an Electronic Portal Imaging Device [EPID]" Australasian Brachytherapy Group, Annual Scientific Meeting, Mar 2013, Brisbane, QLD

"Real-time in vivo Dosimetry in High Dose Rate Brachytherapy Using an Electronic Portal Imaging Device" EPSM (Australian Medical Physics) Scientific Meeting, Nov 2011, Darwin, NT

"High Dose Rate (HDR) brachytherapy in vivo treatment verification using an EPID" 11th International Workshop on Electronic Portal Imaging (EPI2kX), Apr 2010, Leuven, Belgium

Appendix B
Awards

Awards:

B.1 2016 Ian Snook Physics Prize, RMIT University.

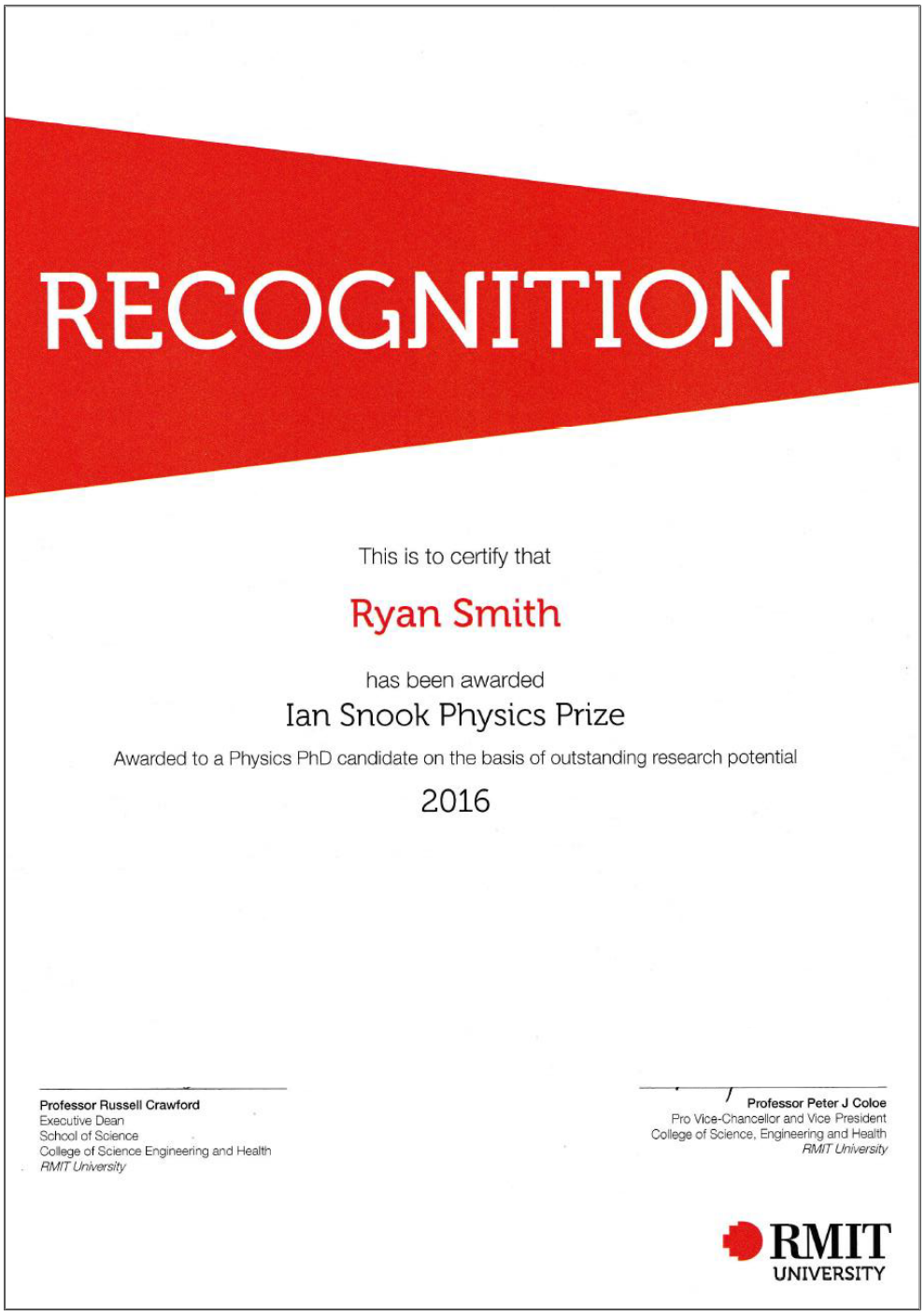

RECOGNITION

This is to certify that

Ryan Smith

has been awarded

Ian Snook Physics Prize

Awarded to a Physics PhD candidate on the basis of outstanding research potential

2016

Professor Russell Crawford
Executive Dean
School of Science
College of Science Engineering and Health
RMIT University

Professor Peter J Coloe
Pro Vice-Chancellor and Vice President
College of Science, Engineering and Health
RMIT University

RMIT UNIVERSITY

B.2 2015 GEC-ESTRO Elekta Brachytherapy Award, 3rd ESTRO Forum, Barcelona, Spain.

ESTRO
European Society for RADIOTHERAPY & ONCOLOGY

Brussels, 18 December 2014

Dear Ryan Smith,

On behalf of the GEC-ESTRO, I am pleased to inform you that you are the winner of the **ESTRO- Elekta Brachytherapy Award**. This award is presented to the most innovative abstract submitted for presentation at the 3rd ESTRO Forum. Your abstract **'Clinical implementation of in vivo source position verification in high dose rate prostate brachytherapy'** was found to meet this criterion.

The prize, amounting to 2000 EURO, will be presented to you during the 3rd ESTRO Forum, taking place in Barcelona, Spain from 24-28 April 2015. In the coming days, you will receive an email from the ESTRO Office informing you that the above-mentioned abstract was accepted for presentation as an oral communication in the **GEC-ESTRO Proffered Papers Session: In vivo dosimetry** on Saturday, 25 April 2015 from 16:45-18:00. You will be allocated 10 minutes for your presentation (discussion time included). The award will be presented to you following your presentation.

Congratulations on this award.

With best wishes,

Yours sincerely,

P. Poortmans
ESTRO President

Clinical implementation of *in vivo* source position verification in high dose rate prostate brachytherapy

Oral Presentation

Ryan L Smith[1,2], Annette Haworth[2,3], Jeremy L Millar[1,2], Bronwyn Matheson[1], Ben Hindson[1], Michael L Taylor[2] and Rick D Franich[1,2]

1 – William Buckland Radiotherapy Centre, The Alfred Hospital, Melbourne, Australia.
2 – School of Applied Sciences, RMIT University, Melbourne, Australia.
3 –Physical Sciences, Peter MacCallum Cancer Centre, East Melbourne, Australia.

Aim.

High dose rate (HDR) brachytherapy treatment is widely practiced but lacks independent routine treatment delivery verification to identify potential errors and ensure patient safety. We report our initial clinical experience with a novel, non-invasive, position-sensitive source-tracking system based on a flat panel detector (FPD) for treatment verification in HDR prostate brachytherapy.

Materials & Method.

The FPD was mounted in a standard operating theatre couch (BetaStar, Marquet) under a customised carbon fibre couch top assembly. Four prostate patients (8 treatment fractions) were included in this initial study. At treatment each patient was aligned on the couch with the target region centred over the sensitive imaging area of the FPD. Prior to treatment, three x-ray dwell position markers were inserted into selected catheters and a radiograph captured with the FPD to localise the implant relative to the detector. As the HDR source treatment dwells were delivered, images were acquired with the FPD and post-processed to determine the position of the source inside the patient. The source positions determined by the tracking system were compared to the treatment plan to verify correct treatment delivery.

Results.

Measured source dwell positions confirmed correct transfer tube connection, source step size and patient/plan selection. The mean linear distance between measured and planned positions (example fraction shown in Figure 1) was 1.8mm (range 0.7 to 3.9mm) after rigid registration with the plan. The average measured dwell step size for all measured catheters was 2.5mm (range 1.9 to 3.1mm; s.d. 0.2mm). The absolute position of the measured source dwells was evaluated by comparing the measured dwell positions with x-ray dwell position markers from the pre-treatment radiograph (mean 3.9mm, range 0.8 to 9.9mm). This, together with the implanted gold fiducial markers, visible on the radiograph, provided verification of programmed treatment indexer length and therefore delivery to the correct anatomical location. The total impact on procedure time was less than 15 minutes.

Conclusion.

The novel, non-invasive HDR brachytherapy treatment verification system was implemented clinically, providing verification of many treatment parameters by tracking the position of the HDR source as treatment was delivered. The novel application of the FPD allows verification that treatment delivery was free of most potential human related errors identified in ICRP 97. This concept and system will meaningfully improve safety standards by allowing routine treatment verification in HDR brachytherapy across a range of clinical applications.

Appendix C
Software

This appendix contains a brief description and screen shot of the different software modules that were developed during this project to enable the application of many of the concepts described in this work.

- **BrachyLAB** – A multi-purpose module that allows various source position calculation algorithms to be applied to FPD images, compared, and raw profile data exported.
- **Patient Analysis** – A module that allows pre-treatment image analysis, identification of fiducial markers, identification of catheter marker points, importing of TPS catheter and dwell position data and 2D registration function for treatment verification.
- **Pre-Treatment Verification 2D** – A module with a structured user-interface allowing clinical staff to import data from the TPS, import a pre-treatment A-P image and perform catheter displacement evaluation at the treatment console in real-time.
- **Pre-Treatment Verification 3D** – A module that allows two oblique images to be loaded and corresponding features in each image to be identified for the purpose of 3D implant reconstruction.

C.1 BrachyLAB

The 'BrachyLAB' software was developed to allow various source position calculation algorithms to be applied to FPD images, compared, and raw profile data exported.

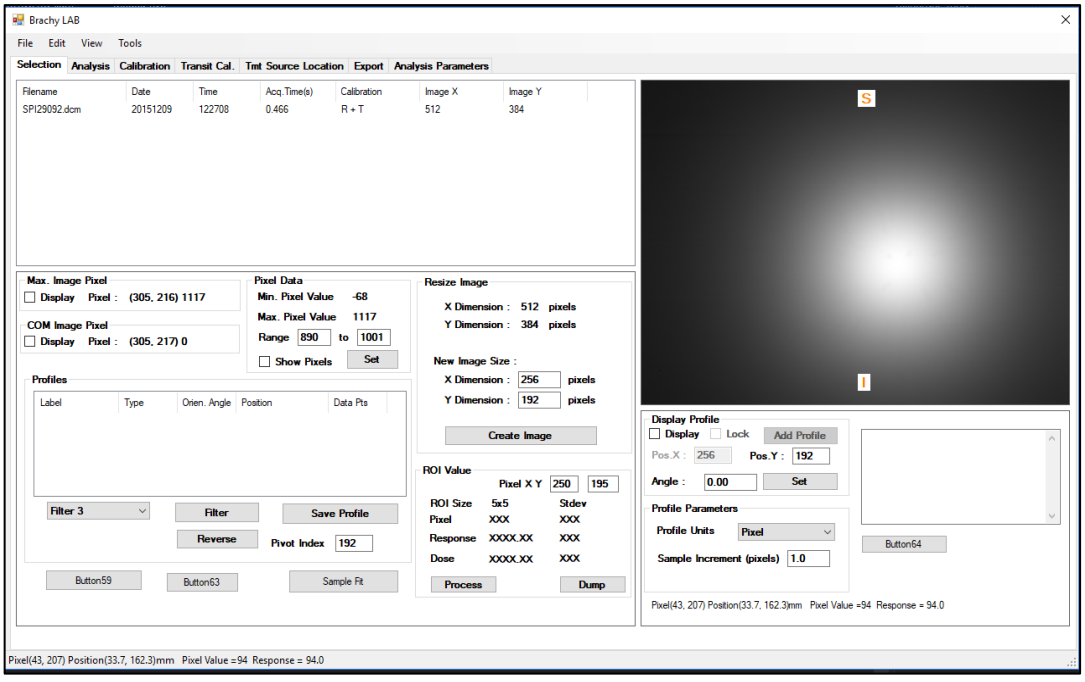

C.2 Patient Analysis

The 'Patient Analysis' software was developed to perform post treatment processing of the A-P images acquired during pre-treatment imaging. The software functionality enabled the fiducial markers and catheter marker points in the image to be identified, importing of the TPS data for registration and comparison with the measured positions. The comparison data could be exported for further analysis.

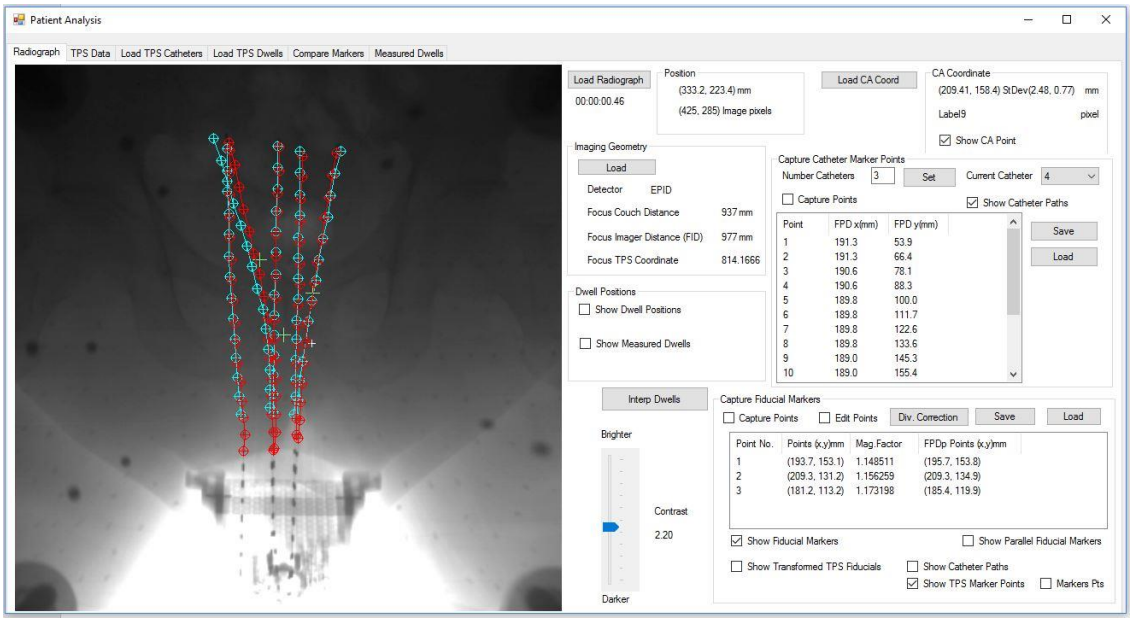

C.3 Pre-Treatment Verification 2D

The 'Pre-Treatment Verification 2D' software was with a structured user-interface allowing clinical staff to import data from the TPS, import a pre-treatment A-P image and perform catheter displacement evaluation at the treatment console in real-time.

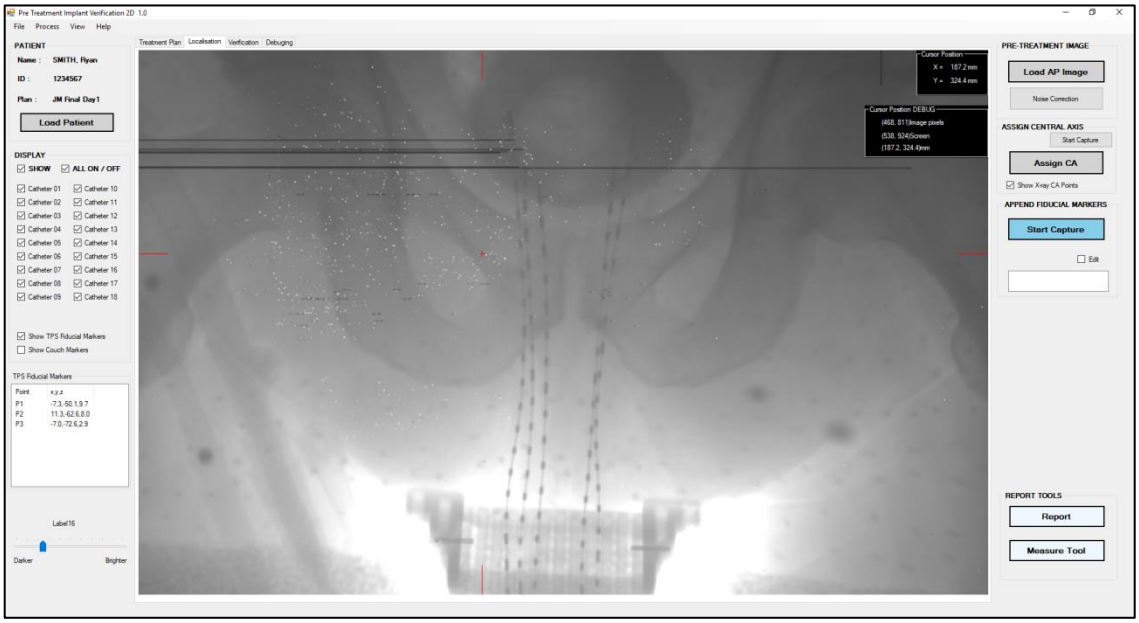

C.4 Pre-Treatment Verification 3D

The 'Pre-Treatment Verification 3D' software was developed to allow two oblique images to be loaded and corresponding features in each image to be identified for the purpose of 3D implant reconstruction.

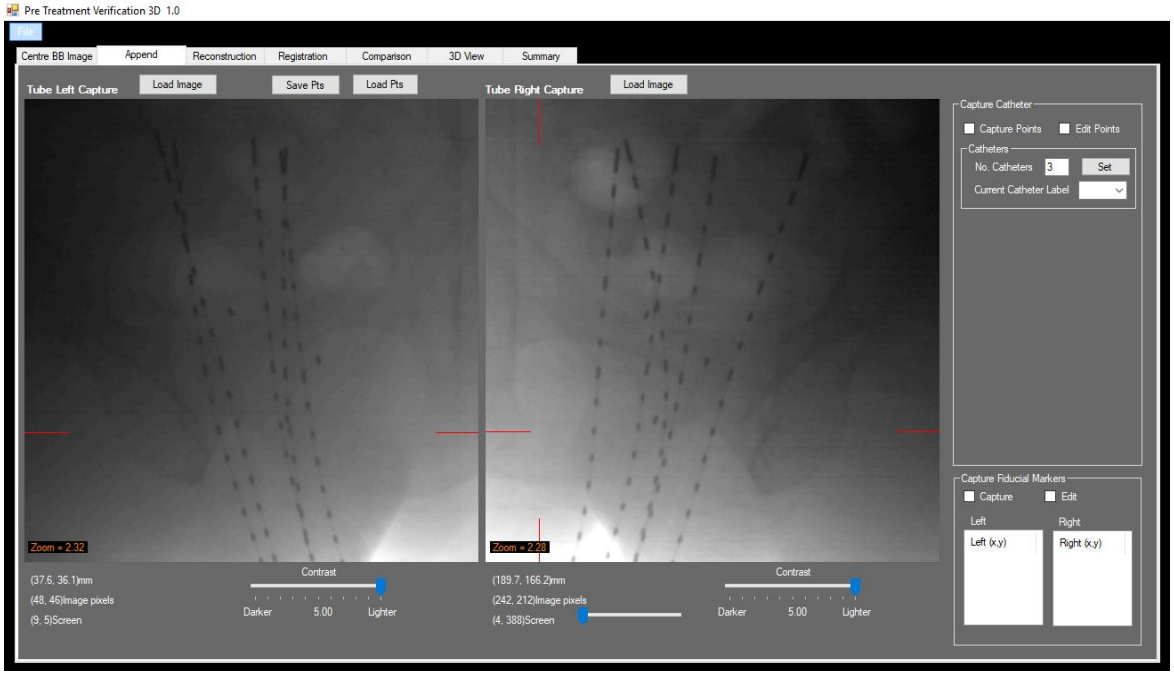

References

1. Tanderup, K., et al., *In vivo dosimetry in brachytherapy.* Med Phys, 2013. **40**(7): p. 070902.
2. Kertzscher, G., et al., *In vivo dosimetry: trends and prospects for brachytherapy.* Br J Radiol, 2014. **87**(1041): p. 20140206.
3. White, E.C., et al., *High-dose-rate prostate brachytherapy consistently results in high quality dosimetry.* Int J Radiat Oncol Biol Phys, 2013. **85**(2): p. 543-8.
4. Han, K., et al., *Trends in the utilization of brachytherapy in cervical cancer in the United States.* Int J Radiat Oncol Biol Phys, 2013. **87**(1): p. 111-9.
5. Grimm, P., et al., *Comparative analysis of prostate-specific antigen free survival outcomes for patients with low, intermediate and high risk prostate cancer treatment by radical therapy. Results from the Prostate Cancer Results Study Group.* BJU Int, 2012. **109 Suppl 1**: p. 22-9.
6. Morton, G.C., *High-dose-rate brachytherapy boost for prostate cancer: rationale and technique.* J Contemp Brachytherapy, 2014. **6**(3): p. 323-30.
7. Siebert, F.A., et al., *Imaging of implant needles for real-time HDR-brachytherapy prostate treatment using biplane ultrasound transducers.* Med Phys, 2009. **36**(8): p. 3406-12.
8. Dempsey, C., et al., *Optimal single 3T MR imaging sequence for HDR brachytherapy of cervical cancer.* J Contemp Brachytherapy, 2014. **6**(1): p. 3-9.
9. Tanderup, K., et al., *Magnetic resonance image guided brachytherapy.* Semin Radiat Oncol, 2014. **24**(3): p. 181-91.
10. Petric, P., et al., *Uncertainties of target volume delineation in MRI guided adaptive brachytherapy of cervix cancer: a multi-institutional study.* Radiother Oncol, 2013. **107**(1): p. 6-12.
11. Hellebust, T.P., et al., *Dosimetric impact of interobserver variability in MRI-based delineation for cervical cancer brachytherapy.* Radiother Oncol, 2013. **107**(1): p. 13-9.
12. Kirisits, C., et al., *Review of clinical brachytherapy uncertainties: analysis guidelines of GEC-ESTRO and the AAPM.* Radiother Oncol, 2014. **110**(1): p. 199-212.
13. Lessard, E. and J. Pouliot, *Inverse planning anatomy-based dose optimization for HDR-brachytherapy of the prostate using fast simulated annealing algorithm and dedicated objective function.* Med Phys, 2001. **28**(5): p. 773-9.
14. Lahanas, M., D. Baltas, and S. Giannouli, *Global convergence analysis of fast multiobjective gradient-based dose optimization algorithms for high-dose-rate brachytherapy.* Phys Med Biol, 2003. **48**(5): p. 599-617.
15. Valentin, J., *Prevention of high-dose-rate brachytherapy accidents. ICRP Publication 97.* Ann ICRP, 2005. **35**(2): p. 1-51.
16. Thilmann, C., et al., *Correction of patient positioning errors based on in-line cone beam CTs: clinical implementation and first experiences.* Radiat Oncol, 2006. **1**: p. 16.
17. Rogus, R.D., R.L. Stern, and H.D. Kubo, *Accuracy of a photogrammetry-based patient positioning and monitoring system for radiation therapy.* Med Phys, 1999. **26**(5): p. 721-8.
18. Moore, C., et al., *Opto-electronic sensing of body surface topology changes during radiotherapy for rectal cancer.* Int J Radiat Oncol Biol Phys, 2003. **56**(1): p. 248-58.

19. Jaffray, D.A., et al., *A radiographic and tomographic imaging system integrated into a medical linear accelerator for localization of bone and soft-tissue targets.* Int J Radiat Oncol Biol Phys, 1999. **45**(3): p. 773-89.
20. van der Horst, A., et al., *Interfractional position variation of pancreatic tumors quantified using intratumoral fiducial markers and daily cone beam computed tomography.* Int J Radiat Oncol Biol Phys, 2013. **87**(1): p. 202-8.
21. Hamming-Vrieze, O., et al., *Evaluation of tumor shape variability in head-and-neck cancer patients over the course of radiation therapy using implanted gold markers.* Int J Radiat Oncol Biol Phys, 2012. **84**(2): p. e201-7.
22. Mijnheer, B., et al., *In vivo dosimetry in external beam radiotherapy.* Med Phys, 2013. **40**(7): p. 070903.
23. McDermott, L.N., et al., *Replacing pretreatment verification with in vivo EPID dosimetry for prostate IMRT.* Int J Radiat Oncol Biol Phys, 2007. **67**(5): p. 1568-77.
24. Kirby, M.C. and P.C. Williams, *The use of an electronic portal imaging device for exit dosimetry and quality control measurements.* Int J Radiat Oncol Biol Phys, 1995. **31**(3): p. 593-603.
25. Barney, B.M., et al., *Image-guided radiotherapy (IGRT) for prostate cancer comparing kV imaging of fiducial markers with cone beam computed tomography (CBCT).* Int J Radiat Oncol Biol Phys, 2011. **80**(1): p. 301-5.
26. Keall, P.J., et al., *The first clinical treatment with kilovoltage intrafraction monitoring (KIM): a real-time image guidance method.* Med Phys, 2015. **42**(1): p. 354-8.
27. Shah, A.P., et al., *Real-time tumor tracking in the lung using an electromagnetic tracking system.* Int J Radiat Oncol Biol Phys, 2013. **86**(3): p. 477-83.
28. Zelefsky, M.J., et al., *Improved clinical outcomes with high-dose image guided radiotherapy compared with non-IGRT for the treatment of clinically localized prostate cancer.* Int J Radiat Oncol Biol Phys, 2012. **84**(1): p. 125-9.
29. Brabbins, D., et al., *A dose-escalation trial with the adaptive radiotherapy process as a delivery system in localized prostate cancer: analysis of chronic toxicity.* Int J Radiat Oncol Biol Phys, 2005. **61**(2): p. 400-8.
30. Pham, D., et al., *Stereotactic ablative body radiation therapy for primary kidney cancer: a 3-dimensional conformal technique associated with low rates of early toxicity.* Int J Radiat Oncol Biol Phys, 2014. **90**(5): p. 1061-8.
31. Hoskin, P.J., et al., *High dose rate afterloading brachytherapy for prostate cancer: catheter and gland movement between fractions.* Radiother Oncol, 2003. **68**(3): p. 285-8.
32. Damore, S.J., et al., *Needle displacement during HDR brachytherapy in the treatment of prostate cancer.* Int J Radiat Oncol Biol Phys, 2000. **46**(5): p. 1205-11.
33. Whitaker, M., et al., *Prostate HDR brachytherapy catheter displacement between planning and treatment delivery.* Radiother Oncol, 2011. **101**(3): p. 490-4.
34. Kim, Y., I.C. Hsu, and J. Pouliot, *Measurement of craniocaudal catheter displacement between fractions in computed tomography-based high dose rate brachytherapy of prostate cancer.* J Appl Clin Med Phys, 2007. **8**(4): p. 2415.
35. Holly, R., et al., *Use of cone-beam imaging to correct for catheter displacement in high dose-rate prostate brachytherapy.* Brachytherapy, 2011. **10**(4): p. 299-305.
36. Mullokandov, E. and G. Gejerman, *Analysis of serial CT scans to assess template and catheter movement in prostate HDR brachytherapy.* Int J Radiat Oncol Biol Phys, 2004. **58**(4): p. 1063-71.
37. Kawakami, S., et al., *Catheter displacement prior to the delivery of high-dose-rate brachytherapy in the treatment of prostate cancer patients.* J Contemp Brachytherapy, 2014. **6**(2): p. 161-6.
38. Alecu, R. and M. Alecu, *In-vivo rectal dose measurements with diodes to avoid misadministrations during intracavitary high dose rate brachytherapy for carcinoma of the cervix.* Med Phys, 1999. **26**(5): p. 768-70.

39. Tanderup, K., et al., *Geometric stability of intracavitary pulsed dose rate brachytherapy monitored by in vivo rectal dosimetry.* Radiother Oncol, 2006. **79**(1): p. 87-93.
40. Brezovich, I.A., et al., *In vivo urethral dose measurements: a method to verify high dose rate prostate treatments.* Med Phys, 2000. **27**(10): p. 2297-301.
41. Andersen, C.E., et al., *Time-resolved in vivo luminescence dosimetry for online error detection in pulsed dose-rate brachytherapy.* Med Phys, 2009. **36**(11): p. 5033-43.
42. Kertzscher, G., et al., *Identifying afterloading PDR and HDR brachytherapy errors using real-time fiber-coupled Al(2)O(3):C dosimetry and a novel statistical error decision criterion.* Radiother Oncol, 2011. **100**(3): p. 456-62.
43. Therriault-Proulx, F., et al., *A phantom study of an in vivo dosimetry system using plastic scintillation detectors for real-time verification of 192Ir HDR brachytherapy.* Med Phys, 2011. **38**(5): p. 2542-51.
44. Therriault-Proulx, F., S. Beddar, and L. Beaulieu, *On the use of a single-fiber multipoint plastic scintillation detector for 192Ir high-dose-rate brachytherapy.* Med Phys, 2013. **40**(6): p. 062101.
45. Das, R., et al., *Thermoluminescence dosimetry for in-vivo verification of high dose rate brachytherapy for prostate cancer.* Australas Phys Eng Sci Med, 2007. **30**(3): p. 178-84.
46. Mason, J., et al., *Real-time in vivo dosimetry in high dose rate prostate brachytherapy.* Radiother Oncol, 2016. **120**(2): p. 333-8.
47. Waldhausl, C., et al., *In-vivo dosimetry for gynaecological brachytherapy: physical and clinical considerations.* Radiother Oncol, 2005. **77**(3): p. 310-7.
48. Seymour, E.L., et al., *In vivo real-time dosimetric verification in high dose rate prostate brachytherapy.* Med Phys, 2011. **38**(8): p. 4785-94.
49. Cartwright, L.E., et al., *The angular dependence and effective point of measurement of a cylindrical scintillation dosimeter with and without a radio-opaque marker for brachytherapy.* Phys Med Biol, 2009. **54**(7): p. 2217-27.
50. Suchowerska, N., et al., *Clinical trials of a urethral dose measurement system in brachytherapy using scintillation detectors.* Int J Radiat Oncol Biol Phys, 2011. **79**(2): p. 609-15.
51. Haughey, A., G. Coalter, and K. Mugabe, *Evaluation of linear array MOSFET detectors for in vivo dosimetry to measure rectal dose in HDR brachytherapy.* Australas Phys Eng Sci Med, 2011. **34**(3): p. 361-6.
52. Zaman, Z.K., et al., *Comparison of planned and measured rectal dose in-vivo during high dose rate Cobalt-60 brachytherapy of cervical cancer.* Phys Med, 2014.
53. Toye, W., et al., *An in vivo investigative protocol for HDR prostate brachytherapy using urethral and rectal thermoluminescence dosimetry.* Radiother Oncol, 2008.
54. Anagnostopoulos, G., et al., *In vivo thermoluminescence dosimetry dose verification of transperineal 192Ir high-dose-rate brachytherapy using CT-based planning for the treatment of prostate cancer.* Int J Radiat Oncol Biol Phys, 2003. **57**(4): p. 1183-91.
55. Kertzscher, G., C.E. Andersen, and K. Tanderup, *Adaptive error detection for HDR/PDR brachytherapy: guidance for decision making during real-time in vivo point dosimetry.* Med Phys, 2014. **41**(5): p. 052102.
56. Reniers, B., et al., *In vivo dosimetry for gynaecological brachytherapy using a novel position sensitive radiation detector: feasibility study.* Med Phys, 2012. **39**(4): p. 1925-35.
57. Jursinic, P., *Quality assurance measurements for high-dose-rate brachytherapy without film.* J Appl Clin Med Phys, 2014. **15**(1): p. 4586.
58. Kojima, H., et al., *New method for obtaining position and time structure of source in HDR remote afterloading brachytherapy unit utilizing light emission from scintillator.* Journal of applied clinical medical physics / American College of Medical Physics, 2009. **10**(3): p. 2983.
59. Duan, J., et al., *Real-time monitoring and verification of in vivo high dose rate brachytherapy using a pinhole camera.* Med Phys, 2001. **28**(2): p. 167-73.

60. Espinoza, A., et al., *The feasibility study and characterization of a two-dimensional diode array in "magic phantom" for high dose rate brachytherapy quality assurance.* Med Phys, 2013. **40**(11): p. 111702.
61. Safavi-Naeini, M., et al., *BrachyView, a novel inbody imaging system for HDR prostate brachytherapy: design and Monte Carlo feasibility study.* Med Phys, 2013. **40**(7): p. 071715.
62. Nose, T., et al., *In vivo dosimetry of high-dose-rate interstitial brachytherapy in the pelvic region: use of a radiophotoluminescence glass dosimeter for measurement of 1004 points in 66 patients with pelvic malignancy.* Int J Radiat Oncol Biol Phys, 2008. **70**(2): p. 626-33.
63. Gagliardi, F.M., et al., *Intra-cavitary dosimetry for IMRT head and neck treatment using thermoluminescent dosimeters in a naso-oesophageal tube.* Phys Med Biol, 2009. **54**(12): p. 3649-57.
64. Carrara, M., et al., *In vivo rectal wall measurements during HDR prostate brachytherapy with MOSkin dosimeters integrated on a trans-rectal US probe: Comparison with planned and reconstructed doses.* Radiother Oncol, 2016. **118**(1): p. 148-53.
65. Gambarini, G., et al., *Online in vivo dosimetry in high dose rate prostate brchytherapy with MOSkin detectors: in phantom feasibility study.* Appl Radiat Isot, 2014. **83 Pt C**: p. 222-6.
66. Therriault-Proulx, F., et al., *In vivo dose measurements for high-dose-rate brachytherapy using a new scintillating fiber dosimetry system: A prostate phantom study.* Brachytherapy, 2009. **8**(2).
67. Evans, M.D., S. Devic, and E.B. Podgorsak, *High dose-rate brachytherapy source position quality assurance using radiochromic film.* Med Dosim, 2007. **32**(1): p. 13-5.
68. Rickey, D.W., D. Sasaki, and J. Bews, *A quality assurance tool for high-dose-rate brachytherapy.* Med Phys, 2010. **37**(6): p. 2525-32.
69. Nakano, T., et al., *High dose-rate brachytherapy source localization: positional resolution using a diamond detector.* Phys Med Biol, 2003. **48**(14): p. 2133-46.
70. Song, H., et al., *Tracking brachytherapy sources using emission imaging with one flat panel detector.* Med Phys, 2009. **36**(4): p. 1109-11.
71. Espinoza, A., et al., *The evaluation of a 2D diode array in "magic phantom" for use in high dose rate brachytherapy pretreatment quality assurance.* Med Phys, 2015. **42**(2): p. 663-73.
72. Kojima, H., et al., *New method for obtaining position and time structure of source in HDR remote afterloading brachytherapy unit utilizing light emission from scintillator.* J Appl Clin Med Phys, 2009. **10**(3): p. 2983.
73. Nose, T., et al., *Real-Time Verification of a High-Dose-Rate Iridium 192 Source Position Using a Modified C-Arm Fluoroscope.* Int J Radiat Oncol Biol Phys, 2017. **97**(4): p. 858-865.
74. Martinez, A.A., et al., *Phase II prospective study of the use of conformal high-dose-rate brachytherapy as monotherapy for the treatment of favorable stage prostate cancer: a feasibility report.* Int J Radiat Oncol Biol Phys, 2001. **49**(1): p. 61-9.
75. Simnor, T., et al., *Justification for inter-fraction correction of catheter movement in fractionated high dose-rate brachytherapy treatment of prostate cancer.* Radiother Oncol, 2009. **93**(2): p. 253-8.
76. Tiong, A., et al., *A small tolerance for catheter displacement in high-dose rate prostate brachytherapy is necessary and feasible.* Int J Radiat Oncol Biol Phys, 2010. **76**(4): p. 1066-72.
77. Yoshida, K., et al., *Needle applicator displacement during high-dose-rate interstitial brachytherapy for prostate cancer.* Brachytherapy, 2010. **9**(1): p. 36-41.
78. Takenaka, T., et al., *Assessment of daily needle applicator displacement during high-dose-rate interstitial brachytherapy for prostate cancer using daily CT examinations.* J Radiat Res, 2012. **53**(3): p. 469-74.

79. Kovalchuk, N., et al., *Dosimetric effect of interfractional needle displacement in prostate high-dose-rate brachytherapy.* Brachytherapy, 2012. **11**(2): p. 111-8.
80. Huang, Y., et al., *Online correction of catheter movement using CT in high-dose-rate prostate brachytherapy.* Brachytherapy, 2013. **12**(3): p. 260-6.
81. Peddada, A.V., et al., *Prevention of needle displacement in multifraction high-dose-rate prostate brachytherapy: A prospective volumetric analysis and technical considerations.* Pract Radiat Oncol, 2015. **5**(4): p. 228-37.
82. Lauche, O., et al., *Single-fraction high-dose-rate brachytherapy using real-time transrectal ultrasound based planning in combination with external beam radiotherapy for prostate cancer: dosimetrics and early clinical results.* J Contemp Brachytherapy, 2016. **8**(2): p. 104-9.
83. Damato, A.L., et al., *A system to use electromagnetic tracking for the quality assurance of brachytherapy catheter digitization.* Med Phys, 2014. **41**(10): p. 101702.
84. Bharat, S., et al., *Electromagnetic tracking for catheter reconstruction in ultrasound-guided high-dose-rate brachytherapy of the prostate.* Brachytherapy, 2014. **13**(6): p. 640-50.
85. Poulin, E., et al., *Fast, automatic, and accurate catheter reconstruction in HDR brachytherapy using an electromagnetic 3D tracking system.* Med Phys, 2015. **42**(3): p. 1227-32.
86. Beaulieu, L., et al., *Real-time electromagnetic tracking-based treatment platform for high-dose-rate prostate brachytherapy: Clinical workflows and end-to-end validation.* Brachytherapy, 2017.
87. Meertens, H., et al., *First clinical experience with a newly developed electronic portal imaging device.* Int J Radiat Oncol Biol Phys, 1990. **18**(5): p. 1173-81.
88. O'Neill, A.G., et al., *Fiducial marker guided prostate radiotherapy: a review.* Br J Radiol, 2016. **89**(1068): p. 20160296.
89. Woodruff, H.C., et al., *First Experience With Real-Time EPID-Based Delivery Verification During IMRT and VMAT Sessions.* Int J Radiat Oncol Biol Phys, 2015. **93**(3): p. 516-22.
90. Fuangrod, T., et al., *A system for EPID-based real-time treatment delivery verification during dynamic IMRT treatment.* Med Phys, 2013. **40**(9): p. 091907.
91. Van Esch, A., et al., *Pre-treatment dosimetric verification by means of a liquid-filled electronic portal imaging device during dynamic delivery of intensity modulated treatment fields.* Radiother Oncol, 2001. **60**(2): p. 181-90.
92. Wendling, M., et al., *Accurate two-dimensional IMRT verification using a back-projection EPID dosimetry method.* Med Phys, 2006. **33**(2): p. 259-73.
93. McDermott, L.N., et al., *3D in vivo dose verification of entire hypo-fractionated IMRT treatments using an EPID and cone-beam CT.* Radiother Oncol, 2008. **86**(1): p. 35-42.
94. McCurdy, B.M., K. Luchka, and S. Pistorius, *Dosimetric investigation and portal dose image prediction using an amorphous silicon electronic portal imaging device.* Med Phys, 2001. **28**(6): p. 911-24.
95. Kirkby, C. and R. Sloboda, *Consequences of the spectral response of an a-Si EPID and implications for dosimetric calibration.* Med Phys, 2005. **32**(8): p. 2649-58.
96. Vial, P., et al., *Initial evaluation of a commercial EPID modified to a novel direct-detection configuration for radiotherapy dosimetry.* Med Phys, 2008. **35**(10): p. 4362-74.
97. Smith, R.L., et al., *Source position verification and dosimetry in HDR brachytherapy using an EPID.* Med Phys, 2013. **40**(11): p. 111706.
98. Varian-Medical-Systems, *Portal Vision aS500 Reference Manual.* 2000. **PV6005RM_aS500**.
99. Rivard, M.J., et al., *Update of AAPM Task Group No. 43 Report: A revised AAPM protocol for brachytherapy dose calculations.* Med Phys, 2004. **31**(3): p. 633-74.
100. International-Organization-for-Standardization, *X and gamma reference radiation for calibrating dosemeters and doserate meters and for determining their response as a*

function of photon energy - Part 1: Radiation characteristics and production methods. International Standards ISO 4037-1, ISO, Geneva, 1996.
101. Daskalov, G.M., E. Loffler, and J.F. Williamson, *Monte Carlo-aided dosimetry of a new high dose-rate brachytherapy source.* Med Phys, 1998. **25**(11): p. 2200-8.
102. Russell, K.R. and A. Ahnesjo, *Dose calculation in brachytherapy for a 192Ir source using a primary and scatter dose separation technique.* Physics in medicine and biology, 1996. **41**(6): p. 1007-24.
103. McDermott, L.N., et al., *Dose-response and ghosting effects of an amorphous silicon electronic portal imaging device.* Med Phys, 2004. **31**(2): p. 285-95.
104. Winkler, P., A. Hefner, and D. Georg, *Implementation and validation of portal dosimetry with an amorphous silicon EPID in the energy range from 6 to 25 MV.* Phys Med Biol, 2007. **52**(15): p. N355-65.
105. McDermott, L.N., et al., *Comparison of ghosting effects for three commercial a-Si EPIDs.* Med Phys, 2006. **33**(7): p. 2448-51.
106. Arun, K.S., T.S. Huang, and S.D. Blostein, *Least-squares fitting of two 3-d point sets.* IEEE Trans Pattern Anal Mach Intell, 1987. **9**(5): p. 698-700.
107. Cuijpers, J.P., *Clinical use of a non-isocentric C-arm unit for on-line filmless reconstruction of brachytherapy applicators.* Radiother Oncol, 2001. **61**(2): p. 203-9.
108. Liu, L., et al., *On the use of C-arm fluoroscopy for treatment planning in high dose rate brachytherapy.* Med Phys, 2003. **30**(9): p. 2297-302.
109. Palvolgyi, J., *To what extent can digital images obtained with a non-isocentric C-arm be used for brachytherapy treatment planning in gynaecology.* Radiother Oncol, 2003. **67**(1): p. 107-12.
110. Kolkman-Deurloo, I.K., et al., *Reconstruction accuracy of a dedicated localiser for filmless planning in intra-operative brachytherapy.* Radiother Oncol, 1997. **44**(1): p. 73-81.
111. Brunet-Benkhoucha, M., et al., *Clinical implementation of a digital tomosynthesis-based seed reconstruction algorithm for intraoperative postimplant dose evaluation in low dose rate prostate brachytherapy.* Med Phys, 2009. **36**(11): p. 5235-44.
112. Haworth, A., et al., *Registration of prostate volume with radiographically identified I-125 seeds for permanent implant evaluation.* J. Brachytherapy Int., 2000. **16**: p. 157-167.
113. Murphy, M.J. and D.A. Todor, *Demonstration of a forward iterative method to reconstruct brachytherapy seed configurations from x-ray projections.* Phys Med Biol, 2005. **50**(11): p. 2715-37.
114. Todor, D.A., et al., *Operator-free, film-based 3D seed reconstruction in brachytherapy.* Phys Med Biol, 2002. **47**(12): p. 2031-48.
115. Johansen, J.G., et al., *Time-resolved in vivo dosimetry for source tracking in brachytherapy.* Brachytherapy, 2017.
116. Zwahlen, D.R., et al., *High-dose-rate brachytherapy in combination with conformal external beam radiotherapy in the treatment of prostate cancer.* Brachytherapy, 2010. **9**(1): p. 27-35.
117. Martinez, A.A., et al., *Dose escalation improves cancer-related events at 10 years for intermediate- and high-risk prostate cancer patients treated with hypofractionated high-dose-rate boost and external beam radiotherapy.* Int J Radiat Oncol Biol Phys, 2011. **79**(2): p. 363-70.
118. Zelefsky, M.J., et al., *Dose escalation for prostate cancer radiotherapy: predictors of long-term biochemical tumor control and distant metastases-free survival outcomes.* Eur Urol, 2011. **60**(6): p. 1133-9.